Structure-led Studies of SLC4 Transporters in Physiology and Pathophysiology

by

Katherine Emily Badior

A thesis submitted in partial fulfillment of the requirements for the degree of

Doctor of Philosophy

Department of Biochemistry
University of Alberta

Abstract

AE1 mediates electroneutral Cl^-/HCO_3^- exchange in red blood cells and kidney. The X-ray crystal structure of AE1 at 3.5 Å resolution provided the first human SLC4 protein structure at resolution sufficient to gain mechanistic insights, to AE1 specifically and to SLC4 family members by extension. Here, the structure of the AE1 membrane domain was used to guide studies of SLC4 proteins AE1 (SLC4A1) and SLC4A11.

SLC4A11 mutants cause the blinding corneal dystrophy Congenital Hereditary Endothelial Dystrophy (CHED) and some cases of Fuchs Endothelial Corneal Dystrophy (FECD). A three-dimensional homology model of the SLC4A11 membrane domain was created, using the AE1 structure as a template. To assess the validity of the homology model we predicted molecular phenotypes of *de novo* membrane domain mutations, on the basis of the model. The biochemical properties of these mutants were consistent with predictions, revealing the reliability of the homology model. The model was used to map forty-five identified corneal dystrophy-causing mutations, and for each mutation the disease-causing effect was rationalized and categorized. Amongst membrane domain mutants 73% were predicted to cause disease by affecting protein folding and 27% by directly affecting protein function.

AE1 is the predominant integral membrane protein in red blood cells (RBCs). Senescent RBCs are cleared from circulation by macrophages, which recognize RBCs coated by AE1-directed auto-antibodies. Senescence auto-antibodies react with AE1 residues 812-830, a region which has characteristics of both extracellular and intracellular localization. To investigate the discrepancy in localization of the AE1 812-830 region, we tested the accessibility of AE1 residues

to extracellular, membrane-impermeant probes. In live HEK293 cells, residues within the AE1 812-830 region demonstrated extracellular accessibility inconsistent with the intracellular localization seen in the X-ray crystal structure. Conversely, in fixed HEK293 cells, 84% of AE1 molecules displayed intracellular localization of the 812-830 region. Taken together, these data indicate that the AE1 812-830 senescent antigen undergoes transient intracellular to extracellular reorientation. This reorientation was not abolished by inhibiting transporter movements required for anion exchange or restricted by modifications used to crystallize AE1. Extracellular antibody directed against the AE1 812-830 region bound AE1 expressed in HEK293 cells but was unable to bind AE1 in RBCs, suggesting a role of the glycocalyx in limiting RBC opsonization.

IgG eluted from RBCs could immunoprecipitate AE1 but did not bind to AE1 on immunoblots. This indicates that the antibody requires a conformational epitope. Thus, senescent cell IgG recognizes a conformational epitope of AE1, comprised of a reorienting region with limited surface exposure. This collectively indicates that the red blood cell senescence signalling is mediated by extracellular exposure of the AE1 senescent cell epitope.

Together, these structure-led studies provide new insight into established (AE1 senescence) and emerging (SLC4A11) fields of SLC4 protein physiology and pathophysiology.

Preface

The experiments and results in this thesis are the original work by Katherine Badior, unless otherwise indicated.

A version of chapter 3 has been published as Badior, K. E., Alka, K., and Casey, J. R. (2017) SLC4A11 Three-Dimensional Homology Model Rationalizes Corneal Dystrophy-Causing Mutations. *Hum Mutat* **38**, 279-288 (reproduced with permission). All experiments were carried out by Katherine Badior except cloning, characterization of cell surface trafficking, and transport activity of novel SLC4A11 point mutants, which were carried out by Dr. Kumari Alka. The manuscript was written by KB with edits by JRC and KA.

A version of chapter 4 is in preparation for submission as Badior, K. E., Branch, D., and Casey, J. R. (2020) AE1 as a Molecular Clock for Red Cell Senescence. All experiments in chapter 4 were carried out by Katherine Badior except preparation of senescent cell IgG, which was carried out by Dr. Evgenia Bloch (University of Toronto). Red blood cells used in chapter 4 were obtained after Canadian Blood Services Research Ethics Board approval (Project Name: Molecular mechanism for signaling red blood cell senescence, REB ID 2019.045).

Acknowledgements

I have many people to thank for their support and guidance throughout my graduate studies. First and foremost, I would like to thank my supervisor Dr. Joseph Casey, a constant source of guidance, unwavering support and encouragement. I am thankful for the opportunities I've had during my degree thanks to him. In addition to lessons learned at the bench, my graduate studies in his lab have included many life lessons about professionalism and people. While I've stopped being surprised by how much his advice has been applicable to life outside of the lab, I will continue to carry it forward with me. I'm eternally grateful for his guidance and support through my Ph.D., and for shaping me into the scientist I am today.

I would like to thank my committee members, Dr. Joanne Lemieux and Dr. Bernard Lemire. They have kept me inspired and focused with their input and advice. In particular, the guidance and passion of Dr. Joanne Lemieux has been a great source of inspiration throughout my Ph.D., as well as continued motivation to pursue research further. I am deeply appreciative of the suggestions and thoughtful insights of Dr. Reinhart Reithmeier, whose enthusiasm is both unceasing and contagious. I am thankful for the support of Dr. Mark Glover, Dr. Nicolas Touret, Dr. Jason Acker, and Dr. Donald Branch through various times of my Ph.D.

The support of my lab mates cannot be understated. Dr. Darpan Malhotra has been a great source of support and friendship, always ready to talk through an experiment, celebrate a success, or share a commiserative coffee following a failure. I am thankful for the support of my colleagues over the years, Dr. Bernardo Alvarez, Dr. Sampath Loganathan, Chris Lukowski, Nada Alshumaimeri, and Dr. Alka Kumari. I am thankful to the fellow graduate students, staff, and

members of Department of Biochemistry and Physiology, and the members of Membrane Protein Research Disease Group.

I would like to extend a special thank you to my parents for their constant encouragement and moral support. They have wholeheartedly embraced and supported my passion for science since the early days of forming gallium spoons in the family freezer, and I would not have been able to do this without them. Finally, I would like to thank my husband Michael, who handled a lot of my late nights at the lab, science-related frustrations, and immunoblots presented without context with unyielding support and confidence.

Table of Contents

List of Figures

List of Tables

List of Abbreviations

α814-827; Rabbit antibody against a peptide corresponding to human AE1 amino acids 814-827

αEL3; Rabbit antibody against a peptide corresponding to human SLC4A11 extracellular loop 3 amino acids 527–540

AE1; Cl^-/HCO_3^- anion exchanger SLC4A1, also called Band 3

AE1C$^-$; AE1 with five endogenous cysteines mutated to serine

AE1MD; AE1 membrane domain

BCA; Bicinchoninic acid

BSA; Bovine serum albumin

CAII; Carbonic anhydrase II

CD; Cytoplasmic domain

CHED; Congenital hereditary endothelial dystrophy

CP; Catalytic pathway

DAPI; 4′,6-diamidino-2-phenylindole

DI; Dimer interface

DIDS; 4,4'-Diisothiocyano-2,2'-stilbenedisulfonic acid

DMEM; Dulbecco's modified Eagle's medium

DMSO; Dimethyl sulfoxide

eAE1; Erythrocyte AE1

ECL; Extracellular loop

ECL Reagent; Enhanced chemiluminescence immunoblot detection reagent

EDTA; Ethylenediaminetetraacetic acid

ER; Endoplasmic reticulum

ExScEp; Extracellular Senescent Cell Epitope

Fab; Antigen-binding fragment

FECD; Fuchs endothelial corneal dystrophy

FBS; Fetal bovine serum

GAPDH; Glyceraldehyde 3-phosphate dehydrogenase

GPA; Glycophorin A

GPC; Glycophorin C

H-Bonding; Hydrogen bonding

H_2DIDS; 4,4'-Diisothiocyanatodihydrostilbene-2,2'-disulfonic acid

HA; Hemagglutinin

HEK293 cells; Human embryonic kidney 293 cells

HEK293F; FreeStyle 293-F Human embryonic kidney suspension cells

HP; Helix packing

HRP; Horseradish peroxidase

HS; Harboyan syndrome

IgG; Immunoglobulin G

InScEp; Intracellular senescent cell epitope

IPB; Immunoprecipitation Buffer

kAE1; Kidney AE1

kDa; kiloDalton

L; Extramembraneous loop

LYIA; Lucifer yellow iodoacetamide

MD; Membrane domain

PBS; Phosphate-buffered saline

PMSF; Phenylmethylsulfonyl fluoride

PVDF; Polyvinylidene fluoride

qBBR; Monobromo(trimethylammonio)bimane bromide (Bromobimane q)

RBC; Red blood cell

ScIgG; Senescent cell immunoglobulin G

SEM; standard error of the mean

SDS-PAGE; sodium dodecyl sulfate polyacrylamide gel electrophoresis

SLC; Solute carrier

SLC4A1; Solute carrier family 4 member 1

SLC4A11; Solute carrier family 4 member 11

TM; Transmembrane segment

v/v; volume per volume

w/v; weight per volume

WT; Wild-type

Chapter 1: General Introduction

1.1 Thesis overview

The objective of this thesis is to pursue structure-led studies brought to light by the molecular structure of membrane protein AE1 (SLC4A1). The X-ray crystal structure of AE1 membrane domain (1) presents a structural framework and tool to examine mechanisms of disease associated with SLC4 membrane proteins, including SLC4A11, and to investigate discrepancies in localization of AE1 senescent cell antigen. Here, a three-dimensional homology model of SLC4A11 was created using the AE1 structure as a template, and this model was used to rationalize molecular phenotypes of blinding corneal dystrophies. In addition, the structure-led inquiry into localization of the AE1 senescent cell antigen revealed a molecular mechanism for the red blood cell senescence 'clock'.

This thesis centers on studies of SLC4 family transporters prompted by the X-ray crystal structure of the AE1 membrane domain. The introduction begins with an overview of membrane protein structure, covering structural biology techniques and common membrane transporter protein folds. The introduction then continues with a discussion of the SLC4 family of membrane transporters, including an overview of shared architecture and proposed transport mechanism. Since the studies here followed from an X-ray crystal structure of the founding SLC4 family member SLC4A1 (AE1), the introduction continues with a discussion of the physiological role of AE1 in erythrocytes and kidney, followed by a detailed examination of the AE1 three-dimensional structure and anion exchange mechanism. Since a unique role of AE1 in red blood cells is examined in this thesis, a section of the introduction describes the production, composition, and clearance mechanisms of red blood cells. Following this, the role of SLC4A11 in human cornea in both healthy and diseased states is discussed.

1.2 Membrane Proteins in Health and Disease

Cells are bounded by the plasma membrane, a semi-permeant lipid bilayer that maintains cell integrity by separating intracellular components from the extracellular environment. Embedded in the lipid bilayer, integral membrane proteins mediate the flux of molecules and information between the cell and the extracellular environment. Between 20-30% of genes encode membrane proteins in most organisms, including the human genome at ~25% (2,3).

Half of drug targets are predicted to be membrane proteins, exceeding their relative genomic representation (4). The prevalence of membrane proteins in essential physiological processes, as well as the array of membrane proteins implicated in diseases, further emphasises the importance of fully understanding membrane protein function and dysfunction (5).

1.2.1 Techniques to Obtain High Resolution Membrane Protein Structures

Membrane protein structures are typically determined using techniques implemented to study soluble proteins. However, the highly hydrophobic transmembrane region of integral membrane proteins poses a unique challenge. The 30 year gap between the first experimentally determined structure of a cytosolic protein and the first experimentally determined structure of a membrane protein highlights the additional level of difficulty membrane proteins bring to structural biology (6,7).

Protein structural studies require large amounts of purified protein. While highly-expressed membrane proteins may be purified directly from their physiological source (1), others require heterologous overexpression (8). Membrane proteins must be extracted from the lipid bilayer and maintained in a stable, non-aggregated state, which may be accomplished using detergents (9).

Membrane protein expression, purification, and stability remain significant bottlenecks to structural determination.

Purified, detergent-solubilized membrane proteins can self-organize into a repeating crystal lattice, maintained in part by hydrophilic protein interactions. These protein crystals can be examined with X-ray beams. Electrons of crystallized proteins interact with incident X-ray beams, resulting in an X-ray diffraction pattern. Diffraction patterns are then converted into a model of the electron density within the crystal, using the mathematical Fourier transform. Structural determination by X-ray crystallography requires that proteins be chemically homogenous, conformationally homogenous, thermodynamically stable, and have minimal dynamic regions (10). Limited proteolysis, deglycosylation, thermodynamically stabilizing mutations (11), and addition of monoclonal antibodies (12), substrates (13), and ligands (14) have all been effective in producing well-diffracting protein crystals. Co-crystallization of proteins with monoclonal antibody fragments creates a large polar surface area amenable to crystal contact formation (15). Techniques developed with the goal of enhancing protein stability have successfully been employed in membrane protein crystallization, including nanodiscs (16), amphipols (17), styrene maleic acid copolymer lipid particles (SMALPs) (18), bicelles (19), and lipidic cubic phase (LPC) (20).

A recent surge in membrane protein structures determined by cryo-electron microscopy (cryo-EM) has been driven by advances in direct electron detectors and microscopes (21,22). Unlike X-ray crystallography, cryo-EM does not require protein crystals. Instead, cryo-EM determines protein structure by interrogating randomly-oriented molecules embedded in a thin layer of vitreous ice with electrons, and subsequently averaging those images to create a composite

three-dimensional structure (23). Since protein crystals are not required, cryo-EM remains viable with a higher degree of protein heterogeneity than X-ray crystallography, although heterogeneity will be reflected in poorly resolved structure (24). Cryo-EM is most suited to large molecules and complexes, due to the low contrast images obtained. G-protein coupled receptors smaller than 100 kDa have been successfully studied with cryo-EM when complexed with soluble proteins, including G-proteins (25) and Fab fragments (26).

While X-ray crystallography and cryo-EM represent two predominant techniques in membrane protein structural biology, membrane protein structure can also been determined by nuclear magnetic resonance spectroscopy (NMR) (27) and mass spectrometry (28). In all techniques used to determine membrane protein structure, sample preparation remains a significant bottleneck. In cases of especially difficult proteins, structures can be computationally modelled using experimentally determined structures of evolutionarily related (homologous) proteins.

1.2.2 Membrane Transporter Protein Folds

Membrane transport proteins facilitate the transport of solutes against their electrochemical gradient. While transport proteins vary greatly in primary sequence, transported substrates, and modes of transport, many transporters share common tertiary protein folds (29). Two structural motifs are common within transport proteins: 1. Transmembrane helix (TM) pseudosymmetry, and 2. Discontinuous transmembrane helices (30,31). These motifs are evident in the two most abundant transporter folds, the major facilitator fold and the LeuT fold (30,31).

The major facilitator superfamily (MFS) is the largest superfamily of transport proteins, found ubiquitously across all kingdoms of life (32). MFS proteins vary widely in both transported substrates (including lactose (33), glycerol-3-phosphate (34), glucose (35), and drugs (36)) and

mode of transport (symport (33), antiport (34), uniport (35)). MFS proteins comprise 12 TMs, which separate into two separately folded bundles of six TMs (TMs1-6, TMs7-12) (30). The N- and C-terminal bundles are linked by an intracellular loop or domain, and do not interlace with each other. Within each six TM bundle are two bundles of three helices, related by a two-fold pseudosymmetry axis perpendicular to the plane of the lipid bilayer. This pseudosymmetry is termed a '3 + 3' inverted repeat, where the first three TMs demonstrate structural similarity to the second three following a rotation of 180° about the x-axis. Unlike the N- and C-terminal 6-helix bundles, TMs within each bundle are tightly interwoven. Thus, MFS fold proteins contain four structural repeats of three TMs (29). Helical structure of some TMs is interrupted by a region of extended peptide, thus the term 'discontinuous helix' (33,37,38). Substrate binding sites lie predominantly at the interface of the two six TM bundles (39,40).

The LeuT fold was named based off the first reported structure with this arrangement, a bacterial neurotransmitter/Na^+ symporter (41). LeuT fold proteins are comprised of 10 TMs arranged into a 5 + 5 inverted repeat, with TMs 1-5 displaying structural similarity to TMs 6-10 following a rotation of 180° about the x-axis. In contrast to the MFS fold, TMs 1-5 and 6-10 are highly interwoven (29). The first TM in each structural repeat is discontinuous, consisting of two short α-helices connected by a highly conserved region of extended structure (42). The LeuT fold is shared by transporters with no similarity in sequence or function (42). LeuT-fold proteins accommodate transport of diverse solutes including amino acids (43), neurotransmitters (41), galactose (44), and divalent metal cations (45).

The common structural motifs found in MFS and LeuT folds (pseudosymmetry and discontinuous helices) extend to unrelated transporters, including Na^+/H^+ antiporter NhaA (46),

Apical Na^+-dependent bile acid transporter ASBT (47), and Cl^-/HCO_3^- exchanger AE1 (1). Specific characteristics of the 7 + 7 inverted repeat fold shared by transporters AE1, NBCe1, AtBor1, Bor1p, UraA, UapA, SLC26Dg, and SLC29A9 will be discussed further below.

1.2.3 Homology Modelling

Proteins that share a common evolutionary origin are grouped into a protein family (48). This common evolutionary background (homology) is reflected in similarities in function, amino acid sequence, and three-dimensional structure. Three-dimensional protein structure is more evolutionarily conserved than primary sequence, and thus proteins with low sequence identity within the same family will often have highly similar three-dimensional structure (49). Because of these relationships, experimentally determined protein structures can be used as templates to computationally create structural models of family members (homologs), which can then be used to examine physiology and pathophysiology in a three-dimensional structural context. This process is called homology modelling, comparative modeling or template-based modeling.

Homology models have inherent limits over experimentally determined structures. The reliability of a homology model is dependent on selection of an appropriate template. Criteria for template selection include high resolution, high homology to the query protein, and maximum completeness (or coverage) of the template structure (50). Gaps in the template structure will result in the corresponding region of the query lacking a template for modelling. The reliability of a homology model is limited by the accuracy of the initial sequence alignment between the template and query protein, as any errors will propagate through to the final model. These caveats underline the importance of both *in silico* and *in vitro* assessments of homology models.

1.3 Solute Carrier Family 4

1.3.1 SLC4 Membrane Transporters

Proteins that transport solutes across plasma membranes are classified as SoLute Carriers (SLC) by the Human Genome Organization (51). There are ten members in the SLC4 family (*SLC4A1-5, SLC4A7-11*) of bicarbonate transporters, summarized in Table 1.1 (52). These can be grouped by transported substrates and mechanism: electroneutral Cl^-/HCO_3^- (anion) exchangers (AE1, AE2, AE3), electrogenic Na^+-coupled HCO_3^- cotransporters (NBCe1 and NBCe2), and electroneutral Na^+-coupled HCO_3^- cotransporters (NBCn1, NDCBE, NBCn2, and SLC4A9) (Fig. 1.1). SLC4A11 is the most phylogenetically distant SLC4 family member, and is the only family member that does not display HCO_3^- transport activity (52). As transporters of bicarbonate, or H^+/OH^- equivalents in the case of SLC4A11 (53), SLC4 family members contribute to acid-base homeostasis (54). The discovery of SLC4 transporters by independent labs, over a span of time, has resulted in multiple names for the same protein (Table 1.1).

The importance of SLC4 proteins and their role in acid-base homeostasis is emphasised by their prevalence in diseased states. SLC4 transporters have been implicated in human diseases including red blood cell disorders hereditary spherocytosis and hereditary stomatocytosis (55-70), kidney diseases proximal and distal renal tubular acidosis (71-76), epilepsy (77,78), blindness (79), and corneal dystrophies congenital hereditary endothelial dystrophy (CHED) and Fuchs endothelial dystrophy (FECD) (80-101).

Table 1.1 SLC4 transporters and their properties. Leftmost column: Genes italicized at top, most commonly used protein name in bold, followed by alternate names.

Gene **Protein**	**Expression Profile**	**Transport Activity**	**Physiological Roles**	**Associated Diseases**
SLC4A1 **AE1** eAE1 kAE1 Band 3	Erythrocytes, kidney, heart	Electroneutral Cl^-/HCO_3^- exchange	CO_2 buffering in cellular respiration (102), HCO_3^- reabsorption in kidney (kAE1) (103)	Hereditary spherocytosis (55-65,104-106) Hereditary stomatocytosis (66-69,107,108) Distal renal tubular acidosis (56,57,61,109-122)
SLC4A2 **AE2**	Widespread	Electroneutral Cl^-/HCO_3^- exchange	Acid secretion by osteoclasts (123) and gastric parietal cells (124), regulation of intracellular pH and volume (125)	Primary biliary cholangitis (126-129)
SLC4A3 **AE3** AE3c AE3fl	Brain, heart, retina, pituitary, adrenal gland, kidney	Electroneutral Cl^-/HCO_3^- exchange	pH regulation of excitable tissues (77,130)	Idiopathic generalized epilepsy (78) Short QT syndrome (131)
SLC4A4 **NBCe1** NBC1	Pancreas, kidney, heart, cornea,	Electrogenic Na^+/HCO_3^- co-transport	Cardiac action potential (132), endothelial cell fluid	Proximal renal tubular acidosis with ocular

hhNBC pNBC kNBC1	prostate, colon, stomach, thyroid, brain		movement, (133), renal Na^+ and HCO_3^- reabsorption (134), ocular abnormalities (73)	abnormalities (72,73,135) Band keratopathy (136)
SLC4A5 **NBCe2** NBC4	Brain, epididymis, cardiac muscle, smooth muscle, kidney, choroid plexus, liver, spleen	Electrogenic Na^+/HCO_3^- co-transport	Regulation of Na^+ and HCO_3^- levels in cerebrospinal fluid (137,138)	Hypertension (139-143)
SLC4A7 **NBCn1** SLC4A6 NBC2 NBC3	Heart, kidney, skeletal muscle, smooth muscle, submandibular gland, pancreas, stomach, spleen, liver, lungs	Electroneutral Na^+/HCO_3^- co-transport	Resting neuronal pH (144)	Hypertension (145) Breast cancer susceptibility (146-149)
SLC4A8 **NDCBE** NDAE1	Prefrontal cortex of brain, testis,	Electroneutral Na^+-dependent Cl^-/HCO_3^-	Neuronal pH regulation (150,151),	

kNBC-3	cardiac myocytes, oocytes, kidney	exchange	Cl^- reabsorption in kidney (152), cerebrospinal fluid secretion by the choroid plexus (153)	
SLC4A9 AE4	Kidney, testis, pancreas, widespread	Electroneutral Na^+/HCO_3^- co-transport	Renal Na^+ and HCO_3^- reabsorption (154)	
SLC4A10 **NBCn2** NCBE	Cardiac myocytes, neurons, kidney, uterus, adrenal cortex, choroid plexus	Electroneutral $Na^{+/}HCO_3^-$ co-transport or Na^+-dependent Cl^-/HCO_3^- exchange	Cerebrospinal fluid production (138,155), control of neuronal pH (155)	Autism with idiopathic generalized epilepsy (156-159)
SLC4A11 **SLC4A11** BTR1 NaBC1	Cornea, kidney, salivary gland, testis, thyroid, trachea	Water flux, Na^+/OH^- cotransport, Na^+-independent H^+ (OH^-) transport, and NH_3 transport	Fluid reabsorption (98)	Corneal dystrophies (80-101)

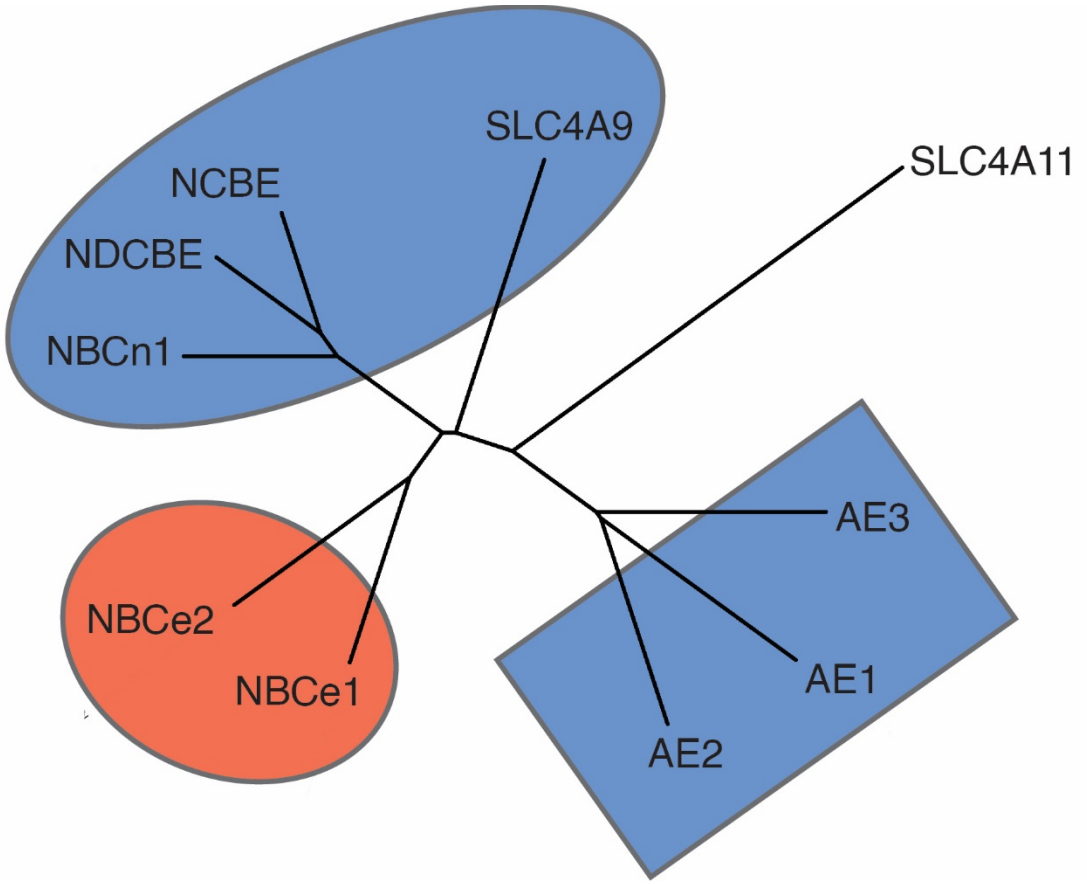

Figure 1.1 Phylogenetic dendrogram of SLC4 membrane transporters. Clustal Omega software was used to align amino acid sequences of human SLC4 family members and calculate relative phylogenetic distances (https://www.ebi.ac.uk/Tools/msa/clustalo/) (160-162). Unrooted dendrogram was visualized using iTOL software (https://itol.embl.de/) (163). Line lengths indicate evolutionary distance. Shapes highlight electroneutral (blue), electrogenic (red), sodium dependent (ovals), and sodium independent (rectangle) bicarbonate transport activity.

1.3.2 SLC4 Architecture

Sequence similarity among the SLC4 family membrane domains (30–45% identity and 37–54% similarity) indicates that they share a common ancestor (Fig. 1.1) (48,164). As such, they likely share similar three-dimensional structures, and comparable transport mechanisms (134). Shared SLC4 architecture includes a large intracellular N-terminal domain, followed by an N-glycosylated solute transporting transmembrane domain, and a short C-terminal cytoplasmic tail (54). The structural and functional independence between the cytoplasmic and membrane domains varies between SLC4 family members (165-168). SLC4 transporters are homodimeric (169-173), while some are able to form higher order oligomers (174,175).

The N-terminal, homodimeric cytoplasmic domains of SLC4 transporters accounts for 32-55% of the polypeptide (54,176-178). Crystallographic studies of the isolated cytoplasmic domains of AE1 and NBCe1 indicate that these domains are globular and form dimers (176,177). SLC4 protein cytoplasmic domains can impart pH-sensitivity to transport (168,179,180), act as protein interaction hubs (181), or stimulate or inhibit transport activity (182,183). The mechanisms governing these regulatory roles have yet to be fully addressed.

The membrane domains of SLC4 transporters mediate substrate transport. Functional studies with NBCe1 and AE1 indicate that each protomer within the dimeric unit exhibits independent substrate transport (170,184,185). Protomers are comprised of 14 transmembrane helices, embedded within the lipid bilayer (1,8). N-glycosylation consensus sites are present in all SLC4 family members at extracellular loop 3, with the exception of AE1, which has a N-glycosylation site in extracellular loop 4 instead (54).

The membrane domain structures of human AE1 and NBCe1 have been experimentally determined (1,8). Sequence identity indicates that other SLC4 family members share the same general membrane domain fold as AE1 and NBCe1 (186). Subtle differences in amino acid sequences are responsible for the different functional properties of SLC4 proteins, including ion transport specificity and exchange vs. symport (8). The three–dimensional fold of the NBCe1 and AE1 membrane domains is also shared by transporters from both eukaryotes and prokaryotes, with a range of substrate specificity including Cl^- and HCO_3^- (8,187-189), borate (190-193), uracil (194), fumarate (195), and xanthine (196) (Fig. 1.2). The diverse functional capabilities of this '7 + 7 inverted repeat' fold is reflected by this array of substrates, and ubiquitous representation from cyanobacteria to humans.

1.3.3 Alternating Access Transport Mechanism

Each SLC4 protomer contains 14 TMs organized into two subdomains: a gate domain, which forms the dimer interface, and a core domain, coordinating substrate binding. Substrate is transported through the cleft formed at the interface of the two domains, through an alternating-access model (197). In this mechanism, the substrate binding site at the domain interface is accessible to either the intracellular or the extracellular environment, alternating accessibility through global structural transitions induced by substrate binding (198).

Three prevailing mechanisms of alternating access transport differ mechanistically in the relative movements of domains (Fig. 1.3) (198). In 'rocker switch' transport, two structurally similar domains move essentially equally around the substrate, centered around a relatively static substrate binding site. 'Rocking bundle' transport shares this central binding site, however structurally dissimilar domains result in one of the domains (usually the smaller of the two) moving

relative to a larger, less mobile domain (199). In the ‘elevator model’, substrate binding is confined largely to one domain, which moves against a structurally dissimilar, immobile domain (200). The main difference in the elevator model of transport is that the substrate crosses the bilayer by physical displacement of the substrate binding site on one mobile domain. Whether SLC4 proteins transport solutes through a rocking bundle (186,192), an elevator mechanism (193,201,202), or an unknown mechanism, is still to be conclusively determined. Furthermore, how one mechanism can support both anion exchange (e.g. AE1) and symport (e.g. NBCe1), or whether the mechanism used by anion exchangers is dissimilar to that of symporters, has yet to be elucidated.

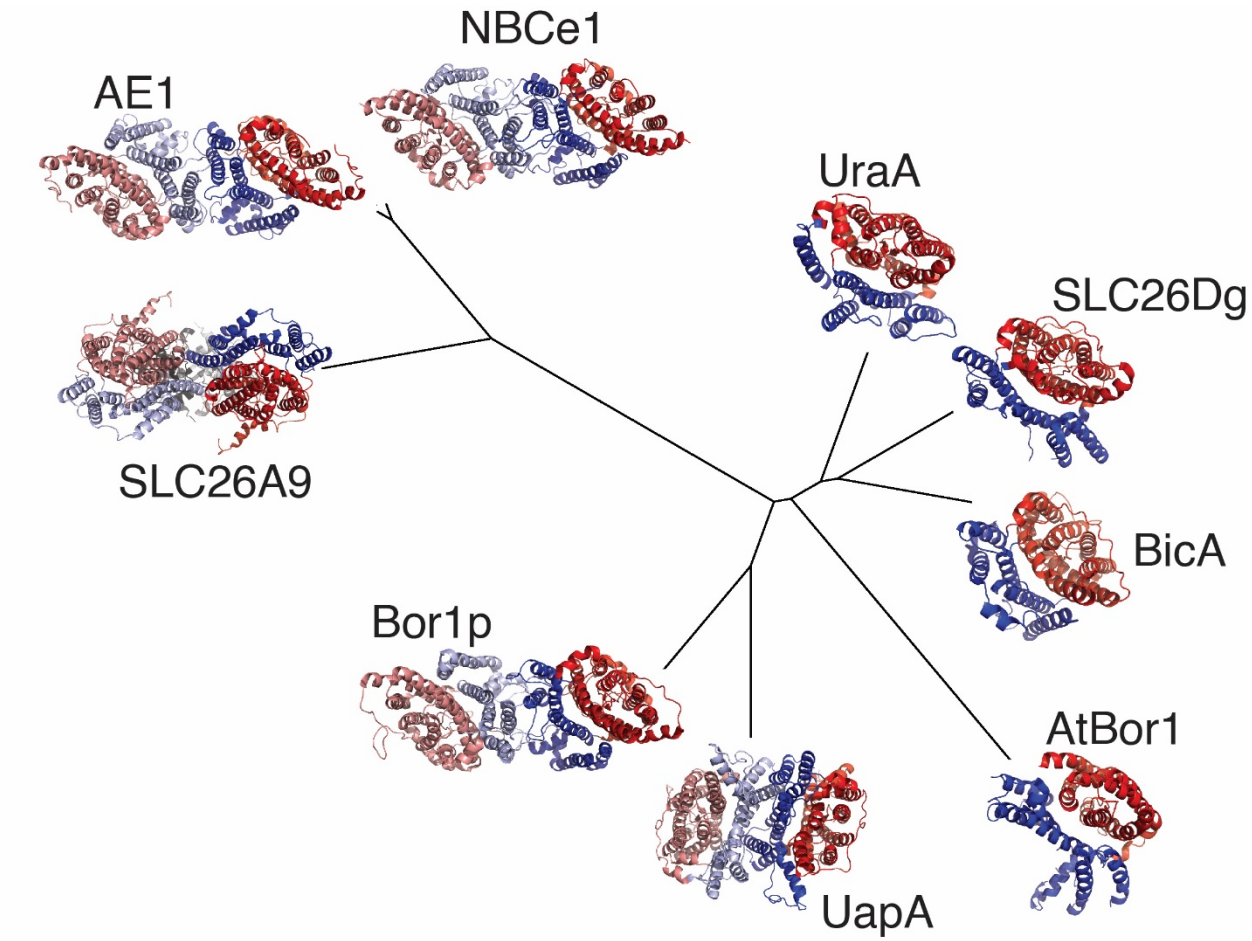

Figure 1.2 Membrane domain structures of 7 + 7 inverted repeat fold proteins. Structures of 7 + 7 inverted repeat proteins, visualized in PyMOL from the extracellular face (203). Core domains are red, and gate domains are blue. Protomers within the dimeric unit displayed in vibrant and light colors, where applicable. Unrooted phylogenetic tree made with iTOL software (https://itol.embl.de/) (163). Line lengths indicate evolutionary distance. Structures used: *Homo sapiens* AE1 (PDB ID 4YZF) (1); *Homo sapiens* NBCe1 (PDB ID 6CAA) (8); *Mus musculus* SLC26A9 (PDB ID 6RTC) (189); *Saccharomyces mikatae* Bor1p (PDB ID 5SV9) (192); *Aspergillus nidulans* UapA (PDB ID 5I6C) (196); *Arabidopsis thaliana* AtBor1 (PDB ID 5L25) (193); *Escherichia coli* UraA (PDB ID 3QE7) (194); *Synechocystis sp. PCC6803* BicA (PDB ID 6KI1) (188); *Deinococcus geothermalis* SLC26Dg (PDB ID 5IOF) (195).

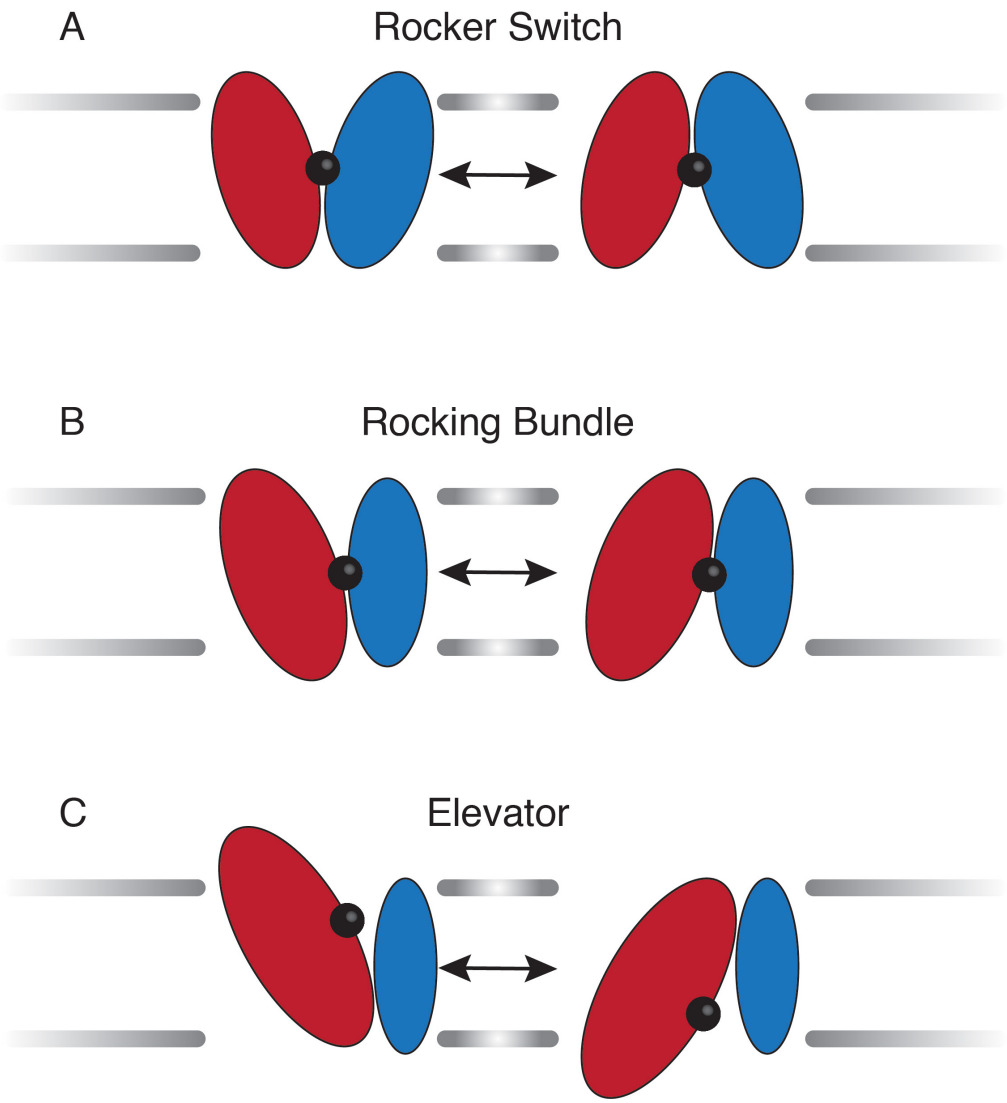

Figure 1.3 Mechanisms of alternating access transport. The differences in relative domain (blue and red ovals) movements within the bilayer (grey lines) of three mechanisms of alternating access transport, shown in order of decreasing structural similarity of domains. A) In Rocker Switch transport, two structurally similar domains pivot around a central substrate binding site (black circle). Both domains undergo parallel movements in the bilayer. B) In Rocking Bundle transport, one domain (red) moves relative to a less mobile, structurally dissimilar domain (blue). C) In the Elevator transport mechanism, substrate binding is largely confined to one domain (red). Substrate translocation results from displacement of the substrate binding domain within the bilayer, while the structurally dissimilar domain (blue) remains relatively immobile.

1.4 SLC4A1

The first member of the SLC4 family to be named, identified, and cloned, integral membrane glycoprotein SLC4A1 (AE1; Band 3) exchanges chloride for bicarbonate in a 1:1 electroneutral stoichiometry (187,204-206). The turnover rate of AE1 is a rapid 1 x 10^5 Cl^- s^{-1}, only one order of magnitude slower than some ion channels (19). In addition to Cl^-/HCO_3^- exchange, AE1 catalyzes rapid transport of HS^-, Br^- and F^-, and slower transport of I^-, HPO_3^{2-}, and SO_4^{2-} (187,207-209). AE1 can also transport organic phosphates and N-(4-azido-2-nitrophenyl)-2-aminoethylsulfonate (NAP-taurine) at very slow rates (187,208).

AE1 is organized into two structural domains: a 55 kDa membrane domain that carries out anion transport, and a 43 kDa N-terminal cytoplasmic domain (166,210). AE1 is expressed as two isoforms that differ in their size and tissue distribution, erythrocyte AE1 (eAE1) and kidney AE1 (kAE1) (211,212).

1.4.1 Erythrocyte AE1

Erythrocyte AE1 (eAE1, 911 residues) is expressed in red blood cells, where it comprises 50% of the red cell membrane protein at 1.2 x 10^6 copies per cell (204). AE1 exists as a mixture of dimers and tetramers in the red cell membrane and in detergent solutions (174,175). AE1 is also known by the name Band 3, from its migration pattern third from the top on SDS-PAGE gels of red cell membrane proteins (204). AE1 Cl^-/HCO_3^- exchange is essential for efficient respiration, and yields increased CO_2 carrying capacity of blood (102).

During blood circulation, metabolic waste CO_2 from respiring tissues diffuses down its concentration gradient into red cells (Fig. 1.4). Once inside the cell, carbonic anhydrase II (CAII) catalyzes CO_2 hydration and results in production of one H^+ and one HCO_3^-. The proton resulting

from CO_2 hydration lowers intracellular pH, which promotes the release of oxygen from hemoglobin through the Bohr shift (213). To prevent HCO_3^- accumulation, HCO_3^- is exported in exchange for extracellular Cl^- through the actions of AE1. As HCO_3^- is more soluble than CO_2, this increases the CO_2 carrying capacity of blood. This process is reversed in the high O_2, low CO_2 environment of the lungs.

The efficiency of AE1 Cl^-/HCO_3^- exchange in red cells is maximized by the anchoring of CAII on the C-terminal tail of AE1 (214). This physical interaction may promote rapid transport by localizing HCO_3^- production at HCO_3^- extrusion sites in high CO_2 environments, and by promoting immediate consumption of HCO_3^- in low CO_2 environments, thus maintaining a high transmembrane HCO_3^- concentration gradient in both efflux and influx conditions (215). The physical interaction of AE1 and CAII creates a membrane–anchored bicarbonate metabolon, increasing bicarbonate flux through AE1 by 40% (214).

The structurally independent 43-kDa N-terminal cytoplasmic domain (CD) is a major organizing center for membrane-associated proteins (181). The AE1 CD anchors the intracellular spectrin-actin cytoskeleton to the plasma membrane, through interactions with ankyrin and protein 4.2 (176,181,216-221). The deformability and flexibility of the red blood cell (RBC) cytoskeleton is essential to maintain cell integrity as RBCs experience extreme shear stress, transiting through capillaries with diameters smaller than the cells (222). Other AE1 cytoplasmic domain binding partners include protein 4.1 (223), glyceraldehyde-3-phosphate dehydrogenase (GAPDH) (224), phosphofructokinase (225), aldolase (226), hemoglobin (227,228), denatured hemoglobin (hemichromes) (229), and protein kinase $p72^{syk}$ (230). Some of these protein-protein interactions are dependent on the phosphorylation state of the AE1 cytoplasmic domain (glycolytic enzymes,

hemoglobin, protein 4.1 and 4.2) (181,231). Due to interactions with the cytoskeleton, RBC structure and morphology are compromised in cells deficient in AE1 (232). Compromised or reduced AE1 content in RBCs results in spherocytosis and decreased RBC stability leading to hemolysis and anemia (233,234), while mutations in eAE1 can cause Southeast Asian ovalocytosis (235,236), hereditary stomatocytosis (237), and hereditary spherocytosis (55).

In addition to maintaining RBC structure and anion transport, eAE1 has a central role in IgG-mediated clearance of senescent RBCs. As RBCs mature from erythrocyte precursors they expel their nuclei and lose their organelles (238), rendering them unable to undergo apoptosis. Senescent RBCs are cleared from circulation through phagocytosis by macrophages (239). Opsonization (cell coating by immune system components to enable recognition by macrophages) by serum Immunoglobulin G (IgG) is essential for recognition of senescent RBCs by macrophages (239). These naturally produced IgG "auto-antibodies" are directed against AE1 (239,240). While uncertainty surrounds how AE1 binds auto-antibodies at a molecular level, the central role of AE1 in signalling red cell senescence has been replicated in several laboratories (239,241,242).

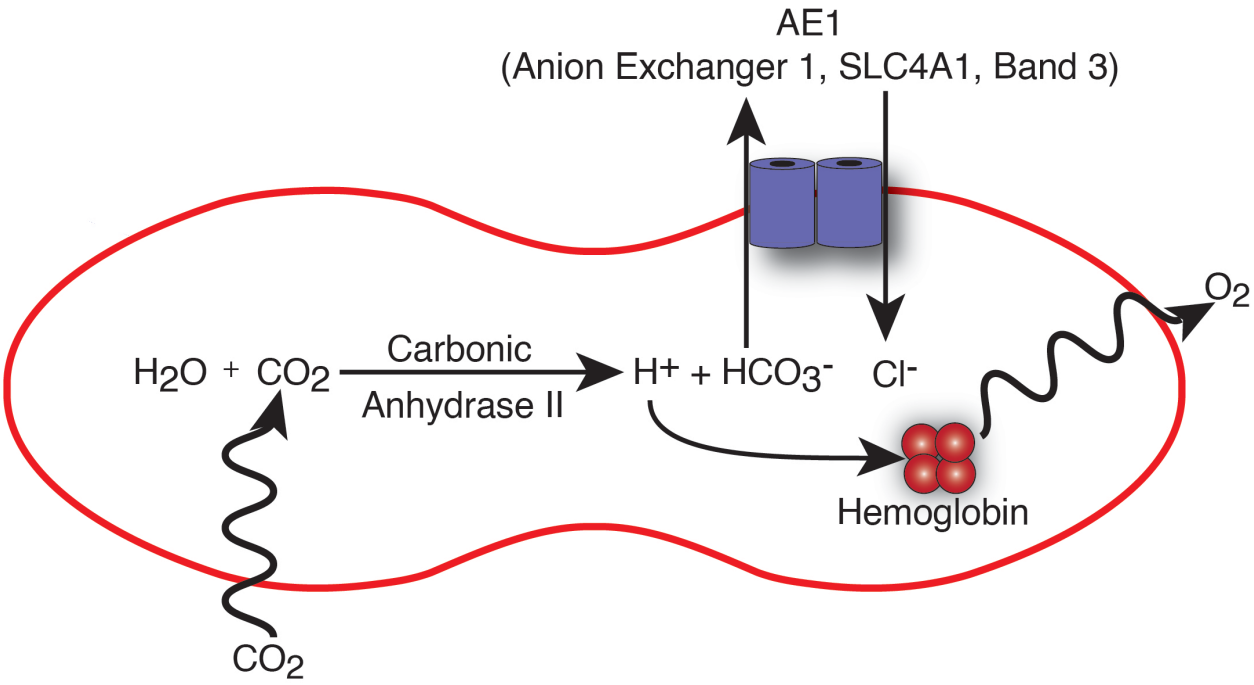

Figure 1.4 Function of AE1 in RBC membranes. Carbon dioxide from tissues diffuses through red cell membranes into cytoplasm. Intracellular carbonic anhydrase II (CAII) catalyzes CO_2 hydration to produce bicarbonate (HCO_3^-) and a proton (H^+). Intracellular bicarbonate is exchanged for extracellular chloride through AE1 in a 1:1 stoichiometry. The resulting lowered intracellular pH from H^+ promotes off-loading of oxygen from hemoglobin to tissues through the Bohr shift. This process is reversed in the lungs. Figure modified from (243) and reproduced with permission.

1.4.2 Kidney AE1

A truncated form of AE1 is expressed in the kidneys, resulting from transcription from a promoter within an intron of *SLC4A1* (244). Kidney AE1 (kAE1, 846 residues) lacks the 65 N-terminal residues present in eAE1, and is expressed in the basolateral membrane of acid-secreting type A-intercalated cells (α-intercalated cells) of the renal collecting duct (212). Here, kAE1 is a predominant mediator of acid-base homeostasis, carrying out bicarbonate reabsorption into blood (245). CO_2 that enters renal collecting duct α-intercalating cells is hydrated by intracellular CAII, resulting in the production of a proton and HCO_3^- (Fig. 1.5). The proton is excreted into urine by apical H^+ and H^+/K^+ ATPase, while HCO_3^- is reabsorbed into blood by basolateral kAE1 in exchange for extracellular Cl^-. The combined actions of CAII, apical H^+ and H^+/K^+ ATPase, and basolateral kAE1, prevent systemic acidosis and acidify urine (246). To maintain ion homeostasis in α-intercalated cells, Cl^- is recycled into the blood through basolateral ClC chloride channels and Cl^-/K^+ co-transporters (KCC).

kAE1 mutations cause distal renal tubular acidosis (dRTA), characterized by difficulty to thrive, renal stones, hypokalaemia, hyperchloraemia, metabolic acidosis and defective urine acidification (247). Molecular phenotypes of dRTA kAE1 mutants include compromised transport function, and mistargeted or ER-retained protein (134,186). Dominantly inherited dRTA is typically caused by kAE1 mutations resulting in ER retention, while recessively inherited disease is generally caused by kAE1 mutants with poor transport function and impaired basolateral trafficking (76,112,248). C-terminal and cytoplasmic regions of kAE1 have been implicated as important for proper trafficking and sorting (111,119,248,249).

Mutations in the *SLC4A1* gene, encoding both eAE1 and kAE1, can cause red cell and kidney disorders. However, patients with AE1 mutations leading to disease in one system rarely exhibit defects in the other (250). This is likely due to cell type specific differences (186). While kAE1 experiences endocytosis and turnover in α-intercalated cells, eAE1 is present for the duration of the RBC lifetime (251). Chaperone proteins involved in membrane glycoprotein biosynthesis are lost during RBC maturation, which may permit surface expression of AE1 mutants that experience turnover in α-intercalated cells (252). RBCs express glycophorin A, a transmembrane protein which interacts with and facilitates cell surface expression of eAE1, and which is not present in α-intercalated cells (61,253-256). In addition to cell type specific differences, the dominance of *SLC4A1* mutations contributes to disease presentation. Coinciding kidney and red blood cell phenotypes may occur in patients with recessive dRTA (57,257).

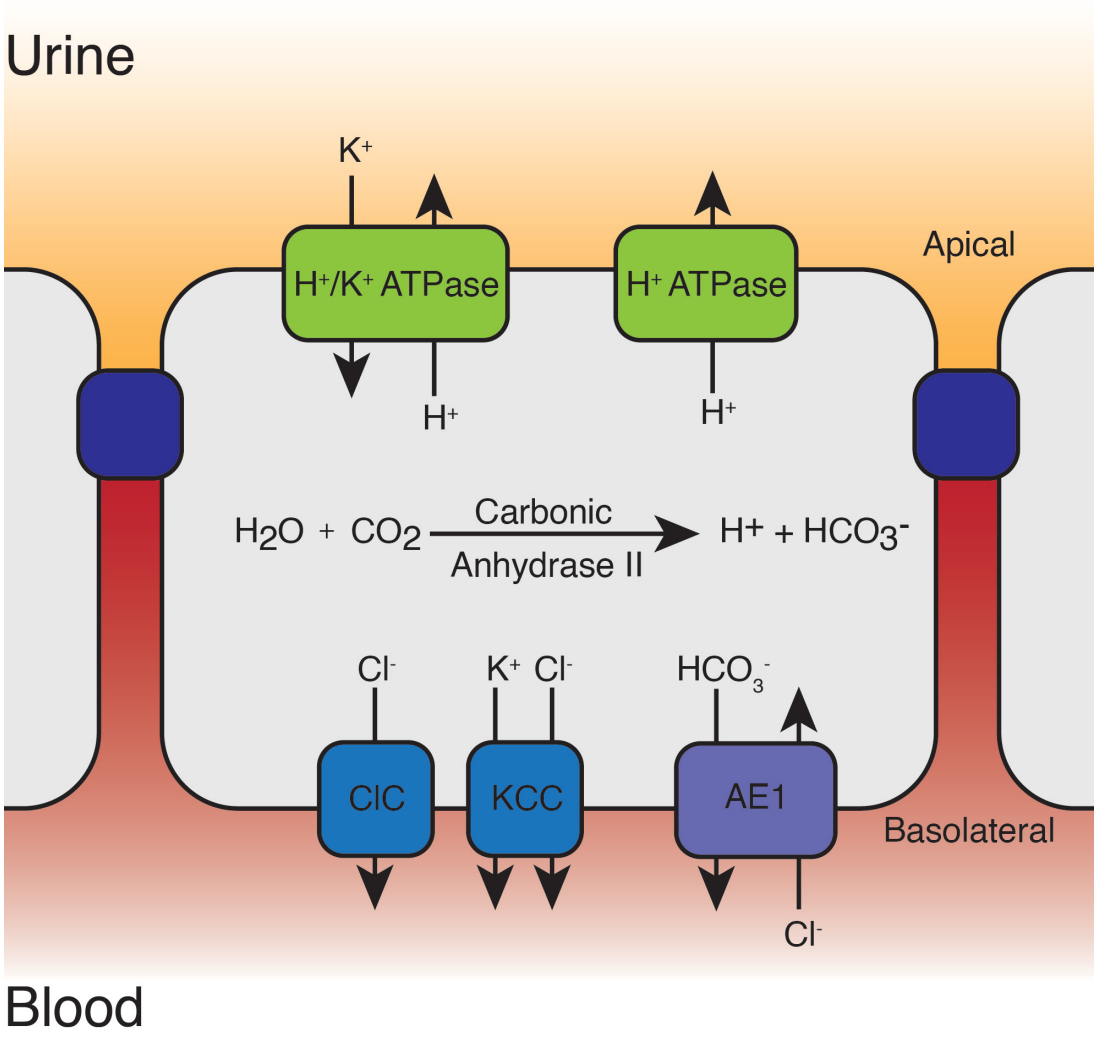

Figure 1.5 Function of AE1 in kidney α-intercalated cells. Kidney α-intercalated cells (grey) regulate acid-base homeostasis in distal portions of the kidney tubule. In kidney α-intercalated cells, intracellular carbonic anhydrase II (CAII) catalyzes CO_2 hydration to produce bicarbonate (HCO_3^-) and a proton (H^+). The proton is extruded into urine (upper) by apical H^+ and H^+/K^+ ATPases (green), acidifying urine. Bicarbonate is reabsorbed into the blood in exchange for extracellular chloride through AE1 (slate) in a 1:1 stoichiometry. Cl^- homeostasis of α-intercalated cells is maintained by Cl^- efflux through ClC Cl^- channels and KCC Cl^-/K^+ cotransporters (blue). Tight junctions shown in navy.

1.4.3 AE1 Membrane Domain Three-Dimensional Structure

The crystal structure of AE1 membrane domain has been solved at 3.5 Å resolution (1), offering the opportunity to rationalize decades of experimental data with the three-dimensional protein structure. The structure covers AE1 residues 381 to 887, with some unresolved extra-membraneous loops (residues 553 to 567, 640 to 649, and 742 to 753). The 14 AE1 TMs are organized into a fold termed '7 + 7 inverted repeat' (Fig. 1.6). In this fold, TMs 1-7 show strong structural similarity to TMs 8-14, after 180° rotation about the x-axis (Fig. 1.7). The 14 helices of AE1 further arrange into a core domain, comprising TMs1-4 and TMs8-11, and a gate domain, comprising TMs5-7 and TMs12-14 (Fig. 1.8). The gate domain creates the dimerization interface, through a four-helix bundle formed by TM5 and TM6, with contributions from TM7. The core domain contains substrate-binding residues and helices. Two half helices in the core domain, TM3 and TM10, are oriented with their N-termini helical dipoles facing each other, creating a positive environment halfway through the lipid bilayer (Fig. 1.6 C). This arrangement of half helices within the core domain is a common feature of 7 + 7 inverted repeat fold, also seen in the structures of UraA (194), SLC26Dg (195), UapA (196), AtBor1 (193), Bor1p (192), NBCe1 (8), SLC26A9 (189), and BicA (188). In the AE1 crystal structure, the interface between the core and gate subdomains contains 4,4'-diisothiocyanatodihydrostilbene-2,2'-disulfonic acid (H_2DIDS), a covalent SLC4 inhibitor added to restrict the conformational flexibility normally associated with transport function (258). H_2DIDS lies in a V-shaped cleft on the extracellular side of the transporter, locking it in an outward-facing state (259). Although there was no density for anion substrate in the crystal structure, structures of 7 + 7 inverted repeat proteins with bound substrates suggest that the putative anion binding site sits at the vertex of this cleft (188,192,194,196).

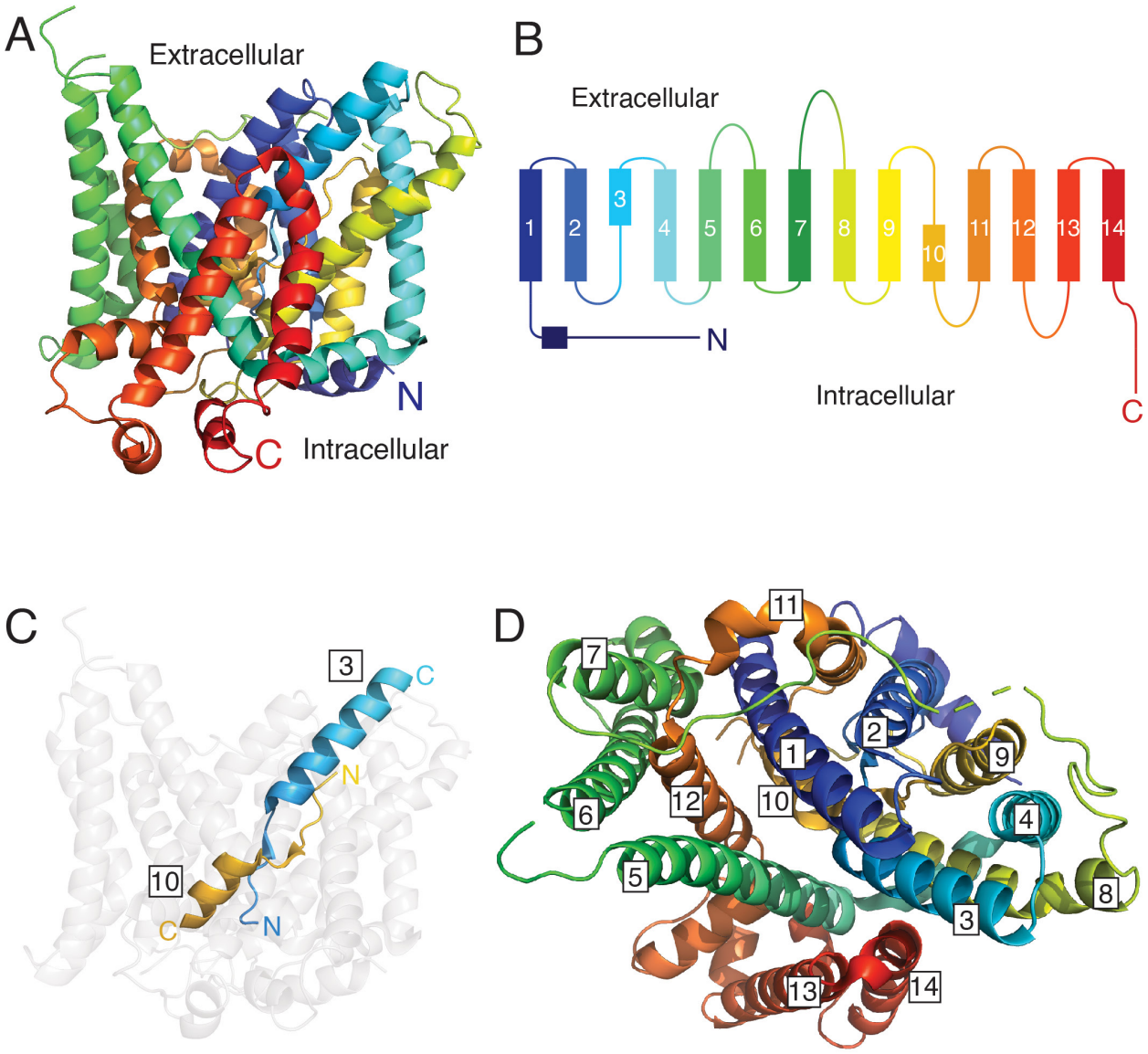

Figure 1.6 Organization of AE1 membrane domain. AE1 membrane domain (PDB ID: 4YZF) (1) is comprised of 14 transmembrane helices, colored from N-terminus (blue) to C – terminus (red). A) View of AE1 membrane domain from the plane of the lipid bilayer. AE1 shown in cartoon representation. B) Linear topology model of A. C) Orientation of discontinuous helices TM3 and TM10, coloring as in A and B. D) Extracellular view, with transmembrane helices numbered.

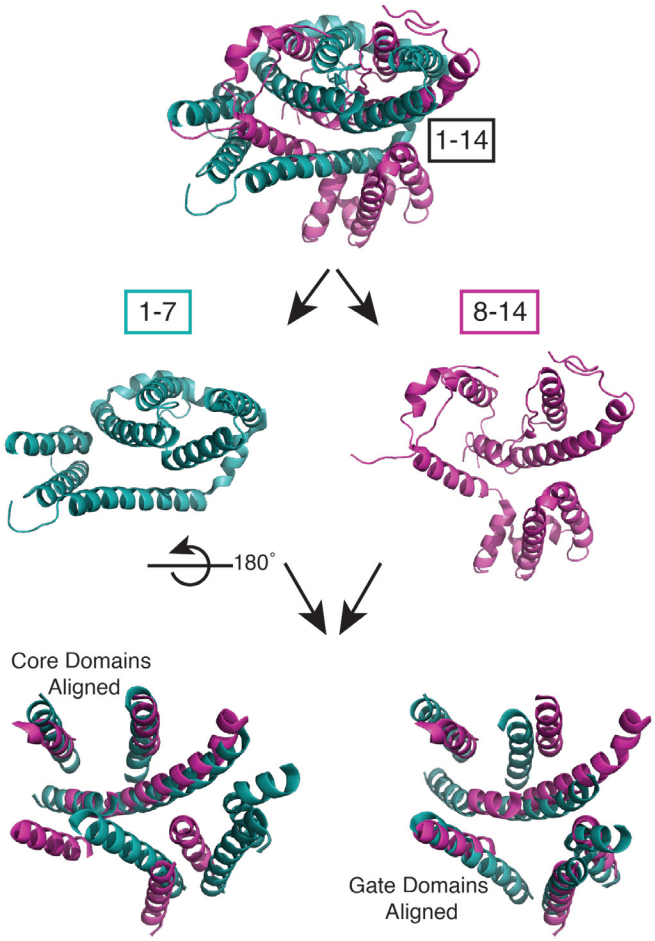

Figure 1.7 The AE1 membrane domain 7 + 7 inverted repeat fold. The AE1 membrane domain (upper) can be divided into two halves or repeats, with structural similarity of helices 1-7 (teal) and helices 8-14 (pink) apparent by superposition following rotation of one of the repeats (helices 1-7 here) by 180° about the x-axis (inversion) (lower). Superposition of transmembrane helices in the core (left) and gate (right) domains reveal structural similarity, but not uniformity, between the two repeats. AE1 structure (PDB ID: 4YZF) (1) shown from extracellular face. Helices shown in cartoon representation. Extra-membraneous regions were excluded to visualize superposition.

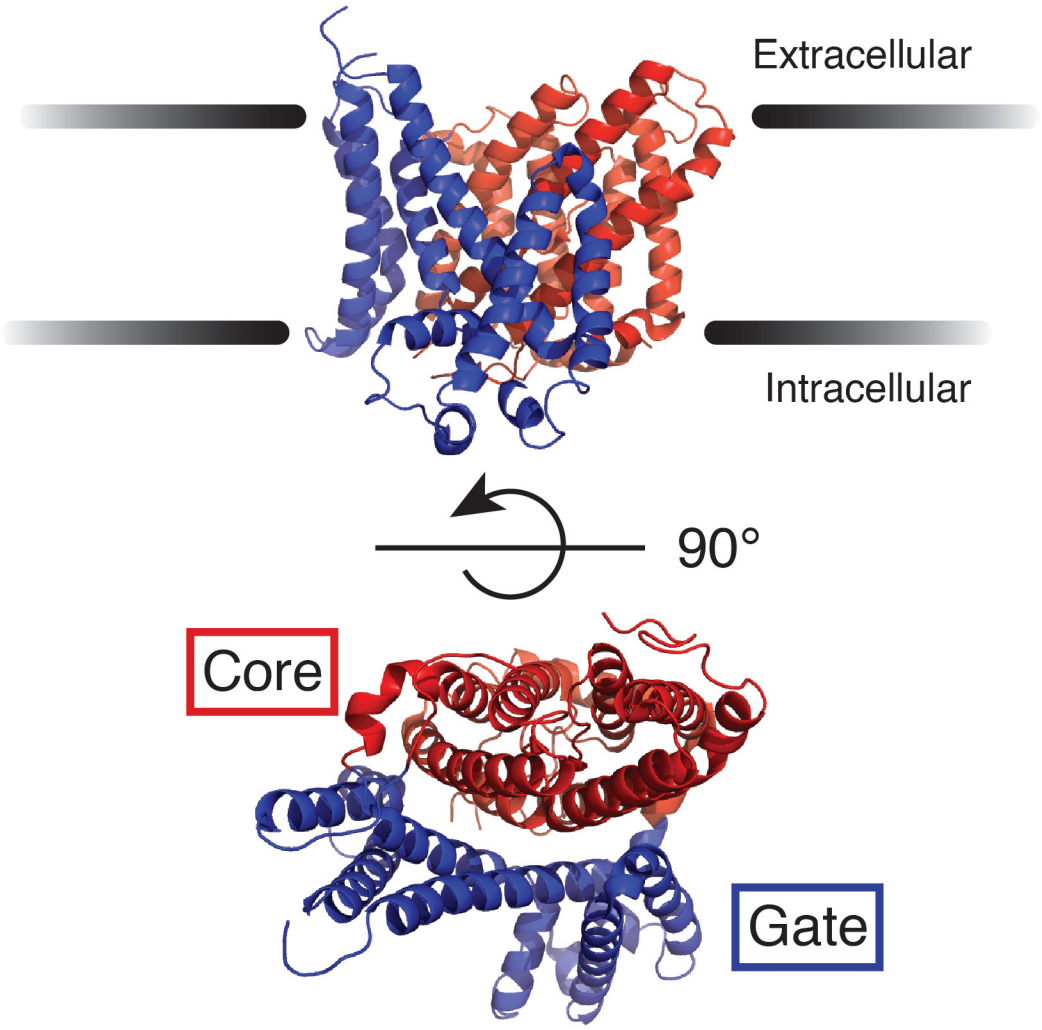

Figure 1.8 Core and gate organization of AE1 membrane domain. AE1 transmembrane helices span the plasma membrane bilayer. Approximate plasma membrane limits are represented by black lines (upper). Extracellular view (lower) reveals organization into two subdomains: 1) a core domain (red, helices 1-4 and 8-11) containing anion-coordinating residues and helices, and 2) a gate domain (blue, helices 5-7 and 12-14), which mediates oligomerization. Anions are transported through the cleft formed at the interface of the two subdomains (1).

1.4.4 AE1 Transport Mechanism

AE1 transports by an alternating access mechanism (187,260,261). In this model, the anion binding site is alternatively exposed to either the extracellular or the intracellular environment (197). Anions bind at the interface of the core and gate domains. Access of the binding site to either the extracellular or intracellular environment is regulated by relative movements of the two domains.

Substrate anion binding is accomplished by the core domain. Although no substrate anion was bound in the crystal structure, the anion binding site is likely located at the ends of contiguous half-helices 3 and 10, similar to UapA, UraA and BicA (1,188,194,196,262). Helical dipoles from the N-termini of these helices create a positively charged environment partway across the bilayer. R730 on TM10 is essential to Cl^-/HCO_3^- exchange, and has been identified as the putative anion binding residue for both Cl^- and HCO_3^- (66,187,263,264). E681 on adjacent TM8 is also essential for transport, possibly acting as an ionic gate and occupying the anion binding site in the absence of substrate (265,266). The transport-deficient E681Q mutant is unable to carry out Cl^-/HCO_3^- exchange, despite trafficking correctly to the plasma membrane (266). E681 also appears bind the proton co-transported with SO_4^{2-} during electroneutral Cl^-/H^+-SO_4^{2-} exchange (267,268). The anion binding site is then created by contributions from residue R730 and TM3 and 10 helix dipoles, with negative E681 in close proximity. This weakly positive anion binding environment may contribute to the transporter's low affinity for chloride, which supports a rapid transport rate by allowing quick release of the anion from the binding site (186,269).

The putative AE1 transport cycle starts at the outward-open conformation, with extracellular chloride binding R730 at the substrate binding site. Binding induces a conformational change in AE1, promoting relative movements of the core and/or gate domain to result in an

inward-facing conformation and cytosolic exposure of bound substrate. Bound chloride then moves down its concentration gradient and exits the transporter. The transporter is now able to bind intracellular HCO_3^-, which induces conformational changes resulting in access to the extracellular environment. Extracellular release of HCO_3^- returns AE1 to its original state.

Although the membrane domain alone can carry out anion exchange following proteolytic cleavage of the cytoplasmic domain (166,167), the existence of a transport-impaired cytoplasmic domain point mutant suggests a functional interaction between the membrane and cytoplasmic domains (270).

1.4.5 Inhibitors of AE1 Transport

AE1 Cl^-/HCO_3^- exchange is inhibited by some organic anions, including a class of inhibitors called stilbene disulfonates. Stilbene disulfonate binding at the anion transport site is competitive with substrate and can be reversible or irreversible (covalent) (271-273). AE1 residues K539 on TM5 and K851 on TM13 can covalently react with isothiocyanate groups present on some stilbene disulfonates, in a pH-dependent manner (274-276). These residues are not directly involved in Cl^-/HCO_3^- exchange (277-279). Stilbene disulfonates bind the extracellular face of AE1, deep within the membrane domain (1). Here, stilbene disulfonates block translocation by locking the protein in an outward conformation, preventing relative movement of the two domains (280-283). Stilbene disulfonate H_2DIDS was used in AE1 crystallization to reduce protein dynamics and ensure conformationally homogenous AE1, two prerequisites to obtain well-diffracting crystals (1). Binding induces conformational changes in regions of AE1 not directly involved in inhibitor binding (284).

AE1 Cl^-/HCO_3^- exchange is also inhibited by niflumic acid (285), flufenamic acid (286,287), oxonol dyes (288,289), squalamines (289), phloretin (290), N-(4-azido-2-nitrophenyl)-2-aminoethyl sulfonate (NAP-taurine) (208), and furosemide (291). Chemical modifications of AE1 residues, including reductive methylation (292), dinitrophenylation (293), pyridoxal 5-phosphate binding (294), and phenylglyoxal treatment (102), can also inhibit Cl^-/HCO_3^- exchange.

1.4.6 Role of AE1 in Red Blood Cell Senescence

Red blood cells are specialized to fulfil their role in gas transport and exchange. RBC characteristics that enable maximal gas transport efficacy include biconcave morphology, deformable membrane cytoskeleton, and high hemoglobin content. Due to the unique biochemical composition of RBCs, their production and clearance is distinct from other cell types. In addition to fulfilling essential functional and structural roles during circulation, AE1 is instrumental in signalling senescence at the end of the RBC lifespan.

1.4.7 Red Blood Cell Production

Red blood cells are created in bone marrow, through a tightly regulated process of hematopoietic stem cell differentiation called erythropoiesis (295,296). RBCs are highly differentiated and specialized for optimal gas exchange. At the final stages of differentiation, pre-erythrocytes (reticulocytes) shed their nuclei, ribosomes, endoplasmic reticulum, Golgi apparatus, and mitochondria (295). Thus, mature erythrocytes are unable to proliferate or produce new proteins. In the terminal maturation steps from reticulocytes to erythrocytes, membrane remodelling by endocytosis and exocytosis results in the loss of 20-30% of the cell membrane (297,298), along with excess membrane proteins including AQP1 (299), CD71, Na^+/K^+ ATPase (300), Na^+/H^+ antiporter NHE1 (300), and glucose transporter (301). Cytoskeletal remodeling also occurs during

the maturation from reticulocyte to erythrocyte, resulting in a highly deformable cell (302). Approximately 2 x 10^{11} red blood cells are formed every day under steady-state conditions, with an equal number removed from circulation (303,304). This represents daily turnover of about 1% of the total circulating RBCs (295).

1.4.8 Red Blood Cell Composition

Mature RBCs are specialized for their role in gas transport. In contrast to other cells, RBCs must survive the varied physical and chemical environments they experience in circulation. The intracellular RBC cytoskeleton is responsible for the highly reversible deformability of RBCs and their characteristic biconcave shape, which maximizes cells surface area and thus gas exchange (Fig. 1.9) (305,306). This deformability allows RBCs (8 μm diameter) to traverse 3 μm diameter capillaries and 0.5 μm splenic endothelial slits (307), environments encountered often as a RBC circulates the vascular system 1.7 x 10^5 times during its lifetime (308). The cytoskeleton is comprised of a triangular network of tetrameric α- and β-spectrin molecules (309-312), anchored to the red cell membrane by AE1, protein 4.2, and ankyrin (218,223,313) (Fig. 1.9). The flexibility of the spectrin network allows large and rapid deformations, essential for the integrity of circulating RBCs (306).

Hemoglobin is the major cytoplasmic protein component of RBCs, comprising 97% of RBC dry weight (314). Hemoglobin is a heterotetrameric oxygen-binding protein, composed of two α- and two β-hemoglobin subunits (315). Each subunit contains one oxygen-binding heme group, for a total of four oxygen binding sites per hemoglobin (316). Oxygen binding at one subunit induces structural changes that increase oxygen affinity in the other three subunits, resulting in cooperative binding (317). Cl^-/HCO_3^- exchange by AE1 maintains low intracellular

pH in RBCs, which promotes the offloading of oxygen (213). The molecular structure of hemoglobin was one of the first biological structures determined by X-ray crystallography (318).

Transmembrane glycophorins are a major component of the RBC membrane, second only to AE1 (319). There are four glycophorins in RBCs, named glycophorins A-D in order of decreasing apparent molecular weight by SDS-PAGE (320,321). The glycophorins are single-span transmembrane proteins, with sialic acid moieties at their extracellular N-termini (322). These sialic acids contribute to the net negative charge of RBCs, preventing agglutination and adherence to vascular endothelial cells (323). Glycans on RBC membrane proteins including glycophorins and AE1 comprise the RBC pericellular matrix, the glycocalyx. Glycophorin A interacts with AE1 and assists in trafficking to the plasma membrane (253-255,324,325).

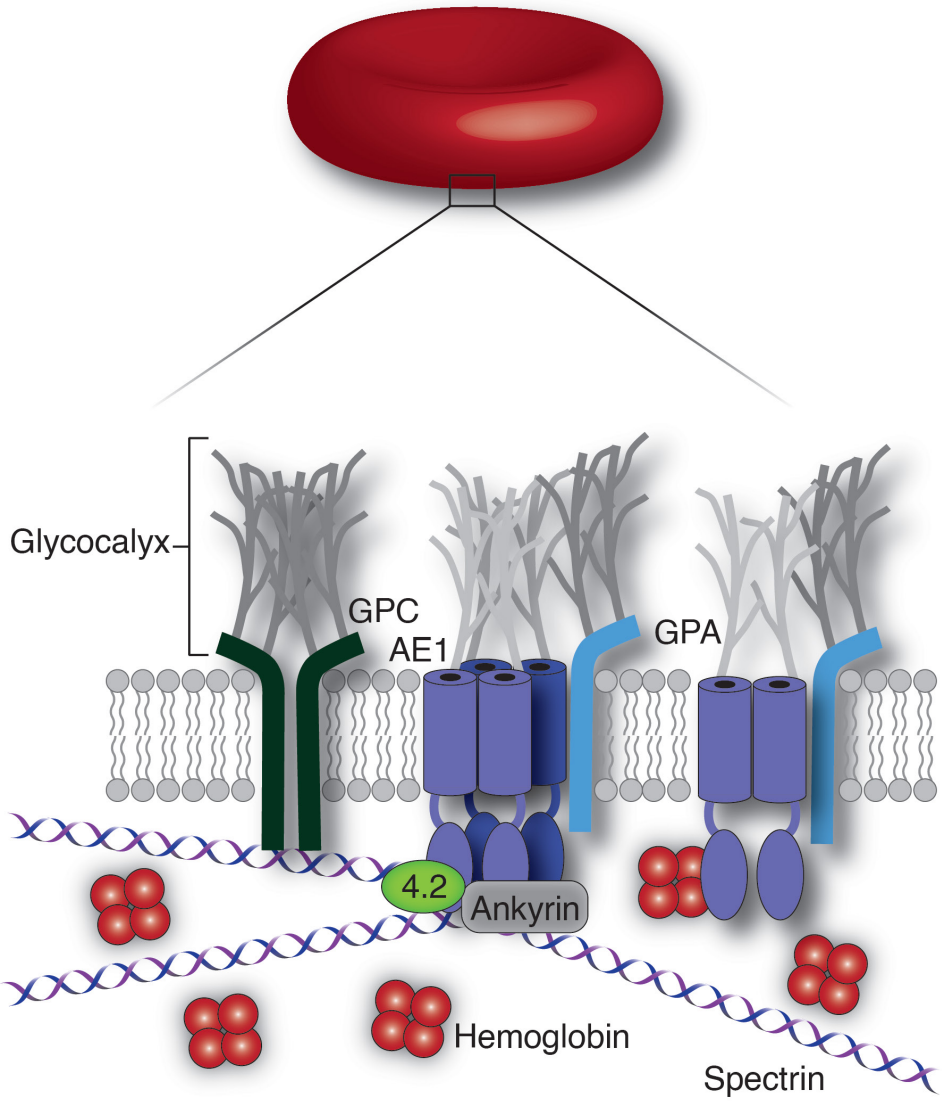

Figure 1.9 Components of red blood cells. Mature red blood cells have a biconcave shape (top). In the RBC lipid membrane (lower), AE1 (slate) associates as dimers and tetramers. AE1 tetramers form complexes with protein 4.2 (green) and ankyrin (grey) through cytosolic domain interactions. These complexes serve as anchoring points for the spectrin cytoskeleton (blue and magenta helices). The membrane domain of AE1 interacts with transmembrane protein glycophorin A (GPA, light blue). Extracellular regions of RBC glycoproteins including AE1, glycophorin A and glycophorin C (GPC, dark green), contribute to the RBC pericellular matric, the glycocalyx (grey). Tetrameric hemoglobin (red circles) comprises the major cytosolic protein component of RBCs.

1.4.9 Red Blood Cell Clearance

As mature red blood cells lack nuclei and membrane-bound organelles, they are unable to undergo apoptosis. At the end of their 120 day life span (326), senescent RBCs are cleared by immune system macrophages, which recognize red cells opsonized by AE1-directed IgG (239,240,327). The following alternate mechanisms prematurely clear RBCs in biochemical distress, ensuring optimal efficiency of the circulatory system.

Mechanical clearance of poorly deforming RBCs occurs at narrow inter-endothelial slits in the spleen (328,329). These 0.5 μm slits present a drastic challenge to RBCs with impaired deformability, leading to their retention in the spleen (328,330). This mechanical clearance contributes to anemia in diseases with impaired red cell deformity, including hereditary spherocytosis, thalassemia, and malaria (331-334).

RBCs can also undergo a type of premature suicidal death, termed eryptosis (335,336). Eryptosis can be induced by chemical injuries including oxidative stress (337,338), osmotic shock (339), energy depletion (340), increased temperature (341), and heavy metal toxicity (342-344). Eryptosis is characterized by cell shrinkage, membrane blebbing, and loss of membrane lipid asymmetry (345,346). Exposed phosphatidylserine on eryptotic RBCs is recognized by splenic macrophages, followed by phagocytosis (347,348).

Splenic retention and eryptosis enable controlled removal of faltering RBCs at early stages of distress. Severely compromised RBCs can undergo intravascular hemolysis, stress-induced RBC membrane rupture (349). Intravascular hemolytic diseases are often accompanied by severe organ damage, as the released hemoglobin overwhelms hemoglobin-scavenging haptoglobin in serum (349,350). Once free in plasma, iron in hemoglobin is oxidized from ferrous (Fe^{2+}) to ferric

(Fe^{3+}), followed by the release of free heme (351). The hydrophobicity of free heme allows it to readily partition into the cell membrane (352). Accumulated heme can promote oxidative damage directly, or indirectly by the release of iron and production of reactive oxygen species (353-355). The vascular endothelium is particularly susceptible to oxidative injury in RBC diseases with marked intravascular hemolysis and circulating free hemoglobin (356-358). Controlled removal of compromised RBCs in early stages of distress is thus preferred over, and less damaging than, spontaneous intravascular hemolysis.

1.6 SLC4A11

SLC4A11 is the most phylogenetically distinct member of the SLC4 family (Fig. 1.1). SLC4A11 contains a 41 kDa cytoplasmic domain and a 57 kDa membrane domain. Unlike the other SLC4 family members, SLC4A11 does not mediate HCO_3^- transport (359-362). SLC4A11 has demonstrated transmembrane water flux (359,363), Na^+/OH^- cotransport (360,361), Na^+-independent H^+ (OH^-) transport (53,364), electroneutral NH_3 transport (362), and H^+/NH_3 cotransport (365,366). While plant and yeast orthologs of SLC4A11 transport borate (367,368), early reports of human SLC4A11 mediating $Na^+/B(OH)^-_4$ cotransport (191) were unable to be replicated (360,361). Recently, SLC4A11 was found to play a role in cell adhesion in the cornea (369). Mutations in SLC4A11 cause some incidences of blinding corneal dystrophies (80-101).

1.6.1 Human Cornea

The cornea is the outermost layer of the eye, and acts as a protective barrier for the inner structures while providing about two thirds of the eye's refractive power (370). The cornea is a highly organized avascular tissue, which offers structural protection while maintaining optical

transparency. The human cornea is arranged into five different layers (from anterior to posterior): epithelium, Bowman's layer, stroma, Descemet's membrane, and endothelium (Fig. 1.10 A).

The epithelium is the outermost layer of the eye, and is made up of five to seven layers of fairly uniform cells (371). The epithelium contributes to the refractive index of the eye, and acts as a barrier to chemicals and microbes. Corneal epithelial cells are regenerative, with a lifetime of 7-10 days (372). The corneal epithelium basement membrane is comprised of collagen and laminin (373).

Posterior to the epithelial basement membrane is the acellular Bowman's layer, which is composed of randomly arranged collagen fibrils (374). The Bowman's layer contains collagen and proteoglycans, and its smooth structure helps the cornea maintain its shape. Bowman's layer has no regenerative ability.

The next posterior layer, the stroma, comprises 80-85% of the thickness of the cornea (375). The stroma contains glycosaminoglycans and highly organized collagen fibrils, which impart structural strength to the cornea while maintaining visual clarity (376-378). The regular packing of the collagen fibrils into layers, or lamellae, is essential for transparency. The stroma is mostly acellular, with the exception of sparsely distributed keratocytes (379). These keratocytes synthesize collagen, glycosaminoglycans, and matrix metalloproteases to maintain stromal homeostasis (380). While the lamellae in the anterior stroma are densely packed and interwoven, the posterior stroma is more hydrated (381,382). The hydrated posterior stroma is more prone to fluid swelling than the anterior stroma (383).

Following the stroma is Descemet's membrane, the basement membrane for corneal endothelial cells. The Descemet's membrane is made of collagen and laminin which are

continuously secreted by endothelial cells (384). The final layer of the cornea is the corneal endothelium, formed of a single layer of hexagonal cells. (385). Corneal endothelial cells are non-regenerative (386,387). Posterior to the cornea lies the aqueous humor, the main source of nutrients for the avascular cornea. The composition of the aqueous humor is similar to plasma, with the exception of a lower protein concentration (200-fold less) (388).

The corneal endothelium performs two functions essential for corneal clarity: 1. As a passive barrier between aqueous humor and stroma, the endothelium is permeable to nutrients and other molecules supplied to the cornea (385). 2. The corneal endothelium regulates stromal fluid levels, maintaining a level of deturgescence that is critical for corneal clarity. High concentration of proteoglycans and collagen in the stroma creates an osmotic force for fluid accumulation, which is countered by the fluid reabsorption function of the corneal endothelium. To fulfil dual functional roles as a passive (leaky) barrier and a fluid pump, the corneal endothelium has a 'pump-leak' mechanism (389), which is complex and poorly understood (390). In brief, contributions from stromal glycosaminoglycans, nutrient transport across the endothelium, and high paracellular permeability of the endothelium promote osmotically – driven water movement from the aqueous humor into the stroma (leak). This water movement is countered by the endothelial 'pump', in which fluid movement out of the stroma is coupled to ion secretion from the stroma to the aqueous humor (133). This mechanism is essential for corneal fluid balance and clarity, and corneal endothelial dysfunction is one of the most common causes of corneal blindness (391).

1.6.2 Role of SLC4A11 in the Corneal Endothelium

SLC4A11 resides at the basolateral side of corneal endothelial cells, facing stroma (359,392) (Fig. 1.10 B). Here, SLC4A11 promotes fluid reabsorption back to the aqueous humor, either directly

or by promoting the ongoing health of endothelial cells. SLC4A11 has proposed roles maintaining stromal deturgescence by two modes of action: 1. solute-driven water reabsorption, and 2. trans-membrane water flux.

In solute-driven water reabsorption, basolateral proteins NBCe1 and H^+-coupled lactate transporter MCT1 transport Na^+, HCO_3^-, and $lactate^-$ from the stroma to the aqueous humor, to establish a localized osmotic gradient driving the return of water to the aqueous humor (Fig. 1.10) (133). As an acid loader, SLC4A11 could maintain intracellular pH by alkalinizing HCO_3^- import by NBCe1 with H^+ import (53). As an acid extruder, SLC4A11 could promote the continued action of H^+-dependent MCT1 by providing surface H^+ (53). Additionally, both basolateral SLC4A11 and apical aquaporin1 (AQP1) promote trans-membrane water flux, suggesting they may work cooperatively to provide a water conductive pathway across the corneal endothelium (359). SLC4A11 is further reported to transport NH_3, either alone (362) or cotransported with H^+ (365,393). Endothelial cell glutaminolysis (394) gives rise to NH_3, which promotes production of detrimental reactive oxygen species. SLC4A11-facilitated NH_3 efflux then promotes endothelial cell health by limiting production of reactive oxygen species.

Recently, SLC4A11 ECL3 was found to play a role promoting corneal endothelial cell adhesion to Descemet's membrane (369). SLC4A11 interacts with Descemet's membrane through extracellular loop 3 (369). Endothelial cell anchorage to a basement membrane is essential for healthy cellular physiology (395). Compromised cell adhesion to the basement membrane triggers programmed cell death in epithelial cells (396), which is particularly poignant in the non-regenerative corneal endothelium.

1.6.3 SLC4A11 Mutations Cause Some Forms of Corneal Dystrophy

SLC4A11 mutations cause the blinding corneal dystrophy congenital hereditary endothelial disorder (CHED) (82-98) and some cases of Fuchs endothelial dystrophy (FECD) (86,98-101). SLC4A11 mutations also cause Harboyan Syndrome (81), corneal dystrophy accompanied by progressive sensorineural hearing loss, which has recently been interpreted as a manifestation of CHED (397). About 70 corneal dystrophy-causing point mutations have been identified in SLC4A11, located in both the membrane domain and the cytoplasmic domain (80-101).

CHED is a rare autosomal-recessive dystrophy which presents at birth or within the first decade of life (391). Patients exhibit decreased endothelial cell count, corneal edema, and thickened Descemet's membrane (398). The corneas of CHED patients are 2-3 times the thickness of normal corneas due to extensive corneal edema, and have a distinct ground-glass appearance (399).

FECD is a dominantly inherited disease, with a lifetime incidence of about 4% (399). FECD is a progressive disorder predominantly affecting individuals above 40 years of age (400). FECD is characterized by decreased visual acuity, progressive decrease in endothelial cell count (401), thickening of the Descemet's membrane (402) and stroma (399), and collagen deposits (guttae) secreted by endothelial cells onto the Descemet's membrane (403). There is evidence that FECD progression is initiated by failure of the endothelial water flux pathway, followed by failure of the barrier function (404). Patients experience painful corneal erosions, and hazy vision which can progress to blindness (399).

Both CHED and FECD patients suffer corneal edema followed by clouding of the cornea, which leads to eventual blindness (399). CHED and FECD patients experience blurred vision, and

mild discomfort to severe pain. Therapeutic approaches are mostly aimed at lessening discomfort and pain, and are not effective at late stages of disease (391). These include hypertonic saline eye drops and eye drying. The only definitive treatment for these dystrophies is corneal transplant (391).

Molecular defects of SLC4A11 leading to corneal dystrophies can be classified in two ways: folding defects, leading to retention in the endoplasmic reticulum, and mechanistic defects, where SLC4A11 traffics to the cell membrane but is non-functional (Fig. 1.11). While both defects can cause corneal disease from a loss of SLC4A11 function at the cell membrane, treatment options vary depending on the molecular mechanism of disease. Protein folding correctors have the potential to rescue misfolded proteins and restore function at the plasma membrane, treatments which will be ineffective for properly folding, non-functional mutants. Thus, molecular characterization of SLC4A11 mutants is essential to determine potential therapeutics for patients (405). While categorizing SLC4A11 mutants by prevalent molecular phenotype is practical in the context of assessing candidates for folding correction therapy, mutants classified as non-functional likely exhibit some degree of misfolding, and misfolded mutants may be non-functional even if present at the plasma membrane. Targeted medical treatments based off individual molecular phenotypes is termed personalized medicine, or precision medicine. At the foreground of personalized medicine is Cystic Fibrosis, a disease arising from defects in the membrane protein CF transmembrane regulator (CFTR) (406). The efficacy of mutation-specific drugs used in Cystic Fibrosis treatment provides a framework for personalized therapies in diseases resulting from defects in membrane proteins (407).

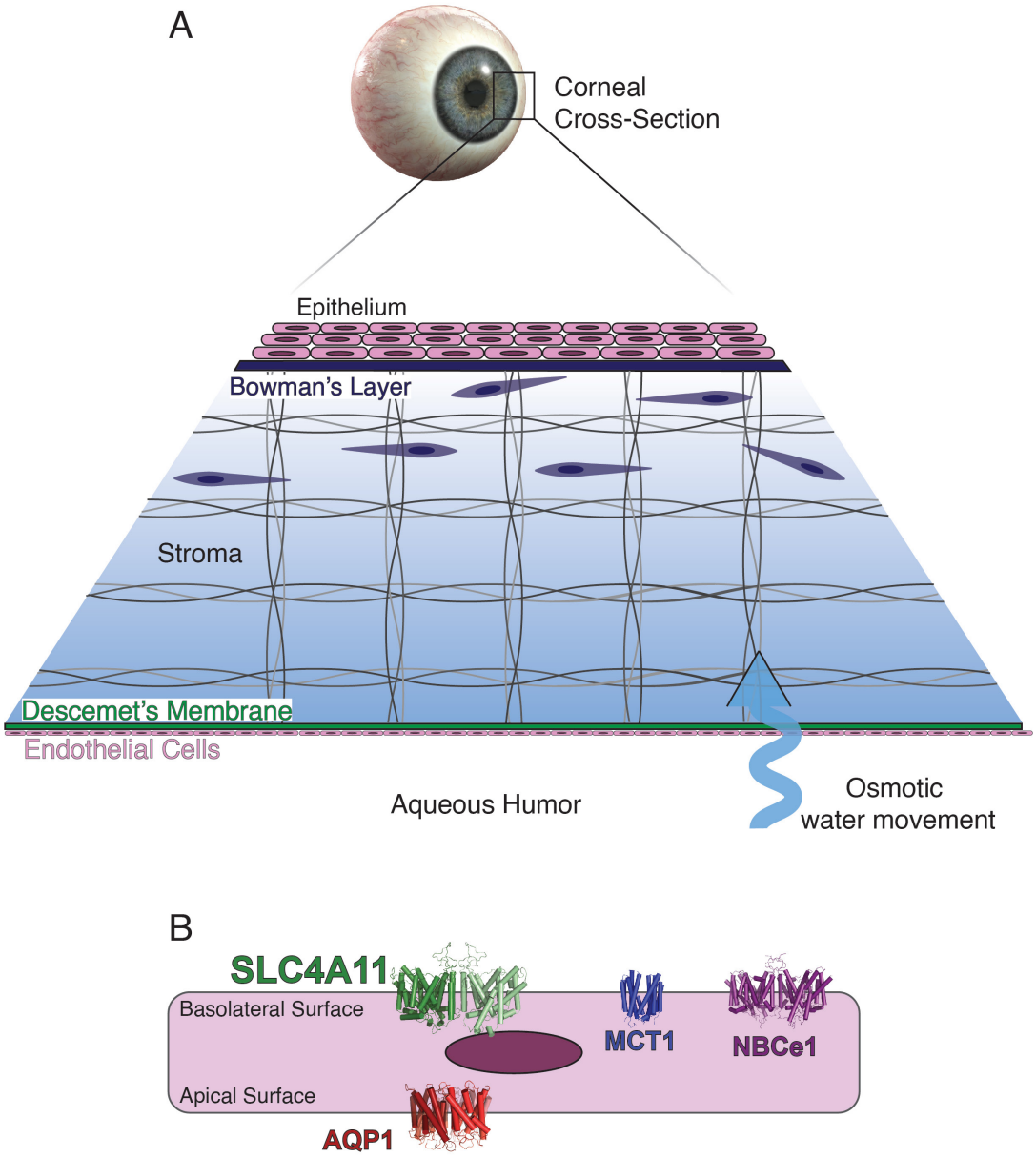

Figure 1.10 SLC4A11 in healthy human cornea. A) The cornea is divided into layers (from anterior to posterior, thickness shown approximately to scale): epithelium, Bowman's layer (dark blue), stroma, Descemet's membrane (green), endothelial cells (light pink), aqueous humor. The thickest layer, the stroma, contains anterior keratocytes (dark blue) and high concentrations of dissolved solutes, creating an osmotic drive for water to leave the aqueous humor (blue arrow). Stromal accumulation of water results in edema and disturbance of ordered collagen fibrils (grey

line array). B) To combat fluid accumulation, SLC4A11 (green cartoon structure) on the basolateral side of endothelial cells (pink, lower) promotes water flux back into the aqueous humor directly, in conjunction with apical aquaporin 1 (AQP1, red cartoon structure), or indirectly by either supporting continued actions of basolateral MCT1 (blue cartoon structure) and NBCe1 (purple cartoon structure) in solute-driven water reabsorption, or promoting continued endothelial cell health by NH_3 export.

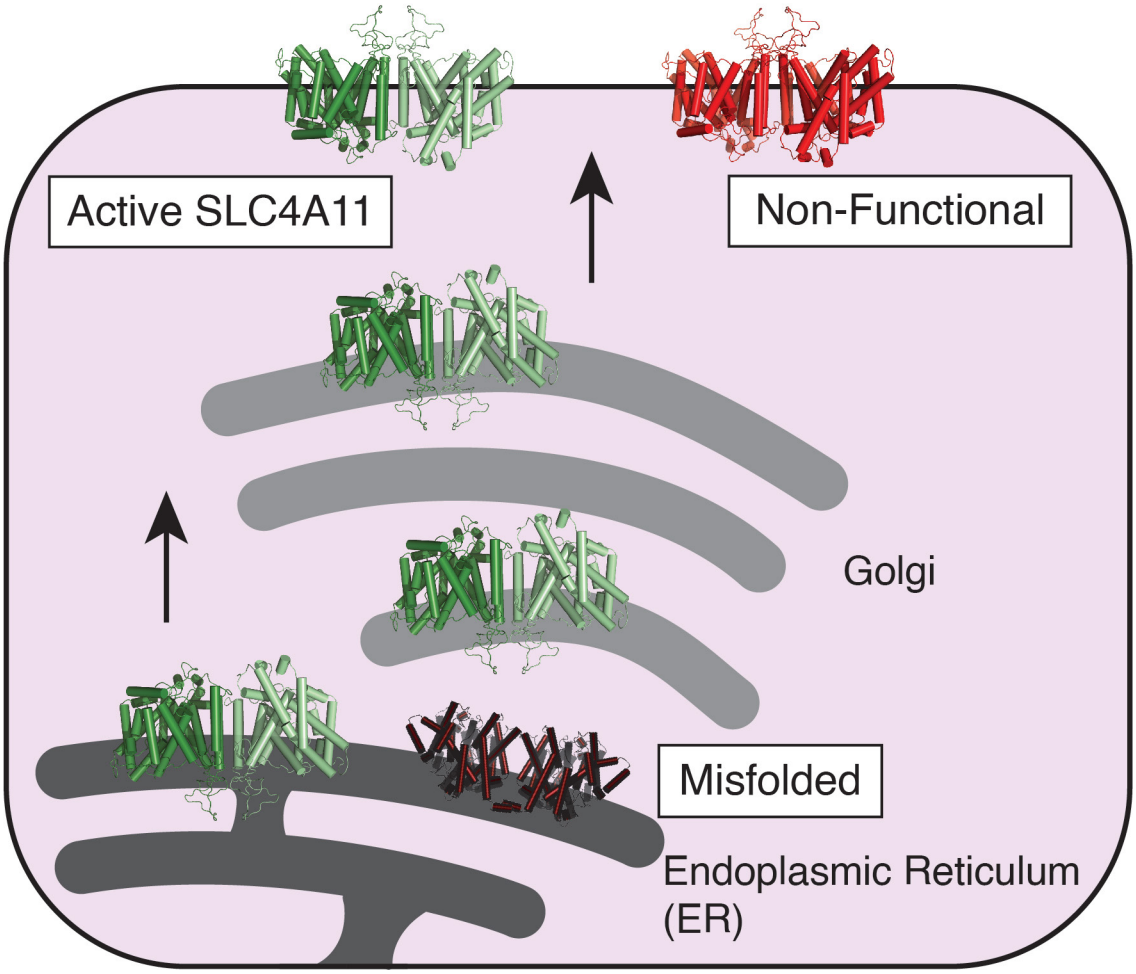

Figure 1.11 Molecular mechanisms of disease caused by SLC4A11 defects. SLC4A11 (green) is cotranslationally inserted into the ER (dark grey), and if properly folded progresses through the Golgi network (light grey) to the plasma membrane ('Active SLC4A11'). Point mutations causing misfolding result in ER retention of SLC4A11 ('Misfolded', dark red cylinders), followed by degradation. Non-functional SLC4A11 disease variants mature to the plasma membrane but are functionally inactive ('Non-Functional', bright red cylinders).

Chapter 2: Materials and Methods

2.1 Materials

Oligonucleotides were from Integrated DNA Technologies (Coralville, IA). Red blood cells were obtained from Canadian Blood Services after Canadian Blood Services Research Ethics Board approval (Project Name: Molecular mechanism for signaling red blood cell senescence, REB ID 2019.045) (Vancouver, Canada). Dulbecco's modified Eagle's medium (DMEM), fetal bovine serum (FBS), calf serum (CS), and penicillin-streptomycin-glutamine (PSG) were from Life Technologies (Carlsbad, CA, USA). Cell culture dishes (60 and 100 mm) were from Sarstedt (Montreal, QC, Canada). Poly-L-lysine, glutaraldehyde, sodium borohydride, and Corning Erlenmeyer cell culture flasks were from Sigma-Aldrich (Oakville, ON, Canada). HEK293-F cells, Freestyle 293 Expression Medium, Freestyle MAX Reagent, Dynabeads Protein G, 4,4'-diisthiocyanodihydrostilbene-2,2'-disulfonate (H_2DIDS), ProLong Gold antifade reagent with DAPI, Alexa Fluor 647 Chicken anti-Mouse IgG Secondary Antibody, and Alexa Fluor 594 Chicken anti-Rabbit IgG Secondary Antibody were from Invitrogen (Carlsbad, CA, USA). BCA Protein Assay Kit was from Pierce (Rockford, IL, USA). Complete Protease Inhibitor cocktail tablets were from Roche Applied Science (Indianapolis, IN, USA). Phenyl methane sulfonyl fluoride (PMSF), glass coverslips and bovine serum albumin (BSA) were from Thermo Fisher Scientific (Ottawa, ON, Canada). Immobilon-P PVDF membranes and Immobilon Crescendo Western HRP Substrate were from Millipore (Millipore Corp., MA, USA). Streptavidin-Biotinylated HRP Complex and HRP-conjugated sheep anti-mouse secondary antibody (CAS. NXA931) were from GE Healthcare (Piscataway, NJ, USA). Q5 Site-directed mutagenesis kit was from New England Biolabs (Ipswich, USA). Paraformaldehyde was from Electron Microscopy Sciences (Hatfield, PA, USA). Lucifer Yellow Iodoacetamide (LYIA) was from Setareh Biotech (Eugene, OR, USA). Purified anti-HA.11 Epitope Tag Antibody was from Biolegend (Cat.

901503) (San Diego, CA, USA). Monoclonal antibody against glyceraldehyde-3-phosphate dehydrogenase (GAPDH) (sc-47724), and monoclonal antibody against human glycophorin C residues 1-85, recognizing glycophorin C and D (GPC) (sc-365599) were from Santa Cruz Biotechnology (Santa Cruz, CA, USA). Cy3 AffiniPure Donkey Anti-Mouse IgG (Code 715-165-150) and Alexa Fluor 488 AffiniPure Donkey Anti-Rabbit IgG (Code 711-545-152) were from Jackson ImmunoResearch Laboratories (West Grove, PA, USA). Custom rabbit anti-SLC4A11 Extracellular Loop 3 antibody (αEL3) and rabbit anti-AE1 814-827 Antibody (α814-827) were from Primm Biotech (Cambridge, MA, USA). Nα-(3-Maleimidylpropionyl) Biocytin (biotin maleimide), Chicken anti-Mouse IgG Secondary Antibody, Alexa Fluor 647 (A-21463), and Chicken anti-Rabbit IgG Secondary Antibody, Alexa Fluor 594 (A-21442) were from Invitrogen (Eugene, OR, USA). Anti-AE1 COOH-terminal mouse monoclonal antibody IVF12 was a gift from Dr. Michael Jennings (University of Arkansas) (408).

2.2 DNA constructs

Integrity of all the clones was confirmed by DNA sequencing (Molecular Biology Facility, Department of Biological Sciences, University of Alberta).

2.2.1 SLC4A11 Expression constructs

The eukaryotic expression construct (pAMC1) for a shortened version of splicing variant 2 of human SLC4A11 (891 amino acid, NCBI reference: NG_017072.1), encoding an 856 amino acid protein with an N-terminal Hemagglutinin tag (HA-tag) was described previously (409). This shortened version of SLC4A11 splicing variant 2 results from transcription initiating at an alternative start site at M36 (amino acid numbering is based on reference sequence NG_017072.1), resulting in protein lacking the N-terminal 35 amino acids of 891 amino acid SLC4A11 variant 2. The shortened SLC4A11 variant 2 represents the predominant form of SLC4A11 present in human

cornea (410). Q5 Site-Directed Mutagenesis Kit with mutagenic oligonucleotides (Table. 2.1) was used to create expression constructs for point mutants c.2023G > C (p.Glu675Gln), c.2171A > G (p.His724Arg), c.2170_2171delinsGC (p.His724Ala), c.2158_2159delinsCT (p.Ala720Leu), and c.1525_1527delinsAAA (p.Gly509Lys), using pAMC1 as template for mutagenesis. Amino acid numbering is based on reference sequence NG_017072.1, with HGVS numbering recommendations. cDNA encoding enhanced green fluorescent protein (eGFP) was obtained from Clontech (peGFP-C1 vector; Clontech, Mountain View, CA, U.S.A.).

2.2.2 AE1 Expression Constructs

A mammalian expression construct encoding full-length erythrocyte AE1 (911 amino acid, NCBI reference: NG_007498) with the five endogenous cysteines mutated to serine ($AE1C^-$) was previously constructed (411) in the expression vector pRBG4 (412). AE1 single cysteine point mutants p.Cys201 (C201), p.Ala456Cys (A456C), p.Ser517Cys (S517C), p.Tyr555Cys (Y555C), p.Lys817Cys (K817C), p.Val822Cys (V822C), p.Lys826Cys (K826C), and p.Lys892Cys (K892C) were previously constructed in $AE1C^-$ background (265). Q5 Site-directed mutagenesis kit was used to clone transport-deficient mutant p.Glu681Gln using AE1 K817C as a template (K817C(E681Q)), using a PCR-based strategy (Table 2.2). Membrane domain (MD) constructs of single cysteine point mutants Y555C, K817C, K817C(E681Q) and K892C were constructed using Q5 Site-directed mutagenesis kit with a PCR-based deletion strategy to remove AE1 cytoplasmic domain residues 2-368. The resulting MD constructs encode AE1 p.(Glu2_Pro368del) with single cysteine point mutations Y555CMD, K817CMD, K817C(E681Q)MD, and K892CMD.

AE1 constructs AE1-557HA and AE1-911HA, with extracellular and intracellular HA tags, respectively, were a generous gift from Dr. Reinhart Reithmeier. The AE1-HA constructs encode human AE1 cDNA in pcDNA3, with an insertion of codons 3′-TAC CCA TAC GAT GTT

CCA GAT TAC GCT-5′ encoding the HA-epitope, following positions 557 or 911 (413). Construction of pDEJ4 expression construct encoding full-length wild-type eAE1 in pcDNA3 was previously described (414).

Table 2.1 Oligonucleotides used in cloning of SLC4A11 variants. Underlining indicates position of mutated codons. Amino acid numbering is based on NCBI reference sequence NG_017072.1, using HGVS recommended numbering.

SLC4A11 Mutant	**Mutant Shorthand**	**Forward Primer**	**Reverse Primer**
c.1525_1527delinsAAA p.(Gly509Lys)	G509K	TGCCGTCAAGAAA ACGGTTAAAATC	TCCAGCACAAACGTG ATG
c.2158_2159delinsCT p.(Ala720Leu)	A720L	TTGGATCCATCTC GCCTACCCCC	GGCAGCCCAAACAGA GAC
c.2171A>G p.(His724Arg)	H724R	CGCCTACCCCCGC TCCCCGCTGC	GCATGGATCCAAGGC AGCCCAAACAGAGAC
c.2170_2171delinsGC p.(His724Ala)	H724A	CGCCTACCCCGCC TCCCCGCTGC	GCATGGATCCAAGGC AGC
c.2023G>C p.(Glu675Gln)	E675Q	CTTCTTCATCCAG CAGAACTTGGTG	AGCATGGACAGCAGG AAG

Table 2.2 Oligonucleotides used in cloning of AE1 variants. Underlining indicates position of mutated codons.

AE1 Mutant	**Mutant Shorthand**	**Forward Primer**	**Reverse Primer**
c.2041G>C p.(Glu681Gln)	E681Q	CATATTCCTGCAGTCTCAGATCAC	AGGATGAAGACCAGCAGAG
c.4_1104del p.(Glu2_Pro368del)	AE1MD	GATGACCCTCTGCAGCAG	CATGGCGTGGTCCTGAGT

2.3 Cell Culture

2.3.1 HEK293 Cell Culture

HEK293 cells were grown in T-75 flasks in 10 mL DMEM with 5% (v/v) fetal bovine serum, 5% (v/v) calf serum, and 1% (v/v) penicillin-streptomycin-glutamine, and cultured in a humidified incubator at 5% CO_2, 37 °C. For transfection, cells were plated on poly-L-lysine coated 60 mm dishes, or 100 mm dishes (containing poly-L-lysine coated coverslips for immunofluorescence slides). Cells were transfected 4-6 h after plating, using the calcium phosphate precipitation method (415). Substituted cysteine accessibility analysis and confocal immunofluorescence was performed 24 h post-transfection, and immunoblotting 48 h post-transfection.

HEK293-F cells were grown in Freestyle 293 Expression Medium, in a humidified 37 °C incubator at 8% CO_2, in Corning Erlenmeyer cell culture flasks shaken at 100 rpm. Cells were transfected at a density of 1 x 10^6 cells/mL using Freestyle MAX Reagent and harvested 48 h post-transfection.

2.3.2 Poly-L-Lysine Coating

60 mm cell culture dishes, or 25 mm circular glass coverslips in 100 mm cell culture dishes, were treated with 5 M NaOH for 15 min. NaOH was aspirated, and dishes were washed with autoclaved H_2O for 5 m. Aspiration and washing was repeated with 95% ethanol, H_2O, and twice with PBS (140 mM NaCl, 3 mM KCl, 6.5 mM Na_2HPO_4, 1.5 mM KH_2PO_4, pH 7.4), for 5 min each wash. Dishes were treated with poly-L-lysine solution (0.1 mg/mL poly-L-lysine in PBS, pH 7.4) for 15 min. Excess poly-L-lysine solution was removed by aspiration, and remaining solution was left to dry under UV light for 18 h. Poly-L-lysine coated dishes and coverslips were rinsed with PBS prior to use with HEK293 cells to remove dried salts.

2.4 Anti-AE1 Amino Acid 814-827 Antibody

A peptide corresponding to human AE1 residues 814-827 was used to raise a polyclonal antibody in rabbits (called α814-827). A custom antibody against SLC3A11 extracellular loop 3 was previously described (369), wherein a peptide corresponding to human SLC4A11 amino acids 527–540 of extracellular loop 3 was used to raise a polyclonal antibody in rabbits (called αEL3). Both custom antibodies were from Primm Biotech (Cambridge, MA, USA).

2.5 Water Flux Assays

Water flux assays were performed as previously described (359). HEK293 cells, grown on poly-L-lysine coated 25 mm circular glass cover slips, were transiently co-transfected with cDNA encoding enhanced green fluorescent protein (eGFP) and N-terminally HA tagged SLC4A11-WT, G509K, A720L, H724R, H724A, E675Q, or empty pcDNA 3.1 vector in 1:8 molar ratio. After 48 h of incubation, coverslips were mounted in a 35 mm diameter Attofluor Cell Chamber. During experiments, the chamber was perfused with isotonic MOPS-buffered saline solution (MBSS: 90 mM NaCl, 5.4 mM KCl, 0.4 mM $MgCl_2$, 0.4 mM $MgSO_4$, 3.3 mM $NaHCO_3$, 2 mM $CaCl_2$, 5.5 mM glucose, 100 mM D-mannitol, 10 mM HEPES, pH 7.4, 300 mOsm/kg) followed by hypotonic (200 mOsm/kg) MBSS buffer, pH 7.4 (same composition as previous but lacking D-mannitol). Solution osmolality was measured using an Advanced Instruments model 3D3 osmometer (Advanced Instruments Inc., Norwood, MA). A live cell environment chamber (Chamlide, Seoul, Korea), set to 24 °C throughout the experiment, was mounted on the stage of a Wave FX spinning disc confocal microscope (Quorum Technologies, Guelph, ON, Canada), with a Yokogawa CSU10 scanning head (Tokyo, Japan). The microscope has a motorized XY stage with Piezo Focus Drive (MS-4000 XYZ Automated Stage; ASI, Eugene, OR). Acquisition was performed with a Hamamatsu C9100–13 Digital Camera (EM-CCD; Chamlide) and a 20× objective during

excitation with a laser (Spectral Applied Research, Richmond Hill, ON, Canada) at 491 nm. Green fluorescent protein fluorescence, collected through a dichroic cube (Quorum Technologies) at wavelengths 520–540 nm, was acquired at 1 point s^{-1} for 4 min. Quantitative image analysis was performed by selecting a region of interest for each HEK293 cell with Volocity 6.0 software (PerkinElmer, Waltham, MA). Following the switch to hypotonic MBSS buffer, the rate of fluorescence change was determined from the initial 15 s of linear fluorescence change.

2.6 Homology Modelling and Validation

A three-dimensional homology model of the human SLC4A11 membrane domain was created, using the crystal structure of human AE1 membrane domain at 3.5 Å resolution (PDB ID 4YZF) (1) as template. Pairwise alignment of AE1 and SLC4A11 membrane domains was performed using PSI/TMCoffee (416) with manual adjustment to remove N- and C-termini protein sequence from homology modeling due to a lack of template. Homology modeling was performed on the SWISS-MODEL server (417-420) (https://swissmodel.expasy.org) with default parameters, using a modified AE1 PDB structure file as template. AE1 PDB file was modified by removal of AE1 chains B-D, and 4,4-diisothiocyanatodihydrostilbene-2,2-disulfonic acid (H_2DIDS) inhibitor molecule and Fab antibody fragments used in crystallization to leave a single AE1 monomer for modeling (Chain A). Crystallization of AE1 with H_2DIDS resulted in solving the structure in the outward-open conformation, and thus the SLC4A11 homology model is found in the outward-open conformation as well. Demonstrated sensitivity of SLC4A11 to stilbene disulfonates including H_2DIDS (359) indicates that this is a valid SLC4A11 structural conformation. The AE1 crystal structure was unable to resolve some extramembraneous loops; corresponding regions of SLC4A11 were modeled de novo by SWISS-MODEL. Verify3D and PROCHECK servers were used to assess model quality *in silico* (421-424). SLC4A11 dimer was modeled by aligning two

SLC4A11 monomers with the AE1 dimer, using PyMOL. Amino acid residue conservation of AE1 and SLC4A11 was analyzed using amino acid sequences from 30 species, including mammals, birds, and fish (Table 2.3). Multiple sequence alignment was performed by Clustal Omega (160-162). Mapping residue conservation was performed with the ConSurf server (425-428). Structural effects of disease-causing point mutations were estimated using PyMOL and the MolProbity (http://molprobity. Biochem.duke.edu/) (429,430), PDB2PQR (http://nbcr-222.ucsd.edu/pdb2pqr_2.1.1/) (431-433), and StrucTools (https://hpcwebapps.cit.nih.gov/structbio/) (434) servers.

Table 2.3 NCBI reference sequences used in mapping conservation of amino acid residues of AE1 and SLC4A11 membrane domains with the ConSurf server.

Species	**AE1**	**SLC4A11**
Homo sapiens	NP_000333.1	NG_017072.1
Rattus norvegicus	NP_036783.2	NP_001101245.1
Mus musculus	AAA37278.1	NP_001074631.1
Danio rerio	NP_938152.1	XP_005156613.1
Bos taurus	NP_851379.1	NP_001178243.1
Equus caballus	NP_001075257.1	XP_014590544.1
Canis lupus familiaris	NP_001041496.1	XP_005634909.1
Chrysemys picta bellii	XP_008160863.1	XP_008167829.1
Esox lucius	XP_012991339.1	XP_010877621.1
Jaculus jaculus	XP_004655358.1	XP_004661495.1
Maylandia zebra	XP_004552471.1	XP_004554836.1
Dipodomys ordii	XP_012887504.1	XP_012866580.1
Echinops telfairi	XP_004707274.1	XP_004697924.1
Sorex araneus	XP_004621081.1	XP_004611052.2
Clupea harengus	XP_012681230.1	XP_012693688.1
Otolemur garnettii	XP_003786322.1	XP_012659525.1
Cariama cristata	XP_004684149.2	XP_009708451.1
Orcinus orca	XP_004286037.1	XP_004285355.1
Octodon degus	XP_004633882.1	XP_004634378.1

Nomascus leucogenys	XP_003270611.1	XP_003278003.1
Pongo abelii	NP_001127339.1	XP_009231688.1
Oreochromis niloticus	AAQ89898.1	XP_005453432.1
Cricetulus griseus	ERE68362.1	XP_007635183.1
Camelus ferus	EPY72637.1	XP_014416765.1
Cyprinodon variegatus	XP_015227525.1	XP_015256792.1
Macaca mulatta	XP_014975343.1	XP_001111005.2
Poecilia latipinna	XP_014873768.1	XP_014914044.1
Sturnus vulgaris	XP_014744934.1	XP_014731682.1
Equus asinus	XP_014704844.1	XP_014717350.1
Tupaia chinensis	XP_006167421.1	XP_014437791.1

2.7 Substituted Cysteine Accessibility Assay

HEK293 cells on poly-L-lysine coated 60 mm dishes were transfected with cDNA encoding AE1 single cysteine point mutants in an AE1C$^-$ background. 24 h after transfection, HEK293 cells were washed with 5 mL PBS (140 mM NaCl, 3 mM KCl, 6.5 mM Na_2HPO_4, 1.5 mM KH_2PO_4, pH 7.4, 300 mOsm). For assays with H_2DIDS, cells were incubated with 50 µM H_2DIDS in PBS, or PBS alone for control samples, at 37 °C for 30 min prior to LYIA labeling. Cells were then incubated with PBS containing 2 mM LYIA, or PBS alone, for 20 min at 20 °C. After 20 min, biotin maleimide was added to a final concentration of 0.2 mM from a 20 mM stock in DMSO. Reaction was stopped after 10 min by addition of 5 mL of stop buffer (DMEM with 10% (v/v) FBS, 0.14% (v/v) 2-mercaptoethanol). Cells were washed with 5 mL of 4 °C PBS and lysed in 300 µL IPB buffer (1% (v/v) Igepal, 0.5% (v/v) sodium deoxycholate, 5 mM EDTA, 150 mM NaCl, 10 mM Tris-HCl, pH 7.5) containing 1 mM PMSF and Complete Protease Inhibitor cocktail at 1x, on ice for 20 min. Insoluble cell material was removed from lysates by centrifugation in a Thermo IEC Micromax Centrifuge at 16000 x g for 10 min at 4 °C. Protein concentration was determined using BCA assay, following the manufacturer's instructions.

2.8 Immunoprecipitation

Dynabeads Protein G (5 µL slurry) were incubated with anti-AE1 polyclonal 1658 antibody raised against AE1 C-terminus (265) for 1 h on ice, preceding addition of 200 µg total protein HEK293 cell lysate and incubation at 4 °C for 10-16 h with rotation. After incubation, resin was separated from liquid in a magnetic stand, and washed three times with 200 µL cold IPB containing 1 mM PMSF and Complete Protease Inhibitor cocktail. Washed resin was mixed with SDS-PAGE sample buffer (10% (v/v) glycerol, 2% (w/v) SDS, 0.5% (w/v) bromophenol blue, 75 mM Tris, pH

6.8) containing 2% (v/v) 2-mercaptoethanol, and heated at 65 °C for 5 min before SDS-PAGE analysis.

2.9 SDS-PAGE and Immunoblotting

Protein samples were resolved on 8% (w/v) SDS-PAGE gels and transferred onto Immobilon-P PVDF membranes (Millipore Corp., MA, USA). Biotinylation of immunoprecipitated proteins was detected using streptavidin-biotinylated HRP, diluted 1:2500 in TBST-BSA (0.1% (v/v) Tween-20, 137 mM NaCl, 20 mM Tris, pH 7.5, containing 0.5% (w/v) bovine serum albumin), and Immobilon Crescendo Western HRP Substrate reagent. Following visualization with streptavidin-biotinylated HRP, blots were stripped in stripping buffer (62.5 mM Tris, 2% (w/v) SDS, 100 mM 2-mercaptoethanol, pH 6.7) for 10 min at 55 °C, and re-probed in TBST-M (TBST containing 5% (w/v) nonfat dry milk powder (Carnation)) with mouse monoclonal anti-AE1 COOH-terminal antibody IVF12 used at 1:3000, kindly provided by Dr. Michael Jennings (University of Arkansas) (408). After washing, blots were probed with HRP-conjugated sheep anti-mouse 1:4000 in TBST-M and visualized with ECL reagent. All immunoblots were visualized using an ImageQuant LAS4000 (GE Healthcare) photodocumentation system. Quantitative densitometric analyses were performed using ImageQuant TL 8.1 software.

2.10 Antibody Binding Assays in HEK293 Suspension Cells

HEK293-F cells were counted using a Countess II Automated Cell Counter (Invitrogen) and assessed for viability using Trypan Blue 48 h post-transfection with either wild-type AE1, wild-type SLC4A11, or vector control. Cells were washed once with isosmotic PBS. Cells transfected with wild-type AE1 or empty vector were incubated with either rabbit pre-immune serum, a polyclonal antibody raised in rabbits against a peptide corresponding to AE1 residues 814-827 (α814-827), or anti-AE1 C-terminal polyclonal 1658 antibody, each at 0.5 μg/mL. Cells

transfected with wild-type SLC4A11 or empty vector were incubated with an antibody raised in rabbits against a peptide (NH_2-HTKRTSSLVSLSGL-COOH) corresponding to amino acids 527–540 of human SLC4A11-EL3 (αEL3) by Primm Biotech as an extracellular control (369). For each binding condition, 1.5 x 10^5 cells were incubated in 500 µL PBS containing 0.1% (w/v) BSA, and indicated primary antibodies or pre-immune serum, with rotation at 37 °C for 30 min. Following binding, cells were centrifuged in a Thermo IEC Micromax Centrifuge for 5 min at 500 x g and washed three times with PBS+0.1% (w/v) BSA before lysing on ice for 20 min with 30 µL IPB containing 2 mM PMSF and Complete Protease Inhibitor cocktail. Insoluble material was removed by centrifugation in a Thermo IEC Micromax Centrifuge at 16000 x g for 20 min at 4 °C. Solubilized lysates were mixed 1:1 with non-reducing SDS-PAGE sample buffer, and heated at 65 °C for 5 min. Protein samples were resolved by 6% (w/v) SDS-PAGE gels and transferred onto Immobilon-P PVDF membranes. Immunoblots were cut at the position of the 70 kDa prestained marker band. Above 70 kDa, immunoblots were probed with 1:4000 HRP-conjugated goat anti-rabbit IgG in TBST-M, and visualized with ECL reagent. Below the 70 kDa pre-stained marker, immunoblots were incubated with 1:3000 mouse anti-GAPDH for loading control, followed by 1:4000 HRP-conjugated sheep anti-mouse IgG and visualized with ECL reagent. Immunoblots were visualized using an ImageQuant LAS4000 (GE Healthcare) photodocumentation system. Quantitative densitometric analyses were performed using ImageQuant TL 8.1 software.

2.11 Immunofluorescence

2.10.1 Immunofluorescence of HEK293 Cells

HEK293 cells were plated on poly-L-lysine coated glass coverslips in 100-mm dishes. Cells were fixed in 3.7% (w/v) paraformaldehyde and 0.2% glutaraldehyde in PBS for 12 min at 37 °C, 24 h post-transfection. Coverslips were washed four times in PBS, reduced in 0.2% (w/v) sodium

borohydride for 10 min at 20 °C. Coverslips were washed three times with PBS before blocking for 30 min in blocking buffer (3% (w/v) BSA in PBS), containing 0.2% (v/v) Triton-X 100 for permeabilized conditions. Cells were co-labeled with primary antibodies, each at 4 μg/mL, for 30 min at 20 °C. Primary antibodies used were mouse anti-HA Epitope Tag Antibody from Biolegend, and a custom antibody that was raised in rabbits against a peptide (NH_2-KPPKYHPDVPYVKR-COOH) corresponding to amino acids 814–827 of human AE1 by Primm Biotech (α814-827). Coverslips were then washed five times in washing buffer (0.2% (w/v) BSA in PBS, containing 0.1% (v/v) Triton-X 100 for permeabilized conditions), followed by incubation with secondary antibodies Cy3 Donkey Anti-Mouse IgG and Alexa Fluor 488 Donkey Anti-Rabbit IgG at 1:250 in blocking buffer, for 30 min at 20 °C. All steps including and following secondary antibody incubation were performed in the dark. Cells were washed three times for 10 min in washing buffer, followed by post-fixation for 10 min at 20 °C with 4% (w/v) paraformaldehyde in PBS. Cells were washed three times in PBS before mounting with ProLong Gold antifade reagent with DAPI and slides were dried overnight at 20 °C before sealing with nail polish. Microscopy slides were visualized on a Wave FX spinning disc confocal microscope (Quorum Technologies, Guelph, ON, Canada) with a Yokogawa CSU10 scanning head (Tokyo, Japan), and fluorescence was quantified using Volocity 6.0 software (PerkinElmer, Waltham, MA, USA). For analysis, mean fluorescence intensities of a cell population were pooled, and mean fluorescence in permeabilized conditions was set to 100% for each of the primary antibodies used.

2.10.2 Immunofluorescence of Red Blood Cells

A dual immunofluorescence staining technique was used to label extracellular and intracellular antigens. Surface antigens on RBCS were first labeled in intact conditions, followed by labeling in permeabilized conditions, using the same primary antibody in both conditions. To first detect

surface-exposed antigens, 2 µL of red cell concentrate was incubated with rabbit α814-827 IgG at 4 µg protein/mL, IVF12 mouse monoclonal anti-AE1 COOH-terminus 1:250, or mouse anti-glycophorin C (GPC) 1:50 in 100 µL PBS with 1% (w/v) BSA for 30 min at 4 °C. Red cells were washed in PBS with 1% (w/v) BSA three times by centrifugation in a Thermo IEC Micromax Centrifuge at 400 x g for 1 min at 4 °C. Washes were followed by incubation with secondary antibody in PBS with 1% (w/v) BSA. Secondary antibodies used were: Alexa Fluor 488 Donkey Anti-Rabbit IgG at 1:100 for rabbit primary antibody α814-827, and Cy3 Donkey Anti-Mouse IgG 1:200 for mouse primary antibodies IFV12 and αGPC. All secondary antibodies were incubated for 30 min at 4 °C in the dark, which was maintained until imaging. Following incubation, cells were washed with PBS with 1% (w/v) BSA by centrifugation in a Thermo IEC Micromax Centrifuge for 1 min at 900 x g at 4 °C three times. Cells were resuspended in 40 µL PBS with 1% (w/v) BSA, and 5 µL was streaked onto glass microscopy slides. Slides were dried at 20 °C for 1 h, before fixing with 4% (w/v) paraformaldehyde in PBS for 10 min in a 20 °C fume hood. Slides were washed with PBS for 30 s, followed by permeabilization in 0.1% (v/v) Triton X-100 in PBS for 5 min, followed by a 30 s wash in PBS. Slides were blocked in PBS + 1% (w/v) BSA for 30 min before a 30 s wash in PBS. To detect internal antigens, cells were incubated with the same primary antibodies that were used in non-permeabilizing conditions (rabbit α814-827 at 4 µg protein/mL, IVF12 mouse anti-AE1 COOH-terminus 1:250, or mouse anti-glycophorin C (GPC) 1:50) in 1% (w/v) BSA in PBS in a humidified chamber at 4 °C for 1 h. After incubation, slides were washed three times in PBS for 5 min each. Slides were incubated with secondary antibodies Alexa Fluor 594 Chicken anti-Rabbit IgG for rabbit primary antibody, and Alexa Fluor 647 Chicken anti-Mouse IgG for mouse primary antibodies, in PBS + 1% (w/v) BSA in a humidified chamber at 4 °C for 30 min. Secondary antibodies used in permeabilized condition labeling were

conjugated to fluorophores spectrally distinct from those used in above nonpermeabilized labeling. Slides were washed three times in PBS for 5 min each, followed by a 10 s wash in distilled water, and air dried at 20 °C for 1 h. Dried slides were mounted with Prolong reagent, and air dried for 10-16 h before sealing with nail polish. Coverslips were visualized on a Wave FX spinning disc confocal microscope (Quorum Technologies, Guelph, ON, Canada) with a Yokogawa CSU10 scanning head (Tokyo, Japan), and fluorescence was quantified using Volocity 6.0 software (PerkinElmer, Waltham, MA, USA).

2.12 Hypotonic Lysis of Red Blood Cells

Packed red blood cells from the network of Centers of Applied Development (netCAD) (Canadian Blood Services, Vancouver, BC) were washed twice in ten volumes of PBS by centrifugation at 6500 x g for 5 min at 4 °C. The final supernatant was aspirated, and washed red blood cells were resuspended in ten volumes of 4 °C 5P8 buffer (5 mM sodium phosphate, pH 8.0, 1 mM PMSF) and incubated on ice for 20 min. Red blood cell membranes were centrifuged at 30, 000 x g for 20 min at 4 °C. Supernatant was aspirated, and membranes were resuspended in 5P8 and centrifuged five times, until red blood cell membranes were no longer pink. Membranes were resuspended to 0.5 mL membrane/mL total and solubilized in 10 volumes 5P8 with 1% (v/v) $C_{12}E_8$ for 20 min at 4 °C with slow rotation. Insoluble material was removed by centrifugation at 50 000 x g for 30 min at 4 °C. Protein concentration was determined using BCA assay, following the manufacturer's instructions.

2.13 Preparation of Senescent Cell IgG

Twenty units of whole blood (450 mL of blood in each bag) were obtained from the network of Centers of Applied Development (netCAD) (Canadian Blood Services, Vancouver, BC). Whole blood was stored at 4 °C for 50-60 days to allow cells to bind maximum amount of autoantibody.

After aging, whole blood was centrifuged using a Roto Silenta 630RS Centrifuge (Hettich, Tuttlingen, Germany) to separate red blood cells from plasma, leukocytes, and platelets. The top layers of plasma, leukocytes and platelets were removed by aspiration. Remaining packed red blood cells were aliquoted into 10 mL samples in 50 mL Falcon tubes and washed eight times in 50 mL PBS in an accuSpin 3R centrifuge (Fisher Scientific, Ottawa, ON, Canada). Washed red blood cells were lysed by hypotonic lysis in 5P8 buffer (5 mM sodium phosphate, pH 8.0) for 20 min on ice. Following lysis, red blood cell ghosts were centrifuged at 15 000 x g for 20 min. Hypotonic lysis by 5P8 buffer and ultracentrifugation was repeated four additional times. Following the final spin, prepared red blood cell membranes were pooled and stored at -80 °C.

Red blood cell membranes were thawed and washed with 5P8 and centrifuged at 15, 000 x g for 20 m five times. Washed red blood cell membranes were incubated with 2 volumes of 4 °C glycine-HCl elution buffer (0.1 M glycine, 2% (w/v) EDTA, 0.9% (w/v) NaCl, pH 1.5), mixed, and incubated at 20 °C for 1-3 min. After incubation, samples were neutralized by the addition of 1 M Tris-NaCl (1 M Tris base, 1 M NaCl) to a final concentration of 32 mM Tris-NaCl. Samples were mixed and immediately centrifuged at 1000 x g for 60 s, 20 °C. Supernatant eluate was transferred into a fresh Falcon tube and pH was adjusted to 7.9-7.4 by dropwise addition of 1 M Tris-NaCl. Precipitates were removed following centrifugation at 1000 x g for 2 m at 20 °C. Eluate was concentrated using a Centriprep filtration concentration unit with 100 kDa cut-off (Millipore Corp., MA, USA), and the amount of IgG in the eluate was quantified using a Nanodrop spectrophotometer (Thermo Scientific, Ottawa, ON, Canada).

2.14 Statistical Analysis

Quantification was performed using Volocity 6.0 software (PerkinElmer, ON, Canada) and ImageQuant TL 8.1 software (GE Healthcare). Analysis was performed using GraphPad Prism

Software (v5; GraphPad, La Jolla, CA, USA). Values are represented as mean ± standard error. Data was analyzed using one-way ANOVA, with $P < 0.05$ considered significant.

Chapter 3: Homology Modelling of SLC4A11

3.1 Introduction

Integral membrane proteins constitute about 26% of human genes (3). Given their critical roles in processes including solute transport, ion channel function and cell signaling (G-protein coupled receptors), membrane proteins may have a disease burden out scale to their representation in the genome. Indeed, 60% of drugs target membrane proteins (435). Misfolding of proteins is a common result of disease mutations and membrane proteins may be especially vulnerable to this insult (436). Many other mutations, however, impair residues central to protein function without affecting folding, a class termed catalytic mutants. To begin to explain the ways that point mutations can disrupt membrane proteins, we set about to map a large collection of disease mutations onto a membrane transport protein.

Mutations of corneal endothelial membrane transport protein SLC4A11 (SLC4A11, MIM# 610206) give rise to corneal dystrophies, including some cases of congenital hereditary endothelial corneal dystrophy (CHED, MIM# 217700) (80-98) and Fuchs endothelial corneal dystrophy (FECD, MIM# 136800) (98-101). Both CHED and FECD manifest as clouding of the cornea, leading to eventual blindness (399). While CHED is relatively rare (399), FECD has a lifetime incidence of 4% (437). Harboyan syndrome (HS, MIM# 217400), marked by early onset corneal dystrophy and sensorineural deafness, has recently been suggested to represent a progression of CHED (86,397). About 70 point mutations have been identified in SLC4A11 to cause corneal dystrophy (80-101). While the majority of disease-causing SLC4A11 point mutants lead to loss-of-function by endoplasmic reticulum (ER) retention of SLC4A11, other mutants process normally to the cell surface, suggesting compromised SLC4A11 function (438). SLC4A11 has been reported by different investigators to mediate a variety of functions, including Na^+ coupled OH^- transport (360,361,366), Na^+ independent H^+ (OH^-) transport (53,364,366), H^+/NH_3 co-transport (365,366),

NH_3 transport (362), and water transport (359,363). ER-retained disease mutants are tempting targets for therapies that rescue SLC4A11 to the plasma membrane (409). Understanding the molecular defect and resulting phenotype for each disease-causing mutant is essential to design targeted and personalized therapies for corneal dystrophy patients.

At the molecular scale, protein function is innately linked to three-dimensional structure. The structure of SLC4A11 has not yet been solved, limiting our understanding of the protein. Like other SLC4 proteins (186), SLC4A11 has a two domain structure, with a 41 kDa N-terminal cytoplasmic domain and 57 kDa integral membrane. Recently, the crystal structure of the membrane domain of a homologous member of the SLC4 family, AE1 (SLC4A1), was solved at 3.5 Å resolution (1). AE1 shares an overall membrane domain organization with transport proteins UraA (194), UapA (196), a bacterial SLC26 family fumarate transporter (195) and plant Bor1 (193). These proteins have 14 transmembrane segments (TMs), arranged into two inverted repeats of seven TMs each. The membrane domain can be divided into two structural subdomains; a core domain and a gate domain, with the proposed substrate translocation pathway at the interface of the two domains, and substrate transported by an alternating access mechanism (1). AE1 and SLC4A11 are predicted to share the same overall fold within the membrane domain, due to sequence similarity within the membrane domain of the SLC4 family (186).

In this study, we created a three-dimensional homology model of the membrane domain of human SLC4A11, using AE1 as a template. We tested the validity of the homology model by *in silico* analysis and predicted the molecular phenotype of membrane domain mutations on the basis of the model. We subsequently tested the biochemical properties of these mutants, revealing the validity of the homology. This model was used to map known CHED, FECD, and HS point mutants, and subsequently rationalize their disease-causing effects.

3.2 Results

3.2.1 SLC4A11 Homology Model

Homology modeling was used to develop a three-dimensional model of the membrane domain of human SLC4A11. The membrane domain of human AE1, which starts at Gly381, was aligned with human SLC4A11 amino acid sequence (Fig. 3.1). The two sequences share 30.6% amino acid sequence identity and 40.4% similarity over their membrane domains. In addition, conservation is higher in TMs than in extramembraneous loops. The alignment clearly shows conservation of residues essential for transport in AE1 (Fig. 3.1). A three-dimensional model of SLC4A11 membrane domain (Fig. 3.2) was created using the SWISS-MODEL server, with SLC4A11 membrane domain amino acid sequence (amino acids 345–885) and a modified PDB file of AE1 structure (1) as template. The SLC4A11 model is almost identical to the AE1 structure within the TMs. The two differ most in the extramembraneous loops. In particular, extracellular loop 3 of SLC4A11 is much larger than in AE1 and lies at the dimeric interface (Fig. 3.2A). The SLC4A11 model shares the two-domain organization (Fig. 3.2B) seen in AE1 (1). Coordinates for the SLC4A11 membrane domain homology model are available upon request and can be viewed using the PyMOL program (www.pymol.org).

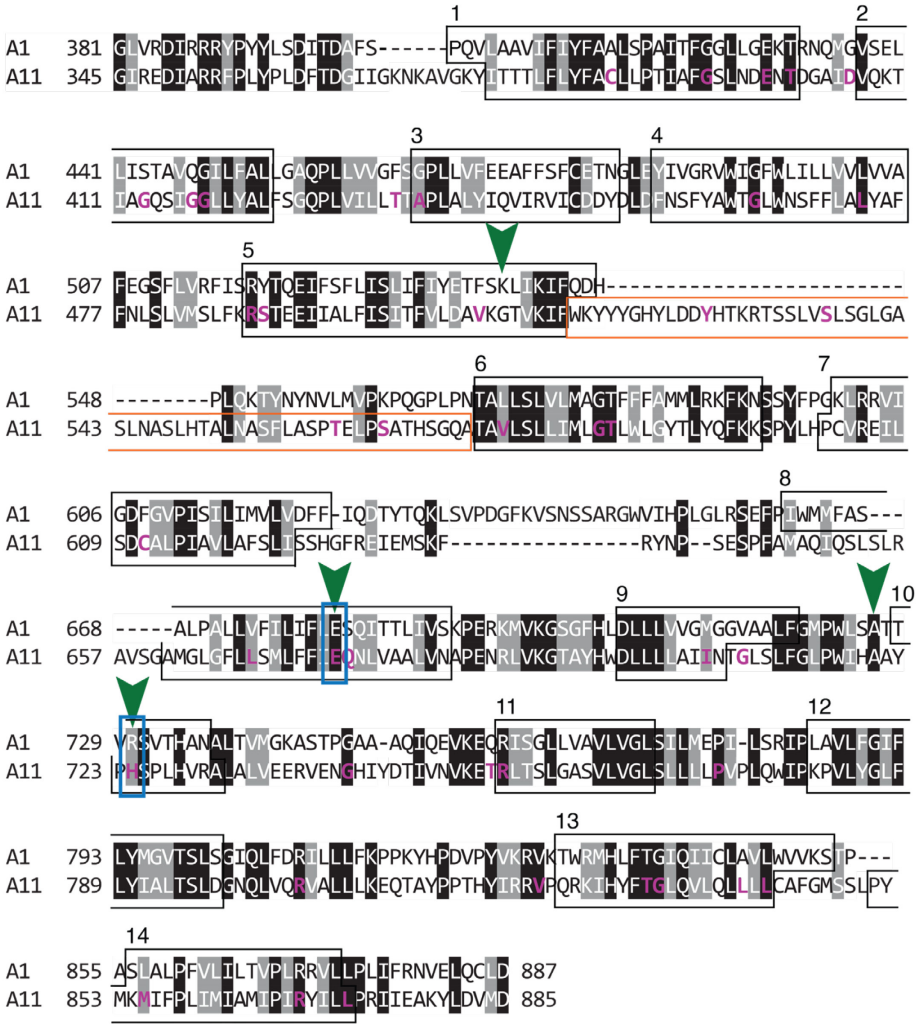

Figure 3.1 AE1 (‘A1’) and SLC4A11 (‘A11’) homology within the membrane domain. The AE1 crystal structure did not resolve the C-terminal cytosolic region of the protein (amino acids 888-911). Therefore, the sequence of human AE1 membrane domain (amino acids 381-887) was aligned with the corresponding sequence of human SLC4A11. Helical portions of transmembrane regions in AE1 crystal structure and SLC4A11 homology model are boxed in black, with helix number indicated above. SLC4A11 corneal dystrophy-causing mutations are shown in magenta in the lower sequence. Mutations created to test model validity are marked by green arrows. Blue boxes indicate AE1 residues essential for anion transport. SLC4A11 extracellular loop 3 is in an orange box. Black and grey highlighting indicates identical and similar residues, respectively, with no highlighting on non-conserved residues. Reference sequences NG_017072.1 and NP_000333.1 were used for SLC4A11 and AE1, respectively.

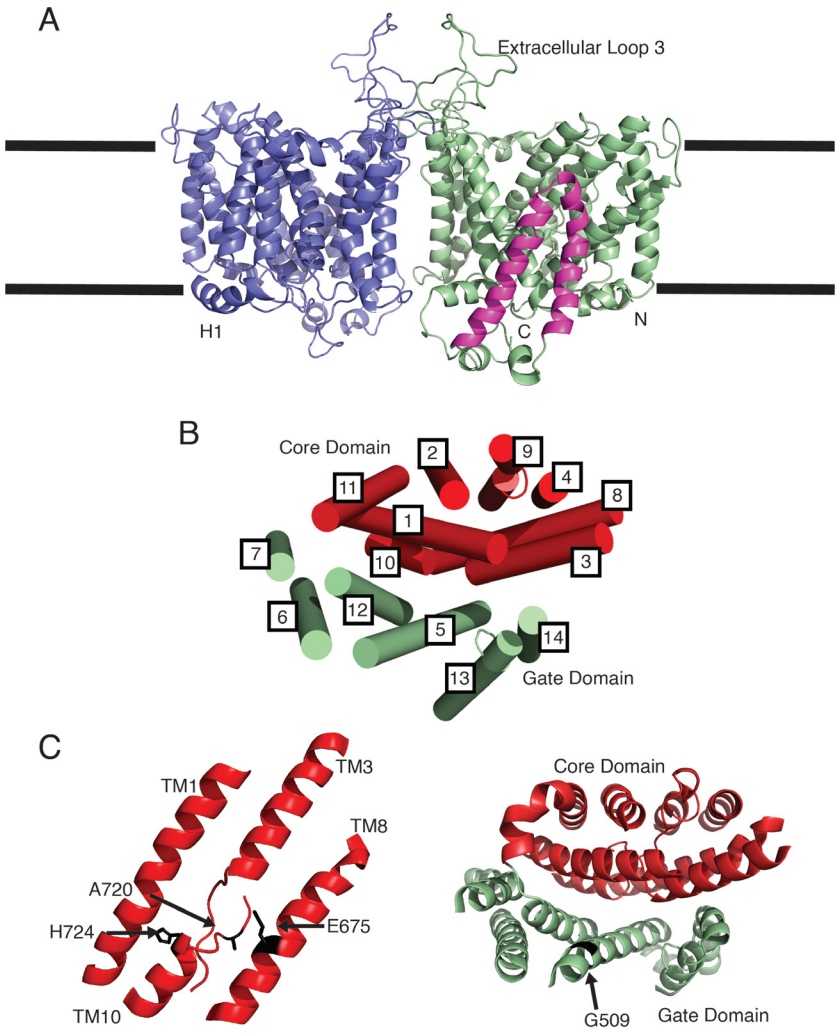

Figure 3.2. Homology model of the membrane domain of human SLC4A11 using the AE1 crystal structure as a template. A) Dimeric hSLC4A11 membrane domain homology model was created using the AE1 crystal structure at 3.5 Å resolution as template. SLC4A11 monomers are shown in purple and green. Extracellular loop 3 and helix H1 are indicated. Transmembrane helices 13 and 14 are highlighted in pink. Plane of lipid bilayer is approximated by black lines. B) View looking onto extracellular face of SLC4A11 transmembrane segments without connecting loops. Core (red) and dimer-forming gate (green) domains have transmembrane segments represented as cylinders and numbered 1–14, indicated in white boxes. C) Positions of mutations created to biochemically test the validity of the homology model. Left panel: Wild-type residues E675, A720, and H724 in the catalytic cleft. Right panel: Wildtype G509 at the extracellular side of the core–gate interface (same view as B).

3.2.2 Testing Model Validity

Verify3D and PROCHECK servers were used to assess the homology model's structural validity *in silico* (421-424). Both methods of *in silico* analysis indicate that the areas of low structural quality within the model were limited to extramembraneous loops. PyMOL calculated the root mean square deviation of Cα in homologous TMs of human SLC4A11 and AE1 as 0.392 Å, indicating a close fit between the model and template in the transmembrane regions. *In silico* analysis is thus consistent with a valid SLC4A11 membrane domain homology model.

To test the model's validity biochemically, we designed novel point mutants that have not yet been identified in patients. We predicted the molecular phenotype of these mutants, on the basis of their location in the model. We then expressed these mutants in HEK293 cells and analyzed protein expression level, degree of trafficking to the cell surface, and transport activity, as previously described (409). We selected positions in the three-dimensional model whose location predicted either an effect on transport function, or tolerance of mutation such that no transport defect would arise. In AE1, Glu681 has long been recognized as critical to the anion transport mechanism (267,268). The corresponding residue in the homology model is conserved as Glu675 (Fig. 3.1 and Fig. 3.2C). SLC4A11 p.Glu675Gln (E675Q) converts the acidic side chain to the corresponding amide, thus neutralizing its acidity. We predicted this would compromise functional activity. Similarly, in AE1 Arg730 has been proposed to be central to the transport catalysis site, providing positive charge to ligand substrate anions (186). The homology model shows that the corresponding amino acid in SLC4A11, His724 (Fig. 3.1 and Fig. 3.2C) has a conserved charge but different structure of side chain. We mutated the residue to alanine (SLC4A11 p.His724Ala, H724A) to explore the importance of positive charge at this position. We also mutated to arginine (SLC4A11 p.His724Arg, H724R) to conserve positive charge, but with a

longer side-chain reach. On the basis of the homology model, we anticipated that neither mutant would have functional activity, but that the proteins would fold normally and thus process to the cell surface. Ala720 is in the extended structure region of TM10 (Fig. 3.2C), which is conserved as alanine in all SLC4 proteins. Although its functional role is unclear, it is in a structurally homologous position to the substrate binding site of AE1 (186). SLC4A11 p.Ala720Leu (A720L) increases the alkyl side-chain bulk, a subtle mutation unless the amino acid is in a constrained location. We anticipated that this mutation would cause protein misfolding if in a helix–helix interface, but in an open cleft could sterically block substrate translocation.

The side chain of Gly509 points into an open portion of the external opening of the catalytic cleft (Fig. 3.2C). We thus anticipated that although the wild-type residue (glycine) has the smallest amino acid side chain, SLC4A11 would be tolerant of mutation here. If, on the other hand, the residue was involved in protein–protein interactions, it would be intolerant of mutation, likely leading to protein severe misfolding and ER-retention. We decided to prepare the SLC4A11 p.Gly509Lys (G509K) mutation as the position is homologous to Lys539 of AE1, a position covalently labeled by some stilbene disulfonate inhibitors, such as DIDS (274,275).

SLC4A11 mutants were expressed in transfected HEK293 cells and protein expression was monitored on immunoblots (Fig. 3.3A). SLC4A11 migrated as two bands, a predominant upper band and a less prominent lower band. These have previously been identified as protein with mature glycosylation, found at the plasma membrane (upper band) and immaturely-glycosylated, ER-associated protein (lower band) (98). E675Q, H724A, and H724R expressed (Fig. 3.3B) and trafficked to the cell surface (Fig. 3.3C) indistinguishably from SLC4A11-WT. In contrast, A720L accumulated to a lower level and trafficked to the cell surface significantly less than SLC4A11-WT (Fig. 3.3B, C).

SLC4A11 has been found to increase the rate of hypoosmotically driven cell swelling (359). To assay their functional activity, SLC4A11 mutants were expressed in HEK293 cells along with cytosolic green fluorescent protein. Cells were monitored by confocal microscopy as superfusion solution changed from iso- to hypoosmotic. Fluorescence in a region of interest in the cell was quantified as a measure of the concentration of eGFP in cytosol. As cells swelled upon the switch to hypoosmotic superfusion solution, cytosolic eGFP was diluted and the eGFP signal decreased (Fig. 3.4). Note that a slight acidification was induced in HEK293 cells exposed to hypoosmotic medium, but the rate of acidification was not different between cells expressing SLC4A11 and control cells (359). Also, note that the water flux induced by SLC4A11 expression appears to be mediated directly by SLC4A11 since the flux in cells expressing SLC4A11 is inhibited by stilbene disulfonate, whereas cells expressing the water channel protein, AQP1, were unaffected by the compound (359). The initial rate of change of eGFP fluorescence was used to assess the rate of cell volume change, relative to SLC4A11-WT. As predicted, all four central catalytic pathway mutants (A720L, E675Q, H724R, and H724A) had significantly decreased water flux in comparison to SLC4A11-WT (Fig. 3.4B). Glu675 and His724 have corresponding residues in AE1 that are essential for transport (Fig. 3.1) (186). Loss of functional activity of these mutants suggests that a role important to transport functions is conserved at these residues, supporting the validity of the homology model. Mutation G509K is located in the catalytic pathway but is in an open region of protein structure (Fig. 3.2C) and thus predicted to be insensitive to mutation. G509K expressed and trafficked to the cell surface at lower levels than WT (Fig. 3.3). Nonetheless, the functional activity of G509K was indistinguishable from SLC4A11-WT (Fig. 3.4). Taken together, these *in silico* and *in vitro* analyses provide support for the validity of the homology model presented here.

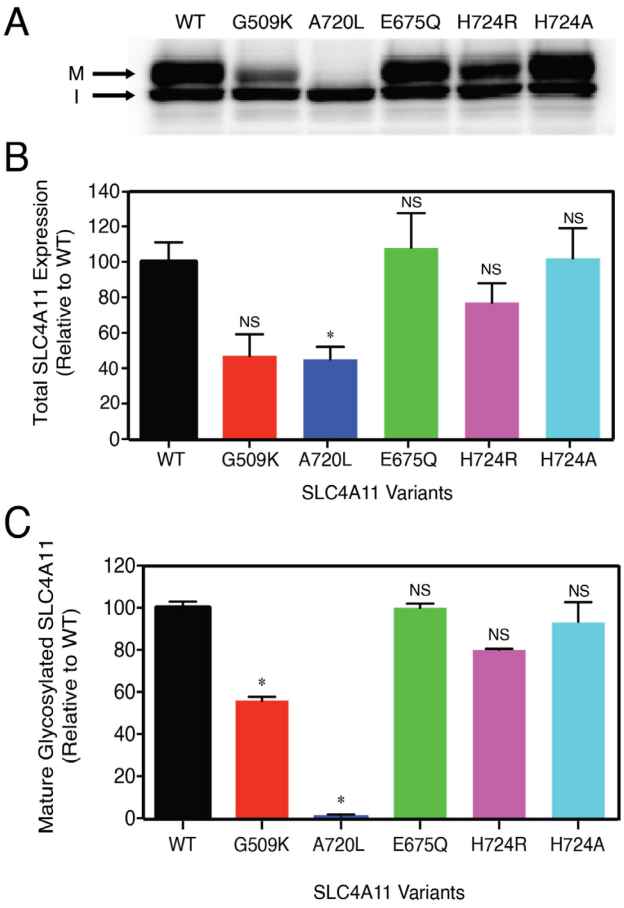

Figure 3.3 Expression and cell surface processing of SLC4A11 mutants. A) Immunoblots representing expression pattern of SLC4A11 mutants. HEK293 cells were transiently transfected with cDNA encoding HA tagged SLC4A11-WT, G509K, A720L, E675Q, H724R, or H724A. Cells were cultured for 2 days at 37°C. Total protein (50 µg) was loaded in each well. Cell lysates were visualized on immunoblots using anti-HA antibody. Arrows indicate immature (I) and mature (M) glycosylated forms of SLC4A11. B) Total expression of HA-SLC4A11 was determined by densitometry and expressed as percentage of SLC4A11-WT expression. Error bars represent SEM (n = 3). Asterisks represent significant difference ($P < 0.05$), whereas NS is no significant difference between SLC4A11-WT and indicated mutants. C) The fraction of mature SLC4A11-WT or indicated mutants (upper band) was determined by densitometry and expressed as percentage of the total protein (upper band + lower band), relative to SLC4A11-WT. Error bars represent SEM (n = 3). Asterisks represent significant difference ($P < 0.05$), whereas NS is no significant difference between SLC4A11-WT and indicated mutants. Experiment and analysis performed by Dr. Kumari Alka.

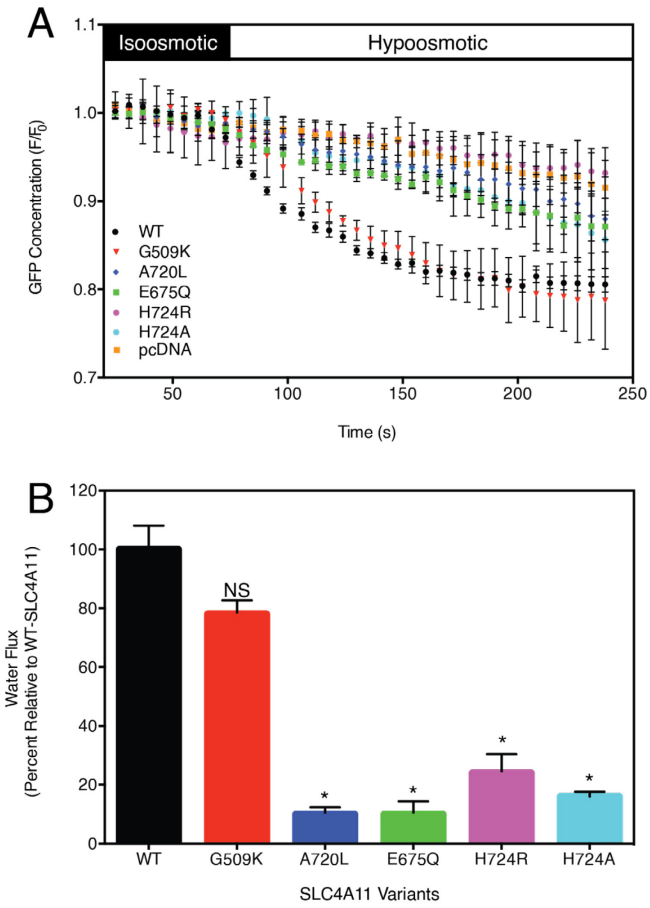

Figure 3.4 Water flux activity of SLC4A11 mutants. A) Osmotically driven water flux activity of SLC4A11 mutants. Experiments were performed as previously described (409). HEK293 cells were transiently co-transfected with vector or cDNA encoding nHA-tagged SLC4A11-WT, G509K, A720L, E675Q, H724R, or H724A, along with eGFP cDNA. The rate of cell swelling was measured as a function of change in the level of eGFP fluorescence in the regions of interest upon hypotonic challenge. Data were corrected for rates measured in vector-transfected cells. eGFP fluorescence (F) was normalized to F averaged for initial 60 s (F_0) of measurement. B) Comparison of water flux activity of SLC4A11-WT with indicated mutants. Data represents mean ± SEM of 3–5 independent experiments of 10–20 cells per coverslip. Rate of fluorescence change was calculated by linear regression of the initial eGFP intensity change during first 15 s of perfusion with hypotonic buffer. A significant difference in water flux function was observed for SLC4A11 mutants A720L, E675Q, H724R, and H724A when compared with SLC4A11-WT ($P < 0.05$). NS, no significant difference between G509K and SLC4A11-WT. Experiment and analysis performed by Dr. Kumari Alka.

3.2.3 Categorizing SLC4A11 Disease Mutants

We mapped 45 disease-causing point mutants of the SLC4A11 membrane domain (residues 345–882) that have been identified to date, to gain insight into their effects on protein structure and function at the molecular level. Examination of the location of the mutated residues indicated that they could be categorized as (1) in the SLC4A11 catalytic pathway, (2) in areas of close transmembrane helix packing, (3) in the dimerization interface, or (4) lying in intracellular and extracellular loops (Table 3.1). Catalytic pathway mutations were either in the translocation pore or the core/gate domain interface. Criteria for mutants predicted to disrupt helix packing was location at a densely packed interface between helices. The third category was mutations at the dimerization interface. Finally, the model places seven mutations in extracellular and cytoplasmic loops. Of the 45 membrane domain point mutants analyzed, five lie in the catalytic pathway, 30 are at regions of close transmembrane helix contact, three are found in the dimeric interface, and seven are in extracellular or cytoplasmic loops (Table 3.1).

We further examined the consequences of SLC4A11 mutations by comparing structural parameters of SLC4A11 membrane domain model with WT sequence and with introduced disease-causing mutations (Table 3.2). Most (28/45 mutants) induced steric clashes larger than the 0.4 Å cut-off used by the modeling program to identify a significant defect (429,430). We estimated the pKa for the WT residue and the mutant amino acid at each point mutation site to determine whether change occurred. A further eight mutations are predicted to be deleterious because of a charge change in the absence of a severe steric clash. Loss (p.Pro773Leu) or gain (p.Leu843Pro) of a proline residue would kink the structure in ways not predicted by the analysis programs and readily explains disease. p.Arg488Lys and p.Ser489Leu give rise to a reduced number of hydrogen bonds and localize at the cytoplasmic end of TM5. This would likely destabilize the TM. In the case of

only four mutants (p.Ala436Val, p.Val507Ile, p.Tyr526Cys, and p.Gly834Ser) did the analysis fail to measure deleterious structural change induced by the mutation (Table 3.2). These four mutants will be discussed later. The structural defects predicted to arise from mutations provide additional support for the validity of the homology model.

Table 3.1 Classification and rationalization of corneal dystrophy-causing SLC4A11 mutations. Mutants are classified as lying in areas of close helix packing, catalytic pathway, dimerization interface, or extramembraneous loops. Amino acid numbering is based on NCBI reference sequence NG_017072.1, using HGVS recommended numbering.

Mutation	Disease	Structural Effects Classification	Predicted Effect on SLC4A11	References
p.Cys386Arg	CHED	Helix Packing	Faces the interior of the core domain, causes steric clash.	(84,87,89)
p.Gly394Arg	CHED	Helix Packing	Faces TM2 and a hydrophobic residue. Arg would cause repulsion between TM1 and 2 due to steric clashing.	(88)
p.Glu399Lys	FECD	Catalytic Pathway	Lies at the core-domain interface, across from K512. Mutation to Lys could induce repulsion of the core and gate domains in the transport pathway.	(99)
p.Thr401Lys	CHED	Helix Packing	Extracellular side of the core – gate domain interface, at the C terminal end of helix 1. Lys would change the positioning of extracellular loop 2, and thus the packing between helices 1 and 2.	(85)
p.Asp406Val	CHED	Loop	Extracellular loop 1	(95)
p.Gly413Arg	CHED	Helix Packing	Located on TM2, introduces charge and steric bulk to interface with adjacent TM9	(96)
p.Ser415Asn	CHED	Helix Packing	Facing adjacent TM11, mutation to Asn increases steric bulk at a region of close helix packing.	(93)
p.Gly417Arg, p.Gly418Asp	CHED	Helix Packing	Both face the translocation pore, and induce changes in size too large to be accommodated, leading to protein misfolding.	(85,88,90)
p.Thr434Ile	FECD	Helix Packing	In the N terminal extended structure of TM3, this mutation adds steric bulk in the center of the core domain.	(101)

p.Ala436Val	CHED	Catalytic Pathway	Initiates helical structure in TM3, lies in the interface of core and gate domains	(95)
p.Gly464Asp	CHED	Helix Packing	Closely faces disease-causing point mutant G709 on adjacent TM9. Large steric change would cause the helices to mispack.	(99)
p.Leu473Arg	CHED	Helix Packing	C terminus of TM4, L473R introduces a charged residue into the hydrophobic membrane environment. Leads to instability in this connecting region from the gate to the core domain.	(85)
p.Arg488Lys	CHED/HS	Helix Packing	May have electrostatic interactions with charged residues on adjacent TM13, 14, or with adjacent core domain through hydrogen bonding.	(81)
p.Ser489Leu	CHED	Helix Packing	Lies in a sensitive region of TM5, 13, 14, at core-gate interface. Loss of hydrogen bonding may induce misfolding.	(85,99)
p.Val507Ile	FECD	Dimer Interface	Located on TM5, involved in the dimer interface. May also displace extracellular loop 3 with unknown function.	(101)
p.Tyr526Cys	FECD	Loop	Extracellular loop 3 (ECL3)	(100)
p. Ser536Cys	CHED	Loop	ECL3	(95)
p.Thr561Met	FECD	Loop	ECL3	(99)
p.Ser565Leu	FECD	Loop	ECL3	(99)
p.Val575Met	FECD	Dimer Interface	Lies at the N terminus of TM6, where it makes the closest contact of any residue in the dimer interface. May also impact the positioning of extracellular loop 3.	(100)
p.Gly583Asp	FECD	Dimer Interface	Faces the dimer interface. Introduction of a charge would cause repulsion between the two protomers and retention of the protein.	(100)
p.Thr584Lys	CHED	Helix Packing	T584 is in a tight bundle of TM6, 7 and 11 with nonpolar residues. Inserting a Lys at this	(85)

			location would disrupt close helix packing.	
p.Cys611Arg	CHED	Helix Packing	Introduces a large change in charge and size into the hydrophobic membrane that would disrupt the packing of TM7 and possibly adjacent helix 1.	(90)
p.Leu668Pro	CHED	Helix Packing	Proline introduces kinks in helices; lies on TM8	(96)
p.Glu675Ala	CHED	Catalytic Pathway	Corresponds to AE1's E681, which is essential for anion transport. SLC4A11 E675 likely shares a vital role in gating and translocation, in a mobile region that can accommodate mutations but impair transport.	(92,186)
p.Gln676Arg	CHED	Helix Packing	Lies on TM8, introduces a charge and steric bulk into the center of the core domain	(97)
p.Ile706Asn	CHED	Helix Packing	Introduces steric bulk and a basic residue into the lipid environment surrounding TM9; closely adjacent to TM2	(95)
p.Gly709Glu	FECD	Helix Packing	Closely faces G464 on adjacent TM4. The large steric change would cause the helices to mispack, and this charged residue may contribute to this effect.	(99)
p.His724Asp	CHED	Catalytic Pathway	Directed into TM1 and the translocation pore in the catalytic core domain, a change in size from a ringed side chain to a long extended side chain could be accommodated in the open pore, but would be detrimental during translocation.	(90)
p.Gly742Arg	FECD	Loop	Intracellular loop 5	(100)
p.Thr754Met	FECD	Helix Packing	On the cytoplasmic loop N terminal to TM11, T574M is adjacent to cytoplasmic H1, and at the intracellular base of TM1 and 2. A change in size or hydrogen bonding in this region	(99)

			could reorient helices in the core domain, leading to helix mispacking.	
p.Arg755Gln	CHED	Helix Packing	Extends under TM2 and above H1, close enough for electrostatic interactions with D360 on H1. R755Q mutation would abolish this interaction and lead to instability in H1.	(82,84,85,99)
p.Arg755Trp	CHED	Helix Packing	Replacing R755 with Trp leads to a large change in size, from a charged, extended side chain to an uncharged ringed side chain, likely disturbing the packing of adjacent TM2 and H1 as R755Q.	(84,85,87)
p.Pro773Leu	CHED	Helix Packing	Located at the hinge of bent helix TM11, mutation of Pro to a Leu would not enable the native kink of TM11, causing misfolding.	(85,87)
p.Arg804His	CHED	Loop	Intracellular loop 5; short helix H5	(82)
p.Val824Met	CHED/HS	Helix Packing	The cluster at the cytoplasmic side of helices 13, 14 and 5 appears to be sensitive to mutations. The homologous region of AE1 has been proposed to be able to pull out of the membrane domain to the extracellular space. If SLC4A11 shares this mobility, mutating Val to a Met would increase polarity and make this movement less energetically favorable.	(85,86,89,186)
p.Thr833Met	CHED	Helix Packing	Lies in a sensitive region of TM5, 13, 14, at core-gate interface. Loss of hydrogen bonding and steric clashing may induce misfolding.	(82)
p.Gly834Ser	FECD	Helix Packing	G834S changes residue size as well as polarity directed outwards into the lipid bilayer, resulting in reorientation of TM13.	(100)

p.Leu840Pro	CHED	Helix Packing	Places kink – inducing proline in the center of TM13	(95)
p.Leu843Pro	CHED/HS	Helix Packing	Introduces a kink near the C-terminus of TM13, detrimental to helix packing.	(81,94)
p.Met856Val	HS	Catalytic Pathway	Lying on the gate domain side of the core-gate interface opposite a number of nonpolar residues, M856V may disrupt core-gate interactions leading to disruption of catalysis.	(81)
p.Arg869Cys	CHED	Helix Packing	On the portion of TM14 on the periphery of the lipid bilayer. Charged R869 may extend and interact with lipid head groups to stabilize helix placement, which is abolished with uncharged cysteine.	(84,85,99)
p.Arg869His	CHED	Helix Packing	R869 is on the portion of TM14 on the periphery of the lipid bilayer. Charged R869 may interact with lipid head groups to stabilize helix placement.	(82,90)
p.Leu873Pro	CHED	Helix Packing	Introducing a helix kink with proline in the C terminal end of TM14 would lead to mispacking of the TM5, 13, 14 bundle, and subsequent misfolding.	(87)

Table 3.2 Computational estimates of structural changes induced by SLC4A11 membrane domain mutations. The SLC4A11 membrane domain model was altered to introduce individual disease mutations, in Pymol. Structural differences between WT and mutated structures were analyzed using MolProbity (http://molprobity.biochem.duke.edu/ (steric clashes)), PDB2PQR (http://nbcr-222.ucsd.edu/pdb2pqr_2.1.1/ (changes of side chain charge)) and StrucTools (https://hpcwebapps.cit.nih.gov/structbio (changes in H-bonding)) servers. Gain and loss of hydrogen bonding partners and steric clashes are indicated by + and -, respectively, followed by the number of partners or clashes gained or lost. Number in brackets under 'Steric Clashes' indicates the measure of the most deleterious overlap, in Å. Deleterious changes were predicted as those with steric clash over 0.4 Å (criteria used by molprobity) or a change of side chain charge (with pKa estimated for the specific amino acid and position in the structure). Mutations inducing a predicted deleterious change on the basis of these criteria are in bold. Mutations were classified as predicted to disrupt helix packing (HP), lying in extramembraneous loops (L), disrupting the dimeric interface (DI), or lying in the catalytic pathway (CP).

Mutation	Disease	Change in Side Chain Charge (WT to mutant)	Change in Hydrogen Bonding Partners	Steric Clashes (# clashes induced (degree of overlap (Å))	Structural Effects Classification
p.Cys386Arg	CHED	0 to +1	0	+29 (1.073)	HP
p.Gly394Arg	CHED	0 to +1	0	+30 (1.365)	HP
p.Glu399Lys	FECD	-1 to +1	0	0	CP
p.Thr401Lys	CHED	0	-2	+37 (1.461)	HP
p.Asp406Val	CHED	-1 to 0	-1	+6 (1.318)	L
p.Gly413Arg	CHED	0 to +1	+2	+11 (1.094)	HP
p.Ser415Asn	CHED	0	+1	+1 (0.590)	HP
p.Gly417Arg	CHED	0	+1	+20 (1.572)	HP
p.Gly418Asp	CHED	0	0	+16 (1.257)	HP
p.Thr434Ile	FECD	0	0	+1 (0.627)	HP

p. Ala436Val	CHED	0	0	0	CP
p.Gly464Asp	CHED	0	+3	+5 (1.159)	HP
p.Leu473Arg	CHED	0 to +1	0	0	HP
p.Arg488Lys	CHED/HS	0	-3	0	HP
p.Ser489Leu	CHED	0	-1	0	HP
p.Val507Ile	FECD	0	0	0	DI
p.Tyr526Cys	FECD	0	0	0	L
p. Ser536Cys	CHED	0	+1	-1 (.549)	L
p.Thr561Met	FECD	0	-1	+3 (1.075)	L
p.Ser565Leu	FECD	0	-2	+24 (1.293)	L
p.Val575Met	FECD	0	0	-3 (0.924)	DI
p.Gly583Asp	FECD	0 to -1	0	0	DI
p.Thr584Lys	CHED	0	0	+18 (1.578)	HP
p.Cys611Arg	CHED	0 to +1	0	0	HP
p.Leu668Pro	CHED	0	0	-1 (0.913)	HP
p.Glu675Ala	CHED	-1 to 0	0	0	CP
p.Gln676Arg	CHED	0 to +1	-1	+13 (1.103)	HP
p.Ile706Asn	CHED	0	0	-6 (0.670)	HP
p.Gly709Glu	FECD	0 to -1	0	+8 (1.260)	HP
p.His724Asp	CHED	0 to -1	**-1**	0	CP
p.Gly742Arg	FECD	0 to +1	**+1**	0	L
p.Thr754Met	FECD	0	-1	+7 (1.034)	HP
p.Arg755Gln	CHED	+1 to 0	**+2, -2**	0	HP
p.Arg755Trp	CHED	+1 to 0	**+1, -2**	+9 (0.928)	HP
p.Pro773Leu	CHED	0	0	0	HP
p.Arg804His	CHED	+ 1 to 0	**-1**	+1 (0.571)	L
p.Val824Met	CHED/HS	0	0	-2 (0.805)	HP
p.Thr833Met	CHED	0	**-1**	+4 (0.796)	HP
p.Gly834Ser	FECD	0	0	0	HP
p.Leu840Pro	CHED	0	-1	0	HP

p.Leu843Pro	CHED/HS	0	-2	0	HP
p.Met856Val	HS	0	0	+1 (0.648)	CP
p.Arg869Cys	CHED	+1 to 0	0	-6 (0.896)	HP
p.Arg869His	CHED	+1 to 0	0	-2 (1.369)	HP
p.Leu873Pro	CHED	0	+1, -1	+13 (1.346)	HP

3.2.3.1 Catalytic Pathway Mutants

Following AE1 transport mechanism, core and gate domains of SLC4A11 move relative to one another while substrate is transported (186). Thus, mutations of the translocation pore and core–gate domain interfaces may affect SLC4A11 transport function. Five of 45 disease mutations were predicted to impair SLC4A11 transport function. Mutations found within the catalytic pore include p.Glu399Lys, p.Ala436Val, p.Glu675Ala (Fig. 3.5A), and p.His724Asp. The protein may properly fold with these mutant amino acids due to their presence in an accessible, dynamic region of structure at the proposed translocation pore (363). Mutations within the pore would thus likely change the translocation pathway, leading to catalytically inactive protein, which nonetheless is able to fold and mature to the cell surface.

The side chain of p.Met856Val lies on the gate domain pointed directly into the core domain. This mutation may interfere with or disrupt gate–core interactions necessary for relative movement during translocation.

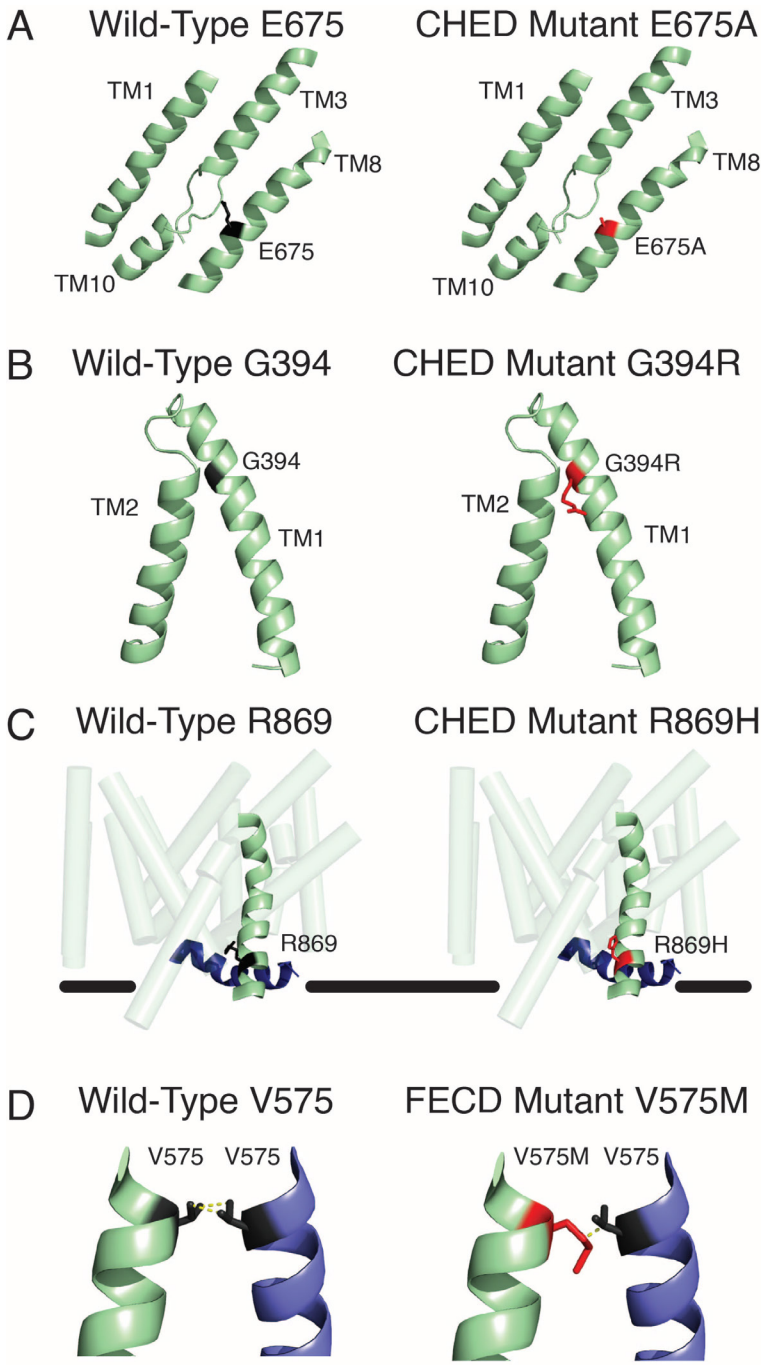

Figure 3.5 Categorizing disease-causing point mutants of SLC4A11 by their location on the homology model. A) The gate domain-facing side of the core domain, composed of transmembrane segments (TM) 1, 3, 8, and 10. Left panel: Wild-type Glu675 (E675), modeled in black, points into the translocation pore of the core domain. Right panel: Point mutant p.Glu675Ala (E675A), colored in red, extends into the N-terminal extended structure of helices 3 and 10. B) Left panel: Wild-type Gly394 comes into close proximity with the N-terminal end of TM2. Right

panel: Helix packing CHED mutant p.Gly394Arg, modeled in red. C) Left panel: Wild-type Arg869 faces the inner leaflet of the lipid bilayer (position approximated by black lines), slightly above amphipathic helix H1 (modeled in blue; SLCA11 membrane domain shown with transparent representation). Right panel: CHED mutant p.Arg869His results in a shorter, likely uncharged side-chain substitution. D) Left panel: Val575 on each monomer of SLC4A11 at the dimerization interface on TM6. Residues Val575 are shown as sticks, with monomers of the dimer shown in green and purple. Right panel: Heterozygous FECD mutant p.Val575Met modeled in red.

3.2.5 Helix Packing Mutants

The majority of mutations in the membrane domain are located at helix–helix interfaces. Disturbance of helix interfaces may disrupt helix packing, leading to protein misfolding, causing SLC4A11 to be ER-retained. Many of these helix packing mutations change the size and charge of a side chain in a tightly packed region of the protein. These mutants include p.386Arg, p.Gly394Arg (Fig. 3.5B), p.Thr401Lys, p.Gly413Arg, p.Ser415Asn, p.Gly417Arg, p.Gly418Asp, p.Gly464Asp, p.Leu473Arg, p.Thr584Lys, p.Cys611Arg, p.Gln676Arg, p.Ile706Asn, and p.Gly709Glu.

Alternatively, some diseased states arise from the replacement of a charged residue. Charged residues may stabilize helix placement by formation of salt bridges with adjacent residues or lipid head groups. p.Arg755Gln and p.Arg755Trp, abolish a positive charge that may interact with highly charged H1. Arg869 in TM14, which sits low in the plane of the lipid bilayer, may be involved in stabilizing charges with anionic lipid head groups. Supporting this, Arg869 lies in a plane slightly above amphipathic helix H1 (Fig. 3.5C). In AE1, this helix makes contact with the membrane surface, and interacts with lipid head groups in molecular simulations with the lipid, POPC (186). CHED mutant, p.Arg869Cys, abolishes this predicted stabilizing charge, as structure-assisted pKa calculations predict cysteine at this location at physiological pH to be uncharged (pKa estimated to be 10.11) (431-433). Another CHED mutant, p.Arg869His, is also predicted to be uncharged (pKa estimated to be 5.48), thus unable to form salt links to acidic lipid head groups.

Other helix disrupting mutations are caused by introduction or lack of a proline, which may disrupt the helical nature of a TM, causing reorientation and thus a misfolded protein. p.Leu668Pro in TM8, p.Leu840Pro and p.Leu843Pro in TM13, and p.Leu873Pro in TM14 respectively are such

mutants. p.Pro773Leu substitutes a leucine for a proline, which may prohibit TM11 from making the kink necessary for connection from the core domain to the gate domain.

Very subtle mutations likely cause misfolding due to location in a particularly sensitive region of the protein. The subtle p.Thr754Met mutation may lead to ER-retention (99) by being located directly adjacent to highly charged H1, or displacing core and gate domain-linking TM11. p.Arg488Lys and p.Ser489Leu on TM5, and p.Val824Met, p.Thr833Met, and p.Gly834Ser on TM13 lie at the cluster of TM5, 13, and 14, and at the core–gate interface, where they may destabilize and misplace helices.

p.Thr434Ile, while located in the extended structure TM3, is likely a mis-packing mutant. The ability of the extended structure to accommodate side-chain changes is not known or inferable from the model, however our biochemical validation mutant A720L, in TM10 extended structure (Fig. 3.2 C), indicates that misfolding and ER retention would occur.

3.2.6 Dimeric Interface Mutants

The SLC4A11 dimeric interface is formed by interactions between TM5 and 6 on each subunit with additional contributions from TM7. Three FECD mutants are found at the dimeric interface. p.Val575Met creates the closest contact between subunits and processes to the cell surface similarly to WT *in vitro* (Fig. 3.5D) (100). p.Val575Met results in a lack of symmetry at this close contact point, altering the dimeric interface. Similarly, p.Val507Ile on TM5 is located at the dimeric interface, and may disrupt subunit interactions.

The third dimeric interface mutation, p.Gly583Asp, introduces a charge directly into the interface of the two subunits, which likely inhibits the formation of dimers, and leads to the ER retained phenotype seen *in vitro* (100).

3.2.7 Extramembraneous Loop Mutants

This model places CHED mutant p.Ser536Cys (95) and FECD mutants p.Tyr526Cys, p.Thr561Met, and p.Ser565Leu (99,100) in large extracellular loop 3. Additional FECD mutant p.Gly742Arg (100) is found in cytoplasmic loop 5. CHED mutants in extracellular loops include p.Asp406Val (95) in intracellular loop 1, and p.Arg804His (82) located in cytoplasmic loop 6, in short helix H5. The locations and properties of SLC4A11 mutants are summarized on a topology model (Fig. 3.6).

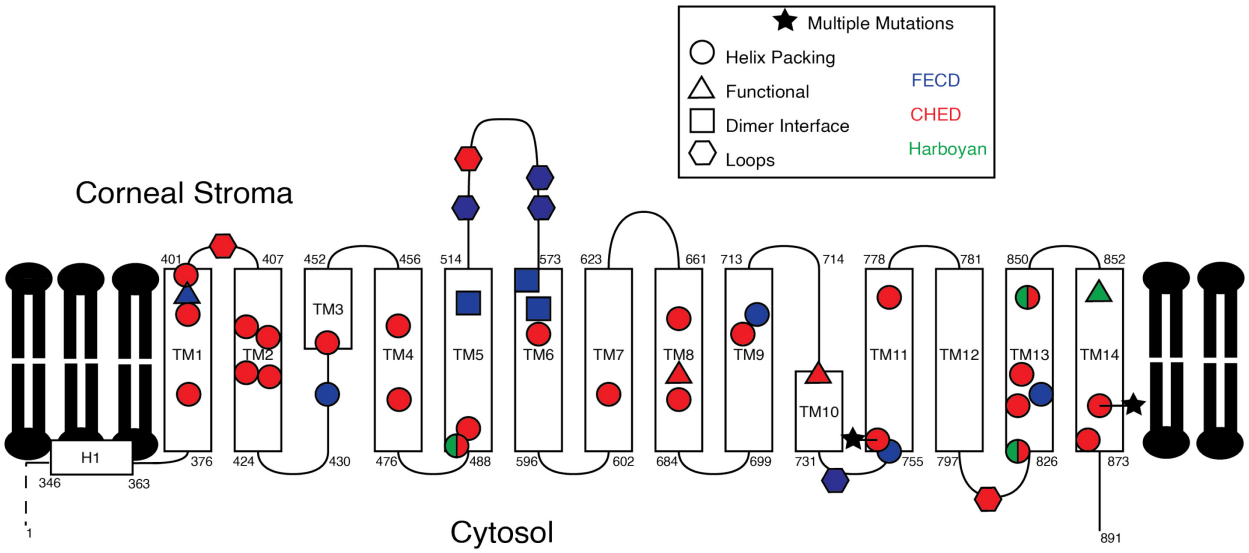

Figure 3.6 Disease mutants mapped on SLC4A11 topology model. Topology model was developed on the basis of the three-dimensional homology model. Intracellular helix H1 and TM1 –14 are represented as rectangles and labeled, with initiating and terminating residue numbers indicated. Relative loop sizes are approximate, and the large N-terminal domain has been excluded. Stars indicate residues with multiple known mutations. Disease-causing mutations of the membrane domain are mapped and labeled by disease and proposed underlying molecular cause; FECD (blue), CHED (red), and HS (green), helix packing (○), catalytic pathway (△), dimer interface (□), and extramembraneous loops (⬡). Mutations shown include TM1: p.Cys386Arg, p.Gly394Arg, p.Glu399Lys, p.Thr401Lys. ECL1: p.Asp406Val. TM2: p.Gly413Arg, p.Ser415Asn, p.Gly417Arg, p.Gly418Asp. TM3: p.Thr434Ile, p.Ala436Val. TM4: p.Gly464Asp, p.Leu473Arg. TM5: p.Arg488Lys, p.Ser489Leu, p.Val507Ile. Extracellular loop 3: p.Tyr526Cys, p.Ser536Cys, p.Thr561Met, p.Ser565Leu. TM6: p.Val575Met, p.Gly583Asp, p.Thr584Lys. TM7: p.Cys611Arg. TM8: p.Leu668Pro, p.Glu675Ala. p.Gln676Arg. TM9: p.Ile706Asn, p.Gly709Glu. TM10: p.His724Asp. Intracellular loop 5: p.Gly742Arg TM11: p.Thr754Met, p.Arg755Gln, p.Arg755Trp, p.Pro773Leu. Intracellular loop 6: p.Arg804His. TM13: p.Val824Met, p.Thr833Met, p.Gly834Ser, p.Leu840Pro, p.Leu843Pro. TM14: p.Met856Val, p.Arg869Cys, p.Arg869His, p.Leu873Pro. Amino acid numbering is based on reference sequence NG_017072.1, with HGVS numbering recommendations.

3.2.8 Amino Acid Sequence Conservation

Although SLC4All and AE1 are both members of the SLC4 family, they differ in their transport substrates and in the interaction of their cytoplasmic and membrane domains (165). We thus analyzed amino acid sequence conservation in AE1 and SLC4A11 across the membrane domains of 30 species, including fish, birds, and mammals, using the program ConSurf (425,426,428) (Table 2.3).

The degree of sequence conservation of each protein was mapped on the AE1 structure and SLC4A11 homology model (Fig. 3.7). A cartoon representation was used for the half of the proteins showing the lowest difference in conservation between the two proteins, to emphasize the structural homology and alignment of the two structures. The boxed region with highest difference in conservation was rendered as a space-filling model to emphasize the amino acid conservation on the surface of the cytoplasmic face (Fig. 3.7). Amino acid residues for which the confidence interval is too large for reliable assignment of a conservation score are assigned a score of "Insufficient Data" (426).

The highest difference in sequence conservation between AE1 and SLC4A11 is revealed as the cytoplasmic face of the SLC4A11. In particular, TM5, 13, and 14 and their corresponding cytoplasmic loops are much more strongly conserved in SLC4A11 than in AE1. Such conservation would be consistent with a critical role, or protein-protein contact in SLC4A11 that is not found in AE1.

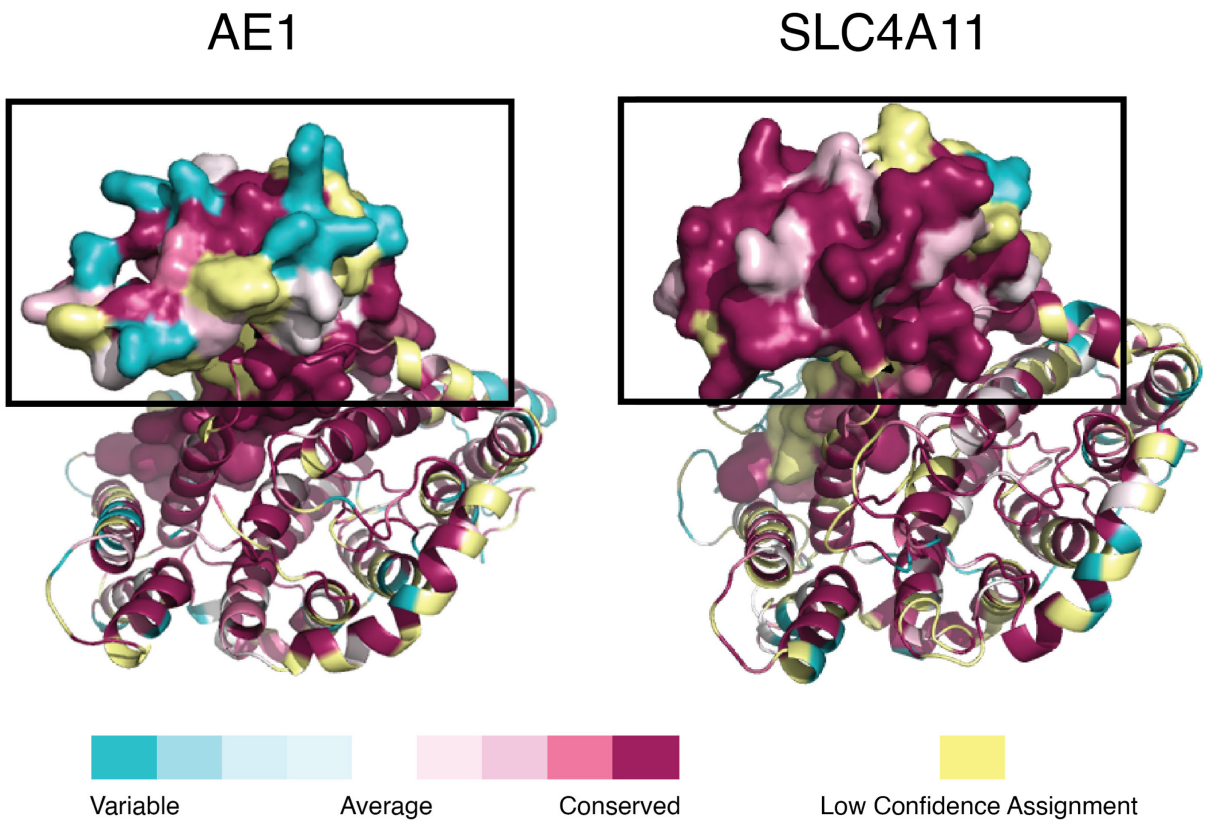

Figure 3.7 Conservation of cytosolic face residues of AE1 and SLC4A11 membrane domains. Amino acid sequence conservation across sequences of 30 species (Table 2.3) each for AE1 (left) and SLC4A11 (right) was analyzed, using a multiple sequence alignment performed by Clustal Omega. Degree of conservation was color-coded (inset scale) and mapped onto AE1 membrane domain structure and the SLC4A11 homology model, using ConSurf server. Models show the cytosolic face of the two proteins, with helices represented as cartoons with the exception of TM5, 13, and 14, represented as space-filling models (boxed). Amino acid residues for which the confidence interval is too large for reliable assignment of a conservation score are assigned a score of "Insufficient Data."

3.3 Discussion

We developed a three-dimensional homology model for human SLC4A11 on the basis of the AE1 crystal structure. Analysis of the expression, cell trafficking and functional activity of targeted SLC4A11 mutants supported the validity of the resulting homology model. The 45 identified corneal dystrophy-causing mutations within the membrane domain were mapped onto the homology model and classified depending on their location in the SLC4A11 model. These differing locations suggested the basis for effects on SLC4A11 solute transport function, overall structure, and dimerization, which in some cases are already supported by biochemical evidence. A final model classifying the predicted molecular defect of all reported membrane domain SLC4A11 disease-causing mutations is presented (Fig. 3.6).

Point mutants can be classified by molecular phenotype into two groups; 1. Those that misfold and are retained in the ER, failing to reach the plasma membrane, (98,99,439) and 2. Mutants that process to the plasma membrane but are catalytically inactive (438) (Fig. 1.11). Mutants located in the dimeric interface and regions of close transmembrane helix packing are expected to cause misfolding and be ER retained, while catalytic pathway mutants are predicted to be catalytically impaired at the plasma membrane. This model and categorization can thus be used to rationalize phenotypes of currently known corneal dystrophy-causing SLC4A11 mutants, and to predict the molecular mechanism of disease in newly discovered mutants.

3.3.1 Model Validation

The SLC4A11 homology model developed here was validated *in silico* and by biochemical analysis. PROCHECK and Verify3D indicated good structural quality through TMs, where the homology model Cα deviated from the AE1 structure by 0.392 Å. Mutations were made at two positions that were predicted to impair transport function of SLC4A11 (E675, H724). In each case

the anticipated phenotype, uncompromised folding, but catalytic defect, was observed. A third mutant, G509K, was predicted to have little or no effect on processing or transport activity of SLC4A11, due to location in an open area of the homology model. Expression level and maturation of the mutant, however, were reduced relative to SLC4A11-WT, but transport activity was not significantly different from wild-type protein. This phenotype suggests a mild misfolding of the protein, consistent with the prediction based on the homology model.

Mutant A720L, however, was also predicted to impair transport function due to location in the region of extended structure of TM10, in the catalytic pathway (Fig. 3.2C). This mutant expressed and matured to low levels compared to wild-type (Figs. 3.3, 3.4), indicating an unanticipated sensitivity to mutation. The failure to accurately predict the phenotype of the A720L mutation could be viewed as providing evidence against the validity of the homology model. On the other hand, we predicted that this mutation was close to the catalytic core of SLC4A11, in an area critical for transport function. The homology model places Ala720 directly adjacent to Glu675, which is homologous to functionally critical AE1 residue Glu681 (267,268). We found Glu675 to be sensitive to mutation to glutamine (Fig. 3.4). While we anticipated that SLC4A11 would tolerate a larger alkyl group here, we were incorrect. This serves as a caveat for the use of the homology model in predicting the molecular phenotype of disease alleles.

Together the primary sequence similarity and biochemical results indicate that SLC4A11 and AE1 share a fold, and thus that the homology model is valid at least for residues in the plane of the lipid bilayer.

3.3.2 Extracellular Loop 3

Extracellular loop 3 (ECL3, residues 515–572) is a large, 58 residue region between TM5 and TM6 at the dimer interface (Fig. 3.2A). In other SLC4 proteins, the loop is much smaller (23 amino

acids in AE1) and has no discernable sequence conservation or sequence similarity to any other protein. The homology model places three FECD mutants and one CHED mutant within ECL3, but the absence of a structural correlate in AE1 makes it challenging to identify the role of this region in SLC4A11 function. FECD-causing mutants p.Val507Ile and p.Val575Met at the extracellular periphery of TM5 and TM6 lie at the initiating and terminating ends of ECL3. These mutants could displace ECL3, disrupting its normal role. Supporting this, both mutants process to the cell surface *in vitro* (100,101), suggesting that disease is caused by a loss-of-function at the plasma membrane. Mutant p.Tyr526Cys, in ECL3, also processes to the cell surface in cell models (100). Recently, SLC4A11 ECL3 has demonstrated a role promoting corneal endothelial cell adhesion to Descemet's membrane (369).

3.3.3 Catalytic Pore

Transported substrates of AE1 (Cl^- and HCO_3^-) differ from those reported for SLC4A11 (unique substrates: Na^+, H_2O, NH_3, and OH^-/H^+) (53,359-366,438). To explore whether differences in the catalytic site might explain these functional differences, we examined the catalytic pore residues for sequence conservation. The most notable difference between the two structures is the presence of a histidine residue in SLC4A11 at position 724. SLC4A11 is the only SLC4 family member without an arginine at this position, and is also the only SLC4 member with no HCO_3^- transport activity (186). Conserved through all SLC4 family members is a glutamate within the catalytic pore, Glu675 in SLC4A11, which is proposed to act as a gate, occupying the anion binding site when no substrate is present (186,440).

3.3.4 Cytoplasmic Domain

AE1 and SLC4A11 have N-terminal cytoplasmic domains and C-terminal membrane domains of similar size. The cytosolic domain of SLC4A11 contains approximately one-third of reported

corneal dystrophy-causing mutations, and is essential for transport and overall stability of SLC4A11 (165). Recently the cytoplasmic and membrane domains of SLC4A11 were suggested to closely associate on the basis of: 1. An inability for either domain to accumulate when heterologously expressed alone in a tissue culture model, 2. An association between the two domains when co-expressed, and 3. The catalytic defect found in the cytoplasmic domain mutation, p.Arg125His, which suggested a role of the cytoplasmic domain in transport mechanism (165).

Interestingly, the AE1 cytoplasmic domain is not strongly associated with its membrane domain (166,441), providing a strong point of structural difference between the two SLC4 proteins (178). If cytoplasmic domain interactions with the cytoplasmic face of the membrane domain occur in SLC4A11, but not in AE1, we would expect greater evolutionary pressure to conserve the cytoplasmic face of SLC4A11 than AE1. The greater amino acid sequence conservation on the cytoplasmic face of SLC4A11 than AE1, in particular at the cytoplasmic ends of TM5, 13, and 14 (Fig. 3.7), is consistent with a role of this region in protein–protein interaction, potentially the interaction of the membrane domain with the cytoplasmic domain. In addition, the model reveals that the TM13-14 region (Fig. 3.2A, pink) has portions well exposed to cytosol, consistent with a binding site for cytoplasmic partners.

3.3.5 Conclusions

We developed a three-dimensional homology model of the SLC4A11 membrane domain on the basis of the AE1 crystal structure. *In silico* and *in vitro* testing indicate that the model is valid. This model provides a molecular rationalization for the 45 corneal dystrophy-causing point mutants of the membrane domain. Mutations fall into four categories as located in: 1. the catalytic pathway, 2. helix–helix interfaces, 3. dimerization interface, or 4. extracellular and cytoplasmic loops.

Unexpected amino acid sequence conservation points toward important roles of the cytosolic face of TM5, 13, and 14. This homology model provides a tool to study newly discovered corneal dystrophy mutants to predict their molecular phenotypes. Currently, consequence and pathogenicity of point mutations can be predicted using non-specific matrices (442,443), which provide analysis only of the severity of an amino acid change generically, without reference to the structural context. Finally, this work provides a structural explanation for the preponderance of misfolding mutants observed for mutant membrane proteins (436). If SLC4A11 is a guide in understanding mutant membrane proteins, amongst membrane domain mutants 73% (helix–helix packing and dimeric interface) affect protein folding, and 27% directly affect transport function (catalytic pathway and extramembraneous loops).

Chapter 4: AE1 as a Molecular Clock for Red Cell Senescence

4.1 Introduction

Here we examined the role of the integral membrane protein, AE1, in signaling the senescence status of red blood cells (RBCs). RBCs are the most abundant cell type of the human body, numbering 20-30 x 10^{12} and comprising nearly 25% of human cells (444,445). The circulating lifetime of a RBC is 120 ± 4 days, during which they endure mechanical and chemical stresses (326). The central role of RBCs in gas transport and exchange makes them particularly vulnerable to oxidative species and free radicals. RBCs undergo deformation and mechanical membrane stress as they transit through capillaries with diameters well below that of RBCs (222). As mature RBCs lack the ability to synthesize new proteins, chemical and mechanical injuries accumulate during the RBC's lifetime. Efficient removal of these damaged, senescent RBCs is critical to maintain circulatory system efficiency.

RBCs acquire irreversible age-related biochemical damage during circulation. Characteristics of compromised RBCs include increased extracellular surface exposure of the lipid phosphatidylserine (446-449), reduced levels of sialic acid, cholesterol, and phospholipids (450,451), decreased enzyme activities (452-457), and increased protein 4.1a/4.1b ratio (458). Through a process called microvesiculation, circulating RBCs shed extracellular membrane vesicles containing cell membrane components and oxidized hemoglobin, which decreases cell volume and surface area (459-467). A proposed combination of decreased cell volume from microvesiculation, and dehydration resulting from loss of hemoglobin results in older red cells having an increased density over younger cells (448,468). This difference in density allows older RBCs to be separated from younger cells by density gradient ultracentrifugation (469-471). The densest fraction of cells represents the oldest cells, or 'senescent' cells.

AE1 (also called Band 3) is an integral membrane protein with essential roles in RBC physiology. The red cell membrane contains 1.2×10^6 AE1 molecules, comprising 50% of RBC membrane protein (204). In a central component of respiratory physiology, metabolic waste CO_2 from tissues diffuses through the RBC membrane and enters the RBC cytosol, where carbonic anhydrase II (CAII) catalyzes CO_2 hydration to produce H^+ and HCO_3^- (Fig. 1.4). A CAII binding site on the AE1 membrane domain anchors CO_2 hydration at the RBC membrane, forming a bicarbonate metabolon (214,215,472). The H^+ resulting from CO_2 hydration lowers intracellular pH, which promotes the off-loading of hemoglobin-bound O_2 to tissues through a process known as the Bohr shift (213). To maintain low intracellular pH, and thus optimal O_2 off-loading, the HCO_3^- is extruded through AE1 in exchange for extracellular chloride at a rate of 1×10^5 anions s^{-1} (187). Preventing HCO_3^- accumulation in RBCs ensures the continued catalytic action of CAII. Taken together, this increases the CO_2 carrying capacity of blood, as HCO_3^- is much more water soluble than CO_2. The process is then reversed in the lungs.

While the AE1 membrane domain is responsible for anion exchange, the structurally independent cytoplasmic domain (CD) (473) anchors the red cell plasma membrane to the cytoskeleton though interactions with ankyrin (218,313) and protein 4.2 (474,475). AE1 is involved in processes relevant to malaria, including parasite invasion and the adherence of parasitized RBCs to the vascular endothelium (476-480). In addition to its roles catalyzing Cl^-/HCO_3^- exchange and anchoring the plasma membrane to the cytoskeleton, AE1 is also involved in signalling red cell senescence (327,481).

Mature human RBCs are enucleated and lack the organelles such as the endoplasmic reticulum, lysosomes and mitochondria necessary for autophagy or apoptosis. Instead, aged RBCs are cleared from circulation by macrophages, which recognize senescent cells in an IgG-dependant

manner (239,482). The densest (and thus oldest) fraction of RBCs in circulation have greater than 10-fold enrichment of surface-bound IgG, over younger cell fractions (242,327,482). The senescent cell IgG (ScIgG) auto-antibody enriched on aged RBCs is specific for AE1 and is omnipresent in sera (240,327,481). IgG on high-density RBCs co-localizes with membrane aggregates composed of AE1 protein, partially denatured hemoglobin (hemichromes), and immune system protein component complement C3 (242,483). Both immune system components, anti-AE1 ScIgG and C3 complement, are required to induce phagocytosis by macrophages (241,484).

While uncertainty surrounds the mechanism governing surface exposure of the AE1 senescence antigen, the general progression followed by RBCs as they senesce and are degraded by macrophages has been replicated in various laboratories (239,240,242). The crystal structure of the AE1 integral membrane domain at 3.5 Å resolution creates the opportunity to revisit the role of AE1 in signaling RBC senescence at the molecular level (1). It is important to recognize that the AE1 crystal structure represents the protein stabilized by crosslinking with the inhibitor H_2DIDS and a monoclonal antibody against an external epitope, and was solved in the presence of detergent, not in a lipid bilayer.

The senescent cell IgG recognizes two regions of the AE1 membrane domain, distant in the primary sequence: residues 538–554 and 812–830 (485-487). The crystal structure is consistent with previous biochemical assessment that these two regions lie outside the plane of the bilayer. However, in contrast to the extracellular 538–553 region (Extracellular Senescence Cell Epitope; ExScEp), residues 812–830 are intracellularly localized in the crystal structure (Intracellular Senescence Cell Epitope; InScEp; AE1 812-830 region), where they would be inaccessible to extracellular ScIgG (Fig. 4.1). The AE1 812-830 InScEp region displays both extracellular and

intracellular characteristics (1,488-495). Data supporting extracellular localization of this region include substituted cysteine accessibility assays (488,496), labeling by membrane impermeant compounds in RBCs (497), the ability of peptides corresponding to the AE1 824-829 region to inhibit vascular adherence of malaria-infected RBCs (489), and consistent identification of this region as binding senescence auto-antibodies (486,498). Data supporting intracellular localization of the InScEp region include accessibility to monoclonal mouse antibody BRIC 132 (492), labeling RBCs with membrane impermeant reagents (495), evidence of zero-length crosslinking between the AE1 cytoplasmic domain and residues D821 and K826 (494), the crystal structure (1), and scanning N-glycosylation mutagenesis studies (493). In the N-glycosylation mutagenesis studies, replacing the 812-830 region with natively glycosylated AE1 extracellular loop 4 resulted in poor glycosylation when expressed in a cell-free system, which may indicate a degree of mobility in this region of the protein, or an experimental artifact.

Studies in RBCs indicate that the senescent cell antigen on AE1 is a cryptic discontinuous epitope, requiring a conformational change for exposure to ScIgG (240). This, together with the extracellular and intracellular characteristics of the AE1 812-830 region, led us to hypothesize that the dynamic and cryptic component of senescent cell antigen is the AE1 812-830 region (243).

In this study, we set out to examine the localization of the AE1 812-830 region. We tested the extracellular accessibility of residues within this region in heterologously expressed AE1, using substituted cysteine accessibility, antibody binding assays, and immunofluorescence. We also tested whether the inhibitor labeling, and proteolysis required for AE1 crystallization could influence the extracellular accessibility of amino acid residues within this region. In addition to cell culture models, we studied the accessibility of residues 812-830 in AE1's native RBC environment. Furthermore, we characterized the binding properties of senescent cell IgG isolated

from aged red cells. On the basis of our results, we propose a model for the molecular mechanism of AE1-mediated red cell senescence signalling.

4.2 Results

4.2.1 Accessibility of Residues to Cysteine-Reactive Compound LYIA

To assess extracellular accessibility of AE1 residues, we analyzed a series of previously characterized single cysteine point mutants in a cysteine-less background, AE1C^{-} (411,488,496). Single cysteine mutants K817C, V822C, and K826C interrogated the 812-830 residue region. These mutants previously demonstrated anion exchange activity (488,496). Y555C was chosen as an extracellular control, as its extracellular accessibility has been established through chymotryptic cleavage studies (499), the Y555H Diego blood group antigen (500), and scanning N-glycosylation mutagenesis (493). Native cysteine C201 in the cytoplasmic domain was chosen as an intracellular control for its reactivity towards cysteine-directed compounds (501). Additional intracellular mutants A456C and S517C, localized in intracellular loops 1 and 2 in the crystal structure, were examined to determine if LYIA accessibility is shared throughout AE1 intracellular regions, or unique to the 812-830 region (Fig. 4.1).

Intracellular or extracellular localization of cysteine point mutants was assessed by their reactivity with charged, membrane impermeant LYIA (502). LYIA labeling was quantified upon cell treatment with membrane-permeant biotin maleimide. Accessibility of cysteine residues to LYIA was quantified using the ratio of biotinylation in the absence (-) relative to the presence (+) of LYIA during preincubation. In this way, intracellular residues unaffected by LYIA would be expected to have a value of 1.0, while extracellular residues would have a ratio >1 (502).

The ratio of biotin maleimide labeling of intracellular control C201 (LYIA accessibility = 1.3 ± 0.1) was consistent with intracellular localization (Fig. 4.2). The ratio of biotinylation was

slightly larger than 1.0, indicating a slight degree of LYIA labeling possibly arising from cell lysis. This represents the background LYIA labeling. Point mutants A456C and S517C had similarly low sensitivity to pre-blocking (LYIA accessibility A456C = 1.7 ± 0.6, S517C = 1.8 ± 0.5), again consistent with the intracellular localization shown in the crystal structure (Fig. 4.2). These intracellular loops had an accessibility ratio not statistically different than C201 (Fig. 4.2B).

In stark contrast, mutants Y555C, K817C, V822C and K826C all demonstrated an LYIA accessibility ratio of much greater than 1.0 (LYIA accessibility Y555C = 5.4 ± 0.8, K817C = 6.2 ± 1.3, V822C = 8.6 ± 1.9, K826C = 4.6 ± 0.2), consistent with extracellular accessibility (Fig. 4.2B). Notably, residues K817C, V822C, and K826C were accessible to extracellular membrane impermeant labeling compound LYIA to a degree statistically indistinguishable from extracellular control mutant Y555C (Fig. 4.2). This is consistent with previous extracellular accessibility within this region (488).

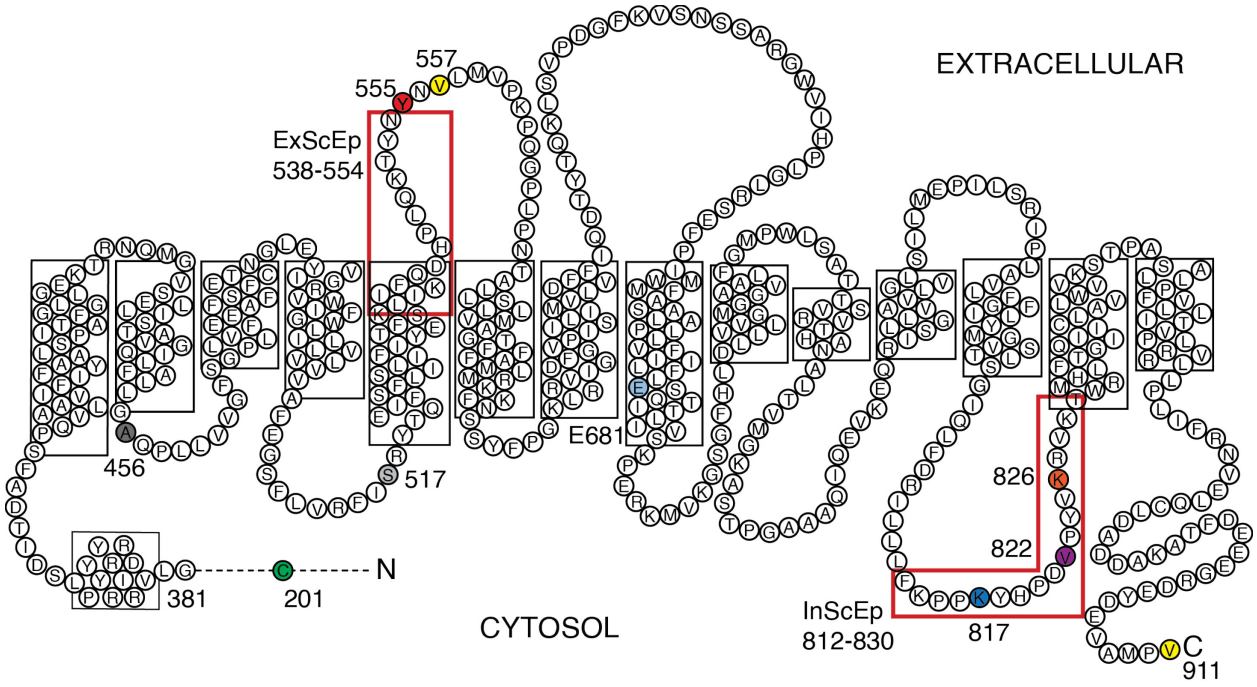

Figure 4.1 AE1 topology model, based on the membrane domain crystal structure (PBD ID: 4YZF) (1). Regions of alpha-helical secondary structure are shown in black boxes. Epitopes reactive with senescent cell autoantibodies are in red boxes (ExScEp and InScEp, extracellular and intracellular senescent cell epitopes, respectively) (490). Locations of introduced cysteine residues (or endogenous in the case of C201) are green (C201), dark grey (A456C), light grey (S517C), red (Y555C), dark blue (K817C), purple (V822C), and orange (K826C). Locations of introduced HA-tags shown in yellow (557, 911). Location of E681Q, a mutation impairing anion transport, is shown in pale blue. The cytoplasmic domain is represented by the dashed line, not shown to scale.

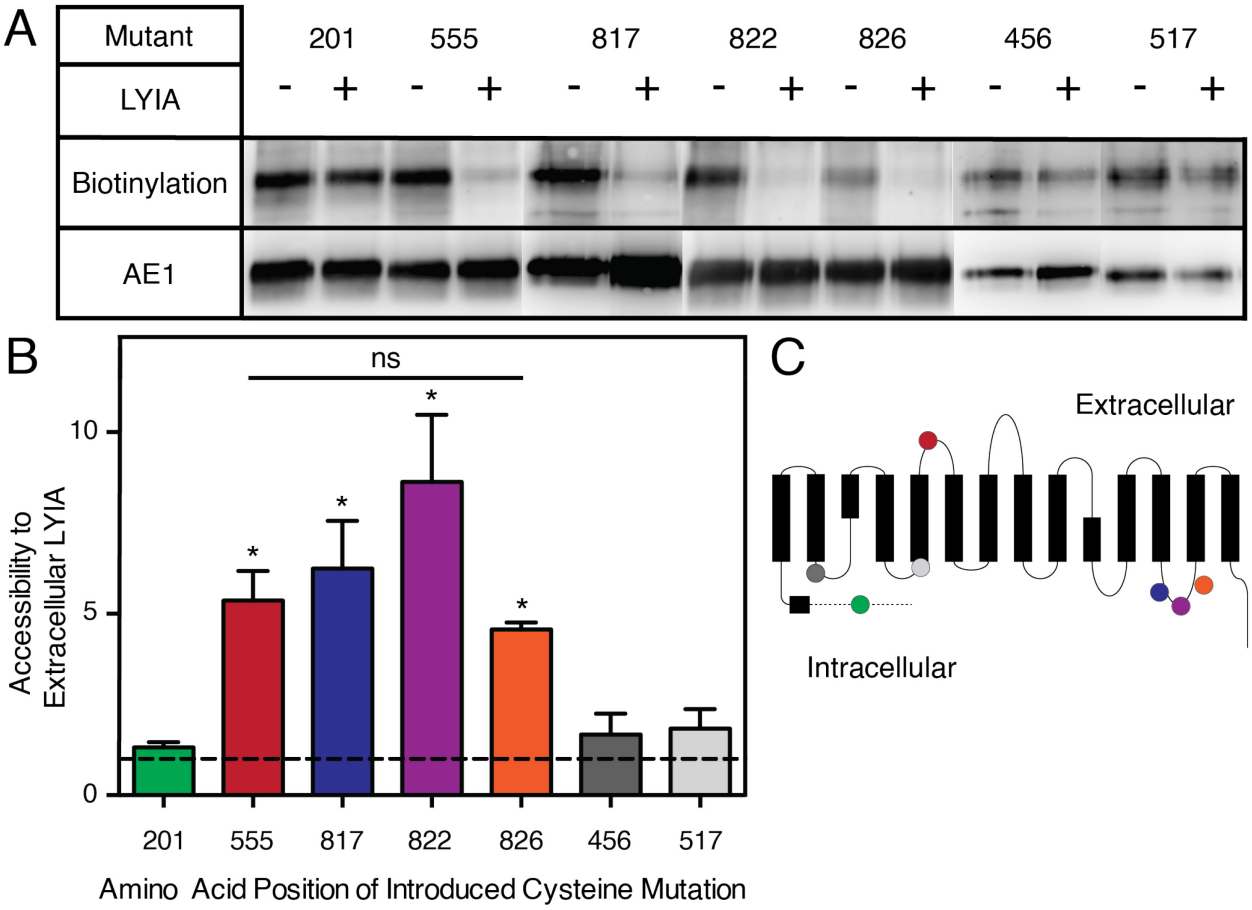

Figure 4.2 Accessibility of AE1 single cysteine point mutants to membrane-impermeant LYIA. HEK293 cells were transiently transfected with single point cysteine mutants in an otherwise cysteine-less background. Cells were incubated in PBS without (-) or with (+) 2 mM LYIA for 20 min, prior to incubation with 0.2 mM biotin maleimide for 10 min at 20 °C. A) Biotinylation of each mutant was assessed on blots probed with HRP-conjugated streptavidin (upper), followed by stripping and probing with αAE1 antibody (lower). Amino acid positions of Cys residues are indicated at top. B) Accessibility to extracellular LYIA was calculated. Data represent mean ± SEM of 3-8 repetitions. Asterisks indicate mean values significantly different ($P < 0.05$) than intracellular control, C201 (green), by one-way ANOVA. C) Simplified topology diagram of AE1, with locations of single cysteine point mutations assessed for LYIA accessibility shown, color coded as in B.

4.2.2 Time Course of Accessibility to Extracellular LYIA

Accessibility to extracellular LYIA of residues K817C, V822C, and K826C was indistinguishable from extracellular control Y555C at a single time point of 20 min. We thus analyzed accessibility to LYIA of the mutant series over a time course, to determine if there was a difference in the rate of labeling of these residues. Point mutants were assessed for their extracellular accessibility to LYIA at 0, 5, 15, and 30 min pre-blocking time (Fig. 4.3). A one-phase association model determined the halftime of LYIA labeling (Fig. 4.3B, C). The curve for intracellular control mutant C201 could not be fitted using this model, consistent with inaccessibility of an intracellular residue to membrane impermeant LYIA in intact cells (Fig. 4.3B).

The halftime of LYIA labeling of all three mutants assessed within the 812-830 region was not significantly different than extracellular control, Y555C (Table 4.1) (Fig. 4.3C). This, together with single time point LYIA accessibility data (Fig. 4.2), led us to conclude that the residues analyzed within the AE1 812-830 region are accessible to extracellular LYIA to a degree indistinguishable from extracellular loop 3 residue Y555C at these time scales.

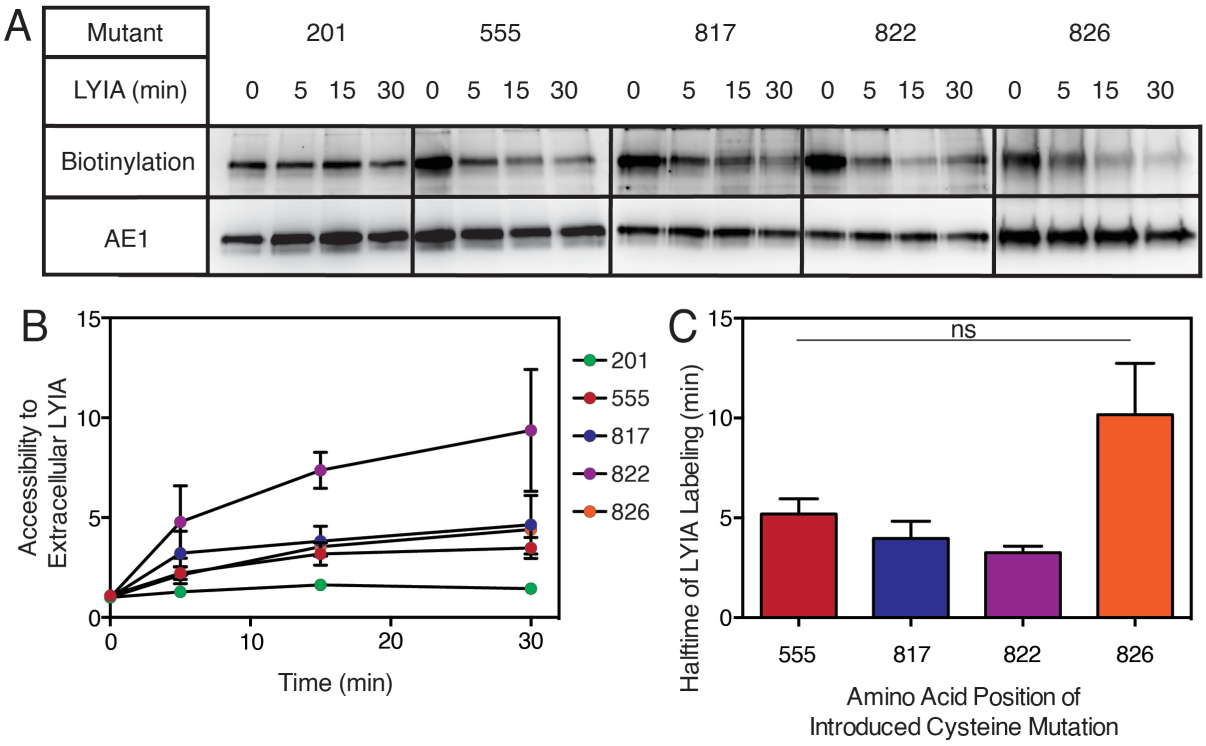

Figure 4.3 Time course of accessibility of AE1 single cysteine point mutants to membrane-impermeant LYIA. A) Transfected HEK293 cells were treated as in Fig. 4.2, with varied times of pre-incubation with 2 mM LYIA, before incubation with 0.2 mM biotin maleimide. Each mutant's biotinylation was assessed on blots probed with HRP-conjugated streptavidin (upper), followed by stripping and probing with αAE1 antibody (lower). B) Accessibility of single cysteine point mutants to LYIA. Data points indicate mean ± SEM for each time point, n=3. C) Halftime of LYIA labeling for indicated mutants. Data from B were fit using a one-phase association model, and means compared with one-way ANOVA, ns = not significant.

Table 4.1 Halftime of LYIA labeling of AE1 single cysteine mutants. Cells were incubated with 2 mM LYIA at 20 ℃. Kinetics were assessed by fitting accessibility curves using a one-phase association model in Prism. Intracellular control C201 could not be fitted using this model.

Location of Introduced Cysteine	LYIA Halftime (min)
Y555C	5.2 ± 1.7
K817C	4.0 ± 1.7
V822C	3.3 ± 0.5
K826C	10.2 ± 2.6

4.2.3 Accessibility to LYIA in Modified AE1

AE1 is the fastest transporter reported, with anion exchange kinetics of ~ 10^5 anions s^{-1} (187). Mutation of active site residue E681 to Q abolishes Cl^-/HCO_3^- exchange (267,503). To determine whether the molecular movements required for anion transport are required for extracellular accessibility of the 812-830 region, we created transport-compromised single cysteine mutant K817C(E681Q). The extracellular accessibility of K817C was unchanged when expressed in this transport-compromised background (LYIA accessibility K817C = 4.5 ± 1.0, K817C(E681Q) = 6.8 ± 0.4) (Fig. 4.4). This indicates that the structural rearrangements associated with anion transport are not required for the extracellular accessibility of residues within the 812-830 region.

AE1 isolated from RBCs was modified to generate human AE1 crystals suitable for structural determination (24): labeling with the covalent inhibitor 4,4′-diisothiocyanatodihydrostilbene-2,2′-disulfonic acid (H_2DIDS), tryptic removal of the 43 kDa N-terminal cytoplasmic domain, deglycosylation with N-glycosidase F, and incubation with antigen-binding fragment (Fab) prepared from a monoclonal antibody raised against an AE1MD conformational epitope. We thus examined whether these conditions led to the intracellular localization of residues 812-830 seen in the crystal structure.

The AE1 membrane domain facilitates anion exchange following tryptic removal of the cytoplasmic domain (166,167). To determine if the cytoplasmic domain influenced extracellular accessibility of the 812-830 region, we assessed LYIA labeling of cysteine mutants in a cysteine-less, membrane domain (MD, residues 369-911) background (Fig. 4.5A, B). An additional mutant, K892C in the C-terminal tail, was chosen as an intracellular control to assess in both full length and membrane domain backgrounds, as C201 lies in the N-terminal cytoplasmic domain and is thus not present in the membrane domain.

There was no significant difference in LYIA accessibility between full length C201 and K892C intracellular control mutants, indicating that the K892C mutant is a viable intracellular control (LYIA accessibility C201 = 1.6 ± 0.2, K892C = 1.5 ± 0.2). Both intracellular control K892C and extracellular control Y555C displayed no significant difference in accessibility to LYIA whether expressed as full-length or membrane domain constructs (LYIA accessibility K892C = 1.5 ± 0.2, K892CMD = 2.2 ± 0.5, Y555C = 6.7 ± 1.2, Y555CMD = 6.9 ± 1.4). Similarly, K817C showed no significant difference in extracellular accessibility between full-length and membrane domain constructs (LYIA accessibility K817C = 6.8 ± 1.1, K817CMD = 8.5 ± 1.7). Transport-deficient mutant K817C/E681Q also maintained extracellular accessibility in both constructs, with no significant difference between the two (LYIA accessibility K817C(E681Q) = 4.5 ± 0.4, K817C(E681Q)MD = 5.7 ± 1.1) (Fig. 4.5C, D). We conclude that removal of the cytoplasmic domain does not affect extracellular accessibility of the AE1 812-830 region.

The AE1 membrane domain was crystallized with H_2DIDS at the extracellular interface of the core and gate domains to block movements associated with anion transport and thus ensure rigid protein suitable for crystallization. To test whether H_2DIDS affected localization of AE1 812-830, HEK293 cells expressing full length cysteine point mutants were incubated with H_2DIDS, or PBS alone, before LYIA accessibility assays. H_2DIDS pre-treatment did not significantly alter extracellular LYIA accessibility of C201, Y555C or K817C (LYIA accessibility C201 = 1.5 ± 0.3, C201+H_2DIDS = 1.9 ± 0.3, Y555C = 5.8 ± 1.5, Y555C+ H_2DIDS = 4.8 ± 1.4, K817C = 7.4 ± 0.5, K817C+H_2DIDS = 8.5 ± 1.7) (Fig. 4.5C). We conclude that stilbene disulfonate in the inter-domain cleft of AE1 does not affect accessibility of the 812-830 region to the extracellular medium.

Finally, we wanted to assess whether Fab used in AE1 crystallization influenced 812-830 localization. We contacted co-authors of the AE1 crystallization report but were unable to obtain a sample of the antibody preparation.

Neither H_2DIDS nor generation of the membrane domain used in the crystallization conditions abolished the LYIA accessibility of mutant K817C. K817C also maintained LYIA accessibility in transport-deficient E681Q background. Thus, we conclude that 1. the crystallization conditions did not restrict AE1 812-830 region extracellular accessibility, and 2. conformational changes associated with anion transport are not required for extracellular accessibility of this region. We cannot rule out the possibility that the Fab fragment used in crystallization, which was raised against a conformational epitope of AE1 membrane domain, influenced the localization of the 812-830 region, but this is unlikely since the epitope is extracellular and quite distant in the structure.

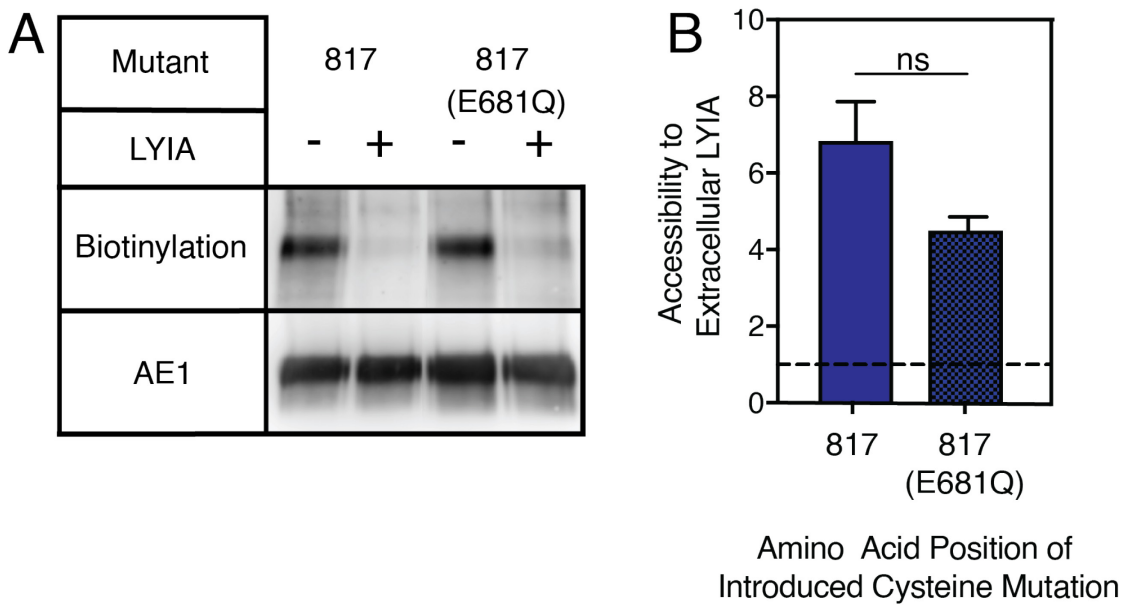

Figure 4.4 Accessibility of transport-deficient AE1 mutant to membrane-impermeant LYIA. A) LYIA accessibility of mutant K817C was assessed in AE1C$^-$ background (817), and in AE1C$^-$ background containing anion transport-deficient mutation E681Q (817 (E681Q)). B) Accessibility to extracellular LYIA was calculated. Data represent mean ± SEM of 4 repetitions. Asterisks indicate mean values significantly different ($P < 0.05$) by one-way ANOVA, ns = not significant.

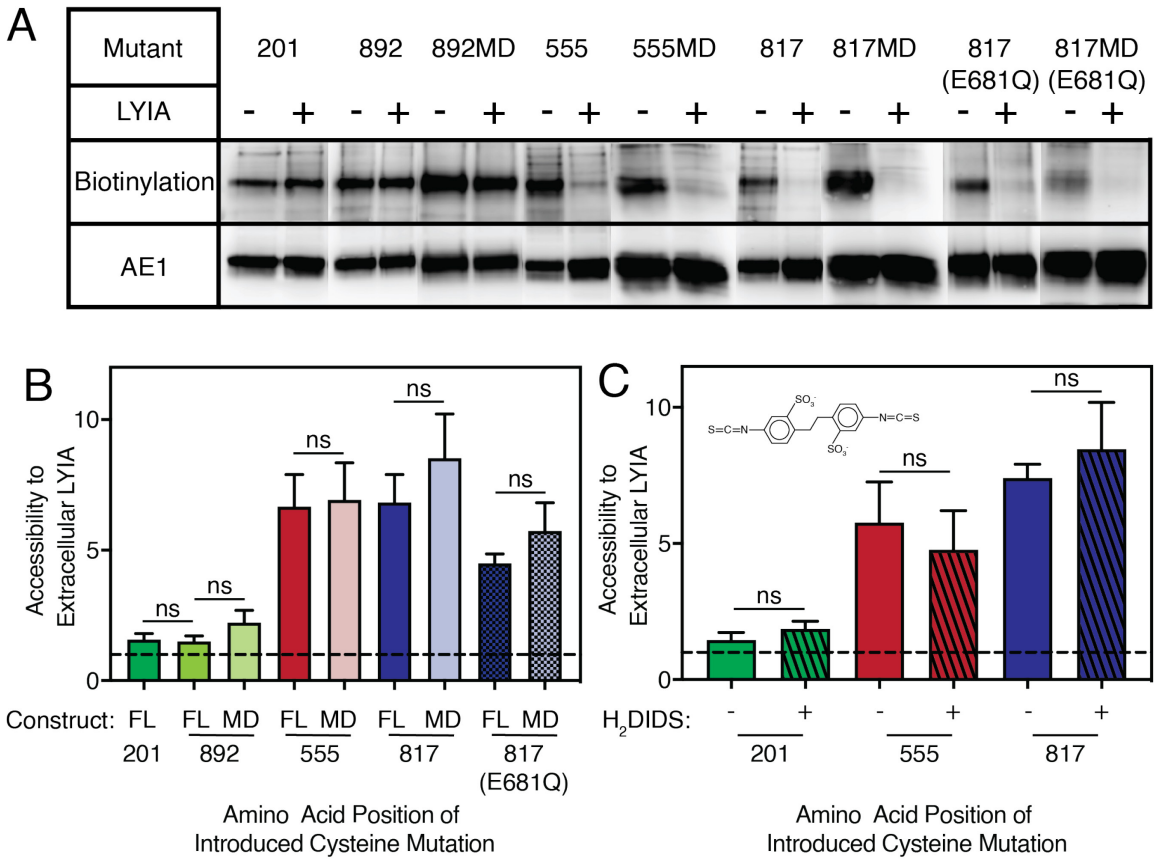

Figure 4.5 Accessibility of AE1 mutants to membrane-impermeant LYIA. A) Accessibility of C201, and Y555C, K892C, K817C and K817C/E681Q single cysteine point mutants in full-length and membrane domain (MD) AE1 constructs. Biotinylation of each mutant was assessed using western blotting and HRP-conjugated streptavidin (upper), followed by stripping and probing with αAE1 antibody (lower). B) Accessibility to extracellular LYIA was calculated for full length (FL) and membrane domain (MD) constructs mutants assessed in parallel. Data represent mean ± SEM of 3-6 repetitions. Asterisks indicate significant difference ($P < 0.05$) between mean values of single cysteine mutants in full length (FL) and membrane domain constructs (MD) by one-way ANOVA, ns = not significant. C) HEK293 cells expressing indicated single point cysteine mutations in full-length AE1C$^-$ background were assessed for accessibility to extracellular LYIA after pre-treatment with 50 μM H_2DIDS (structure inset) (black striped bars), or parallel incubation in PBS alone (solid color bars). Data represent mean ± SEM of 4 repetitions. Asterisks indicate mean values significantly different ($P < 0.05$) than single cysteine mutants assessed in parallel without H_2DIDS pre-treatment, by one-way ANOVA, ns = not significant.

4.2.4 Antibody Accessibility

To determine whether residues within the 812-830 region are sufficiently exposed to the extracellular milieu to act as a ScIgG antigen, we designed an antibody binding assay mimicking the environment in which ScIgG binds eAE1. A peptide corresponding to AE1 residues 814-827 was used to raise a polyclonal antibody in rabbits (called α814-827), which detected AE1 on immunoblots (Fig. 4.6A). We assessed the ability of α814-827 to bind AE1 heterologously expressed in HEK293-F suspension cells, simulating the conditions of circulating RBCs in sera.

HEK293-F suspension cells were transfected with cDNA encoding wild-type AE1, or vector. Cells were incubated with either rabbit pre-immune serum, α814-827, or polyclonal rabbit antibody recognizing the intracellular C-terminal 13 residues of native AE1 (called 1658, AE1 amino acids 899-911 (265)) (Fig. 4.6B). Following incubation with antibodies the HEK293-F cells were washed, and cell lysates were processed for immunoblotting following non-reducing SDS-PAGE. Immunoblots were cut at the 70 kDa position indicated by the prestained protein marker. IgG bound to the HEK293-F cells was quantified by probing immunoblots above the 70 kDa protein marker band with α-rabbit antibody conjugated to horse radish peroxidase (HRP) (Fig. 4.6C, D). As a positive control for antibody binding to the extracellular region of an SLC4 protein, we used a previously-characterized polyclonal rabbit antibody recognizing extracellular loop 3 of SLC4 family member, SLC4A11 (αEL3) (369). αEL3 binding was assessed using HEK293-F cells transfected with SLC4A11 cDNA, or vector. Immunoblotted proteins below the 70 kDa band of the prestained protein marker were probed with αGAPDH antibody as a loading control (Fig. 4.6C, D).

HEK293-F cells expressing SLC4A11 bound αEL3 to a significantly higher level than did vector-transfected cells (Fig. 4.6C, D). SLC4A11 EL3 mediates adhesion of corneal endothelial

cells to Descemet's membrane in the cornea (369), an interaction that can be disrupted by pre-blocking with αEL3 antibody. This demonstrates that 1. antibodies are able to specifically bind extracellular-accessible epitopes on transfected HEK293-F cells over vector-transfected cells, and 2. extracellular regions of SLC4 transporters can be sufficiently exposed to the extracellular milieu to bind antibodies.

There was no significant difference in the amount of bound IgG between vector-transfected cells and those expressing AE1 when cells were exposed to pre-immune serum (Fig. 4.6D). This indicates that IgG components in rabbit pre-immune serum do not bind AE1-expressing cells to a greater degree than vector transfected cells (or vice versa), and thus any signal for bound IgG is due to specific binding by the antibody used in incubation. Similarly, there was no significant difference in the amount of bound IgG after exposure to antibody 1658 between vector-transfected cells and those expressing AE1. Since 1658 recognizes the cytoplasmic intracellular AE1 C-terminus, this confirms that cells did not lyse and expose intracellular epitopes during incubation. Thus, any significant IgG binding arises from extracellular antigen accessibility.

HEK293-F cells expressing AE1 bound α814-827 to a significantly higher extent than vector transfected cells (Fig. 4.6C, D). As 1658 antibody was unable to bind AE1-expressing cells to a greater degree than vector-transfected cells, bound α814-827 is not due to IgG accessing intracellular epitopes of AE1. The observation that αEL3 bound SLC4A11-expressing cells to a significant degree more than to vector-transfected cells shows that IgG can specifically bind an extracellular region of an SLC4 protein. Together, this indicates that α814-827 binds an extracellular region of AE1. We conclude that the AE1 812-830 region is able to access the extracellular environment to a degree sufficient to bind extracellular IgG.

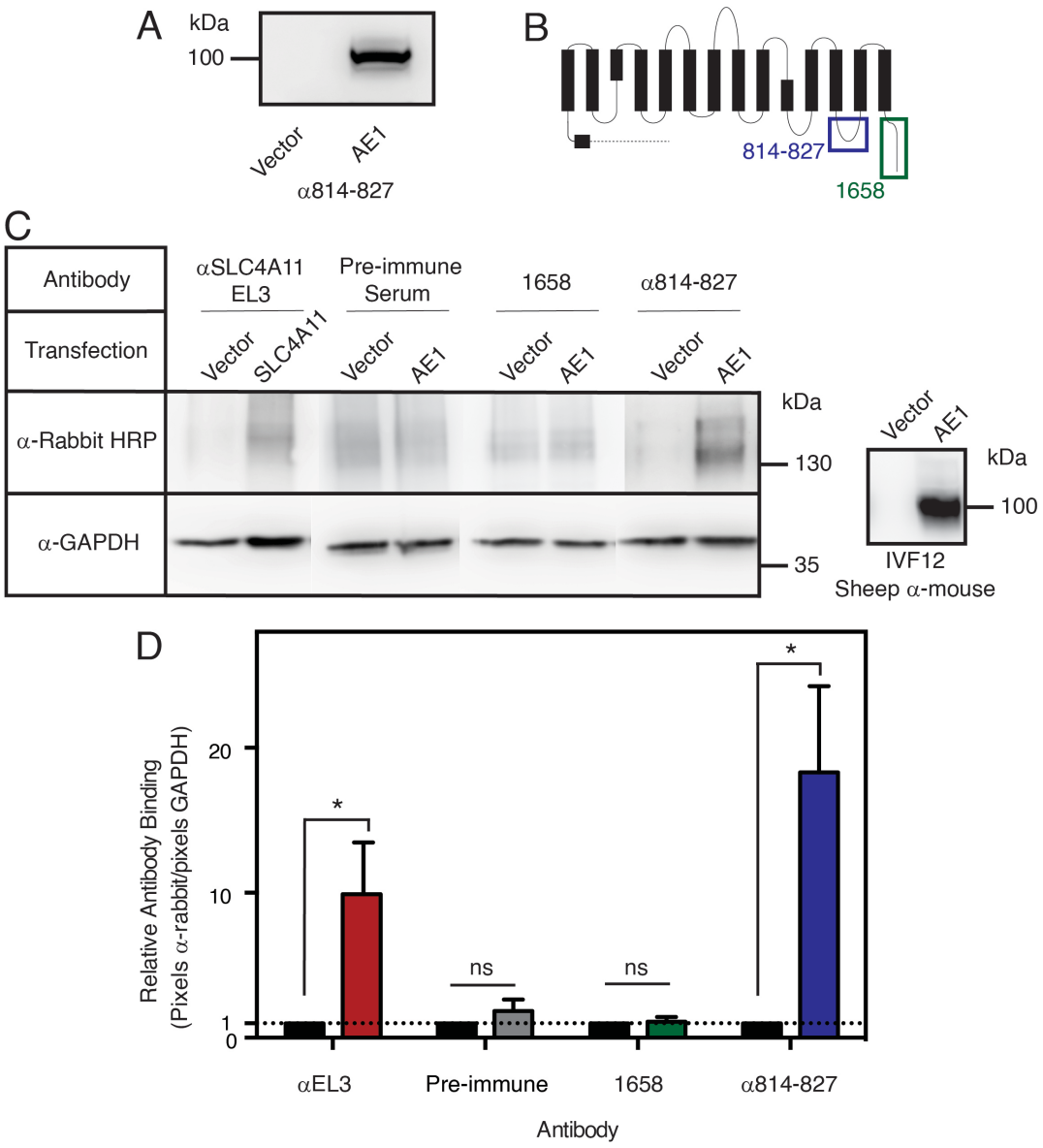

Figure 4.6 Extracellular accessibility of AE1 to α814-827 antibody A) Cell lysates from HEK293 cells transfected with empty vector, or cDNA encoding full length wild-type AE1, were probed on immunoblots with antibody raised against a peptide corresponding to AE1 amino acid residues 814-827 (α814-827). B) Simplified topology diagram of AE1. Epitopes for anti-peptide antibodies α814-827 (blue box) and 1658 (green box, amino acids 899-911) are indicated. C) HEK293-F suspension cells were transfected with empty vector, or cDNA encoding wild-type AE1, except in the case of αSLC4A11 EL3 antibody, where cells were transfected with cDNA encoding SLC4A11. Live cells were incubated with indicated antibody, or rabbit pre-immune

serum, followed by washing. Cell lysates were prepared and processed for immunoblotting. Immunoblots were cut at the position of the 70 kDa prestained protein marker band. Cell-associated IgG was detected by probing immunoblots above the 70 kDa marker band with Goat α-rabbit IgG conjugated to HRP (upper). Below 70 kDa, immunoblots were probed with α-GAPDH antibody (lower). AE1 expression was monitored by probing immunoblots with anti-AE1 C-terminus antibody (IVF12). D) Quantification of densitometry of C. Bound IgG signal (α-rabbit HRP) was normalized to GAPDH and is presented normalized to the value for vector-transfected cells. Data represent mean ± SEM of 3 repetitions. Asterisks indicate significant difference ($P < 0.05$), by one-way ANOVA.

4.2.5 Immunofluorescence of HEK293 Cells

Confocal immunofluorescence assessed AE1 812-830 localization in fixed HEK293 cells. To determine the fraction of AE1 with extracellular localization of the 812-830 region, we used AE1 constructs with hemagglutinin (HA) epitope tags introduced at extracellular or intracellular sites. In this way, we were able to set quantitative benchmarks for extracellular and intracellular epitope localization. HEK293 cells on glass coverslips were transfected with cDNA encoding AE1 with HA at 557 (in extracellular loop 3) or 911 (at the cytosolic C-terminus) (Fig. 4.1A). Localization of the HA epitope was assessed by confocal immunofluorescence in permeabilized cell and non-permeabilized conditions (Fig. 4.7). Cells were processed for immunofluorescence and probed with mouse αHA IgG, followed by secondary antibody Donkey α-Mouse IgG coupled to Cy3 dye. In permeabilized cells, a pattern of pericellular HA signal confirmed trafficking of mature AE1-557HA and AE1-911HA to the plasma membrane (Fig. 4.7B).

To define benchmark values for the fluorescent signal associated with intracellular and extracellular epitopes, cells were processed for immunofluorescence with αHA under permeabilized and non-permeabilized conditions. Permeabilized and non-permeabilized cells were imaged using the same confocal microscopy exposure settings. Mean fluorescent values were first corrected for background fluorescence in vector-transfected cells, for permeabilized and non-permeabilized conditions. For each AE1-HA construct, mean fluorescence in non-permeabilized conditions was normalized to the value in permeabilized cells. In this way, any increase in mean fluorescence upon permeabilization can be measured, and quantitative benchmarks can be set for intracellular and extracellular epitopes.

For cells expressing AE1 with an extracellular HA epitope, AE1-557HA, αHA immunofluorescence in non-permeabilized cells was not significantly different than in

permeabilized cells (Fig.4.7B-D). Thus, an extracellular AE1 antigen will display no significant increase in fluorescence upon permeabilization. In contrast, intracellularly-tagged AE1-911HA displayed a significant increase upon permeabilization, from 19% ± 1.9 to 100% (Fig. 4.7). This labeling pattern of AE1-911HA indicates that an exclusively intracellular epitope demonstrates 19% background signal in non-permeabilized cells compared to permeabilized cells (Fig. 4.7E). Background may arise from compromised cell membrane integrity or lysis during the immunofluorescence labeling procedures. Non-specific binding was previously accounted for by subtracting the level of fluorescence observed in vector-transfected cells.

Accessibility of AE1 residues 814-827 was assessed similarly to HA epitopes. The same cells probed with αHA were co-labeled with α814-827, followed by secondary antibody Donkey α-Rabbit IgG coupled to spectrally distinct Alexa Fluor 488. In all AE1-expressing cells, α814-827 immunofluorescence increased upon permeabilization, indicating a predominant intracellular localization of residues 812-830 (Fig. 4.7D, E). The increase in signal upon permeabilization was relatively consistent in both AE1 constructs analyzed, from 38% ± 2.1 to 100% in AE1-557HA, and 35% ± 2.4 to 100% in AE1-911HA. This indicates that the HA tags did not influence localization of the 812-830 region.

The non-permeabilized fluorescent signal from α814-827 was statistically higher than non-permeabilized αHA signal in AE1-911 (19%), representing background labeling of intracellular antigens. By subtracting background labeling of intracellular antigens from α814-827 signal in the same cells, the resulting fluorescence signal of 16% represents extracellular α814-827 labeling. Thus, we estimate that 16% of AE1 is in a conformation with extracellular-localized 812-830 region.

From the fluorescence intensities observed in non-permeabilized HEK293 cells, we conclude that the AE1 814-827 amino acid region is accessible to antibodies in the extracellular environment. HEK293 cells processed for immunofluorescence are fixed using paraformaldehyde, resulting in immobilized proteins that cannot reorient. Thus, fixed cells will represent protein conformation at a single time point. From the magnitude of the increase of signal in permeabilized cells, we propose that the population of AE1 molecules with extracellular 812-830 at a given moment is approximately 16% of the total AE1. Thus, the distribution of extracellular and intracellular localization of AE1 812-830 region at a given time point can be assessed by immunofluorescence in fixed cells, and approximately 16% of the AE1 molecules are in the conformation with extracellular 812-830 region.

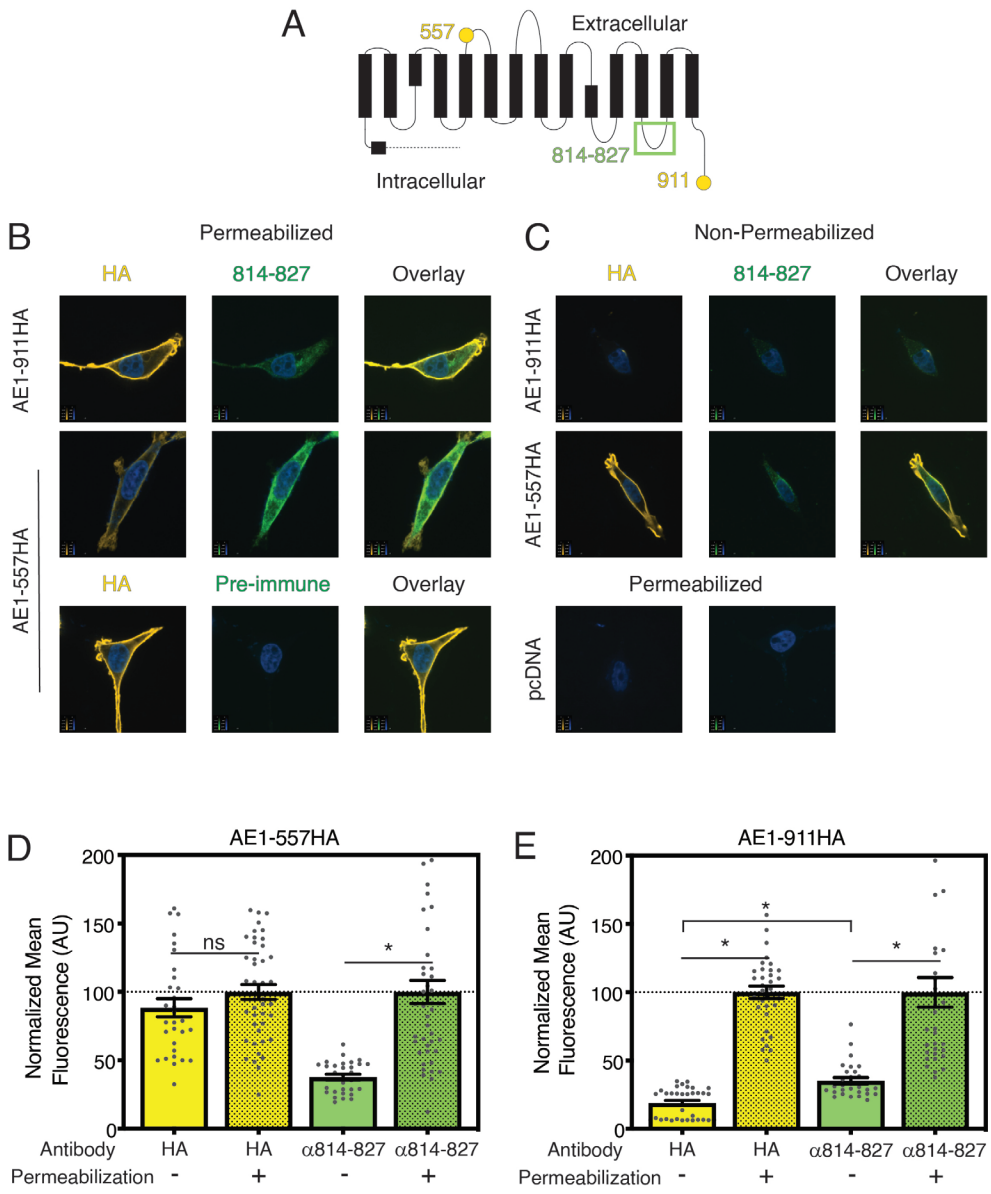

Figure 4.7 Localization of amino acid 814-827 region to extracellular surface by immunofluorescence. HEK293 cells were transfected with cDNA encoding AE1 with a C-terminal HA epitope tag (AE1-911HA), or with an HA tag in the third extracellular loop following amino acid 557 (AE1-557HA). Cells were either permeabilized (+) or non-permeabilized (-). Cells were incubated with anti-HA antibody (HA, yellow), and α814-827 antibody (814-827, green) or pre-immune serum (Pre-immune, green). Cells were processed for immunofluorescence and images were collected by confocal microscopy. Nuclei were stained with DAPI (blue). A) Simplified topology diagram of AE1, based on crystal structure 4YZF. Locations of external (557)

and internal (911) introduced HA tags shown in yellow. Residues 814-827 in green. B) Immunofluorescence of permeabilized HEK293 cells expressing wild-type AE1 with an intracellular hemagglutinin tag (AE1-911HA, top row) or extracellular hemagglutinin tag (AE1-557HA, middle and bottom rows). AE1 was co-labeled using αHA with anti-mouse Cy3 (yellow), and either α814-827 or rabbit pre-immune serum, with anti-rabbit Alexa Fluor 488 (green). Overlay represents merged image from all three channels. C) Cells were processed and labeled as in B, but in non-permeabilized conditions. pcDNA-transfected cells were permeabilized and probed with αHA and α814-827 for background correction. D) Quantification of confocal microscopy images of cells expressing AE1-557HA, extracellular HA tag. Mean fluorescence intensities of a cell population were pooled, and permeabilized conditions mean was set to 100% for both Cy3 (αHA) and Alexa Fluor 488 (α814-827). Normalized mean fluorescence intensities indicated in boxes. Data represent mean ± SEM of 30-50 cells for each condition, from two biological repetitions. E) Quantification of confocal microscopy images of cells expressing AE1-911HA, intracellular HA tag. Data was quantified as in D. Asterisks indicate significant difference ($P < 0.05$), by one-way ANOVA.

4.2.6 Accessibility of 812-830 Region in Red Blood Cells

To study the localization of the AE1 812-830 region in RBCs, we performed confocal immunofluorescence. As an intracellular epitope control, we used a previously-characterized mouse monoclonal antibody recognizing the AE1 intracellular C-terminus (IVF12) (408). As an extracellular control, we used a monoclonal antibody raised against amino acids 1-85 of human glycophorin C (αGPC), which has extracellular N-terminus (504).

Dual immunofluorescence staining assessed the localization of AE1 812-830 in RBCs (505) which were not age-fractionated. RBCs were labeled with α814-827, in combination with two secondary antibodies coupled to spectrally distinct fluorescent dyes: Alexa Fluor 488 Donkey Anti-Rabbit IgG (AF488), and Alexa Fluor 594 Chicken anti-Rabbit IgG (AF594). First, non-permeabilized RBCs were labeled with α814-827 and AF488. RBCs were then fixed, permeabilized, and labeled with α814-827 and AF594. Since the RBC membrane is impermeant to IgG, any labeling in non-permeabilized conditions arises from extracellular-localized antigen, and any labeling arising after fixation and permeabilization occurs because the antigen is intracellular. Thus, the staining from the two fluorophores represents two possible localizations of AE1 812-830.

Extracellular GPC and intracellular AE1 C-terminal control epitopes were assessed similarly, using spectrally distinct Cy3 Donkey Anti-Mouse IgG (Cy3) and Alexa Fluor 647 Chicken anti-Mouse IgG (AF647). Intact cells were labeled with αGPC or IVF12, and Cy3. Cells were fixed, permeabilized, and labeled with αGPC or IVF12, and AF647. As neither GPC nor AE1 C-terminus undergo posttranslational reorientation, we expect to only see immunofluorescence in non-permeabilized and permeabilized conditions, respectively. In order to quantify cell surface exposure, immunofluorescence in non-permeabilized conditions was normalized to

immunofluorescence in permeabilized conditions, for each fluorophore-conjugated secondary antibody.

Extracellular N-terminal GPC was detected by Cy3 immunofluorescence, indicating that surface-exposed antigens were successfully labeled in non-permeabilized conditions (Fig. 4.8A). No additional fluorescence was detected after permeabilization, consistent with GPC's exclusively extracellular N-terminal epitope. Thus, extracellular antigens are visualized by immunofluorescence in non-permeabilized conditions. Conversely, when RBCs were labeled with IVF12 antibody detecting AE1 C-terminus, fluorescence was only detected following permeabilization (Fig. 4.8B). Thus, intracellular antigens are only labeled under permeabilized conditions, which indicates that IgG is unable to access intracellular RBC antigens in non-permeabilized conditions. Cells were also prepared with fluorescent secondary antibodies used in the reverse order to ensure there was no signal bleed-through between the two fluorescent channels. Bleed-through could result in emission from one fluorophore being detected in the channel for the second fluorophore. This could inaccurately indicate extracellular antigen localization. Normalized immunofluorescent signal in non-permeabilized cells was similar for both secondary antibodies assessed (10% ± 0.00 for Cy5, 16% ± 1.53 for Cy3) (Fig. 4.8B), indicating no significant bleed-through. This represents background immunofluorescence in non-permeabilized conditions for an intracellular epitope.

Similar to IVF12 staining, immunofluorescence of RBCs probed with α814-827 was detected exclusively in permeabilized conditions, with low background fluorescence in non-permeabilized cells (16% ± 0.02 for Cy3, 13% ± 0.00 for AF488) (Fig. 4.8C). There was no statistically significant difference in the normalized fluorescence of non-permeabilized cells labeled with IVF12 cells and α814-827, indicating intracellular accessibility of both epitopes.

Immunofluorescent signal arising from both IVF12 and α814-827 was diffuse throughout permeabilized RBCs, consistent with the high abundance of AE1 target protein detected by each antibody.

There was no significant difference between α814-827 and IVF12 immunofluorescence in non-permeabilized cells. Since non-permeabilized IVF12 immunofluorescence represents background labeling of intracellular antigens, this indicates that the 812-830 region is not accessible to extracellular antibody in RBCs. This supports the intracellular localization of the 812-830 region seen in the crystal structure. We conclude that the AE1 812-830 region is intracellularly localized in RBCs, and that the crystal structure represents a physiologically relevant state of AE1 in its native environment.

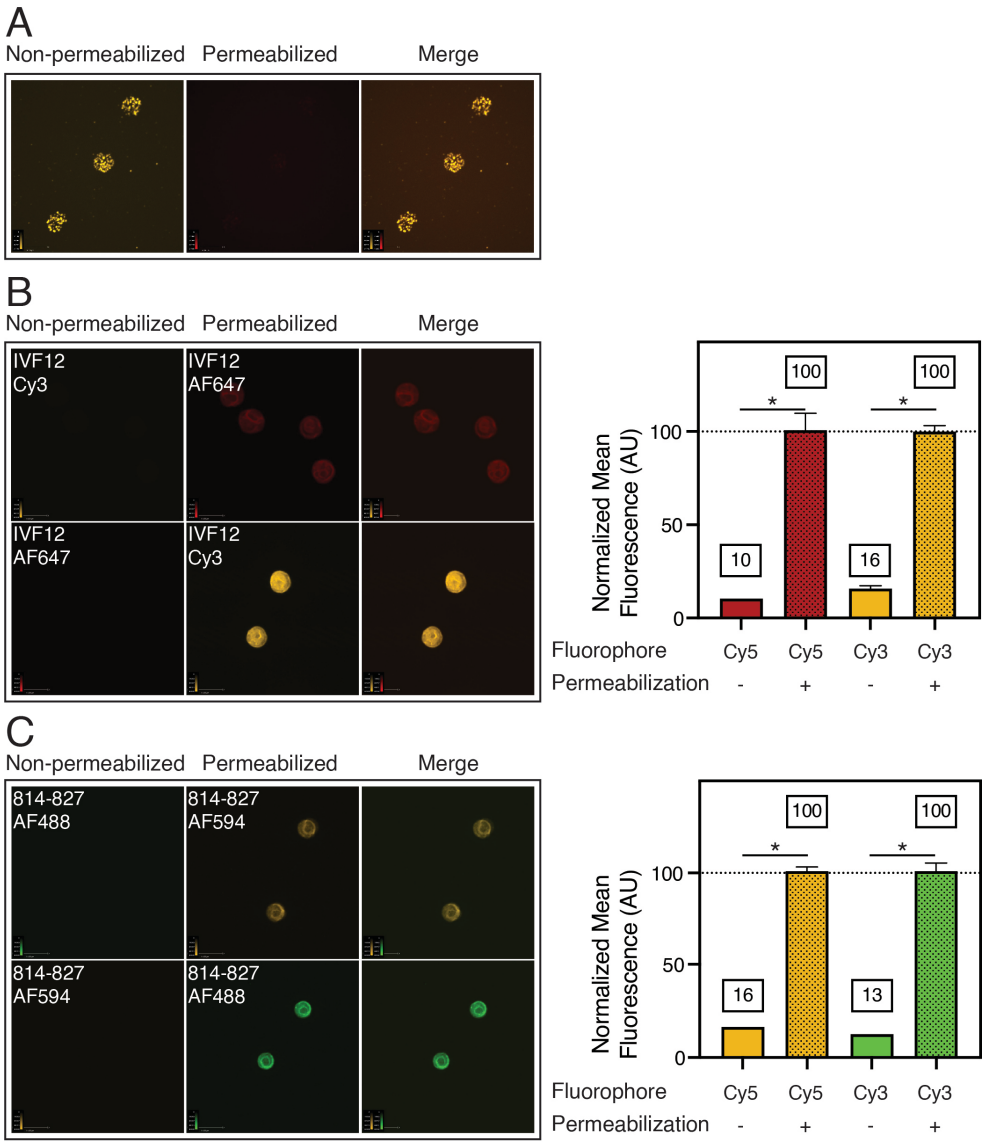

Figure 4.8 Immunofluorescence of AE1 in erythrocytes, using α814-827 antibody. Human red blood cells were probed with antibodies raised against: A) glycophorin C N-terminus (αGPC), B) AE1 C-terminus (IVF12), and C) AE1 residues 814-827 (α814-827). Localization was assessed by confocal immunofluorescence in non-permeabilized (-) and permeabilized (+) conditions. Surface-exposed antigens were visualized by probing intact RBCs (non-permeabilized, leftmost column) with A) αGPC and Cy3 Donkey Anti-Mouse IgG (Cy3), B) IVF12 and Cy3 Donkey Anti-Mouse IgG (Cy3), or C) α814-827 and Alexa Fluor 488 Donkey Anti-Rabbit IgG (AF488). To visualize intracellular localization of these antigens in the same cells, labeled RBCs were fixed, permeabilized (permeabilized, middle column), and incubated with A) αGPC and Alexa Fluor 647

Chicken anti-Mouse IgG (AF647), B) IVF12 and Alexa Fluor 647 Chicken anti-Mouse IgG (AF647), or C) α814-827 and Alexa Fluor 594 Chicken anti-Rabbit IgG (AF594). RBCs probed with IVF12 and α814-827 were also assessed with fluorophore-conjugated secondary antibodies detecting surface and internal antigens reversed (B, lower; C, lower). Merged channels shown at right column. Mean fluorescence intensities were pooled, and permeabilized condition mean values were set to 100% for Cy5 and Cy3 (IVF12), and Alexa Fluor 488 and Cy3 (α814-827). Normalized mean fluorescence intensities indicated in boxes. Data represent mean ± SEM of 35-75 cells for each condition, from two biological repetitions. Quantification of confocal microscopy images shown at right.

4.2.7 Senescent Cell IgG Recognizes a Conformational Epitope

Aged red cell density increases towards the end of their lifetime, so the oldest RBCs can be isolated using density gradient ultracentrifugation (447,469,470). These RBCs are highly opsonized, and associated IgG can be eluted from RBCs (239,482,486,506). We eluted IgG from membranes of aged RBCs. We assessed the antibody preparation on immunoblots. The presence of IgG auto-antibody was confirmed by probing eluates on non-reducing immunoblots with HRP-conjugated goat anti-human IgG (Fig. 4.9A). The antigenic band is consistent with the mass of two IgG heavy chains and two lights chains (507).

IgG auto-antibody (ScIgG) at a range of concentrations was unable to detect denatured AE1 heterologously expressed in HEK293 cells on immunoblots (Fig. 4.9B). ScIgG was also unable to specifically detect AE1 on immunoblots of red cell membrane proteins (Fig. 4.9C). ScIgG was, however, able to immunoprecipitate AE1-911HA expressed in HEK293 cells, albeit at very low amounts (Fig. 4.9D). The inability of ScIgG to detect AE1 on immunoblots, combined with its ability to immunoprecipitate AE1, indicates that ScIgG recognizes a conformational antigen (240,498). The ability of ScIgG to precipitate AE1 from HEK293 cell lysates suggests that heterologously expressed AE1 can adopt the conformation recognized by ScIgG, the conformation necessary for signalling red cell senescence. We conclude that folded AE1 is required for ScIgG binding, and that heterologously expressed AE1 can assume the three-dimensional conformation recognized by ScIgG present on aged red blood cells. This supports the use of heterologous expression systems to probe the molecular mechanisms of RBC senescence and indicates that unique features of RBCs and biochemical damage arising during RBC lifespan are not required for ScIgG to bind AE1.

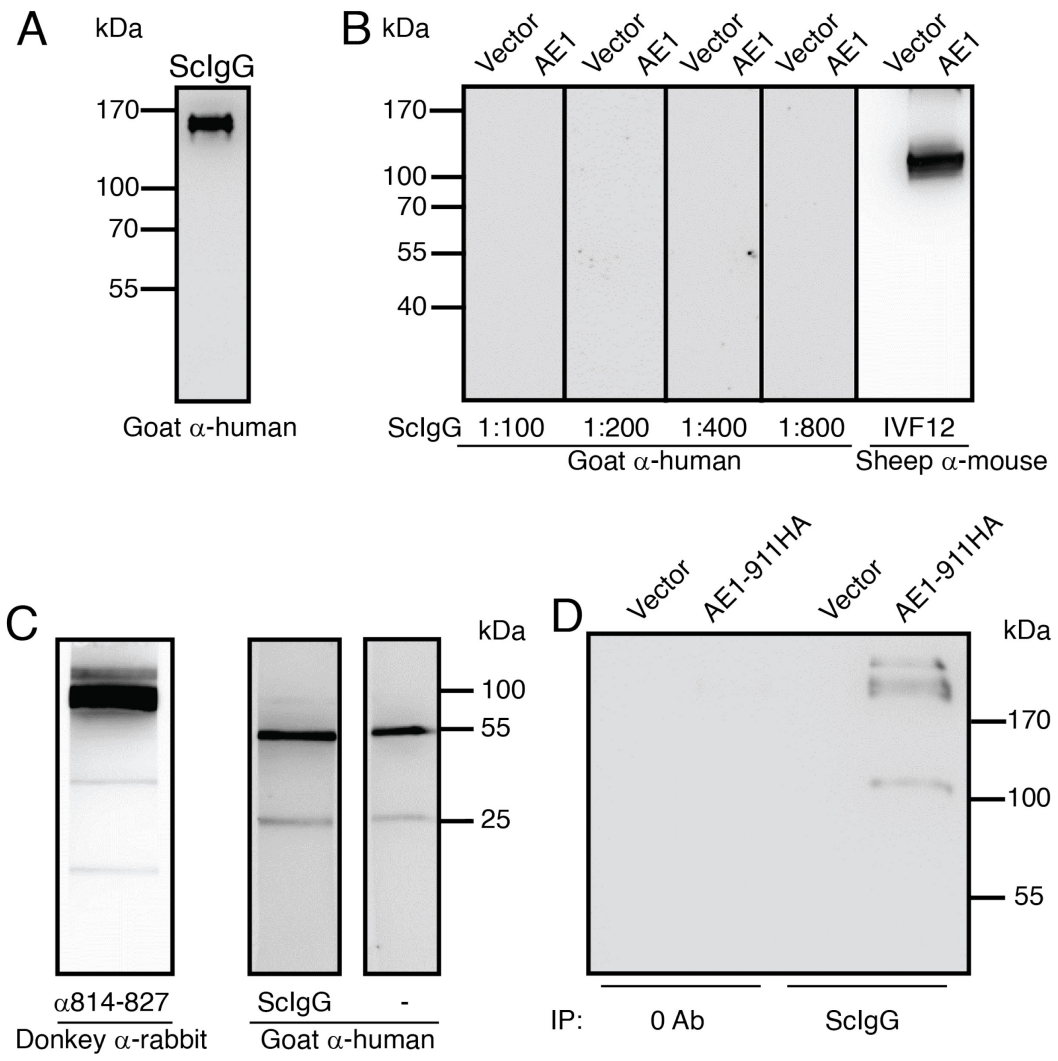

Figure 4.9 Characterization of auto-antibody IgG on immunoblots. A) Eluate from cell membranes of aged RBCs was probed on immunoblots following non-reducing SDS-PAGE, using HRP-conjugated Goat anti-Human IgG to detect human IgG auto-antibody. B) HEK293 cell lysates transfected with vector or cDNA encoding AE1 were processed for immunoblots. Immunoblots were probed with ScIgG at a range of dilutions, or anti-AE1 C-terminus antibody (IVF12). Each lane represents 40 µg cell lysate. C) Red blood cells were lysed by hypotonic lysis, and membranes were processed for immunoblots. Immunoblot strips were probed with either α814-827, ScIgG (1:100), or no primary antibody (-). Following washing, strips were probed with HRP-conjugated Donkey α-rabbit (α814-827 strip), or HRP-conjugated Goat α-human (ScIgG and - strips). Each strip contains 100 µg red cell membrane protein. D) Protein G-coupled magnetic

resin was incubated with senescent cell IgG eluted from red cell membranes (ScIgG) or buffer containing no antibody as a control (0 Ab). Cell lysates from HEK293 cells transfected with vector or cDNA encoding AE1-911HA were incubated with magnetic resin alone (0 Ab), or with magnetic resin coupled with senescent cell IgG (ScIgG). Resin was washed, and bound proteins were processed for immunoblotting. Immunoblots were probed with αHA antibody for detection of immunoprecipitated proteins. Senescent cell IgG prepared by Dr. Evgenia Bloch (University of Toronto).

4.2.8 Structural Modelling

To visualize a potential structure representing AE1 812-830 in an outward-accessible conformation, the AE1 membrane domain crystal structure (PBD ID 4YZF) was manually adjusted using PyMOL (1,203). Manual adjustment was limited to residues C-terminal to G800, which initiates the extra-membraneous region following TM12. Residues were reoriented to reflect extracellular, intracellular, or membraneous localization determined by accessibility to LYIA and biotin maleimide (488,496). Lateral flexibility of TMs 13 and 14 was guided by molecular dynamics simulations (508) and cryo-EM density maps (509) (Fig. 4.10). To reorient AE1 812-830 region residues, pivot points were chosen at the C-terminus of TM12 (G800), and Q840 in TM13. The polar sidechain of Q840 has the potential to snorkel towards cytoplasmic phospholipid head groups to stabilize TMs13-14 and is immediately C-terminal to a progression of residues in TM13 with helical free energy penalty (836-FTGI-839). G800 at the C-terminus of TM12 initiates a region of flexible extended structure, which lacks the structured peptide backbone hydrogen bonding patterns of alpha helices or beta sheets, and thus has greater conformational flexibility. Choosing these pivot points also kept residues G800-L811 within the acyl chain region of the lipid bilayer in State 2. This is consistent with inaccessibility of these residues to aqueous labeling compounds (496), and the low aqueous solubility of peptides corresponding to this region (488,496,510). In State 2, residues most accessible to extracellular labeling compounds are located adjacent to the Extracellular Senescent Cell Epitope residues 538-554 (ExScEp) on TM5 (Fig. 4.10). Viewed in a space-filling representation, State 2 places the AE1 812-830 region adjacent to extracellular 538-554, where they could form a discontinuous binding site for senescence cell IgG.

The AE1 membrane domain is arranged in a 7 + 7 inverted repeat fold (1). This fold is also seen in experimentally determined structures of transporters UraA (194), SLC26Dg (195), UapA

(196), AtBor1 (193), Bor1p (192), NBCe1 (8), SLC26A9 (189), and BicA (188). To determine if the alternative conformations of the AE1 812-830 region could be a conserved feature of the 7 + 7 protein fold, we assessed the conservation of protein structure in this region. We aligned the AE1 crystal structure with the membrane domain of each protein with an experimentally determined 7 + 7 inverted repeat structure, using PyMOL (Fig. 4.11A). The C-terminal structure of each protein was compared to that of AE1 by visualizing only TM12-14. The degree of sequence conservation between the proteins correlated with their structural similarities. That is, proteins with high sequence identity to AE1 shared similar three-dimensional protein structure at the region corresponding to the AE1 812-830 region. Proteins with sequence identity below 26% have a much shorter loop corresponding to AE1 812-830 than proteins with higher sequence identity (AE1: 30 amino acid residues, BicA: 4, SLC26dg: 11, UapA: 5, UraA: 6, SLC26A9: 3). Although the size of this region varied drastically between proteins, the alignment of the three C-terminal TMs was consistent. The lack of structural conservation of the AE1 812-830 region with other 7 + 7 proteins indicates that conformational changes of this region are likely not a shared characteristic of this membrane protein fold. Indeed, the corresponding region in other proteins is much shorter in length (AE1 30 amino acid residues, other proteins 16 residues on average).

We next used analysis of sequence conservation to examine whether the ability to reorient the region between TM12 and 13 was a conserved feature of the 7 + 7 inverted repeat fold proteins. Multiple sequence alignment was performed using Clustal Omega (160,511) of the three proteins with the highest sequence identity to AE1, which shared the most structural similarity to the AE1 812-830 region (NBCe1, AtBor1, Bor1p) (8,192,193) (Fig. 4.11B). We further analyzed the sequence identity at the region corresponding to AE1 812-830 compared to sequence identity through the entire membrane domain, to determine if there was a local increase in conservation,

which could indicate a conserved function. Within the four most structurally similar proteins, the sequence identity at the region corresponding to AE1 812-830 (AE1-NBCe1 = 37%, AE1-AtBor1 = 32%, AE1-Bor1p = 38%) was similar to the sequence identity across the entire membrane domain (AE1-NBCe1 = 45%, AE1-AtBor1 = 28%, AE1-Bor1p = 26%). Thus, the sequence conservation at this location is approximately consistent with conservation throughout the membrane domain, indicating no increased or decreased selection pressure on this region compared to the membrane domain in full. From the structural comparison of 7 + 7 inverted repeat structures, and assessment of sequence identity at the region corresponding to AE1 812-830, we conclude that the reorientation observed in AE1 is not a conserved feature of 7 + 7 inverted repeat proteins.

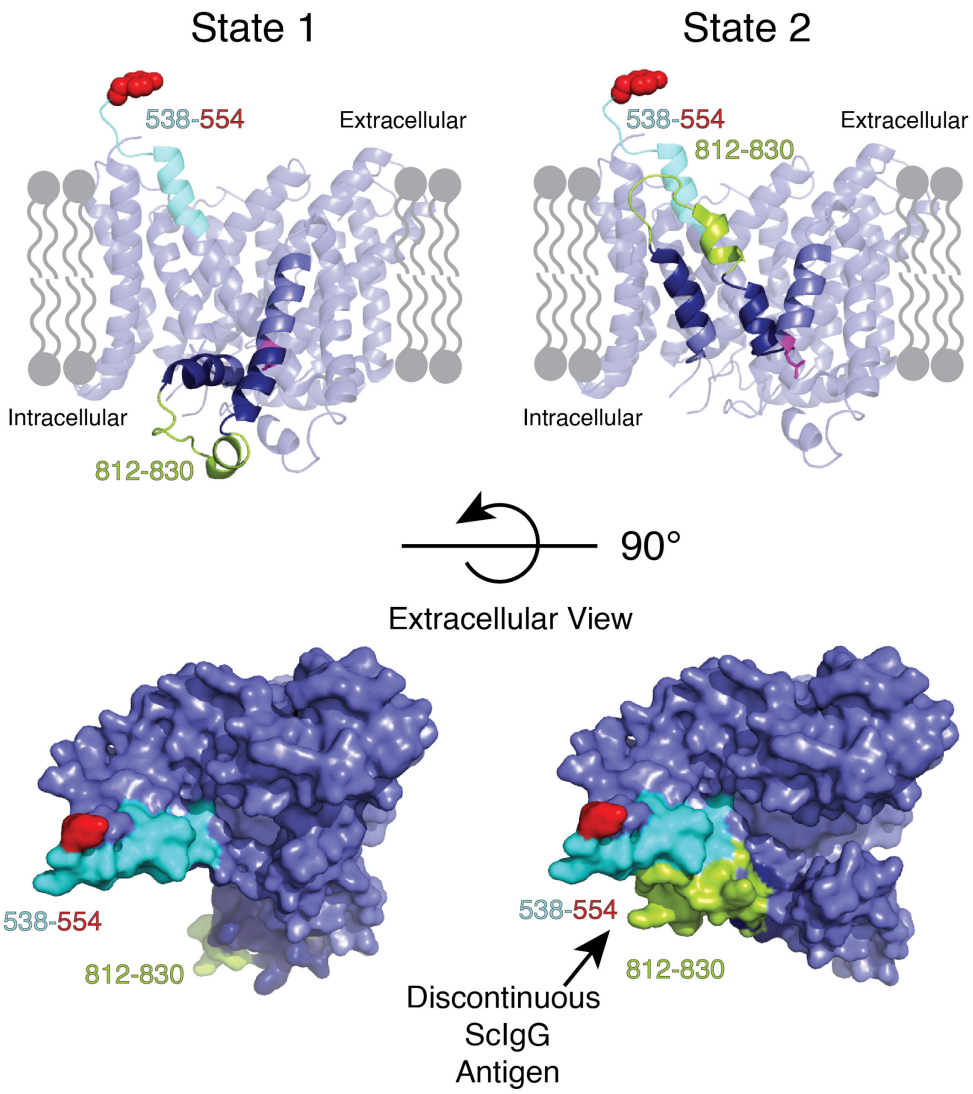

Figure 4.10 Model for AE1 alternative conformations. AE1 represented as in the crystal structure (State 1, left) (1), and alternate conformation with extracellular accessibility of the 812-830 region (State 2, right). Structures shown from side view (upper) and extracellular view (lower). Membrane lipids shown in grey. Residues 812-830 (InScEp) shown in lime, 538-553 (ExScEp) in teal, Extracellular residue 554 as space-filling in red. Q840 shown in pink. Residues 800-814 and 831-839 in dark blue.

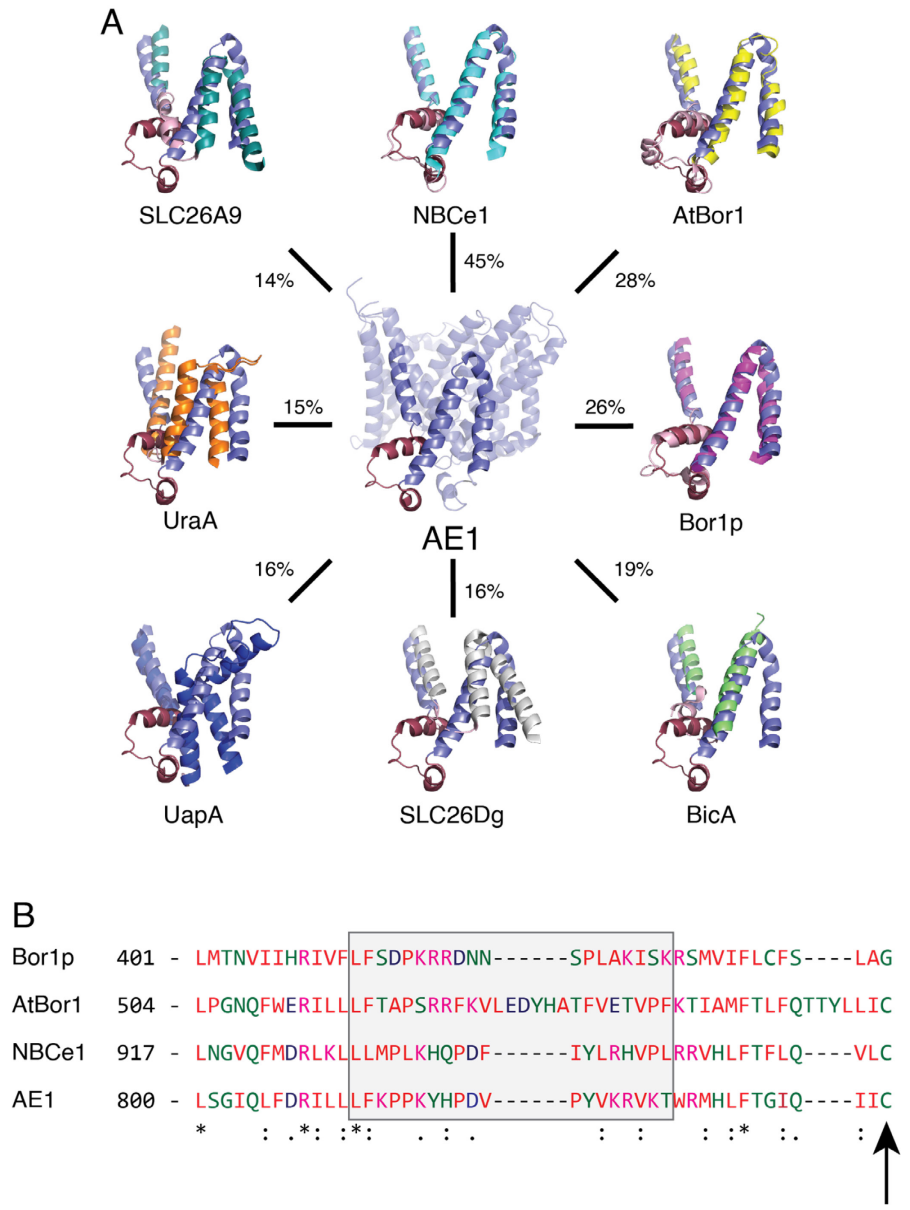

Figure 4.11 Structural similarities of 7 + 7 inverted repeat COOH-terminal helices. A) AE1 membrane domain (center) was aligned with membrane domains of other 7 + 7 inverted repeat proteins in PyMOL. TM12-14 of each structural alignment is shown, with AE1 transmembrane helices in slate. The AE1 region connecting TM12 and TM13 in raspberry, with corresponding region of 7 + 7 inverted repeat protein in light pink. Percent sequence identity to human AE1 membrane domain indicated beside black connecting line. PDB IDs used, in order of decreasing percent sequence identity to AE1: 4YZF (AE1), 6CAA, 5L25, 5SV9, 6KI1, 5IOF, 5I6C, 3QE7, 6RTC. B) Multiple sequence alignment of AE1 and top three most similar structures. Region corresponding to antigenic residues 812-830 in shaded grey box. C843 palmitoylation site indicated by black arrow. Amino acid numbering for each protein indicated at left. Amino acids

are color according to their properties: polar (green), nonpolar (red), acidic (pink), and basic (blue). Bottom row indicates conservation: fully conserved (*), strongly similar properties (:), weakly similar properties (.), or no similarity (no symbol).

4.3 Discussion

Experiments described here reveal a conformational state of AE1 distinct from the published crystal structure (1). While the static crystal structure represents a predominant AE1 conformation, reorientation of AE1 senescent cell epitope residues 812-830 (InScEp) creates an alternate, transient conformation. This transient extracellular conformation can be trapped by molecular probes including IgG. Our initial goal in this study was to reconcile apparently contradictory reports on localization of the AE1 812-830 region, spanning biochemical, physiological and pathological studies of AE1 and red blood cells, and bridge the knowledge gap that exists in the molecular mechanism of RBC senescence. This study provides evidence for conformational polymorphism of AE1 as the "clock" at the centre of the mechanism that detects red blood cell age.

We established that residues within the AE1 812-830 region can access the intracellular and extracellular environments. Extracellular reorientation of this region is not coupled to movements required for anion exchange and is unaffected by removal of the cytoplasmic domain or presence of stilbene disulfonate. Our data suggest that the predominant state has the 812-830 region intracellular. Thus, at a fixed timepoint (as represented by data from fixed cells), intracellular localization of the AE1 812-830 region predominates, while extended time frames (as examined by LYIA labeling) allow for conformational rearrangement and apparent higher extracellular accessibility. Auto-antibody IgG from red blood cells recognizes a conformational AE1 antigen that heterologously-expressed protein can adopt. We propose that extracellular access of residues within the AE1 InScEp creates a transient senescence antigen, and thus act as a cryptic epitope to signal RBC senescence.

4.3.1 Residues in the AE1 812-830 Region Demonstrate Extracellular and Intracellular Localization

When expressed in a heterologous system, the AE1 812-830 region can access both the intracellular and extracellular environments. The AE1 812-830 region demonstrates extensive extracellular localization in live HEK293 cells. Residues in the AE1 812-830 region and residue Y555C in extracellular loop 3 display indistinguishable accessibility to extracellular LYIA (Fig. 4.2). The AE1 812-830 region is as accessible to IgG as extracellular loop 3 of SLC4A11, which may extend up to 32 Å from the plasma membrane (369). The unique behaviour of the 812-830 region, forming most of intracellular loop 6 in the AE1 crystal structure, is shown by contrast to intracellular loop 1 and 2. Introduced Cys mutants in these loops had accessibility to LYIA indistinguishable to Cys201, which is definitively in the cytoplasmic domain. By contrast, the 812-830 region had LYIA accessibility that was the same as residues definitively in the extracellular milieu.

Conversely, fixed HEK293 cells manifest mixed topology of the AE1 812-830 region, with intracellular localization representing the majority (84% intracellular localization). Thus, while intracellular localization of AE1 812-830 region is predominant in a static AE1 ensemble (fixed cell data), over the time scale of LYIA labeling and antibody binding (minutes) the 812-830 region has apparent extracellular accessibility indistinguishable from extracellular surface loops. Residues within the N-terminal cytoplasmic domain, C-terminal tail and intracellular loops 1 and 2 do not share this time-dependent variation in accessibility (Fig. 4.2). The AE1 812-830 region must therefore undergo a change in topology to bind membrane-impermeant LYIA or IgG. The bulk of coupled LYIA or bound IgG will prohibit reorientation of the 812-830 region back to the cytoplasm, accumulating AE1 trapped in this outward orientation. Ultimately, the 812-830 region

can be labeled by LYIA to the same extent as extracellular control Y555C. The use of heterologously expressed AE1 demonstrates that this transient reorientation is an intrinsic ability of the AE1 molecule. Further, since AE1 and introduced Cys mutants facilitate anion exchange (488,496) these proteins maintain a native structure.

The kinetics of the 812-830 region reorientation remain to be quantified. As the halftime of LYIA binding was unable to differentiate between K817C, V822C, K826C and Y555C, we conclude that the kinetics of AE1 812-830 region reorientation are more rapid than the rate-limiting kinetics of LYIA labeling.

The persistence of 812-830 region extracellular accessibility in an anion transport-deficient mutant indicates that the structural rearrangements required for anion transport are not necessary for extracellular orientation of AE1 812-830 region. AE1 operates by an alternating access mode of transport, with the substrate translocation pathway at the cleft between the core and gate domains (Fig. 1.8) (197). Since the 812-830 region lies at the periphery of the gate domain, reorientation occurs distant from the substrate translocation pathway (Fig. 4.10) (1). AE1 may operate by an elevator-like mechanism, wherein the gate domain remains relatively stable in the lipid membrane while movements of the core domain relative to the bilayer plane displace the substrate binding site (193,198,202). Crosslinking the gate domain does not affect anion exchange, suggesting that transport movements of the core domain are independent from gate domain mobility (512). Thus, anion exchange associated movements of the core domain would not be expected to affect the reorientation of the 812-830 region in the stable gate domain, and vice versa. A hallmark of the elevator transport mechanism is a high level of structural asymmetry between domains, paralleled by a high level of functional specialization of each domain (198). Thus,

independent movements of the substrate-binding core domain and the 812-830 region in the gate domain are consistent with an elevator mechanism of alternating access transport (202).

The RBC pericellular matrix, the glycocalyx, may explain accessibility differences of the AE1 812-830 region in RBCs and HEK293 cells. Antibody epitopes are typically five to six residues, at minimum (513,514). Senescent cell IgG isolated from RBCs binds both AE1 regions 538-554 and 812-830 and recognizes a conformational epitope (240,490,498,515). This suggests that senescent cell IgG binds both antigenic regions as a discontinuous antigen (Fig. 4.10). As such, ScIgG binding would only require a fraction of residues from the 812-830 region to be accessible through the glycocalyx, while α814-827 binding requires five to six accessible residues. This may be why α814-827 did not bind intact RBCs but did bind the region when AE1 was expressed in HEK293 cells.

4.3.2 Crystallization Conditions do not Abolish 812-830 Extracellular Accessibility

AE1 residues 812–830 are intracellularly localized in the crystal structure (1). Reduction of protein conformational flexibility and heterogeneity is often necessary to obtain high resolution X-ray crystal structures of membrane transport proteins (10). We therefore considered the possibility that AE1 crystallization conditions altered AE1 conformation, or biased AE1 toward a conformation with amino acids 812-830 intracellular. We assessed the ability of the conditions used for AE1 crystallization to abolish the extracellular accessibility of the AE1 812-830 region.

The crystal structure of AE1 consists of the isolated membrane domain with bound stilbene disulfonate, H_2DIDS (1). Data supporting extracellular localization of the AE1 812-830 region persisted in the absence of the cytoplasmic domain and following H_2DIDS pre-treatment. The persistence of extracellular localization in the presence of H_2DIDS indicates that steric bulk in the

cleft between AE1 core and gate domains does not impede extracellular orientation of the 812-830 region.

Although native AE1 was deglycosylated for crystallization, glycosylation does not affect stilbene disulfonate binding or anion transport of heterologously expressed and native red cell AE1 (516-518). Therefore, any structural changes associated with removal of oligosaccharide are likely minor. As such, we did not investigate the effect of N-glycosylation on AE1 812-830 localization.

AE1 was crystallized with an IgG antigen-binding (Fab) fragment recognizing a conformational epitope in the core domain (1). We were interested to assess the effect of the Fab fragment on intracellular localization of the 812-830 region in the crystal structure. In spite of repeated attempts to contact the authors, we were unable to obtain this antibody. We therefore could not assess the effect of this antibody on AE1 conformational rearrangements. Preliminary reports of AE1 crystals obtained without Fab fragments suggest that Fab has little influence on AE1 conformation (519).

Binding of α814-827 antibody to AE1 in fixed HEK293 cells indicated predominant intracellular localization of 812-830, consistent with the crystal structure. This suggests that intracellular localization of the 812-830 region predominates in the absence of the conditions used to crystallize AE1. That is, it is unlikely that the conformation of active, RBC membrane-embedded AE1 was altered by the conditions used to stabilize AE1 for crystallization.

4.3.3 Dynamics of AE1 Membrane Domain C-terminus

The AE1 812-830 region contains charged residues K814, K817, D821, K826, R827, and K829 (Fig. 4.11B). Intracellular localization of this positively charged region is energetically favored, based on the RBC membrane potential of approximately -10 mV (520-523). Further, interactions of charged residues K817 and K829 with the head groups of phosphatidylserine in the inner leaflet

of the bilayer have been identified in molecular dynamics simulations (524). Reorientation of the AE1 812-830 region from intracellular to extracellular orientation would require charged residues to partition into the nonpolar lipid bilayer. Notably, the predominant charged amino acid species of the AE1 812-830 region is lysine. Molecular dynamics simulations suggest that the partitioning energetics of amphiphilic lysine is the most favorable (least unfavorable) among charged residues, due to its amphipathic nature (525,526). Moreover, the energetics of partitioning multiple charges through a membrane are not additive, so the energetics of partitioning multiple positively charged residues are likely similar to the partitioning of just one (527). The AE1 812-830 region also contains proline, tyrosine, valine, and histidine residues. These residues likely contribute to the energetics of partitioning to a lesser degree than the positively charged residues (526).

The last two transmembrane helices in AE1, TM13 and 14, are directly C-terminal to the AE1 812-830 region. Reorientation of the 812-830 region could be accompanied by structural rearrangements of TM13-14. Consistent with this, two-dimensional crystal projection maps of AE1MD revealed transmembrane density with conformational flexibility relative to the main domains (509). TM13 and 14 are the likely candidates for this density due to their location relative to the dimeric interface. Lateral flexibility of TM13 and 14 would loosen spatial restraints on AE1 812-830 region movements.

Established palmitoylation of AE1 C843 in RBCs also indicates flexibility of the C-terminal two helices (186,528). The state represented by the crystal structure places C843 in TM13, in the middle of the lipid membrane. Conformational reorientation of the 812-830 region may relocate C843 closer to the cytoplasmic interface, where it would be accessible to non-enzymatic acylation (186). This is consistent with the significant deformation of TMs 13-14 revealed by atomistic membrane dynamics simulations (508). Thus, substantial displacement of the C-terminal

region of AE1MD can occur, which would support dynamic movements of the 812-830 region (Fig. 4.10).

4.3.4 Significance to the Red Cell Molecular Clock

Since antigenic AE1 is present in all RBCs regardless of age, ScIgG antigen exposure must be limited in order to prevent clearance of pre-senescent RBCs. The AE1 812-830 region has consistently been identified as an antigen for ScIgG auto-antibody (490,498,515) and, as shown here, manifests both intracellular and extracellular localization (Fig. 4.2-4.8). Thus, it is an ideal candidate for the proposed cryptic component of the ScIgG antigen, as a region with demonstrated antigenicity, but limited cell surface accessibility (240). α814-827 trapping extracellular AE1 InScEp may be analogous to opsonization of RBCs with AE1-directed ScIgG.

ScIgG auto-antibody recognizes a conformational AE1 antigen (240,486). Supporting this, ScIgG isolated from dense RBCs immunoprecipitated folded AE1, but was unable to detect denatured protein on immunoblots (Fig. 4.9). Modelling the extracellular orientation of the AE1 812-830 region places it adjacent to extracellular residues 538-554, which also display ScIgG reactivity (Fig. 4.10) (485). With the two antigenic regions extracellular and in close proximity, they are positioned to create a discontinuous, conformational ScIgG binding site. The transient nature of the AE1 812-830 extracellular orientation, in conjunction with the RBC glycocalyx, ensures that the antigen has very limited accessibility to ScIgG. This restricts opsonization and maintains functional red cells in circulation. In this way, extracellularly localized AE1 812-830 region (InScEp) together with AE1 538-554 (ExScEp) creates a conformational senescent cell epitope with limited surface accessibility.

ScIgG immunoprecipitated heterologously expressed AE1 without the influence of age-related biochemical damage accumulated by aging RBCs. Formation of the senescence antigen is

therefore an intrinsic property of the AE1 molecule, as is reorientation of the InScEp. Thus, damage accumulated during RBC aging is unnecessary to create antigenic ScIgG sites. While aged RBC accrue biochemical damage necessitating their removal, this damage does not catalyze exposure of the senescent cell antigen, and thus does not mediate RBC opsonization.

If the senescence antigen transiently forms throughout the circulating lifetime of RBCs, then the molecular clock determining the lifespan of RBCs is the rate of amino acid 812-830 capture by IgG. The rate of capture is limited by the low titre of circulating ScIgG (240,327), poor antigen accessibility due to the glycocalyx (Fig. 4.8) (529,530), and the limited lifetime of the outward-facing AE1 812-830 conformation (only 16% of AE1 molecules had outward 812-830 orientation in fixed cells). Senescent RBCs are opsonized with relatively low quantities of IgG, a reported 20-200 IgG molecules per cell (239,481,490,506,531). Low ScIgG titre and limited extracellular accessibility of the InScEp is consistent with the low level of opsonization required for clearance of senescent RBC.

The independence of ScIgG antigen formation from age-induced RBC damages is consistent with observations from *in vitro* senescence studies. *In vitro* ScIgG binding is promoted by RBC oxidation and non-oxidative protein clustering (241,242,483,484,506,532-534). As oxidized hemoglobin clusters AE1 through cytoplasmic domain cross-linking (532,535), both *in vitro* aging techniques result in clustered AE1. Clustering AE1 increases the local density of ScIgG antigen, which promotes bivalent IgG binding through avidity (506). *In vitro* aging and phagocytosis assays also use ScIgG at orders of magnitude higher than physiological levels (400-1000 fold higher than physiological concentration) (240,327), further promoting opsonization. Antigen clustering and elevated ScIgG concentration together result in a faster rate of opsonization *in vitro* than *in vivo*. (150-2500 fold faster *in vitro*). This is consistent with RBC lifetime being

determined by the rate of binding of low titre ScIgG to a poorly accessible antigen, rather than by aging-induced antigen formation.

Senescent cell antigen exposure is limited by the occurrence of the AE1 812-830 region reorientation, as well as steric hindrance imparted by the glycocalyx. Removal of the glycocalyx exposes age-related antigens (536) and promotes erythrocyte clearance *in vivo* (537). Notably, phagocytosis of young erythrocytes can be induced following enzymatic removal of the glycocalyx (529,530); the glycocalyx prevents ScIgG binding. Consistent with this, we found that α814-827 antibody bound AE1 in HEK293 cells lacking the glycocalyx but did not bind AE1 in non-permeabilized RBCs. Thus, the glycocalyx plays a considerable role in slowing RBC opsonization by ScIgG (538). This is consistent with erythrocyte lifespan determined by low antigen accessibility, rather than progressive development of an antigen induced by cell damage.

We propose that transient extracellular orientation places AE1 812-830 residues near extracellular 538-554, where the two regions create a discontinuous, temporary epitope for serum autoantibodies. When this reorientation occurs in the presence of circulating ScIgG, which is omnipresent in sera but at low titre (240,327), IgG binding can occur (Fig. 4.12). The glycocalyx further limits the likelihood that ScIgG will access the transient epitope. If no antibody is present, the AE1 812-830 region will revert to intracellular localization, its predominant state. Through the actions of capping by bivalent autoantibodies (472) and intracellular hemoglobin-mediated AE1 clustering, the characteristic clusters comprised of IgG, Band 3, and hemoglobin form on aged cells (242,483,484,506,532). Macrophages recognize senescent red cells to initiate phagocytosis when these clusters exceed a threshold level (539).

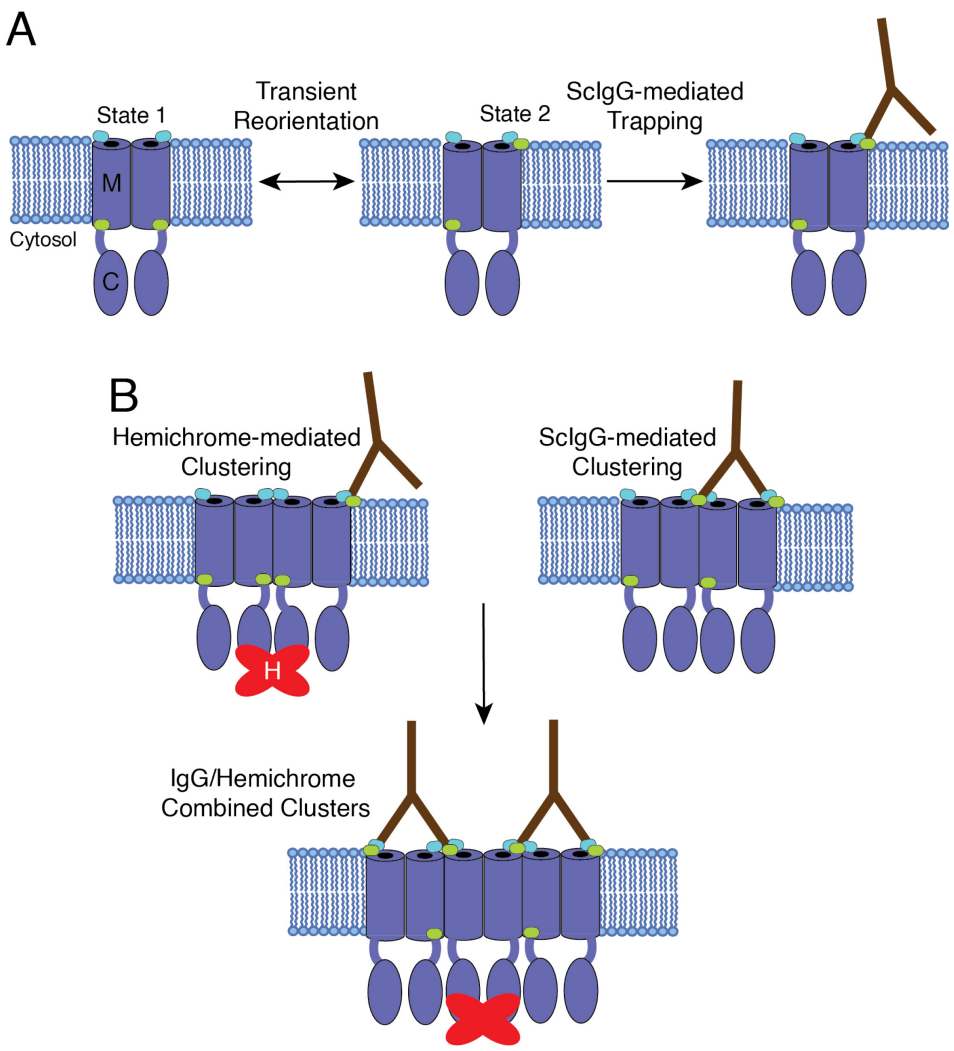

Figure 4.12 Proposed model for the RBC molecular clock. AE1 protein (slate) is a two-domain protein with an integral membrane domain (M) connected by a flexible linker to a cytoplasmic domain (C). The protein associates as dimers. A) The 812–830 (lime oval) region of human AE1 protein normally resides on the cytosolic surface of the protein, but a transient reorientation places this region on the extracellular surface, next to the 538-554 region (teal oval). The conformational change may reverse, or the extracellular conformation may be irreversibly trapped upon interaction with circulating senescence marking auto-antibodies (IgG, brown Y shape). B) Denatured hemoglobin (hemichromes, H) associate with AE1 cytoplasmic domains and induce AE1 clustering. Bivalent IgG can cluster together adjacent AE1 dimers. Large AE1 clusters form from combined IgG and hemichrome-induced clusters, signalling RBC senescence to circulating macrophages.

4.3.5 Conclusion: A Molecular Mechanism for Sensing RBC Age

We found that the AE1 812-830 region is accessible to membrane impermeant LYIA and IgG, to the same extent as exclusively extracellular regions of AE1 and SLC4A11 when expressed in living HEK cells. In RBCs and fixed HEK293 cells, intracellular detection of the AE1 812-830 region predominates. Senescent cell IgG binding is conformation-dependant, and heterologously-expressed AE1 is able to adopt this conformation. Both extracellular reorientation and ScIgG binding are intrinsic properties of the AE1 molecule.

Taken together, we propose a molecular mechanism for RBC senescence signalling, determined by reorientation of AE1 extra-membranous region (Fig. 4.12). During the conformational lifetime of AE1, residues within the InScEp region following TM12 can reorient to access the extracellular environment, perhaps with accommodations by displacement of TM13 and 14. Now located in close proximity to extracellular epitope residues 538–554, the two regions create a transient conformational antigen composed of two discontinuous antigenic sites, close in three-dimensional space but distant in primary sequence. This AE1 conformation can be bound and trapped by low-titer, high affinity senescent cell IgG omnipresent in serum (240). This conformational antigen does not require damage accumulated during RBC aging to form. In the absence of senescent cell IgG, the region returns to the preferred intracellular localization.

Macrophages recognize aged cells by clusters of IgG and complement (241,484). We propose that the molecular clock determining the RBC lifespan is the limited extracellular accessibility of the cryptic senescent cell epitope component, the AE1 812-830 region. Since RBCs lack the protein synthesis machinery necessary to produce new extracellular signals, AE1, the most abundant protein on red cell membranes makes an effective and efficient mechanism to signal clearance of aged red cells.

Chapter 5: Summary and Future Directions

5.1 Summary

The objective of this thesis was to explore issues brought to light by the publication of the AE1 membrane domain crystal structure (1). The SLC4A11 homology model developed here enables better understanding of the molecular mechanisms of disease for blinding corneal dystrophies caused by mutated SLC4A11. This model can be used to predict the molecular phenotypes of novel pathogenic mutations, an essential step towards personalized strategies of treatment for CHED and FECD patients. Examining localization of an AE1 antigen with controversial accessibility, bringing immunological studies from over four decades past together with current techniques, unveiled a molecular mechanism for AE1 conformational polymorphism in determining RBC lifespan.

5.1.1 SLC4A11 Homology Model

Using the AE1 crystal structure as a template, a homology model of SLC4A11 was created. The SLC4A11 homology model was validated by biochemical assessment of SLC4A11 mutants designed to probe the reliability of the three-dimensional model. The SLC4A11 homology model was further used to categorize 45 point mutants that cause blinding corneal dystrophies CHED and FECD. Of the 45 membrane domain point mutants analyzed, five lie in the catalytic pathway, 30 are at regions of close transmembrane helix contact, three lie in the dimeric interface, and seven are in extracellular or cytoplasmic loops. If SLC4A11 is used as a representative disease-causing membrane protein, 73% of disease mutations affect protein folding, and 27% directly affect solute transport function. This is consistent with a genome-wide approximation of misfolding as the primary disease-promoting defect in membrane proteins (5). This is further supported by large-scale mutational analyses of disease-causing membrane proteins, including potassium channels KCNQ1 (72%) (540) and Kv11.1 (88%) (541), and G protein-coupled receptor rhodopsin (71%)

(542). The majority of identified disease-causing mutations in proteins are single amino acid substitutions, making structural modelling of disease variants increasingly prevalent (543).

5.1.2 AE1 in Red Blood Cell Senescence Signalling

The crystal structure guided studies revealed an alternative AE1 conformation. Residues within the AE1 813-830 region undergo dynamic reorientation, which can be trapped in the surface-accessible conformation by membrane-impermeant probes. This reorientation is an innate ability of the AE1 molecule, resulting in extracellular accessibility of a senescent cell antigen to IgG. The senescent cell auto-antibody collected from opsonized RBCs similarly recognizes an intrinsic conformation of AE1. A model of the molecular RBC 'clock' emerged, where reorientation of the intracellular senescent cell epitope creates a discontinuous surface epitope for serum ScIgG. Neither extracellular localization of InScEp, nor ScIgG binding AE1, required biochemical damages accumulated by aging RBCs to occur. Low ScIgG titre, and limited lifetime and restricted surface accessibility of the surface epitope, contribute to the slow rate of IgG trapping and thus opsonization.

In summary, structure-led studies guided by the AE1 membrane domain crystal structure led us to 1. Prepare an SLC4A11 homology model, which can be used to rationalize molecular mechanisms of disease and predict phenotypes of newly discovered mutations, and 2. Elucidate an alternate conformation of AE1, in which cryptic epitope exposure determines opsonization of RBCs and marks their senescence.

5.2 Future Directions

5.2.1 SLC4A11 Structural Studies

While the homology model of SLC4A11 provides a new tool to examine pathogenic mutations, it is an incomplete representation of the molecule. Of the approximately 70 disease-causing

mutations identified in SLC4A11, about one-third are located in the cytoplasmic domain (165). This includes catalytic mutant R125H, which suggests a role of the CD in transport function (363). In addition to the functional role of the CD, considerable structural interdependence of the domains is indicated by the inability to accumulate protein when MD or CD are expressed alone (165). This structural interdependence is not shared by the template protein, AE1 (166,167). While the membrane domain homology model is a valuable tool to assess pathogenicity of mutations, it fails to capture the complexity of full-length SLC4A11. An ideal model would encompass both domains. While a homology model for the SLC4A11 cytoplasmic domain exists (165), how the two domains fit together remains to be determined. Models of full-length AE1 protein encompassing both domains were created on the basis of distance constraints defined by experimental cross-linking (494), which could be applied to the homology models of SLC4A11 MD and CD. Structures of full-length AE1 may guide construction of a complete model of SLC4A11 (169), although low sequence identity between the AE1 and SLC4A11 CDs, particularly at the divergent N-termini (165), may limit the reliability of the resulting model. Experimentally-determined full-length structures of additional SLC4 transporters will likely reveal the intricacies behind variations in functional domain interdependence between SLC4 family members (166-168,179,544).

While a more complete model of SLC4A11 would prove invaluable, an experimentally determined structure would be superior. The emerging method of cryo electron microscopy (cryo-EM) may be amenable to such a task (545). Compared to X-ray crystallography, cryo-EM does not require a crystalline protein array, often requires relatively less protein, does not lack phase information, and can accommodate some degree of protein sample heterogeneity (545-547). However, cryo-EM is not a structural panacea, and a minimum standard of sample stability and

homogeneity is still a considerable bottleneck in structural determination. Cryo-EM was used to determine the structure of full-length SLC4 family member NBCe1, whose cytoplasmic domain is important for transport analogously to SLC4A11 (544), although densities for the NBCe1 cytosolic domain were poorly resolved and excluded from modelling (8).

One of the bottlenecks in membrane protein structure determination is the quantity of material needed. Indeed, prior to 2005 the only membrane proteins with experimentally determined structures were those abundant in their native environments (548-551). Membrane proteins are limited in that they can only accumulate in lipid bilayers, and only accumulate to high densities in membranes similar to their native environments (552). Expressing large amounts of a protein sensitive to mutation such as SLC4A11 requires an expression system as close to its native environment as possible. Successful production of heterologous, functional SLC4A11 in adherent HEK293 cells indicates that HEK293 suspension systems adapted for large-scale production of eukaryotic proteins may yield functional SLC4A11 at quantities sufficient for structural determination by cryo-EM (359,553). Further strategies to maximize the amount of functional protein must also be assessed, including the use of histone deacetylase inhibitors (554-556), different promoters (557), chaperone co-expression (557-559), post-transcriptional regulatory elements (560), and lowered incubation temperatures (561,562) during heterologous protein expression. SLC4A11 is one of the most abundant transporters in native cornea and could alternatively be purified from its native environment for structural studies (563), although purification from a native source would likely be complicated by small tissue mass and the presence of extracellular matrix proteins.

The SLC4A11 homology model can be used to predict the molecular phenotype of *de novo* CHED and FECD mutations by *in silico* assessment, which can then be used in precision (or

personalized) medical treatment. Classifying mutations as causing disease by affecting either protein folding or solute transport function (Fig. 1.11, Fig. 3.5) furthermore indicates whether they are potential candidates for folding correction therapy (363,405,409,438). Reports of *de novo* SLC4A11 point mutants associated with corneal dystrophies will enable further testing and refinement of the homology model, together with *in vitro* testing of the cell surface trafficking and solute transport of these mutants. Elucidating the physiological substrate transported by SLC4A11, and thus the defect relevant to disease, is an essential element in understanding these corneal dystrophies. A streamlined system towards personalized medicine would include identification of the SLC4A11 point mutation, followed by molecular phenotype prediction *in silico*, and subsequent *in vitro* testing of potential therapies, resulting in personalized treatment strategies for corneal dystrophy patients (564).

5.2.2 AE1 in Red Blood Cell Senescence

While studies here have determined a unified model of RBC senescence, the specifics of senescence signalling are still to be determined. The exact structure of the alternate conformation is unknown. Since a framework to crystallize AE1 is established, there is a starting point to begin crystallization trials to reveal the alternate conformation. The AE1 MD crystal structure contained an antibody fragment against a conformational epitope of the protein, a common method to reduce conformational heterogeneity of samples in X-ray crystallography (1,565). Established procedures to purify ScIgG from RBCs enable Fab fragments to be generated from ScIgG to stabilize AE1 in the alternate conformation seen in opsonized cells. Furthermore, the current crystal structure may be useful in solving the phases of future crystals.

Alternatively, one method to deduce the alternate conformation could be dual fluorescence quenching. Similar to the substituted cystine accessibility used here, dual fluorescence quenching

determines the localization of individual residues. Lipophilic and aqueous quenchers are used in combination to obtain a 'quenching ratio' for individual tryptophan residues in a protein. The ratio of quenching by the lipophilic vs. aqueous quenchers has a linear dependency on residue depth in the lipid bilayer, and this can be used to determine the location of tryptophan residues relative to the bilayer. Residues that are displaced during reorientation can be deduced by assessing the quenching ratio of heterologous AE1 in either the predominant conformation, compared to that of AE1 trapped in the alternate conformation (using LYIA or similar probes). This method would elucidate residues that change from the aqueous intracellular environment to the lipid environment in the alternate conformation. This method would require a similar set up to the substituted cysteine accessibility analysis, including construction of a tryptophan-less AE1 mutant (eleven native W residues within AE1, seven in the MD) and assessing the mutant for anion exchange activity, before creating single W point mutants similarly to the cysteine mutants. Mutants would need to be purified from their expression system and reconstituted in proteoliposomes. While the method proposed here to deduce the residues involved in reorientation is complex, it may be a possible strategy if direct structural determination by X-ray crystallography or cryo-EM is not an option.

The dynamics of the reorientation were too rapid to assess with the methods used here. The intrinsic nature of the reorientation may make assessing the dynamics difficult. Dynamic membrane protein reorientation reported thus far have either been inducible (566-570) or slow enough to resolve by substituted cysteine accessibility (571). A potentially useful modified Förster resonance energy transfer (FRET) technique has been developed which avoids inducing protein perturbations from large traditional fluorophores (572). A small membrane-permeant fluorescein derivative with two arsen-(III) substituents (fluorescein arsenical hairpin binder; FlAsH) is used as an acceptor fluorophore, which only fluoresces when bound to an FlAsH-binding motif

(CCPGCC) introduced within the protein of interest (573). FRET signal is only present when the FlAsH molecule is present and bound to the CCPGCC motif. The CCPGCC motif can then be introduced with minimal perturbations of native protein folding, compared to larger fluorophores of several kilodaltons. Cyan Fluorescent Protein (CFP) is used as a donor fluorophore, and CCPGCC-bound FlAsH as an acceptor fluorophore. Introducing the FlAsH binding motif in the InScEp, and a CFP to intracellular regions or extracellular regions, could determine the dynamics of the rearrangement. Using intracellular and extracellular CFP (introduced at AE1 C-terminus and GPA N-terminus, respectively) as a donor fluorophore, the FlAsH acceptor fluorophore can be added in a live-cell imaging chamber, and FRET fluorescence recorded over time as FlAsH binds to the InScEp. Static FlAsH sites should also be used for controls in intracellular and extracellular control regions of AE1, such as the cytoplasmic domain and ECL3. The strength of the FlAsH method lies in the small introduced sequence used as a reporter, however the sensitivity to introductions in this loop are not fully elucidated. Possible setbacks include misfolded protein or changed reorientation dynamics from the introduced binding motif or CFP.

Data presented here indicate a role of the RBC glycocalyx in limiting accessibility of the senescent cell epitope. This is consistent with increased IgG-mediated phagocytosis of RBCs treated with neuraminidase, which removes sialic acids of the RBCs glycocalyx by proteolytic cleavage (529,530,537). Directly assessing α814-827 binding to neuraminidase-treated RBCs, compared to non-treated RBCs, may elucidate the role of the glycocalyx in limiting senescent cell epitope exposure.

The role of AE1 polymorphisms in red cell senescence may be further elucidated using *in vivo* assays. Animals commonly used for *in vivo* studies are often not ideal for models of human RBC aging. Rodent and rabbit RBCs have life spans limited to 50-70 days and exhibit high age-

independent RBC removal (574,575). Animal studies using dogs have been proposed for the long cell life span and low levels of random RBC removal, comparable to humans (574,576-578). A potential method to assess the role of AE1 812-830 in RBC senescence *in vivo* would be intravenous administration of peptides corresponding to the AE1 812-830 region. We would expect circulating AE1 812-830 peptides to bind low-titre ScIgG in serum, reducing availability of free ScIgG available for RBC opsonization. Competitive binding of ScIgG by peptides would likely result in prolonged RBC circulating lifetime. This result would be dependent on significant residence time of peptides in circulation, as immediate clearance of peptides will impede any competitive binding effects.

The RBC senescence signalling pathway is potentially exacerbated in the rare autoimmune disorder warm autoimmune haemolytic anemia (wAIHA), a severe and sometimes fatal disease (579,580). RBCs in patients with wAIHA are aggressively opsonized with anti-AE1 auto-antibodies, and subsequently cleared prematurely (581-585). Pathogenesis appears to be due to dysregulation of the immune system rather than abnormal AE1 (586). Drugs currently used to treat wAIHA patients target and potentially compromise the immune system, with limited long-term success rates (587,588). Elucidating the regions of AE1 that create the antigen recognized by wAIHA antibody could lead to more effective, targeted treatments for wAIHA. Administering low levels of intravenous AE1 fragments (i.e. peptides corresponding to part of the 812-830 region) could competitively block IgG, restoring the native equilibrium of auto-antibody and AE1 sites to normal and limiting hemolysis. No direct comparison of the anti-AE1 IgG involved in clearance of normal senescent RBCs and wAIHA RBCs has yet been completed, so a thorough characterization of the binding motifs for eluted auto-antibody in each condition would be required.

Elucidating the molecular mechanism of RBC opsonization also has potential applications to improve storage of banked RBCs. Stored RBCs accumulate 'storage lesions,' biochemical alterations that likely contribute to removal of up to 25% of cells shortly after transfusion (589,590). Storage lesions notably include accumulated anti-AE1 antibodies (591,592), which may contribute to the rapid removal of transfused cells. Similar to potential treatments for wAIHA then, there is the potential to store blood banked RBC units with peptides corresponding to the AE1 812-830 region to competitively bind auto-antibodies in storage conditions, limiting opsonization of RBCs and improving transfusion efficiency. The use of epitope-tagged AE1 fragments (eg. HA, His epitope tags) could enable the removal of these fragments by affinity chromatography prior to RBC transfusion. In conclusion, while elucidating the molecular 'clock' of RBC aging is notable in itself, the variations of this mechanism in disease states and blood bank storage hint at a wider field in which novel therapies can be developed based on the underlying mechanism.

Bibliography

1. Arakawa, T., Kobayashi-Yurugi, T., Alguel, Y., Iwanari, H., Hatae, H., Iwata, M., Abe, Y., Hino, T., Ikeda-Suno, C., Kuma, H., Kang, D., Murata, T., Hamakubo, T., Cameron, A. D., Kobayashi, T., Hamasaki, N., and Iwata, S. (2015) Crystal structure of the anion exchanger domain of human erythrocyte band 3. *Science* **350**, 680-684
2. Wallin, E., and von Heijne, G. (1998) Genome-wide analysis of integral membrane proteins from eubacterial, archaean, and eukaryotic organisms. *Protein science : a publication of the Protein Society* **7**, 1029-1038
3. Fagerberg, L., Jonasson, K., von Heijne, G., Uhlen, M., and Berglund, L. (2010) Prediction of the human membrane proteome. *Proteomics* **10**, 1141-1149
4. Terstappen, G. C., and Reggiani, A. (2001) *In silico* research in drug discovery. *Trends Pharmacol Sci* **22**, 23-26
5. Marinko, J. T., Huang, H., Penn, W. D., Capra, J. A., Schlebach, J. P., and Sanders, C. R. (2019) Folding and Misfolding of Human Membrane Proteins in Health and Disease: From Single Molecules to Cellular Proteostasis. *Chem Rev* **119**, 5537-5606
6. Deisenhofer, J., Epp, O., Miki, K., Huber, R., and Michel, H. (1985) Structure of the protein subunits in the photosynthetic reaction centre of *Rhodopseudomonas viridis* at 3 Å resolution. *Nature* **318**, 618-624
7. Kendrew, J. C., Bodo, G., Dintzis, H. M., Parrish, R. G., Wyckoff, H., and Phillips, D. C. (1958) A three-dimensional model of the myoglobin molecule obtained by X-ray analysis. *Nature* **181**, 662-666
8. Huynh, K. W., Jiang, J., Abuladze, N., Tsirulnikov, K., Kao, L., Shao, X., Newman, D., Azimov, R., Pushkin, A., Zhou, Z. H., and Kurtz, I. (2018) CryoEM structure of the human SLC4A4 sodium-coupled acid-base transporter NBCe1. *Nat Commun* **9**, 900
9. Seddon, A. M., Curnow, P., and Booth, P. J. (2004) Membrane proteins, lipids and detergents: not just a soap opera. *Biochimica et biophysica acta* **1666**, 105-117
10. Deller, M. C., Kong, L., and Rupp, B. (2016) Protein stability: a crystallographer's perspective. *Acta Crystallogr F Struct Biol Commun* **72**, 72-95
11. Standfuss, J., Xie, G., Edwards, P. C., Burghammer, M., Oprian, D. D., and Schertler, G. F. (2007) Crystal structure of a thermally stable rhodopsin mutant. *J Mol Biol* **372**, 1179-1188
12. Steyaert, J., and Kobilka, B. K. (2011) Nanobody stabilization of G protein-coupled receptor conformational states. *Curr Opin Struct Biol* **21**, 567-572
13. Ho, H., Miu, A., Alexander, M. K., Garcia, N. K., Oh, A., Zilberleyb, I., Reichelt, M., Austin, C. D., Tam, C., Shriver, S., Hu, H., Labadie, S. S., Liang, J., Wang, L., Wang, J., Lu, Y., Purkey, H. E., Quinn, J., Franke, Y., Clark, K., Beresini, M. H., Tan, M. W., Sellers, B. D., Maurer, T., Koehler, M. F. T., Wecksler, A. T., Kiefer, J. R., Verma, V., Xu, Y., Nishiyama, M., Payandeh, J., and Koth, C. M. (2018) Structural basis for dual-mode inhibition of the ABC transporter MsbA. *Nature* **557**, 196-201
14. Aller, S. G., Yu, J., Ward, A., Weng, Y., Chittaboina, S., Zhuo, R., Harrell, P. M., Trinh, Y. T., Zhang, Q., Urbatsch, I. L., and Chang, G. (2009) Structure of P-glycoprotein reveals a molecular basis for poly-specific drug binding. *Science* **323**, 1718-1722

15. Bill, R. M., Henderson, P. J., Iwata, S., Kunji, E. R., Michel, H., Neutze, R., Newstead, S., Poolman, B., Tate, C. G., and Vogel, H. (2011) Overcoming barriers to membrane protein structure determination. *Nature biotechnology* **29**, 335-340
16. Bayburt, T. H., and Sligar, S. G. (2010) Membrane protein assembly into Nanodiscs. *FEBS Lett* **584**, 1721-1727
17. Breyton, C., Pucci, B., and Popot, J. L. (2010) Amphipols and fluorinated surfactants: Two alternatives to detergents for studying membrane proteins *in vitro*. *Methods Mol Biol* **601**, 219-245
18. Postis, V., Rawson, S., Mitchell, J. K., Lee, S. C., Parslow, R. A., Dafforn, T. R., Baldwin, S. A., and Muench, S. P. (2015) The use of SMALPs as a novel membrane protein scaffold for structure study by negative stain electron microscopy. *Biochimica et biophysica acta* **1848**, 496-501
19. Sanders, C. R., 2nd, and Landis, G. C. (1995) Reconstitution of membrane proteins into lipid-rich bilayered mixed micelles for NMR studies. *Biochemistry* **34**, 4030-4040
20. Caffrey, M. (2015) A comprehensive review of the lipid cubic phase or *in meso* method for crystallizing membrane and soluble proteins and complexes. *Acta Crystallogr F Struct Biol Commun* **71**, 3-18
21. McMullan, G., Faruqi, A. R., and Henderson, R. (2016) Direct Electron Detectors. *Methods Enzymol* **579**, 1-17
22. Nogales, E. (2016) The development of cryo-EM into a mainstream structural biology technique. *Nat Methods* **13**, 24-27
23. Cheng, Y., Grigorieff, N., Penczek, P. A., and Walz, T. (2015) A primer to single-particle cryo-electron microscopy. *Cell* **161**, 438-449
24. Cheng, Y. (2018) Membrane protein structural biology in the era of single particle cryo-EM. *Curr Opin Struct Biol* **52**, 58-63
25. Zhang, Y., Sun, B., Feng, D., Hu, H., Chu, M., Qu, Q., Tarrasch, J. T., Li, S., Sun Kobilka, T., Kobilka, B. K., and Skiniotis, G. (2017) Cryo-EM structure of the activated GLP-1 receptor in complex with a G protein. *Nature* **546**, 248-253
26. Wu, S., Avila-Sakar, A., Kim, J., Booth, D. S., Greenberg, C. H., Rossi, A., Liao, M., Li, X., Alian, A., Griner, S. L., Juge, N., Yu, Y., Mergel, C. M., Chaparro-Riggers, J., Strop, P., Tampe, R., Edwards, R. H., Stroud, R. M., Craik, C. S., and Cheng, Y. (2012) Fabs enable single particle cryoEM studies of small proteins. *Structure* **20**, 582-592
27. Ziarek, J. J., Baptista, D., and Wagner, G. (2018) Recent developments in solution nuclear magnetic resonance (NMR)-based molecular biology. *J Mol Med (Berl)* **96**, 1-8
28. Chorev, D. S., Baker, L. A., Wu, D., Beilsten-Edmands, V., Rouse, S. L., Zeev-Ben-Mordehai, T., Jiko, C., Samsudin, F., Gerle, C., Khalid, S., Stewart, A. G., Matthews, S. J., Grunewald, K., and Robinson, C. V. (2018) Protein assemblies ejected directly from native membranes yield complexes for mass spectrometry. *Science* **362**, 829-834
29. Bosshart, P. D., and Fotiadis, D. (2019) Secondary Active Transporters. *Subcell Biochem* **92**, 275-299
30. Bai, X., Moraes, T. F., and Reithmeier, R. A. F. (2017) Structural biology of solute carrier (SLC) membrane transport proteins. *Mol Membr Biol* **34**, 1-32
31. Shi, Y. (2013) Common folds and transport mechanisms of secondary active transporters. *Annu Rev Biophys* **42**, 51-72
32. Pao, S. S., Paulsen, I. T., and Saier, M. H., Jr. (1998) Major facilitator superfamily. *Microbiol Mol Biol Rev* **62**, 1-34

33. Abramson, J., Smirnova, I., Kasho, V., Verner, G., Kaback, H. R., and Iwata, S. (2003) Structure and mechanism of the lactose permease of *Escherichia coli*. *Science* **301**, 610-615
34. Huang, Y., Lemieux, M. J., Song, J., Auer, M., and Wang, D. N. (2003) Structure and mechanism of the glycerol-3-phosphate transporter from *Escherichia coli*. *Science* **301**, 616-620
35. Deng, D., Xu, C., Sun, P., Wu, J., Yan, C., Hu, M., and Yan, N. (2014) Crystal structure of the human glucose transporter GLUT1. *Nature* **510**, 121-125
36. Yin, Y., He, X., Szewczyk, P., Nguyen, T., and Chang, G. (2006) Structure of the multidrug transporter EmrD from *Escherichia coli*. *Science* **312**, 741-744
37. Screpanti, E., and Hunte, C. (2007) Discontinuous membrane helices in transport proteins and their correlation with function. *J Struct Biol* **159**, 261-267
38. Serdiuk, T., Madej, M. G., Sugihara, J., Kawamura, S., Mari, S. A., Kaback, H. R., and Muller, D. J. (2014) Substrate-induced changes in the structural properties of LacY. *Proc Natl Acad Sci U S A* **111**, E1571-1580
39. Newstead, S., Drew, D., Cameron, A. D., Postis, V. L., Xia, X., Fowler, P. W., Ingram, J. C., Carpenter, E. P., Sansom, M. S., McPherson, M. J., Baldwin, S. A., and Iwata, S. (2011) Crystal structure of a prokaryotic homologue of the mammalian oligopeptide-proton symporters, PepT1 and PepT2. *EMBO J* **30**, 417-426
40. Pedersen, B. P., Kumar, H., Waight, A. B., Risenmay, A. J., Roe-Zurz, Z., Chau, B. H., Schlessinger, A., Bonomi, M., Harries, W., Sali, A., Johri, A. K., and Stroud, R. M. (2013) Crystal structure of a eukaryotic phosphate transporter. *Nature* **496**, 533-536
41. Yamashita, A., Singh, S. K., Kawate, T., Jin, Y., and Gouaux, E. (2005) Crystal structure of a bacterial homologue of Na^+/Cl^--dependent neurotransmitter transporters. *Nature* **437**, 215-223
42. Abramson, J., and Wright, E. M. (2009) Structure and function of Na^+-symporters with inverted repeats. *Curr Opin Struct Biol* **19**, 425-432
43. Fang, Y., Jayaram, H., Shane, T., Kolmakova-Partensky, L., Wu, F., Williams, C., Xiong, Y., and Miller, C. (2009) Structure of a prokaryotic virtual proton pump at 3.2 Å resolution. *Nature* **460**, 1040-1043
44. Faham, S., Watanabe, A., Besserer, G. M., Cascio, D., Specht, A., Hirayama, B. A., Wright, E. M., and Abramson, J. (2008) The crystal structure of a sodium galactose transporter reveals mechanistic insights into Na^+/sugar symport. *Science* **321**, 810-814
45. Ehrnstorfer, I. A., Geertsma, E. R., Pardon, E., Steyaert, J., and Dutzler, R. (2014) Crystal structure of a SLC11 (NRAMP) transporter reveals the basis for transition-metal ion transport. *Nat Struct Mol Biol* **21**, 990-996
46. Hunte, C., Screpanti, E., Venturi, M., Rimon, A., Padan, E., and Michel, H. (2005) Structure of a Na^+/H^+ antiporter and insights into mechanism of action and regulation by pH. *Nature* **435**, 1197-1202
47. Hu, N. J., Iwata, S., Cameron, A. D., and Drew, D. (2011) Crystal structure of a bacterial homologue of the bile acid sodium symporter ASBT. *Nature* **478**, 408-411
48. Dayhoff, M. O. (1976) The origin and evolution of protein superfamilies. *Fed Proc* **35**, 2132-2138
49. Chothia, C., and Lesk, A. M. (1986) The relation between the divergence of sequence and structure in proteins. *EMBO J* **5**, 823-826

50. Launay, G., and Simonson, T. (2008) Homology modelling of protein-protein complexes: a simple method and its possibilities and limitations. *BMC Bioinformatics* **9**, 427
51. Wain, H. M., Lush, M. J., Ducluzeau, F., Khodiyar, V. K., and Povey, S. (2004) Genew: the Human Gene Nomenclature Database, 2004 updates. *Nucleic Acids Res* **32**, D255-257
52. Romero, M. F., Chen, A. P., Parker, M. D., and Boron, W. F. (2013) The SLC4 family of bicarbonate (HCO_3^-) transporters. *Mol Aspects Med* **34**, 159-182
53. Myers, E. J., Marshall, A., Jennings, M. L., and Parker, M. D. (2016) Mouse Slc4a11 expressed in *Xenopus* oocytes is an ideally selective H^+/OH^- conductance pathway that is stimulated by rises in intracellular and extracellular pH. *Am J Physiol Cell Physiol* **311**, C945-C959
54. Liu, Y., Yang, J., and Chen, L. M. (2015) Structure and Function of SLC4 Family HCO_3^- Transporters. *Front Physiol* **6**, 355
55. Jarolim, P., Murray, J. L., Rubin, H. L., Taylor, W. M., Prchal, J. T., Ballas, S. K., Snyder, L. M., Chrobak, L., Melrose, W. D., Brabec, V., and Palek, J. (1996) Characterization of 13 novel band 3 gene defects in hereditary spherocytosis with band 3 deficiency. *Blood* **88**, 4366-4374
56. Chu, C., Woods, N., Sawasdee, N., Guizouarn, H., Pellissier, B., Borgese, F., Yenchitsomanus, P. T., Gowrishankar, M., and Cordat, E. (2010) Band 3 Edmonton I, a novel mutant of the anion exchanger 1 causing spherocytosis and distal renal tubular acidosis. *Biochem J* **426**, 379-388
57. Alloisio, N., Texier, P., Vallier, A., Ribeiro, M. L., Morle, L., Bozon, M., Bursaux, E., Maillet, P., Goncalves, P., Tanner, M. J., Tamagnini, G., and Delaunay, J. (1997) Modulation of clinical expression and band 3 deficiency in hereditary spherocytosis. *Blood* **90**, 414-420
58. Dhermy, D., Galand, C., Bournier, O., Boulanger, L., Cynober, T., Schismanoff, P. O., Bursaux, E., Tchernia, G., Boivin, P., and Garbarz, M. (1997) Heterogenous band 3 deficiency in hereditary spherocytosis related to different band 3 gene defects. *Br J Haematol* **98**, 32-40
59. Eber, S. W., Gonzalez, J. M., Lux, M. L., Scarpa, A. L., Tse, W. T., Dornwell, M., Herbers, J., Kugler, W., Ozcan, R., Pekrun, A., Gallagher, P. G., Schroter, W., Forget, B. G., and Lux, S. E. (1996) Ankyrin-1 mutations are a major cause of dominant and recessive hereditary spherocytosis. *Nat Genet* **13**, 214-218
60. Lima, P. R., Baratti, M. O., Chiattone, M. L., Costa, F. F., and Saad, S. T. (2005) Band $3^{Tambaú}$: a *de novo* mutation in the *AE1* gene associated with hereditary spherocytosis. Implications for anion exchange and insertion into the red blood cell membrane. *Eur J Haematol* **74**, 396-401
61. Toye, A. M., Williamson, R. C., Khanfar, M., Bader-Meunier, B., Cynober, T., Thibault, M., Tchernia, G., Dechaux, M., Delaunay, J., and Bruce, L. J. (2008) Band 3 Courcouronnes (Ser667Phe): a trafficking mutant differentially rescued by wild-type band 3 and glycophorin A. *Blood* **111**, 5380-5389
62. Kanzaki, A., Hayette, S., Morle, L., Inoue, F., Matsuyama, R., Inoue, T., Yawata, A., Wada, H., Vallier, A., Alloisio, N., Yawata, Y., and Delaunay, J. (1997) Total absence of protein 4.2 and partial deficiency of band 3 in hereditary spherocytosis. *Br J Haematol* **99**, 522-530
63. Miraglia del Giudice, E., Vallier, A., Maillet, P., Perrotta, S., Cutillo, S., Iolascon, A., Tanner, M. J., Delaunay, J., and Alloisio, N. (1997) Novel band 3 variants (bands 3

Foggia, Napoli I and Napoli II) associated with hereditary spherocytosis and band 3 deficiency: status of the D38A polymorphism within the EPB3 locus. *Br J Haematol* **96**, 70-76
64. Shmukler, B. E., Kedar, P. S., Warang, P., Desai, M., Madkaikar, M., Ghosh, K., Colah, R. B., and Alper, S. L. (2010) Hemolytic anemia and distal renal tubular acidosis in two Indian patients homozygous for SLC4A1/AE1 mutation A858D. *Am J Hematol* **85**, 824-828
65. Iwase, S., Ideguchi, H., Takao, M., Horiguchi-Yamada, J., Iwasaki, M., Takahara, S., Sekikawa, T., Mochizuki, S., and Yamada, H. (1998) Band 3 Tokyo: Thr^{837}-->Ala^{837} substitution in erythrocyte band 3 protein associated with spherocytic hemolysis. *Acta Haematol* **100**, 200-203
66. Stewart, A. K., Kedar, P. S., Shmukler, B. E., Vandorpe, D. H., Hsu, A., Glader, B., Rivera, A., Brugnara, C., and Alper, S. L. (2011) Functional characterization and modified rescue of novel AE1 mutation R730C associated with overhydrated cation leak stomatocytosis. *Am J Physiol Cell Physiol* **300**, C1034-1046
67. Bruce, L. J., Robinson, H. C., Guizouarn, H., Borgese, F., Harrison, P., King, M. J., Goede, J. S., Coles, S. E., Gore, D. M., Lutz, H. U., Ficarella, R., Layton, D. M., Iolascon, A., Ellory, J. C., and Stewart, G. W. (2005) Monovalent cation leaks in human red cells caused by single amino-acid substitutions in the transport domain of the band 3 chloride-bicarbonate exchanger, AE1. *Nat Genet* **37**, 1258-1263
68. Stewart, A. K., Vandorpe, D. H., Heneghan, J. F., Chebib, F., Stolpe, K., Akhavein, A., Edelman, E. J., Maksimova, Y., Gallagher, P. G., and Alper, S. L. (2010) The GPA-dependent, spherostomatocytosis mutant AE1 E758K induces GPA-independent, endogenous cation transport in amphibian oocytes. *Am J Physiol Cell Physiol* **298**, C283-297
69. Iolascon, A., De Falco, L., Borgese, F., Esposito, M. R., Avvisati, R. A., Izzo, P., Piscopo, C., Guizouarn, H., Biondani, A., Pantaleo, A., and De Franceschi, L. (2009) A novel erythroid anion exchange variant (Gly796Arg) of hereditary stomatocytosis associated with dyserythropoiesis. *Haematologica* **94**, 1049-1059
70. Yang, E., Seo-Mayer, P., Lezon-Geyda, K., Badior, K. E., Li, J., Casey, J. R., Reithmeier, R. A. F., and Gallagher, P. G. (2018) A Ser725Arg mutation in Band 3 abolishes transport function and leads to anemia and renal tubular acidosis. *Blood* **131**, 1759-1763
71. Dinour, D., Chang, M. H., Satoh, J., Smith, B. L., Angle, N., Knecht, A., Serban, I., Holtzman, E. J., and Romero, M. F. (2004) A novel missense mutation in the sodium bicarbonate cotransporter (NBCe1/SLC4A4) causes proximal tubular acidosis and glaucoma through ion transport defects. *J Biol Chem* **279**, 52238-52246
72. Igarashi, T., Inatomi, J., Sekine, T., Seki, G., Shimadzu, M., Tozawa, F., Takeshima, Y., Takumi, T., Takahashi, T., Yoshikawa, N., Nakamura, H., and Endou, H. (2001) Novel nonsense mutation in the Na^+/HCO_3^- cotransporter gene (*SLC4A4*) in a patient with permanent isolated proximal renal tubular acidosis and bilateral glaucoma. *J Am Soc Nephrol* **12**, 713-718
73. Igarashi, T., Inatomi, J., Sekine, T., Cha, S. H., Kanai, Y., Kunimi, M., Tsukamoto, K., Satoh, H., Shimadzu, M., Tozawa, F., Mori, T., Shiobara, M., Seki, G., and Endou, H. (1999) Mutations in *SLC4A4* cause permanent isolated proximal renal tubular acidosis with ocular abnormalities. *Nat Genet* **23**, 264-266

74. Inatomi, J., Horita, S., Braverman, N., Sekine, T., Yamada, H., Suzuki, Y., Kawahara, K., Moriyama, N., Kudo, A., Kawakami, H., Shimadzu, M., Endou, H., Fujita, T., Seki, G., and Igarashi, T. (2004) Mutational and functional analysis of SLC4A4 in a patient with proximal renal tubular acidosis. *Pflugers Arch* **448**, 438-444
75. Toye, A. M., Parker, M. D., Daly, C. M., Lu, J., Virkki, L. V., Pelletier, M. F., and Boron, W. F. (2006) The human NBCe1-A mutant R881C, associated with proximal renal tubular acidosis, retains function but is mistargeted in polarized renal epithelia. *Am J Physiol Cell Physiol* **291**, C788-801
76. Cordat, E. (2006) Unraveling trafficking of the kidney anion exchanger 1 in polarized MDCK epithelial cells. *Biochem Cell Biol* **84**, 949-959
77. Vilas, G. L., Johnson, D. E., Freund, P., and Casey, J. R. (2009) Characterization of an epilepsy-associated variant of the human Cl^-/HCO_3^- exchanger AE3. *Am J Physiol Cell Physiol* **297**, C526-536
78. Sander, T., Toliat, M. R., Heils, A., Leschik, G., Becker, C., Ruschendorf, F., Rohde, K., Mundlos, S., and Nurnberg, P. (2002) Association of the 867Asp variant of the human anion exchanger 3 gene with common subtypes of idiopathic generalized epilepsy. *Epilepsy Res* **51**, 249-255
79. Alvarez, B. V., Gilmour, G. S., Mema, S. C., Martin, B. T., Shull, G. E., Casey, J. R., and Sauve, Y. (2007) Blindness caused by deficiency in AE3 chloride/bicarbonate exchanger. *PLoS One* **2**, e839
80. Aldave, A. J., Yellore, V. S., Bourla, N., Momi, R. S., Khan, M. A., Salem, A. K., Rayner, S. A., Glasgow, B. J., and Kurtz, I. (2007) Autosomal recessive CHED associated with novel compound heterozygous mutations in *SLC4A11*. *Cornea* **26**, 896-900
81. Desir, J., Moya, G., Reish, O., Van Regemorter, N., Deconinck, H., David, K. L., Meire, F. M., and Abramowicz, M. J. (2007) Borate transporter *SLC4A11* mutations cause both Harboyan syndrome and non-syndromic corneal endothelial dystrophy. *J Med Genet* **44**, 322-326
82. Jiao, X., Sultana, A., Garg, P., Ramamurthy, B., Vemuganti, G. K., Gangopadhyay, N., Hejtmancik, J. F., and Kannabiran, C. (2007) Autosomal recessive corneal endothelial dystrophy (CHED2) is associated with mutations in SLC4A11. *J Med Genet* **44**, 64-68
83. Kumar, A., Bhattacharjee, S., Prakash, D. R., and Sadanand, C. S. (2007) Genetic analysis of two Indian families affected with congenital hereditary endothelial dystrophy: two novel mutations in *SLC4A11*. *Mol Vis* **13**, 39-46
84. Ramprasad, V. L., Ebenezer, N. D., Aung, T., Rajagopal, R., Yong, V. H., Tuft, S. J., Viswanathan, D., El-Ashry, M. F., Liskova, P., Tan, D. T., Bhattacharya, S. S., Kumaramanickavel, G., and Vithana, E. N. (2007) Novel *SLC4A11* mutations in patients with recessive congenital hereditary endothelial dystrophy (CHED2). Mutation in brief #958. Online. *Hum Mutat* **28**, 522-523
85. Sultana, A., Garg, P., Ramamurthy, B., Vemuganti, G. K., and Kannabiran, C. (2007) Mutational spectrum of the *SLC4A11* gene in autosomal recessive congenital hereditary endothelial dystrophy. *Mol Vis* **13**, 1327-1332
86. Desir, J., and Abramowicz, M. (2008) Congenital hereditary endothelial dystrophy with progressive sensorineural deafness (Harboyan syndrome). *Orphanet J Rare Dis* **3**, 28
87. Hemadevi, B., Veitia, R. A., Srinivasan, M., Arunkumar, J., Prajna, N. V., Lesaffre, C., and Sundaresan, P. (2008) Identification of mutations in the *SLC4A11* gene in patients

with recessive congenital hereditary endothelial dystrophy. *Arch Ophthalmol* **126**, 700-708
88. Aldahmesh, M. A., Khan, A. O., Meyer, B. F., and Alkuraya, F. S. (2009) Mutational spectrum of *SLC4A11* in autosomal recessive CHED in Saudi Arabia. *Invest Ophthalmol Vis Sci* **50**, 4142-4145
89. Paliwal, P., Sharma, A., Tandon, R., Sharma, N., Titiyal, J. S., Sen, S., Nag, T. C., and Vajpayee, R. B. (2010) Congenital hereditary endothelial dystrophy - mutation analysis of *SLC4A11* and genotype-phenotype correlation in a North Indian patient cohort. *Mol Vis* **16**, 2955-2963
90. Kodaganur, S. G., Kapoor, S., Veerappa, A. M., Tontanahal, S. J., Sarda, A., Yathish, S., Prakash, D. R., and Kumar, A. (2013) Mutation analysis of the *SLC4A11* gene in Indian families with congenital hereditary endothelial dystrophy 2 and a review of the literature. *Mol Vis* **19**, 1694-1706
91. Puangsricharern, V., Yeetong, P., Charumalai, C., Suphapeetiporn, K., and Shotelersuk, V. (2014) Two novel mutations including a large deletion of the *SLC4A11* gene causing autosomal recessive hereditary endothelial dystrophy. *Br J Ophthalmol* **98**, 1460-1462
92. Kaul, H., Suman, M., Khan, Z., Ullah, M. I., Ashfaq, U. A., and Idrees, S. (2016) Missense mutation in *SLC4A11* in two Pakistani families affected with congenital hereditary endothelial dystrophy (CHED2). *Clin Exp Optom* **99**, 73-77
93. Kumawat, B. L., Gupta, R., Sharma, A., Sen, S., Gupta, S., and Tandon, R. (2016) Delayed onset of congenital hereditary endothelial dystrophy due to compound heterozygous *SLC4A11* mutations. *Indian J Ophthalmol* **64**, 492-495
94. Hand, C. K., McGuire, M., Parfrey, N. A., and Murphy, C. C. (2016) Homozygous *SLC4A11* mutation in a large Irish CHED2 pedigree. *Ophthalmic Genetics*, 1-4
95. Moazzeni, H., Javadi, M. A., Asgari, D., Khani, M., Emami, M., Moghadam, A., Panahi-Bazaz, M. R., Hosseini Tehrani, M., Karimian, F., Hosseini, B., Nekuie Moghadam, T., Hassanpour, H., Akbari, M. T., and Elahi, E. (2019) Observation of nine previously reported and 10 non-reported *SLC4A11* mutations among 20 Iranian CHED probands and identification of an *MPDZ* mutation as possible cause of CHED and FECD in one family. *Br J Ophthalmol* **0**, 1-8
96. Brejchova, K., Dudakova, L., Skalicka, P., Dobrovolny, R., Masek, P., Putzova, M., Moosajee, M., Tuft, S. J., Davidson, A. E., and Liskova, P. (2019) IPSC-Derived Corneal Endothelial-like Cells Act as an Appropriate Model System to Assess the Impact of *SLC4A11* Variants on Pre-mRNA Splicing. *Invest Ophthalmol Vis Sci* **60**, 3084-3090
97. Zhang, J., Wu, D., Li, Y., Fan, Y., Chen, H., Hong, J., and Xu, J. (2019) Novel Mutations Associated With Various Types of Corneal Dystrophies in a Han Chinese Population. *Front Genet* **10**, 881
98. Vithana, E. N., Morgan, P., Sundaresan, P., Ebenezer, N. D., Tan, D. T., Mohamed, M. D., Anand, S., Khine, K. O., Venkataraman, D., Yong, V. H., Salto-Tellez, M., Venkatraman, A., Guo, K., Hemadevi, B., Srinivasan, M., Prajna, V., Khine, M., Casey, J. R., Inglehearn, C. F., and Aung, T. (2006) Mutations in sodium-borate cotransporter SLC4A11 cause recessive congenital hereditary endothelial dystrophy (CHED2). *Nat Genet* **38**, 755-757
99. Vithana, E. N., Morgan, P. E., Ramprasad, V., Tan, D. T., Yong, V. H., Venkataraman, D., Venkatraman, A., Yam, G. H., Nagasamy, S., Law, R. W., Rajagopal, R., Pang, C. P.,

Kumaramanickevel, G., Casey, J. R., and Aung, T. (2008) *SLC4A11* mutations in Fuchs endothelial corneal dystrophy. *Hum Mol Genet* **17**, 656-666
100. Riazuddin, S. A., Vithana, E. N., Seet, L. F., Liu, Y., Al-Saif, A., Koh, L. W., Heng, Y. M., Aung, T., Meadows, D. N., Eghrari, A. O., Gottsch, J. D., and Katsanis, N. (2010) Missense mutations in the sodium borate cotransporter *SLC4A11* cause late-onset Fuchs corneal dystrophy. *Hum Mutat* **31**, 1261-1268
101. Soumittra, N., Loganathan, S. K., Madhavan, D., Ramprasad, V. L., Arokiasamy, T., Sumathi, S., Karthiyayini, T., Rachapalli, S. R., Kumaramanickavel, G., Casey, J. R., and Rajagopal, R. (2014) Biosynthetic and functional defects in newly identified *SLC4A11* mutants and absence of *COL8A2* mutations in Fuchs endothelial corneal dystrophy. *J Hum Genet* **59**, 444-453
102. Wieth, J. O., Andersen, O. S., Brahm, J., Bjerrum, P. J., and Borders, C. L., Jr. (1982) Chloride-bicarbonate exchange in red blood cells: physiology of transport and chemical modification of binding sites. *Philos Trans R Soc Lond B Biol Sci* **299**, 383-399
103. Alper, S. L., Natale, J., Gluck, S., Lodish, H. F., and Brown, D. (1989) Subtypes of intercalated cells in rat kidney collecting duct defined by antibodies against erythroid band 3 and renal vacuolar H^+-ATPase. *Proc Natl Acad Sci U S A* **86**, 5429-5433
104. Quilty, J. A., and Reithmeier, R. A. (2000) Trafficking and folding defects in hereditary spherocytosis mutants of the human red cell anion exchanger. *Traffic* **1**, 987-998
105. Maillet, P., Alloisio, N., Morle, L., and Delaunay, J. (1996) Spectrin mutations in hereditary elliptocytosis and hereditary spherocytosis. *Hum Mutat* **8**, 97-107
106. Sinha, R., Agarwal, I., Bawazir, W. M., and Bruce, L. J. (2013) Distal renal tubular acidosis with hereditary spherocytosis. *Indian Pediatr* **50**, 693-695
107. Guizouarn, H., Martial, S., Gabillat, N., and Borgese, F. (2007) Point mutations involved in red cell stomatocytosis convert the electroneutral anion exchanger 1 to a nonselective cation conductance. *Blood* **110**, 2158-2165
108. Guizouarn, H., Borgese, F., Gabillat, N., Harrison, P., Goede, J. S., McMahon, C., Stewart, G. W., and Bruce, L. J. (2011) South-east Asian ovalocytosis and the cryohydrocytosis form of hereditary stomatocytosis show virtually indistinguishable cation permeability defects. *Br J Haematol* **152**, 655-664
109. Zhang, Z., Liu, K. X., He, J. W., Fu, W. Z., Yue, H., Zhang, H., Zhang, C. Q., and Zhang, Z. L. (2012) Identification of two novel mutations in the *SLC4A1* gene in two unrelated Chinese families with distal renal tubular acidosis. *Arch Med Res* **43**, 298-304
110. Chang, Y. H., Shaw, C. F., Jian, S. H., Hsieh, K. H., Chiou, Y. H., and Lu, P. J. (2009) Compound mutations in human anion exchanger 1 are associated with complete distal renal tubular acidosis and hereditary spherocytosis. *Kidney Int* **76**, 774-783
111. Toye, A. M., Banting, G., and Tanner, M. J. (2004) Regions of human kidney anion exchanger 1 (kAE1) required for basolateral targeting of kAE1 in polarised kidney cells: mis-targeting explains dominant renal tubular acidosis (dRTA). *J Cell Sci* **117**, 1399-1410
112. Cordat, E., Kittanakom, S., Yenchitsomanus, P. T., Li, J., Du, K., Lukacs, G. L., and Reithmeier, R. A. (2006) Dominant and recessive distal renal tubular acidosis mutations of kidney anion exchanger 1 induce distinct trafficking defects in MDCK cells. *Traffic* **7**, 117-128

113. Wrong, O., Bruce, L. J., Unwin, R. J., Toye, A. M., and Tanner, M. J. (2002) Band 3 mutations, distal renal tubular acidosis, and Southeast Asian ovalocytosis. *Kidney Int* **62**, 10-19
114. Bruce, L. J., Cope, D. L., Jones, G. K., Schofield, A. E., Burley, M., Povey, S., Unwin, R. J., Wrong, O., and Tanner, M. J. (1997) Familial distal renal tubular acidosis is associated with mutations in the red cell anion exchanger (Band 3, *AE1*) gene. *J Clin Invest* **100**, 1693-1707
115. Rungroj, N., Devonald, M. A., Cuthbert, A. W., Reimann, F., Akkarapatumwong, V., Yenchitsomanus, P. T., Bennett, W. M., and Karet, F. E. (2004) A novel missense mutation in AE1 causing autosomal dominant distal renal tubular acidosis retains normal transport function but is mistargeted in polarized epithelial cells. *J Biol Chem* **279**, 13833-13838
116. Bruce, L. J., Wrong, O., Toye, A. M., Young, M. T., Ogle, G., Ismail, Z., Sinha, A. K., McMaster, P., Hwaihwanje, I., Nash, G. B., Hart, S., Lavu, E., Palmer, R., Othman, A., Unwin, R. J., and Tanner, M. J. (2000) Band 3 mutations, renal tubular acidosis and South-East Asian ovalocytosis in Malaysia and Papua New Guinea: loss of up to 95% band 3 transport in red cells. *Biochem J* **350 Pt 1**, 41-51
117. Kittanakom, S., Cordat, E., Akkarapatumwong, V., Yenchitsomanus, P. T., and Reithmeier, R. A. (2004) Trafficking defects of a novel autosomal recessive distal renal tubular acidosis mutant (S773P) of the human kidney anion exchanger (kAE1). *J Biol Chem* **279**, 40960-40971
118. Cheidde, L., Vieira, T. C., Lima, P. R., Saad, S. T., and Heilberg, I. P. (2003) A novel mutation in the anion exchanger 1 gene is associated with familial distal renal tubular acidosis and nephrocalcinosis. *Pediatrics* **112**, 1361-1367
119. Quilty, J. A., Li, J., and Reithmeier, R. A. (2002) Impaired trafficking of distal renal tubular acidosis mutants of the human kidney anion exchanger kAE1. *Am J Physiol Renal Physiol* **282**, F810-820
120. Toye, A. M., Bruce, L. J., Unwin, R. J., Wrong, O., and Tanner, M. J. (2002) Band 3 Walton, a C-terminal deletion associated with distal renal tubular acidosis, is expressed in the red cell membrane but retained internally in kidney cells. *Blood* **99**, 342-347
121. Shao, L., Xu, Y., Dong, Q., Lang, Y., Yue, S., and Miao, Z. (2010) A novel SLC4A1 variant in an autosomal dominant distal renal tubular acidosis family with a severe phenotype. *Endocrine* **37**, 473-478
122. Fry, A. C., Su, Y., Yiu, V., Cuthbert, A. W., Trachtman, H., and Karet Frankl, F. E. (2012) Mutation conferring apical-targeting motif on AE1 exchanger causes autosomal dominant distal RTA. *J Am Soc Nephrol* **23**, 1238-1249
123. Josephsen, K., Praetorius, J., Frische, S., Gawenis, L. R., Kwon, T. H., Agre, P., Nielsen, S., and Fejerskov, O. (2009) Targeted disruption of the Cl^-/HCO_3^- exchanger Ae2 results in osteopetrosis in mice. *Proc Natl Acad Sci U S A* **106**, 1638-1641
124. Recalde, S., Muruzabal, F., Looije, N., Kunne, C., Burrell, M. A., Saez, E., Martinez-Anso, E., Salas, J. T., Mardones, P., Prieto, J., Medina, J. F., and Elferink, R. P. (2006) Inefficient chronic activation of parietal cells in $Ae2_{a,b}^{-/-}$ mice. *Am J Pathol* **169**, 165-176
125. Lindsey, A. E., Schneider, K., Simmons, D. M., Baron, R., Lee, B. S., and Kopito, R. R. (1990) Functional expression and subcellular localization of an anion exchanger cloned from choroid plexus. *Proc Natl Acad Sci U S A* **87**, 5278-5282

126. Aiba, Y., Nakamura, M., Joshita, S., Inamine, T., Komori, A., Yoshizawa, K., Umemura, T., Horie, H., Migita, K., Yatsuhashi, H., Nakamuta, M., Fukushima, N., Saoshiro, T., Hayashi, S., Kouno, H., Ota, H., Muro, T., Watanabe, Y., Nakamura, Y., Komeda, T., Shimada, M., Masaki, N., Komatsu, T., Yagura, M., Sugi, K., Koga, M., Tsukamoto, K., Tanaka, E., Ishibashi, H., and NHOSLJ, P. B. C. S. G. i. (2011) Genetic polymorphisms in CTLA4 and SLC4A2 are differentially associated with the pathogenesis of primary biliary cirrhosis in Japanese patients. *J Gastroenterol* **46**, 1203-1212
127. Poupon, R., Ping, C., Chretien, Y., Corpechot, C., Chazouilleres, O., Simon, T., Heath, S. C., Matsuda, F., Poupon, R. E., Housset, C., and Barbu, V. (2008) Genetic factors of susceptibility and of severity in primary biliary cirrhosis. *J Hepatol* **49**, 1038-1045
128. Juran, B. D., Atkinson, E. J., Larson, J. J., Schlicht, E. M., and Lazaridis, K. N. (2009) Common genetic variation and haplotypes of the anion exchanger SLC4A2 in primary biliary cirrhosis. *Am J Gastroenterol* **104**, 1406-1411
129. Medina, J. F. (2011) Role of the anion exchanger 2 in the pathogenesis and treatment of primary biliary cirrhosis. *Dig Dis* **29**, 103-112
130. Hentschke, M., Wiemann, M., Hentschke, S., Kurth, I., Hermans-Borgmeyer, I., Seidenbecher, T., Jentsch, T. J., Gal, A., and Hubner, C. A. (2006) Mice with a targeted disruption of the Cl^-/HCO_3^- exchanger AE3 display a reduced seizure threshold. *Mol Cell Biol* **26**, 182-191
131. Thorsen, K., Dam, V. S., Kjaer-Sorensen, K., Pedersen, L. N., Skeberdis, V. A., Jurevicius, J., Treinys, R., Petersen, I., Nielsen, M. S., Oxvig, C., Morth, J. P., Matchkov, V. V., Aalkjaer, C., Bundgaard, H., and Jensen, H. K. (2017) Loss-of-activity-mutation in the cardiac chloride-bicarbonate exchanger AE3 causes short QT syndrome. *Nat Commun* **8**, 1696
132. Villa-Abrille, M. C., Petroff, M. G., and Aiello, E. A. (2007) The electrogenic Na^+/HCO_3^- cotransport modulates resting membrane potential and action potential duration in cat ventricular myocytes. *J Physiol* **578**, 819-829
133. Bonanno, J. A. (2012) Molecular mechanisms underlying the corneal endothelial pump. *Exp Eye Res* **95**, 2-7
134. Cordat, E., and Reithmeier, R. A. (2014) Structure, function, and trafficking of SLC4 and SLC26 anion transporters. *Curr Top Membr* **73**, 1-67
135. Gawenis, L. R., Bradford, E. M., Prasad, V., Lorenz, J. N., Simpson, J. E., Clarke, L. L., Woo, A. L., Grisham, C., Sanford, L. P., Doetschman, T., Miller, M. L., and Shull, G. E. (2007) Colonic anion secretory defects and metabolic acidosis in mice lacking the NBC1 Na^+/HCO_3^- cotransporter. *J Biol Chem* **282**, 9042-9052
136. Patel, N., Khan, A. O., Al-Saif, M., Moghrabi, W. N., AlMaarik, B. M., Ibrahim, N., Abdulwahab, F., Hashem, M., Alshidi, T., Alobeid, E., Alomar, R. A., Al-Harbi, S., Abouelhoda, M., Khabar, K. S. A., and Alkuraya, F. S. (2017) A novel mechanism for variable phenotypic expressivity in Mendelian diseases uncovered by an AU-rich element (ARE)-creating mutation. *Genome Biol* **18**, 144
137. Kao, L., Kurtz, L. M., Shao, X., Papadopoulos, M. C., Liu, L., Bok, D., Nusinowitz, S., Chen, B., Stella, S. L., Andre, M., Weinreb, J., Luong, S. S., Piri, N., Kwong, J. M., Newman, D., and Kurtz, I. (2011) Severe neurologic impairment in mice with targeted disruption of the electrogenic sodium bicarbonate cotransporter NBCe2 (*Slc4a5* gene). *J Biol Chem* **286**, 32563-32574

138. Damkier, H. H., Brown, P. D., and Praetorius, J. (2013) Cerebrospinal fluid secretion by the choroid plexus. *Physiol Rev* **93**, 1847-1892
139. Carey, R. M., Schoeffel, C. D., Gildea, J. J., Jones, J. E., McGrath, H. E., Gordon, L. N., Park, M. J., Sobota, R. S., Underwood, P. C., Williams, J., Sun, B., Raby, B., Lasky-Su, J., Hopkins, P. N., Adler, G. K., Williams, S. M., Jose, P. A., and Felder, R. A. (2012) Salt sensitivity of blood pressure is associated with polymorphisms in the sodium-bicarbonate cotransporter. *Hypertension* **60**, 1359-1366
140. Hunt, S. C., Xin, Y., Wu, L. L., Cawthon, R. M., Coon, H., Hasstedt, S. J., and Hopkins, P. N. (2006) Sodium bicarbonate cotransporter polymorphisms are associated with baseline and 10-year follow-up blood pressures. *Hypertension* **47**, 532-536
141. Taylor, J. Y., Maddox, R., and Wu, C. Y. (2009) Genetic and environmental risks for high blood pressure among African American mothers and daughters. *Biol Res Nurs* **11**, 53-65
142. Taylor, J. Y., Sampson, D., Taylor, A. D., Caldwell, D., and Sun, Y. V. (2013) Genetic and BMI risks for predicting blood pressure in three generations of West African Dogon women. *Biol Res Nurs* **15**, 105-111
143. Groger, N., Vitzthum, H., Frohlich, H., Kruger, M., Ehmke, H., Braun, T., and Boettger, T. (2012) Targeted mutation of SLC4A5 induces arterial hypertension and renal metabolic acidosis. *Hum Mol Genet* **21**, 1025-1036
144. Cooper, D. S., Saxena, N. C., Yang, H. S., Lee, H. J., Moring, A. G., Lee, A., and Choi, I. (2005) Molecular and functional characterization of the electroneutral Na/HCO_3 cotransporter NBCn1 in rat hippocampal neurons. *J Biol Chem* **280**, 17823-17830
145. Lu, X., Wang, L., Lin, X., Huang, J., Charles Gu, C., He, M., Shen, H., He, J., Zhu, J., Li, H., Hixson, J. E., Wu, T., Dai, J., Lu, L., Shen, C., Chen, S., He, L., Mo, Z., Hao, Y., Mo, X., Yang, X., Li, J., Cao, J., Chen, J., Fan, Z., Li, Y., Zhao, L., Li, H., Lu, F., Yao, C., Yu, L., Xu, L., Mu, J., Wu, X., Deng, Y., Hu, D., Zhang, W., Ji, X., Guo, D., Guo, Z., Zhou, Z., Yang, Z., Wang, R., Yang, J., Zhou, X., Yan, W., Sun, N., Gao, P., and Gu, D. (2015) Genome-wide association study in Chinese identifies novel loci for blood pressure and hypertension. *Hum Mol Genet* **24**, 865-874
146. Ahmed, S., Thomas, G., Ghoussaini, M., Healey, C. S., Humphreys, M. K., Platte, R., Morrison, J., Maranian, M., Pooley, K. A., Luben, R., Eccles, D., Evans, D. G., Fletcher, O., Johnson, N., dos Santos Silva, I., Peto, J., Stratton, M. R., Rahman, N., Jacobs, K., Prentice, R., Anderson, G. L., Rajkovic, A., Curb, J. D., Ziegler, R. G., Berg, C. D., Buys, S. S., McCarty, C. A., Feigelson, H. S., Calle, E. E., Thun, M. J., Diver, W. R., Bojesen, S., Nordestgaard, B. G., Flyger, H., Dork, T., Schurmann, P., Hillemanns, P., Karstens, J. H., Bogdanova, N. V., Antonenkova, N. N., Zalutsky, I. V., Bermisheva, M., Fedorova, S., Khusnutdinova, E., Search, Kang, D., Yoo, K. Y., Noh, D. Y., Ahn, S. H., Devilee, P., van Asperen, C. J., Tollenaar, R. A., Seynaeve, C., Garcia-Closas, M., Lissowska, J., Brinton, L., Peplonska, B., Nevanlinna, H., Heikkinen, T., Aittomaki, K., Blomqvist, C., Hopper, J. L., Southey, M. C., Smith, L., Spurdle, A. B., Schmidt, M. K., Broeks, A., van Hien, R. R., Cornelissen, S., Milne, R. L., Ribas, G., Gonzalez-Neira, A., Benitez, J., Schmutzler, R. K., Burwinkel, B., Bartram, C. R., Meindl, A., Brauch, H., Justenhoven, C., Hamann, U., Consortium, G., Chang-Claude, J., Hein, R., Wang-Gohrke, S., Lindblom, A., Margolin, S., Mannermaa, A., Kosma, V. M., Kataja, V., Olson, J. E., Wang, X., Fredericksen, Z., Giles, G. G., Severi, G., Baglietto, L., English, D. R., Hankinson, S. E., Cox, D. G., Kraft, P., Vatten, L. J., Hveem, K., Kumle, M.,

Sigurdson, A., Doody, M., Bhatti, P., Alexander, B. H., Hooning, M. J., van den Ouweland, A. M., Oldenburg, R. A., Schutte, M., Hall, P., Czene, K., Liu, J., Li, Y., Cox, A., Elliott, G., Brock, I., Reed, M. W., Shen, C. Y., Yu, J. C., Hsu, G. C., Chen, S. T., Anton-Culver, H., Ziogas, A., Andrulis, I. L., Knight, J. A., kConFab, Australian Ovarian Cancer Study, G., Beesley, J., Goode, E. L., Couch, F., Chenevix-Trench, G., Hoover, R. N., Ponder, B. A., Hunter, D. J., Pharoah, P. D., Dunning, A. M., Chanock, S. J., and Easton, D. F. (2009) Newly discovered breast cancer susceptibility loci on 3p24 and 17q23.2. *Nat Genet* **41**, 585-590

147. Chen, W., Zhong, R., Ming, J., Zou, L., Zhu, B., Lu, X., Ke, J., Zhang, Y., Liu, L., Miao, X., and Huang, T. (2012) The SLC4A7 variant rs4973768 is associated with breast cancer risk: evidence from a case-control study and a meta-analysis. *Breast Cancer Res Treat* **136**, 847-857
148. Long, J., Shu, X. O., Cai, Q., Gao, Y. T., Zheng, Y., Li, G., Li, C., Gu, K., Wen, W., Xiang, Y. B., Lu, W., and Zheng, W. (2010) Evaluation of breast cancer susceptibility loci in Chinese women. *Cancer Epidemiol Biomarkers Prev* **19**, 2357-2365
149. Sueta, A., Ito, H., Kawase, T., Hirose, K., Hosono, S., Yatabe, Y., Tajima, K., Tanaka, H., Iwata, H., Iwase, H., and Matsuo, K. (2012) A genetic risk predictor for breast cancer using a combination of low-penetrance polymorphisms in a Japanese population. *Breast Cancer Res Treat* **132**, 711-721
150. Burette, A. C., Weinberg, R. J., Sassani, P., Abuladze, N., Kao, L., and Kurtz, I. (2012) The sodium-driven chloride/bicarbonate exchanger in presynaptic terminals. *J Comp Neurol* **520**, 1481-1492
151. Sinning, A., Liebmann, L., Kougioumtzes, A., Westermann, M., Bruehl, C., and Hubner, C. A. (2011) Synaptic glutamate release is modulated by the Na^+-driven Cl^-/HCO_3^- exchanger Slc4a8. *J Neurosci* **31**, 7300-7311
152. Leviel, F., Hubner, C. A., Houillier, P., Morla, L., El Moghrabi, S., Brideau, G., Hassan, H., Parker, M. D., Kurth, I., Kougioumtzes, A., Sinning, A., Pech, V., Riemondy, K. A., Miller, R. L., Hummler, E., Shull, G. E., Aronson, P. S., Doucet, A., Wall, S. M., Chambrey, R., and Eladari, D. (2010) The Na^+-dependent chloride-bicarbonate exchanger SLC4A8 mediates an electroneutral Na^+ reabsorption process in the renal cortical collecting ducts of mice. *J Clin Invest* **120**, 1627-1635
153. Chen, L. M., Kelly, M. L., Parker, M. D., Bouyer, P., Gill, H. S., Felie, J. M., Davis, B. A., and Boron, W. F. (2008) Expression and localization of Na^+-driven Cl^--HCO_3^- exchanger (SLC4A8) in rodent CNS. *Neuroscience* **153**, 162-174
154. Purkerson, J. M., Heintz, E. V., Nakamori, A., and Schwartz, G. J. (2014) Insights into acidosis-induced regulation of SLC26A4 (pendrin) and SLC4A9 (AE4) transporters using three-dimensional morphometric analysis of beta-intercalated cells. *Am J Physiol Renal Physiol* **307**, F601-611
155. Jacobs, S., Ruusuvuori, E., Sipila, S. T., Haapanen, A., Damkier, H. H., Kurth, I., Hentschke, M., Schweizer, M., Rudhard, Y., Laatikainen, L. M., Tyynela, J., Praetorius, J., Voipio, J., and Hubner, C. A. (2008) Mice with targeted *Slc4a10* gene disruption have small brain ventricles and show reduced neuronal excitability. *Proc Natl Acad Sci U S A* **105**, 311-316
156. Belengeanu, V., Gamage, T. H., Farcas, S., Stoian, M., Andreescu, N., Belengeanu, A., Frengen, E., and Misceo, D. (2014) A de novo 2.3 Mb deletion in 2q24.2q24.3 in a 20-month-old developmentally delayed girl. *Gene* **539**, 168-172

157. Guo, J., Sueta, A., Nakamura, K., Yoshimoto, N., Baba, M., Ishida, N., Hagio, K., Toyama, T., Iwase, H., Tamakoshi, A., and Yamashita, H. (2017) Genetic and environmental factors and serum hormones, and risk of estrogen receptor-positive breast cancer in pre- and postmenopausal Japanese women. *Oncotarget* **8**, 65759-65769
158. Krepischi, A. C., Knijnenburg, J., Bertola, D. R., Kim, C. A., Pearson, P. L., Bijlsma, E., Szuhai, K., Kok, F., Vianna-Morgante, A. M., and Rosenberg, C. (2010) Two distinct regions in 2q24.2-q24.3 associated with idiopathic epilepsy. *Epilepsia* **51**, 2457-2460
159. Sebat, J., Lakshmi, B., Malhotra, D., Troge, J., Lese-Martin, C., Walsh, T., Yamrom, B., Yoon, S., Krasnitz, A., Kendall, J., Leotta, A., Pai, D., Zhang, R., Lee, Y. H., Hicks, J., Spence, S. J., Lee, A. T., Puura, K., Lehtimaki, T., Ledbetter, D., Gregersen, P. K., Bregman, J., Sutcliffe, J. S., Jobanputra, V., Chung, W., Warburton, D., King, M. C., Skuse, D., Geschwind, D. H., Gilliam, T. C., Ye, K., and Wigler, M. (2007) Strong association of *de novo* copy number mutations with autism. *Science* **316**, 445-449
160. Sievers, F., Wilm, A., Dineen, D., Gibson, T. J., Karplus, K., Li, W., Lopez, R., McWilliam, H., Remmert, M., Soding, J., Thompson, J. D., and Higgins, D. G. (2011) Fast, scalable generation of high-quality protein multiple sequence alignments using Clustal Omega. *Mol Syst Biol* **7**, 539
161. McWilliam, H., Li, W., Uludag, M., Squizzato, S., Park, Y. M., Buso, N., Cowley, A. P., and Lopez, R. (2013) Analysis Tool Web Services from the EMBL-EBI. *Nucleic Acids Res* **41**, W597-600
162. Li, W., Cowley, A., Uludag, M., Gur, T., McWilliam, H., Squizzato, S., Park, Y. M., Buso, N., and Lopez, R. (2015) The EMBL-EBI bioinformatics web and programmatic tools framework. *Nucleic Acids Res* **43**, W580-584
163. Ciccarelli, F. D., Doerks, T., von Mering, C., Creevey, C. J., Snel, B., and Bork, P. (2006) Toward automatic reconstruction of a highly resolved tree of life. *Science* **311**, 1283-1287
164. Alka, K., and Casey, J. R. (2014) Bicarbonate transport in health and disease. *IUBMB Life* **66**, 596-615
165. Loganathan, S. K., Lukowski, C. M., and Casey, J. R. (2016) The cytoplasmic domain is essential for transport function of the integral membrane transport protein SLC4A11. *Am J Physiol Cell Physiol* **310**, C161-174
166. Grinstein, S., Ship, S., and Rothstein, A. (1978) Anion transport in relation to proteolytic dissection of band 3 protein. *Biochimica et biophysica acta* **507**, 294-304
167. Lepke, S., and Passow, H. (1976) Effects of incorporated trypsin on anion exchange and membrane proteins in human red blood cell ghosts. *Biochimica et biophysica acta* **455**, 353-370
168. Stewart, A. K., Chernova, M. N., Shmukler, B. E., Wilhelm, S., and Alper, S. L. (2002) Regulation of AE2-mediated Cl^- transport by intracellular or by extracellular pH requires highly conserved amino acid residues of the AE2 NH_2-terminal cytoplasmic domain. *J Gen Physiol* **120**, 707-722
169. Jiang, J., Magilnick, N., Tsirulnikov, K., Abuladze, N., Atanasov, I., Ge, P., Narla, M., Pushkin, A., Zhou, Z. H., and Kurtz, I. (2013) Single particle electron microscopy analysis of the bovine anion exchanger 1 reveals a flexible linker connecting the cytoplasmic and membrane domains. *PLoS One* **8**, e55408
170. Kao, L., Sassani, P., Azimov, R., Pushkin, A., Abuladze, N., Peti-Peterdi, J., Liu, W., Newman, D., and Kurtz, I. (2008) Oligomeric structure and minimal functional unit of

the electrogenic sodium bicarbonate cotransporter NBCe1-A. *J Biol Chem* **283**, 26782-26794
171. Yamaguchi, T., Ikeda, Y., Abe, Y., Kuma, H., Kang, D., Hamasaki, N., and Hirai, T. (2010) Structure of the membrane domain of human erythrocyte anion exchanger 1 revealed by electron crystallography. *J Mol Biol* **397**, 179-189
172. Steck, T. L. (1972) Cross-linking the major proteins of the isolated erythrocyte membrane. *J Mol Biol* **66**, 295-305
173. Reithmeier, R. A. (1979) Fragmentation of the band 3 polypeptide from human erythrocyte membranes. Size and detergent binding of the membrane-associated domain. *J Biol Chem* **254**, 3054-3060
174. Jennings, M. L. (1984) Oligomeric structure and the anion transport function of human erythrocyte band 3 protein. *J Membr Biol* **80**, 105-117
175. Casey, J. R., and Reithmeier, R. A. (1991) Analysis of the oligomeric state of Band 3, the anion transport protein of the human erythrocyte membrane, by size exclusion high performance liquid chromatography. Oligomeric stability and origin of heterogeneity. *J Biol Chem* **266**, 15726-15737
176. Zhang, D., Kiyatkin, A., Bolin, J. T., and Low, P. S. (2000) Crystallographic structure and functional interpretation of the cytoplasmic domain of erythrocyte membrane band 3. *Blood* **96**, 2925-2933
177. Gill, H. S., and Boron, W. F. (2006) Preliminary X-ray diffraction analysis of the cytoplasmic N-terminal domain of the Na/HCO_3 cotransporter NBCe1-A. *Acta Crystallogr Sect F Struct Biol Cryst Commun* **62**, 534-537
178. Shnitsar, V., Li, J., Li, X., Calmettes, C., Basu, A., Casey, J. R., Moraes, T. F., and Reithmeier, R. A. (2013) A substrate access tunnel in the cytosolic domain is not an essential feature of the solute carrier 4 (SLC4) family of bicarbonate transporters. *J Biol Chem* **288**, 33848-33860
179. Zhang, Y., Chernova, M. N., Stuart-Tilley, A. K., Jiang, L., and Alper, S. L. (1996) The cytoplasmic and transmembrane domains of AE2 both contribute to regulation of anion exchange by pH. *J Biol Chem* **271**, 5741-5749
180. Quade, B. N., Marshall, A., and Parker, M. D. (2020) The pH dependence of the Slc4a11-mediated H^+ conductance is influenced by intracellular lysine residues and modified by disease-linked mutations. *Am J Physiol Cell Physiol*, PMID 32520610
181. Low, P. S. (1986) Structure and function of the cytoplasmic domain of band 3: center of erythrocyte membrane-peripheral protein interactions. *Biochimica et biophysica acta* **864**, 145-167
182. McAlear, S. D., Liu, X., Williams, J. B., McNicholas-Bevensee, C. M., and Bevensee, M. O. (2006) Electrogenic Na/HCO_3 cotransporter (NBCe1) variants expressed in *Xenopus* oocytes: functional comparison and roles of the amino and carboxy termini. *J Gen Physiol* **127**, 639-658
183. Espiritu, D. J., Bernardo, A. A., and Arruda, J. A. (2006) Role of NH_2 and COOH termini in targeting, stability, and activity of sodium bicarbonate cotransporter 1. *Am J Physiol Renal Physiol* **291**, F588-596
184. Macara, I. G., and Cantley, L. C. (1981) Interactions between transport inhibitors at the anion binding sites of the band 3 dimer. *Biochemistry* **20**, 5095-5105

185. Macara, I. G., and Cantley, L. C. (1981) Mechanism of anion exchange across the red cell membrane by band 3: interactions between stilbenedisulfonate and NAP-taurine binding sites. *Biochemistry* **20**, 5695-5701
186. Reithmeier, R. A., Casey, J. R., Kalli, A. C., Sansom, M. S., Alguel, Y., and Iwata, S. (2016) Band 3, the human red cell chloride/bicarbonate anion exchanger (AE1, SLC4A1), in a structural context. *Biochimica et biophysica acta* **1858**, 1507-1532
187. Passow, H. (1986) Molecular aspects of band 3 protein-mediated anion transport across the red blood cell membrane. *Rev Physiol Biochem Pharmacol* **103**, 61-203
188. Wang, C., Sun, B., Zhang, X., Huang, X., Zhang, M., Guo, H., Chen, X., Huang, F., Chen, T., Mi, H., Yu, F., Liu, L. N., and Zhang, P. (2019) Structural mechanism of the active bicarbonate transporter from cyanobacteria. *Nat Plants* **5**, 1184-1193
189. Walter, J. D., Sawicka, M., and Dutzler, R. (2019) Cryo-EM structures and functional characterization of murine Slc26a9 reveal mechanism of uncoupled chloride transport. *Elife* **8**, e46986
190. Parker, M. D., Ourmozdi, E. P., and Tanner, M. J. (2001) Human BTR1, a new bicarbonate transporter superfamily member and human AE4 from kidney. *Biochem Biophys Res Commun* **282**, 1103-1109
191. Park, M., Li, Q., Shcheynikov, N., Zeng, W., and Muallem, S. (2004) NaBC1 is a ubiquitous electrogenic Na^+-coupled borate transporter essential for cellular boron homeostasis and cell growth and proliferation. *Mol Cell* **16**, 331-341
192. Coudray, N., S, L. S., Lasala, R., Zhang, Z., Clark, K. M., Dumont, M. E., Rohou, A., Beckstein, O., and Stokes, D. L. (2017) Structure of the SLC4 transporter Bor1p in an inward-facing conformation. *Protein science : a publication of the Protein Society* **26**, 130-145
193. Thurtle-Schmidt, B. H., and Stroud, R. M. (2016) Structure of Bor1 supports an elevator transport mechanism for SLC4 anion exchangers. *Proc Natl Acad Sci U S A* **113**, 10542-10546
194. Lu, F., Li, S., Jiang, Y., Jiang, J., Fan, H., Lu, G., Deng, D., Dang, S., Zhang, X., Wang, J., and Yan, N. (2011) Structure and mechanism of the uracil transporter UraA. *Nature* **472**, 243-246
195. Geertsma, E. R., Chang, Y.-N., Shaik, F. R., Neldner, Y., Pardon, E., Steyaert, J., and Dutzler, R. (2015) Structure of a prokaryotic fumarate transporter reveals the architecture of the SLC26 family. *Nat Struct Mol Biol* **22**, 803-808
196. Alguel, Y., Amillis, S., Leung, J., Lambrinidis, G., Capaldi, S., Scull, N. J., Craven, G., Iwata, S., Armstrong, A., Mikros, E., Diallinas, G., Cameron, A. D., and Byrne, B. (2016) Structure of eukaryotic purine/H^+ symporter UapA suggests a role for homodimerization in transport activity. *Nat Commun* **7**, 11336
197. Jardetzky, O. (1966) Simple allosteric model for membrane pumps. *Nature* **211**, 969-970
198. Drew, D., and Boudker, O. (2016) Shared Molecular Mechanisms of Membrane Transporters. *Annu Rev Biochem* **85**, 543-572
199. Forrest, L. R., and Rudnick, G. (2009) The rocking bundle: a mechanism for ion-coupled solute flux by symmetrical transporters. *Physiology (Bethesda)* **24**, 377-386
200. Vergara-Jaque, A., Fenollar-Ferrer, C., Kaufmann, D., and Forrest, L. R. (2015) Repeat-swap homology modeling of secondary active transporters: updated protocol and prediction of elevator-type mechanisms. *Front Pharmacol* **6**, 183

201. Chang, Y. N., and Geertsma, E. R. (2017) The novel class of seven transmembrane segment inverted repeat carriers. *Biol Chem* **398**, 165-174
202. Ficici, E., Faraldo-Gomez, J. D., Jennings, M. L., and Forrest, L. R. (2017) Asymmetry of inverted-topology repeats in the AE1 anion exchanger suggests an elevator-like mechanism. *J Gen Physiol* **149**, 1149-1164
203. Schrodinger, LLC. (2015) The PyMOL Molecular Graphics System, Version 1.8.
204. Fairbanks, G., Steck, T. L., and Wallach, D. F. (1971) Electrophoretic analysis of the major polypeptides of the human erythrocyte membrane. *Biochemistry* **10**, 2606-2617
205. Tanner, M. J., Martin, P. G., and High, S. (1988) The complete amino acid sequence of the human erythrocyte membrane anion-transport protein deduced from the cDNA sequence. *Biochem J* **256**, 703-712
206. Ho, M. K., and Guidotti, G. (1975) A membrane protein from human erythrocytes involved in anion exchange. *J Biol Chem* **250**, 675-683
207. Jennings, M. L. (1976) Proton fluxes associated with erythrocyte membrane anion exchange. *J Membr Biol* **28**, 187-205
208. Knauf, P. A. (1979) Erythrocyte Anion Exchange and Band 3 Protein: Transport Kinetics and Molecular Structure. *Current Topics in Membranes and Transport* **12**, 249-363
209. Jennings, M. L. (2013) Transport of H_2S and HS^- across the human red blood cell membrane: rapid H_2S diffusion and AE1-mediated Cl^-/HS^- exchange. *Am J Physiol Cell Physiol* **305**, C941-950
210. Steck, T. L., Ramos, B., and Strapazon, E. (1976) Proteolytic dissection of band 3, the predominant transmembrane polypeptide of the human erythrocyte membrane. *Biochemistry* **15**, 1153-1161
211. Lux, S. E., John, K. M., Kopito, R. R., and Lodish, H. F. (1989) Cloning and characterization of band 3, the human erythrocyte anion-exchange protein (AE1). *Proc Natl Acad Sci U S A* **86**, 9089-9093
212. Kollert-Jons, A., Wagner, S., Hubner, S., Appelhans, H., and Drenckhahn, D. (1993) Anion exchanger 1 in human kidney and oncocytoma differs from erythroid AE1 in its NH_2 terminus. *Am J Physiol* **265**, F813-821
213. Bohr, C., Hasselbalch, K. A., and Krogh, A. (1904) Uber einen in biologischer Beziehung wichtigen Einfluss, den die Kohlensaurespannung des Blutes auf dessen Sauerstoffbindung ubt. *Skand. Arch. Physiol.* **16**, 402-412
214. Sterling, D., Reithmeier, R. A., and Casey, J. R. (2001) A transport metabolon. Functional interaction of carbonic anhydrase II and chloride/bicarbonate exchangers. *J Biol Chem* **276**, 47886-47894
215. McMurtrie, H. L., Cleary, H. J., Alvarez, B. V., Loiselle, F. B., Sterling, D., Morgan, P. E., Johnson, D. E., and Casey, J. R. (2004) The bicarbonate transport metabolon. *J Enzyme Inhib Med Chem* **19**, 231-236
216. Bennett, V. (1979) Immunoreactive forms of human erythrocyte ankyrin are present in diverse cells and tissues. *Nature* **281**, 597-599
217. Thevenin, B. J., and Low, P. S. (1990) Kinetics and regulation of the ankyrin-band 3 interaction of the human red blood cell membrane. *J Biol Chem* **265**, 16166-16172
218. Van Dort, H. M., Moriyama, R., and Low, P. S. (1998) Effect of band 3 subunit equilibrium on the kinetics and affinity of ankyrin binding to erythrocyte membrane vesicles. *J Biol Chem* **273**, 14819-14826

219. Hanspal, M., Golan, D. E., Smockova, Y., Yi, S. J., Cho, M. R., Liu, S. C., and Palek, J. (1998) Temporal synthesis of band 3 oligomers during terminal maturation of mouse erythroblasts. Dimers and tetramers exist in the membrane as preformed stable species. *Blood* **92**, 329-338
220. Tsuji, A., Kawasaki, K., Ohnishi, S., Merkle, H., and Kusumi, A. (1988) Regulation of band 3 mobilities in erythrocyte ghost membranes by protein association and cytoskeletal meshwork. *Biochemistry* **27**, 7447-7452
221. Low, P. S., Willardson, B. M., Mohandas, N., Rossi, M., and Shohet, S. (1991) Contribution of the band 3-ankyrin interaction to erythrocyte membrane mechanical stability. *Blood* **77**, 1581-1586
222. Pries, A. R., Secomb, T. W., and Gaehtgens, P. (1996) Biophysical aspects of blood flow in the microvasculature. *Cardiovasc Res* **32**, 654-667
223. Pasternack, G. R., Anderson, R. A., Leto, T. L., and Marchesi, V. T. (1985) Interactions between protein 4.1 and band 3. An alternative binding site for an element of the membrane skeleton. *J Biol Chem* **260**, 3676-3683
224. Rogalski, A. A., Steck, T. L., and Waseem, A. (1989) Association of glyceraldehyde-3-phosphate dehydrogenase with the plasma membrane of the intact human red blood cell. *J Biol Chem* **264**, 6438-6446
225. Jenkins, J. D., Madden, D. P., and Steck, T. L. (1984) Association of phosphofructokinase and aldolase with the membrane of the intact erythrocyte. *J Biol Chem* **259**, 9374-9378
226. Murthy, S. N., Liu, T., Kaul, R. K., Kohler, H., and Steck, T. L. (1981) The aldolase-binding site of the human erythrocyte membrane is at the NH_2 terminus of band 3. *J Biol Chem* **256**, 11203-11208
227. Walder, J. A., Chatterjee, R., Steck, T. L., Low, P. S., Musso, G. F., Kaiser, E. T., Rogers, P. H., and Arnone, A. (1984) The interaction of hemoglobin with the cytoplasmic domain of band 3 of the human erythrocyte membrane. *J Biol Chem* **259**, 10238-10246
228. Salhany, J. M., and Cassoly, R. (1989) Kinetics of p-mercuribenzoate binding to sulfhydryl groups on the isolated cytoplasmic fragment of band 3 protein. Effect of hemoglobin binding on the conformation. *J Biol Chem* **264**, 1399-1404
229. Waugh, S. M., and Low, P. S. (1985) Hemichrome binding to band 3: nucleation of Heinz bodies on the erythrocyte membrane. *Biochemistry* **24**, 34-39
230. Harrison, M. L., Isaacson, C. C., Burg, D. L., Geahlen, R. L., and Low, P. S. (1994) Phosphorylation of human erythrocyte band 3 by endogenous $p72^{syk}$. *J Biol Chem* **269**, 955-959
231. Perrotta, S., Borriello, A., Scaloni, A., De Franceschi, L., Brunati, A. M., Turrini, F., Nigro, V., del Giudice, E. M., Nobili, B., Conte, M. L., Rossi, F., Iolascon, A., Donella-Deana, A., Zappia, V., Poggi, V., Anong, W., Low, P., Mohandas, N., and Della Ragione, F. (2005) The N-terminal 11 amino acids of human erythrocyte band 3 are critical for aldolase binding and protein phosphorylation: implications for band 3 function. *Blood* **106**, 4359-4366
232. Peters, L. L., Shivdasani, R. A., Liu, S. C., Hanspal, M., John, K. M., Gonzalez, J. M., Brugnara, C., Gwynn, B., Mohandas, N., Alper, S. L., Orkin, S. H., and Lux, S. E. (1996) Anion exchanger 1 (band 3) is required to prevent erythrocyte membrane surface loss but not to form the membrane skeleton. *Cell* **86**, 917-927

233. Inaba, M., Yawata, A., Koshino, I., Sato, K., Takeuchi, M., Takakuwa, Y., Manno, S., Yawata, Y., Kanzaki, A., Sakai, J., Ban, A., Ono, K., and Maede, Y. (1996) Defective anion transport and marked spherocytosis with membrane instability caused by hereditary total deficiency of red cell band 3 in cattle due to a nonsense mutation. *J Clin Invest* **97**, 1804-1817
234. Southgate, C. D., Chishti, A. H., Mitchell, B., Yi, S. J., and Palek, J. (1996) Targeted disruption of the murine erythroid band 3 gene results in spherocytosis and severe haemolytic anaemia despite a normal membrane skeleton. *Nat Genet* **14**, 227-230
235. Jarolim, P., Palek, J., Amato, D., Hassan, K., Sapak, P., Nurse, G. T., Rubin, H. L., Zhai, S., Sahr, K. E., and Liu, S. C. (1991) Deletion in erythrocyte band 3 gene in malaria-resistant Southeast Asian ovalocytosis. *Proc Natl Acad Sci U S A* **88**, 11022-11026
236. Tanner, M. J., Bruce, L., Martin, P. G., Rearden, D. M., and Jones, G. L. (1991) Melanesian hereditary ovalocytes have a deletion in red cell band 3. *Blood* **78**, 2785-2786
237. Barneaud-Rocca, D., Pellissier, B., Borgese, F., and Guizouarn, H. (2011) Band 3 missense mutations and stomatocytosis: insight into the molecular mechanism responsible for monovalent cation leak. *Int J Cell Biol* **2011**, 136802
238. Moras, M., Lefevre, S. D., and Ostuni, M. A. (2017) From Erythroblasts to Mature Red Blood Cells: Organelle Clearance in Mammals. *Front Physiol* **8**, 1076
239. Kay, M. M. (1975) Mechanism of removal of senescent cells by human macrophages *in situ*. *Proc Natl Acad Sci U S A* **72**, 3521-3525
240. Lutz, H. U., Flepp, R., and Stringaro-Wipf, G. (1984) Naturally occurring autoantibodies to exoplasmic and cryptic regions of band 3 protein, the major integral membrane protein of human red blood cells. *J Immunol* **133**, 2610-2618
241. Lutz, H. U., Bussolino, F., Flepp, R., Fasler, S., Stammler, P., Kazatchkine, M. D., and Arese, P. (1987) Naturally occurring anti-band-3 antibodies and complement together mediate phagocytosis of oxidatively stressed human erythrocytes. *Proc Natl Acad Sci U S A* **84**, 7368-7372
242. Kannan, R., Yuan, J., and Low, P. S. (1991) Isolation and partial characterization of antibody- and globin-enriched complexes from membranes of dense human erythrocytes. *Biochem J* **278 (Pt 1)**, 57-62
243. Badior, K. E., and Casey, J. R. (2018) Molecular mechanism for the red blood cell senescence clock. *IUBMB Life* **70**, 32-40
244. Sahr, K. E., Taylor, W. M., Daniels, B. P., Rubin, H. L., and Jarolim, P. (1994) The structure and organization of the human erythroid anion exchanger (AE1) gene. *Genomics* **24**, 491-501
245. Brosius, F. C., 3rd, Alper, S. L., Garcia, A. M., and Lodish, H. F. (1989) The major kidney band 3 gene transcript predicts an amino-terminal truncated band 3 polypeptide. *J Biol Chem* **264**, 7784-7787
246. Eladari, D., and Kumai, Y. (2015) Renal acid-base regulation: new insights from animal models. *Pflugers Arch* **467**, 1623-1641
247. Cordat, E., and Casey, J. R. (2009) Bicarbonate transport in cell physiology and disease. *Biochem J* **417**, 423-439
248. Devonald, M. A., Smith, A. N., Poon, J. P., Ihrke, G., and Karet, F. E. (2003) Non-polarized targeting of AE1 causes autosomal dominant distal renal tubular acidosis. *Nat Genet* **33**, 125-127

249. Chen, J., Vijayakumar, S., Li, X., and Al-Awqati, Q. (1998) Kanadaptin is a protein that interacts with the kidney but not the erythroid form of band 3. *J Biol Chem* **273**, 1038-1043
250. Bertocchio, J. P., Genetet, S., Da Costa, L., Walsh, S. B., Knebelmann, B., Galimand, J., Bessenay, L., Guitton, C., De Lafaille, R., Vargas-Poussou, R., Eladari, D., and Mouro-Chanteloup, I. (2020) Red Blood Cell AE1/Band 3 Transports in Dominant Distal Renal Tubular Acidosis Patients. *Kidney Int Rep* **5**, 348-357
251. Williamson, R. C., Brown, A. C., Mawby, W. J., and Toye, A. M. (2008) Human kidney anion exchanger 1 localisation in MDCK cells is controlled by the phosphorylation status of two critical tyrosines. *J Cell Sci* **121**, 3422-3432
252. Patterson, S. T., Li, J., Kang, J. A., Wickrema, A., Williams, D. B., and Reithmeier, R. A. (2009) Loss of specific chaperones involved in membrane glycoprotein biosynthesis during the maturation of human erythroid progenitor cells. *J Biol Chem* **284**, 14547-14557
253. Groves, J. D., and Tanner, M. J. (1992) Glycophorin A facilitates the expression of human band 3-mediated anion transport in *Xenopus* oocytes. *J Biol Chem* **267**, 22163-22170
254. Groves, J. D., and Tanner, M. J. (1994) The effects of glycophorin A on the expression of the human red cell anion transporter (band 3) in *Xenopus* oocytes. *J Membr Biol* **140**, 81-88
255. Young, M. T., Beckmann, R., Toye, A. M., and Tanner, M. J. (2000) Red-cell glycophorin A-band 3 interactions associated with the movement of band 3 to the cell surface. *Biochem J* **350 Pt 1**, 53-60
256. Pang, A. J., and Reithmeier, R. A. (2009) Interaction of anion exchanger 1 and glycophorin A in human erythroleukaemic K562 cells. *Biochem J* **421**, 345-356
257. Yenchitsomanus, P. T., Vasuvattakul, S., Kirdpon, S., Wasanawatana, S., Susaengrat, W., Sreethiphayawan, S., Chuawatana, D., Mingkum, S., Sawasdee, N., Thuwajit, P., Wilairat, P., Malasit, P., and Nimmannit, S. (2002) Autosomal recessive distal renal tubular acidosis caused by G701D mutation of *anion exchanger 1* gene. *Am J Kidney Dis* **40**, 21-29
258. Lepke, S., Fasold, H., Pring, M., and Passow, H. (1976) A study of the relationship between inhibition of anion exchange and binding to the red blood cell membrane of 4,4'-diisothiocyano stilbene-2,2'-disulfonic acid (DIDS) and its dihydro derivative (H_2DIDS). *J Membr Biol* **29**, 147-177
259. Grinstein, S., McCulloch, L., and Rothstein, A. (1979) Transmembrane effects of irreversible inhibitors of anion transport in red blood cells. Evidence for mobile transport sites. *J Gen Physiol* **73**, 493-514
260. Gunn, R. B., and Frohlich, O. (1979) Asymmetry in the mechanism for anion exchange in human red blood cell membranes. Evidence for reciprocating sites that react with one transported anion at a time. *J Gen Physiol* **74**, 351-374
261. Furuya, W., Tarshis, T., Law, F. Y., and Knauf, P. A. (1984) Transmembrane effects of intracellular chloride on the inhibitory potency of extracellular H_2DIDS. Evidence for two conformations of the transport site of the human erythrocyte anion exchange protein. *J Gen Physiol* **83**, 657-681
262. Yu, X., Yang, G., Yan, C., Baylon, J. L., Jiang, J., Fan, H., Lu, G., Hasegawa, K., Okumura, H., Wang, T., Tajkhorshid, E., Li, S., and Yan, N. (2017) Dimeric structure of

the uracil:proton symporter UraA provides mechanistic insights into the SLC4/23/26 transporters. *Cell Res* **27**, 1020-1033
263. Karbach, D., Staub, M., Wood, P. G., and Passow, H. (1998) Effect of site-directed mutagenesis of the arginine residues 509 and 748 on mouse band 3 protein-mediated anion transport. *Biochimica et biophysica acta* **1371**, 114-122
264. Falke, J. J., and Chan, S. I. (1985) Evidence that anion transport by band 3 proceeds via a ping-pong mechanism involving a single transport site. A ^{35}Cl NMR study. *J Biol Chem* **260**, 9537-9544
265. Tang, X. B., Fujinaga, J., Kopito, R., and Casey, J. R. (1998) Topology of the region surrounding Glu681 of human AE1 protein, the erythrocyte anion exchanger. *J Biol Chem* **273**, 22545-22553
266. Chernova, M. N., Jiang, L., Crest, M., Hand, M., Vandorpe, D. H., Strange, K., and Alper, S. L. (1997) Electrogenic sulfate/chloride exchange in *Xenopus* oocytes mediated by murine AE1 E699Q. *J Gen Physiol* **109**, 345-360
267. Jennings, M. L., and Smith, J. S. (1992) Anion-proton cotransport through the human red blood cell band 3 protein. Role of glutamate 681. *J Biol Chem* **267**, 13964-13971
268. Jennings, M. L., and Anderson, M. P. (1987) Chemical modification and labeling of glutamate residues at the stilbenedisulfonate site of human red blood cell band 3 protein. *J Biol Chem* **262**, 1691-1697
269. Lambert, A., and Lowe, A. G. (1980) Chloride-bicarbonate exchange in human red cells measured using a stopped flow apparatus. *J Physiol* **306**, 431-443
270. Ideguchi, H., Okubo, K., Ishikawa, A., Futata, Y., and Hamasaki, N. (1992) Band 3-Memphis is associated with a lower transport rate of phosphoenolpyruvate. *Br J Haematol* **82**, 122-125
271. Cabantchik, Z. I., and Rothstein, A. (1974) Membrane proteins related to anion permeability of human red blood cells. I. Localization of disulfonic stilbene binding sites in proteins involved in permeation. *J Membr Biol* **15**, 207-226
272. Cabantchik, Z. I., and Rothstein, A. (1972) The nature of the membrane sites controlling anion permeability of human red blood cells as determined by studies with disulfonic stilbene derivatives. *J Membr Biol* **10**, 311-330
273. Zaki, L., Fasold, H., Schuhmann, B., and Passow, H. (1975) Chemical modification of membrane proteins in relation to inhibition of anion exchange in human red blood cells. *J Cell Physiol* **86**, 471-494
274. Jennings, M. L., and Nicknish, J. S. (1985) Localization of a site of intermolecular cross-linking in human red blood cell band 3 protein. *J Biol Chem* **260**, 5472-5479
275. Okubo, K., Kang, D., Hamasaki, N., and Jennings, M. L. (1994) Red blood cell band 3. Lysine 539 and lysine 851 react with the same H_2DIDS (4,4'-diisothiocyanodihydrostilbene-2,2'-disulfonic acid) molecule. *J Biol Chem* **269**, 1918-1926
276. Jennings, M. L., and Passow, H. (1979) Anion transport across the erythrocyte membrane, *in situ* proteolysis of band 3 protein, and cross-linking of proteolytic fragments by 4,4'-diisothiocyano dihydrostilbene-2,2'-disulfonate. *Biochimica et biophysica acta* **554**, 498-519
277. Garcia, A. M., and Lodish, H. F. (1989) Lysine 539 of human band 3 is not essential for ion transport or inhibition by stilbene disulfonates. *J Biol Chem* **264**, 19607-19613

278. Bartel, D., Hans, H., and Passow, H. (1989) Identification by site-directed mutagenesis of Lys-558 as the covalent attachment site of H_2DIDS in the mouse erythroid band 3 protein. *Biochimica et biophysica acta* **985**, 355-358
279. Wood, P. G., Muller, H., Sovak, M., and Passow, H. (1992) Role of Lys 558 and Lys 869 in substrate and inhibitor binding to the murine band 3 protein: a study of the effects of site-directed mutagenesis of the band 3 protein expressed in the oocytes of *Xenopus laevis*. *J Membr Biol* **127**, 139-148
280. Rao, A., Martin, P., Reithmeier, R. A., and Cantley, L. C. (1979) Location of the stilbenedisulfonate binding site of the human erythrocyte anion-exchange system by resonance energy transfer. *Biochemistry* **18**, 4505-4516
281. Landolt-Marticorena, C., Casey, J. R., and Reithmeier, R. A. (1995) Transmembrane helix-helix interactions and accessibility of H_2DIDS on labelled band 3, the erythrocyte anion exchange protein. *Mol Membr Biol* **12**, 173-182
282. Knauf, P. A., Law, F. Y., Leung, T. W., and Atherton, S. J. (2004) Relocation of the disulfonic stilbene sites of AE1 (band 3) on the basis of fluorescence energy transfer measurements. *Biochemistry* **43**, 11917-11931
283. Jennings, M. L., Whitlock, J., and Shinde, A. (1998) Pre-steady state transport by erythrocyte band 3 protein: uphill countertransport induced by the impermeant inhibitor H_2DIDS. *Biochem Cell Biol* **76**, 807-813
284. Tang, X. B., and Casey, J. R. (1999) Trapping of inhibitor-induced conformational changes in the erythrocyte membrane anion exchanger AE1. *Biochemistry* **38**, 14565-14572
285. Cousin, J. L., and Motais, R. (1979) Inhibition of anion permeability by amphiphilic compounds in human red cell: evidence for an interaction of niflumic acid with the band 3 protein. *J Membr Biol* **46**, 125-153
286. Cousin, J. L., and Motais, R. (1982) Inhibition of anion transport in the red blood cell by anionic amphiphilic compounds. I. Determination of the flufenamate-binding site by proteolytic dissection of the band 3 protein. *Biochimica et biophysica acta* **687**, 147-155
287. Cousin, J. L., and Motais, R. (1982) Inhibition of anion transport in the red blood cell by anionic amphiphilic compounds. II. Chemical properties of the flufenamate-binding site on the band 3 protein. *Biochimica et biophysica acta* **687**, 156-164
288. Knauf, P. A., Raha, N. M., and Spinelli, L. J. (2000) The noncompetitive inhibitor WW781 senses changes in erythrocyte anion exchanger (AE1) transport site conformation and substrate binding. *J Gen Physiol* **115**, 159-173
289. Alper, S. L., Chernova, M. N., Williams, J., Zasloff, M., Law, F. Y., and Knauf, P. A. (1998) Differential inhibition of AE1 and AE2 anion exchangers by oxonol dyes and by novel polyaminosterol analogs of the shark antibiotic squalamine. *Biochem Cell Biol* **76**, 799-806
290. Forman, S. A., Verkman, A. S., Dix, J. A., and Solomon, A. K. (1982) Interaction of phloretin with the anion transport protein of the red blood cell membrane. *Biochimica et biophysica acta* **689**, 531-538
291. Brazy, P. C., and Gunn, R. B. (1976) Furosemide inhibition of chloride transport in human red blood cells. *J Gen Physiol* **68**, 583-599
292. Jennings, M. L. (1982) Reductive methylation of the two 4,4'-diisothiocyanodihydrostilbene-2,2'-disulfonate-binding lysine residues of band 3, the human erythrocyte anion transport protein. *J Biol Chem* **257**, 7554-7559

293. Rudloff, V., Lepke, S., and Passow, H. (1983) Inhibition of anion transport across the red cell membrane by dinitrophenylation of a specific lysine residue at the H_2DIDS binding site of the band 3 protein. *FEBS Lett* **163**, 14-21
294. Cabantchik, I. Z., Balshin, M., Breuer, W., and Rothstein, A. (1975) Pyridoxal phosphate. An anionic probe for protein amino groups exposed on the outer and inner surfaces of intact human red blood cells. *J Biol Chem* **250**, 5130-5136
295. Dzierzak, E., and Philipsen, S. (2013) Erythropoiesis: development and differentiation. *Cold Spring Harb Perspect Med* **3**, a011601
296. Dacie, J. V., and White, J. C. (1949) Erythropoiesis with Particular Reference to its Study by Biopsy of Human Bone Marrow: A Review. *J Clin Pathol* **2**, 1-32
297. Waugh, R. E., McKenney, J. B., Bauserman, R. G., Brooks, D. M., Valeri, C. R., and Snyder, L. M. (1997) Surface area and volume changes during maturation of reticulocytes in the circulation of the baboon. *J Lab Clin Med* **129**, 527-535
298. Da Costa, L., Mohandas, N., Sorette, M., Grange, M. J., Tchernia, G., and Cynober, T. (2001) Temporal differences in membrane loss lead to distinct reticulocyte features in hereditary spherocytosis and in immune hemolytic anemia. *Blood* **98**, 2894-2899
299. Blanc, L., Liu, J., Vidal, M., Chasis, J. A., An, X., and Mohandas, N. (2009) The water channel aquaporin-1 partitions into exosomes during reticulocyte maturation: implication for the regulation of cell volume. *Blood* **114**, 3928-3934
300. Liu, J., Guo, X., Mohandas, N., Chasis, J. A., and An, X. (2010) Membrane remodeling during reticulocyte maturation. *Blood* **115**, 2021-2027
301. Johnstone, R. M., Adam, M., Hammond, J. R., Orr, L., and Turbide, C. (1987) Vesicle formation during reticulocyte maturation. Association of plasma membrane activities with released vesicles (exosomes). *J Biol Chem* **262**, 9412-9420
302. Chasis, J. A., Prenant, M., Leung, A., and Mohandas, N. (1989) Membrane assembly and remodeling during reticulocyte maturation. *Blood* **74**, 1112-1120
303. Werre, J. M., Willekens, F. L., Bosch, F. H., de Haans, L. D., van der Vegt, S. G., van den Bos, A. G., and Bosman, G. J. (2004) The red cell revisited - matters of life and death. *Cell Mol Biol (Noisy-le-grand)* **50**, 139-145
304. Bosman, G. J., Willekens, F. L., and Werre, J. M. (2005) Erythrocyte aging: a more than superficial resemblance to apoptosis? *Cell Physiol Biochem* **16**, 1-8
305. Elgsaeter, A., Stokke, B. T., Mikkelsen, A., and Branton, D. (1986) The molecular basis of erythrocyte shape. *Science* **234**, 1217-1223
306. Picas, L., Rico, F., Deforet, M., and Scheuring, S. (2013) Structural and mechanical heterogeneity of the erythrocyte membrane reveals hallmarks of membrane stability. *ACS Nano* **7**, 1054-1063
307. Viallat, A., and Abkarian, M. (2014) Red blood cell: from its mechanics to its motion in shear flow. *Int J Lab Hematol* **36**, 237-243
308. Lasch, J., Kullertz, G., and Opalka, J. R. (2000) Separation of erythrocytes into age-related fractions by density or size? Counterflow centrifugation. *Clin Chem Lab Med* **38**, 629-632
309. Marchesi, V. T., and Steers, E., Jr. (1968) Selective solubilization of a protein component of the red cell membrane. *Science* **159**, 203-204
310. Yu, J., Fischman, D. A., and Steck, T. L. (1973) Selective solubilization of proteins and phospholipids from red blood cell membranes by nonionic detergents. *J Supramol Struct* **1**, 233-248

311. Byers, T. J., and Branton, D. (1985) Visualization of the protein associations in the erythrocyte membrane skeleton. *Proc Natl Acad Sci U S A* **82**, 6153-6157
312. Liu, S. C., Windisch, P., Kim, S., and Palek, J. (1984) Oligomeric states of spectrin in normal erythrocyte membranes: biochemical and electron microscopic studies. *Cell* **37**, 587-594
313. Bennett, V., and Stenbuck, P. J. (1980) Association between ankyrin and the cytoplasmic domain of band 3 isolated from the human erythrocyte membrane. *J Biol Chem* **255**, 6424-6432
314. Weed, R. I., Reed, C. F., and Berg, G. (1963) Is hemoglobin an essential structural component of human erythrocyte membranes? *J Clin Invest* **42**, 581-588
315. Braunitzer, G. (1958) [Comparative studies on the primary structure of protein components of some hemoglobins]. *Hoppe Seylers Z Physiol Chem* **312**, 72-84
316. G.S., A. (1925) The hemoglobin system. IV. The oxygen dissociation curve of hemoglobin. *J Biol Chem*, 529-545
317. Hill, A. V. (1910) The possible effects of the aggregation of the molecules of haemoglobin on its dissociation curves. *J. Physiol.* **40**, (Suppl): iv-vii
318. Perutz, M. F., Rossmann, M. G., Cullis, A. F., Muirhead, H., Will, G., and North, A. C. (1960) Structure of haemoglobin: a three-dimensional Fourier synthesis at 5.5 Å. resolution, obtained by X-ray analysis. *Nature* **185**, 416-422
319. Cartron, J. P., and Rahuel, C. (1992) Human erythrocyte glycophorins: protein and gene structure analyses. *Transfus Med Rev* **6**, 63-92
320. Anstee, D. J., and Tanner, M. J. (1986) Structure and function of the red cell membrane sialoglycoproteins. *Br J Haematol* **64**, 211-215
321. Furthmayr, H. (1978) Glycophorins A, B, and C: a family of sialoglycoproteins. Isolation and preliminary characterization of trypsin derived peptides. *J Supramol Struct* **9**, 79-95
322. Segrest, J. P., Kahane, I., Jackson, R. L., and Marchesi, V. T. (1973) Major glycoprotein of the human erythrocyte membrane: evidence for an amphipathic molecular structure. *Arch Biochem Biophys* **155**, 167-183
323. Ada, G. L., and Stone, J. D. (1950) Electrophoretic studies of virus-red cell interaction: mobility gradient of cells treated with viruses of the influenza group and the receptor-destroying enzyme of *V. cholerae*. *Br J Exp Pathol* **31**, 263-274
324. Hassoun, H., Hanada, T., Lutchman, M., Sahr, K. E., Palek, J., Hanspal, M., and Chishti, A. H. (1998) Complete deficiency of glycophorin A in red blood cells from mice with targeted inactivation of the band 3 (AE1) gene. *Blood* **91**, 2146-2151
325. Young, M. T., and Tanner, M. J. (2003) Distinct regions of human glycophorin A enhance human red cell anion exchanger (band 3; AE1) transport function and surface trafficking. *J Biol Chem* **278**, 32954-32961
326. Shemin, D., and Rittenberg, D. (1946) The life span of the human red blood cell. *J Biol Chem* **166**, 627-636
327. Lutz, H. U., and Stringaro-Wipf, G. (1983) Senescent red cell-bound IgG is attached to band 3 protein. *Biomed Biochim Acta* **42**, S117-121
328. Groom, A. C., Schmidt, E. E., and MacDonald, I. C. (1991) Microcirculatory pathways and blood flow in spleen: new insights from washout kinetics, corrosion casts, and quantitative intravital videomicroscopy. *Scanning Microsc* **5**, 159-173; discussion 173-154

329. Buffet, P. A., Milon, G., Brousse, V., Correas, J. M., Dousset, B., Couvelard, A., Kianmanesh, R., Farges, O., Sauvanet, A., Paye, F., Ungeheuer, M. N., Ottone, C., Khun, H., Fiette, L., Guigon, G., Huerre, M., Mercereau-Puijalon, O., and David, P. H. (2006) *Ex vivo* perfusion of human spleens maintains clearing and processing functions. *Blood* **107**, 3745-3752
330. Koyama, S., Aoki, S., and Deguchi, D. (1964) Electron microscopic observations of the splenic red pulp with special reference to the pitting function. *Mie Med J* **14**, 143-188
331. Safeukui, I., Buffet, P. A., Deplaine, G., Perrot, S., Brousse, V., Ndour, A., Nguyen, M., Mercereau-Puijalon, O., David, P. H., Milon, G., and Mohandas, N. (2012) Quantitative assessment of sensing and sequestration of spherocytic erythrocytes by the human spleen. *Blood* **120**, 424-430
332. Perrotta, S., Gallagher, P. G., and Mohandas, N. (2008) Hereditary spherocytosis. *Lancet* **372**, 1411-1426
333. Cranston, H. A., Boylan, C. W., Carroll, G. L., Sutera, S. P., Williamson, J. R., Gluzman, I. Y., and Krogstad, D. J. (1984) *Plasmodium falciparum* maturation abolishes physiologic red cell deformability. *Science* **223**, 400-403
334. Dondorp, A. M., Chotivanich, K. T., Fucharoen, S., Silamut, K., Vreeken, J., Kager, P. A., and White, N. J. (1999) Red cell deformability, splenic function and anaemia in thalassaemia. *Br J Haematol* **105**, 505-508
335. Bratosin, D., Estaquier, J., Petit, F., Arnoult, D., Quatannens, B., Tissier, J. P., Slomianny, C., Sartiaux, C., Alonso, C., Huart, J. J., Montreuil, J., and Ameisen, J. C. (2001) Programmed cell death in mature erythrocytes: a model for investigating death effector pathways operating in the absence of mitochondria. *Cell Death Differ* **8**, 1143-1156
336. Lang, K. S., Lang, P. A., Bauer, C., Duranton, C., Wieder, T., Huber, S. M., and Lang, F. (2005) Mechanisms of suicidal erythrocyte death. *Cell Physiol Biochem* **15**, 195-202
337. Lang, F., Abed, M., Lang, E., and Foller, M. (2014) Oxidative stress and suicidal erythrocyte death. *Antioxid Redox Signal* **21**, 138-153
338. Kamp, D., Sieberg, T., and Haest, C. W. (2001) Inhibition and stimulation of phospholipid scrambling activity. Consequences for lipid asymmetry, echinocytosis, and microvesiculation of erythrocytes. *Biochemistry* **40**, 9438-9446
339. Lang, K. S., Duranton, C., Poehlmann, H., Myssina, S., Bauer, C., Lang, F., Wieder, T., and Huber, S. M. (2003) Cation channels trigger apoptotic death of erythrocytes. *Cell Death Differ* **10**, 249-256
340. Klarl, B. A., Lang, P. A., Kempe, D. S., Niemoeller, O. M., Akel, A., Sobiesiak, M., Eisele, K., Podolski, M., Huber, S. M., Wieder, T., and Lang, F. (2006) Protein kinase C mediates erythrocyte "programmed cell death" following glucose depletion. *Am J Physiol Cell Physiol* **290**, C244-253
341. Foller, M., Mahmud, H., Gu, S., Wang, K., Floride, E., Kucherenko, Y., Luik, S., Laufer, S., and Lang, F. (2009) Participation of leukotriene C4 in the regulation of suicidal erythrocyte death. *J Physiol Pharmacol* **60**, 135-143
342. Sopjani, M., Foller, M., Dreischer, P., and Lang, F. (2008) Stimulation of eryptosis by cadmium ions. *Cell Physiol Biochem* **22**, 245-252
343. Mahmud, H., Foller, M., and Lang, F. (2009) Arsenic-induced suicidal erythrocyte death. *Arch Toxicol* **83**, 107-113

344. Kempe, D. S., Lang, P. A., Eisele, K., Klarl, B. A., Wieder, T., Huber, S. M., Duranton, C., and Lang, F. (2005) Stimulation of erythrocyte phosphatidylserine exposure by lead ions. *Am J Physiol Cell Physiol* **288**, C396-402
345. Lang, E., Qadri, S. M., and Lang, F. (2012) Killing me softly - suicidal erythrocyte death. *Int J Biochem Cell Biol* **44**, 1236-1243
346. Lang, F., Lang, K. S., Lang, P. A., Huber, S. M., and Wieder, T. (2006) Mechanisms and significance of eryptosis. *Antioxid Redox Signal* **8**, 1183-1192
347. Lang, E., and Lang, F. (2015) Mechanisms and pathophysiological significance of eryptosis, the suicidal erythrocyte death. *Semin Cell Dev Biol* **39**, 35-42
348. Larsson, A., Hult, A., Nilsson, A., Olsson, M., and Oldenborg, P. A. (2016) Red blood cells with elevated cytoplasmic Ca^{2+} are primarily taken up by splenic marginal zone macrophages and CD207+ dendritic cells. *Transfusion* **56**, 1834-1844
349. Belcher, J. D., Beckman, J. D., Balla, G., Balla, J., and Vercellotti, G. (2010) Heme degradation and vascular injury. *Antioxid Redox Signal* **12**, 233-248
350. Kato, G. J. (2009) Haptoglobin halts hemoglobin's havoc. *J Clin Invest* **119**, 2140-2142
351. Umbreit, J. (2007) Methemoglobin--it's not just blue: a concise review. *Am J Hematol* **82**, 134-144
352. Balla, G., Vercellotti, G. M., Muller-Eberhard, U., Eaton, J., and Jacob, H. S. (1991) Exposure of endothelial cells to free heme potentiates damage mediated by granulocytes and toxic oxygen species. *Lab Invest* **64**, 648-655
353. Qian, Q., Nath, K. A., Wu, Y., Daoud, T. M., and Sethi, S. (2010) Hemolysis and acute kidney failure. *Am J Kidney Dis* **56**, 780-784
354. Woollard, K. J., Sturgeon, S., Chin-Dusting, J. P., Salem, H. H., and Jackson, S. P. (2009) Erythrocyte hemolysis and hemoglobin oxidation promote ferric chloride-induced vascular injury. *J Biol Chem* **284**, 13110-13118
355. Yang, F., Haile, D. J., Berger, F. G., Herbert, D. C., Van Beveren, E., and Ghio, A. J. (2003) Haptoglobin reduces lung injury associated with exposure to blood. *Am J Physiol Lung Cell Mol Physiol* **284**, L402-409
356. Frei, A. C., Guo, Y., Jones, D. W., Pritchard, K. A., Jr., Fagan, K. A., Hogg, N., and Wandersee, N. J. (2008) Vascular dysfunction in a murine model of severe hemolysis. *Blood* **112**, 398-405
357. Reiter, C. D., Wang, X., Tanus-Santos, J. E., Hogg, N., Cannon, R. O., 3rd, Schechter, A. N., and Gladwin, M. T. (2002) Cell-free hemoglobin limits nitric oxide bioavailability in sickle-cell disease. *Nat Med* **8**, 1383-1389
358. Kato, G. J., Steinberg, M. H., and Gladwin, M. T. (2017) Intravascular hemolysis and the pathophysiology of sickle cell disease. *J Clin Invest* **127**, 750-760
359. Vilas, G. L., Loganathan, S. K., Liu, J., Riau, A. K., Young, J. D., Mehta, J. S., Vithana, E. N., and Casey, J. R. (2013) Transmembrane water-flux through SLC4A11: a route defective in genetic corneal diseases. *Hum Mol Genet* **22**, 4579-4590
360. Ogando, D. G., Jalimarada, S. S., Zhang, W., Vithana, E. N., and Bonanno, J. A. (2013) SLC4A11 is an EIPA-sensitive Na^+ permeable pH_i regulator. *Am J Physiol Cell Physiol* **305**, C716-727
361. Jalimarada, S. S., Ogando, D. G., Vithana, E. N., and Bonanno, J. A. (2013) Ion transport function of SLC4A11 in corneal endothelium. *Invest Ophthalmol Vis Sci* **54**, 4330-4340

362. Loganathan, S. K., Schneider, H. P., Morgan, P. E., Deitmer, J. W., and Casey, J. R. (2016) Functional Assessment of SLC4A11, an Integral Membrane Protein Mutated in Corneal Dystrophies. *Am J Physiol Cell Physiol* **311**, C735-C748
363. Loganathan, S. K., and Casey, J. R. (2014) Corneal dystrophy-causing SLC4A11 mutants: suitability for folding-correction therapy. *Hum Mutat* **35**, 1082-1091
364. Kao, L., Azimov, R., Abuladze, N., Newman, D., and Kurtz, I. (2015) Human SLC4A11-C functions as a DIDS-stimulatable $H^+(OH^-)$ permeation pathway: partial correction of R109H mutant transport. *Am J Physiol Cell Physiol* **308**, C176-188
365. Zhang, W., Ogando, D. G., Bonanno, J. A., and Obukhov, A. G. (2015) Human SLC4A11 Is a Novel NH_3/H^+ Co-transporter. *J Biol Chem* **290**, 16894-16905
366. Kao, L., Azimov, R., Shao, X. M., Frausto, R. F., Abuladze, N., Newman, D., Aldave, A. J., and Kurtz, I. (2016) Multifunctional Ion Transport Properties of Human SLC4A11: Comparison of the SLC4A11-B and SLC4A11-C Variants. *Am J Physiol Cell Physiol* **311**, C820-C830
367. Takano, J., Kobayashi, M., Noda, Y., and Fujiwara, T. (2007) *Saccharomyces cerevisiae* Bor1p is a boron exporter and a key determinant of boron tolerance. *FEMS Microbiol Lett* **267**, 230-235
368. Takano, J., Noguchi, K., Yasumori, M., Kobayashi, M., Gajdos, Z., Miwa, K., Hayashi, H., Yoneyama, T., and Fujiwara, T. (2002) *Arabidopsis* boron transporter for xylem loading. *Nature* **420**, 337-340
369. Malhotra, D., Jung, M., Fecher-Trost, C., Lovatt, M., Peh, G. S. L., Noskov, S., Mehta, J. S., Zimmermann, R., and Casey, J. R. (2020) Defective cell adhesion function of solute transporter, SLC4A11, in endothelial corneal dystrophies. *Hum Mol Genet* **29**, 97-116
370. Sridhar, M. S. (2018) Anatomy of cornea and ocular surface. *Indian J Ophthalmol* **66**, 190-194
371. Meek, K. M., and Knupp, C. (2015) Corneal structure and transparency. *Prog Retin Eye Res* **49**, 1-16
372. Hanna, C., Bicknell, D. S., and O'Brien, J. E. (1961) Cell turnover in the adult human eye. *Arch Ophthalmol* **65**, 695-698
373. Tuori, A., Uusitalo, H., Burgeson, R. E., Terttunen, J., and Virtanen, I. (1996) The immunohistochemical composition of the human corneal basement membrane. *Cornea* **15**, 286-294
374. Newsome, D. A., Foidart, J. M., Hassell, J. R., Krachmer, J. H., Rodrigues, M. M., and Katz, S. I. (1981) Detection of specific collagen types in normal and keratoconus corneas. *Invest Ophthalmol Vis Sci* **20**, 738-750
375. Chen, S., Mienaltowski, M. J., and Birk, D. E. (2015) Regulation of corneal stroma extracellular matrix assembly. *Exp Eye Res* **133**, 69-80
376. Benedek, G. B. (1971) Theory of transparency of the eye. *Appl Opt* **10**, 459-473
377. Hart, R. W., and Farrell, R. A. (1969) Light scattering in the cornea. *J Opt Soc Am* **59**, 766-774
378. Meyer, K., Linker, A., Davidson, E. A., and Weissmann, B. (1953) The mucopolysaccharides of bovine cornea. *J Biol Chem* **205**, 611-616
379. Patel, S., McLaren, J., Hodge, D., and Bourne, W. (2001) Normal human keratocyte density and corneal thickness measurement by using confocal microscopy *in vivo*. *Invest Ophthalmol Vis Sci* **42**, 333-339

380. West-Mays, J. A., and Dwivedi, D. J. (2006) The keratocyte: corneal stromal cell with variable repair phenotypes. *Int J Biochem Cell Biol* **38**, 1625-1631
381. Bergmanson, J. P., Horne, J., Doughty, M. J., Garcia, M., and Gondo, M. (2005) Assessment of the number of lamellae in the central region of the normal human corneal stroma at the resolution of the transmission electron microscope. *Eye Contact Lens* **31**, 281-287
382. Radner, W., Zehetmayer, M., Aufreiter, R., and Mallinger, R. (1998) Interlacing and cross-angle distribution of collagen lamellae in the human cornea. *Cornea* **17**, 537-543
383. Muller, L. J., Pels, E., and Vrensen, G. F. (2001) The specific architecture of the anterior stroma accounts for maintenance of corneal curvature. *Br J Ophthalmol* **85**, 437-443
384. Sawada, H., Konomi, H., and Hirosawa, K. (1990) Characterization of the collagen in the hexagonal lattice of Descemet's membrane: its relation to type VIII collagen. *J Cell Biol* **110**, 219-227
385. Bourne, W. M. (2003) Biology of the corneal endothelium in health and disease. *Eye (Lond)* **17**, 912-918
386. Bourne, W. M., Nelson, L. R., and Hodge, D. O. (1997) Central corneal endothelial cell changes over a ten-year period. *Invest Ophthalmol Vis Sci* **38**, 779-782
387. Engelmann, K., Bohnke, M., and Friedl, P. (1988) Isolation and long-term cultivation of human corneal endothelial cells. *Invest Ophthalmol Vis Sci* **29**, 1656-1662
388. Reiss, G. R., Werness, P. G., Zollman, P. E., and Brubaker, R. F. (1986) Ascorbic acid levels in the aqueous humor of nocturnal and diurnal mammals. *Arch Ophthalmol* **104**, 753-755
389. Maurice, D. M. (1972) The location of the fluid pump in the cornea. *J Physiol* **221**, 43-54
390. Bonanno, J. A. (2003) Identity and regulation of ion transport mechanisms in the corneal endothelium. *Prog Retin Eye Res* **22**, 69-94
391. Feizi, S. (2018) Corneal endothelial cell dysfunction: etiologies and management. *Ther Adv Ophthalmol* **10**, 2515841418815802
392. Damkier, H. H., Nielsen, S., and Praetorius, J. (2007) Molecular expression of SLC4-derived Na^+-dependent anion transporters in selected human tissues. *Am J Physiol Regul Integr Comp Physiol* **293**, R2136-2146
393. Kao, L., Azimov, R., Shao, X. M., Abuladze, N., Newman, D., Zhekova, H., Noskov, S., Pushkin, A., and Kurtz, I. (2020) SLC4A11 function: evidence for $H^+(OH^-)$ and NH_3-H^+ transport. *Am J Physiol Cell Physiol* **318**, C392-C405
394. Zhang, W., Li, H., Ogando, D. G., Li, S., Feng, M., Price, F. W., Jr., Tennessen, J. M., and Bonanno, J. A. (2017) Glutaminolysis is Essential for Energy Production and Ion Transport in Human Corneal Endothelium. *EBioMedicine* **16**, 292-301
395. Gumbiner, B. M. (1996) Cell adhesion: the molecular basis of tissue architecture and morphogenesis. *Cell* **84**, 345-357
396. Gilmore, A. P. (2005) Anoikis. *Cell Death Differ* **12 Suppl 2**, 1473-1477
397. Siddiqui, S., Zenteno, J. C., Rice, A., Chacon-Camacho, O., Naylor, S. G., Rivera-de la Parra, D., Spokes, D. M., James, N., Toomes, C., Inglehearn, C. F., and Ali, M. (2014) Congenital hereditary endothelial dystrophy caused by *SLC4A11* mutations progresses to Harboyan syndrome. *Cornea* **33**, 247-251
398. Kirkness, C. M., McCartney, A., Rice, N. S., Garner, A., and Steele, A. D. (1987) Congenital hereditary corneal oedema of Maumenee: its clinical features, management, and pathology. *Br J Ophthalmol* **71**, 130-144

399. Klintworth, G. K. (2009) Corneal dystrophies. *Orphanet Journal of Rare Diseases* **4**, 1-38
400. Iliff, B. W., Riazuddin, S. A., and Gottsch, J. D. (2012) The genetics of Fuchs' corneal dystrophy. *Expert Rev Ophthalmol* **7**, 363-375
401. Davies, Y., Fullwood, N. J., Marcyniuk, B., Bonshek, R., Tullo, A., and Nieduszynski, I. A. (1997) Keratan sulphate in the trabecular meshwork and cornea. *Curr Eye Res* **16**, 677-686
402. Mustonen, R. K., McDonald, M. B., Srivannaboon, S., Tan, A. L., Doubrava, M. W., and Kim, C. K. (1998) *In vivo* confocal microscopy of Fuchs' endothelial dystrophy. *Cornea* **17**, 493-503
403. Bourne, W. M., Johnson, D. H., and Campbell, R. J. (1982) The ultrastructure of Descemet's membrane. III. Fuchs' dystrophy. *Arch Ophthalmol* **100**, 1952-1955
404. Wilson, S. E., Bourne, W. M., and Brubaker, R. F. (1988) Effect of dexamethasone on corneal endothelial function in Fuchs' dystrophy. *Invest Ophthalmol Vis Sci* **29**, 357-361
405. Alka, K., and Casey, J. R. (2018) Molecular phenotype of SLC4A11 missense mutants: Setting the stage for personalized medicine in corneal dystrophies. *Hum Mutat* **39**, 676-690
406. Kerem, B., Rommens, J. M., Buchanan, J. A., Markiewicz, D., Cox, T. K., Chakravarti, A., Buchwald, M., and Tsui, L. C. (1989) Identification of the cystic fibrosis gene: genetic analysis. *Science* **245**, 1073-1080
407. Quon, B. S., and Wilcox, P. G. (2015) A new era of personalized medicine for cystic fibrosis - at last! *Can Respir J* **22**, 257-260
408. Jennings, M. L., Anderson, M. P., and Monaghan, R. (1986) Monoclonal antibodies against human erythrocyte band 3 protein. Localization of proteolytic cleavage sites and stilbenedisulfonate-binding lysine residues. *J Biol Chem* **261**, 9002-9010
409. Chiu, A. M., Mandziuk, J. J., Loganathan, S. K., Alka, K., and Casey, J. R. (2015) High Throughput Assay Identifies Glafenine as a Corrector for the Folding Defect in Corneal Dystrophy-Causing Mutants of SLC4A11. *Invest Ophthalmol Vis Sci* **56**, 7739-7753
410. Malhotra, D., Loganathan, S. K., Chiu, A. M., Lukowski, C. M., and Casey, J. R. (2019) Human Corneal Expression of SLC4A11, a Gene Mutated in Endothelial Corneal Dystrophies. *Sci Rep* **9**, 9681
411. Casey, J. R., Ding, Y., and Kopito, R. R. (1995) The role of cysteine residues in the erythrocyte plasma membrane anion exchange protein, AE1. *J Biol Chem* **270**, 8521-8527
412. Lee, B. S., Gunn, R. B., and Kopito, R. R. (1991) Functional differences among nonerythroid anion exchangers expressed in a transfected human cell line. *J Biol Chem* **266**, 11448-11454
413. Cordat, E., Li, J., and Reithmeier, R. A. (2003) Carboxyl-terminal truncations of human anion exchanger impair its trafficking to the plasma membrane. *Traffic* **4**, 642-651
414. Johnson, D. E., and Casey, J. R. (2011) Cytosolic H^+ microdomain developed around AE1 during AE1-mediated Cl^-/HCO_3^- exchange. *J Physiol* **589**, 1551-1569
415. Ruetz, S., Lindsey, A. E., Ward, C. L., and Kopito, R. R. (1993) Functional activation of plasma membrane anion exchangers occurs in a pre-Golgi compartment. *J Cell Biol* **121**, 37-48
416. Notredame, C., Higgins, D. G., and Heringa, J. (2000) T-Coffee: A novel method for fast and accurate multiple sequence alignment. *J Mol Biol* **302**, 205-217

417. Arnold, K., Bordoli, L., Kopp, J., and Schwede, T. (2006) The SWISS-MODEL workspace: a web-based environment for protein structure homology modelling. *Bioinformatics* **22**, 195-201
418. Guex, N., Peitsch, M. C., and Schwede, T. (2009) Automated comparative protein structure modeling with SWISS-MODEL and Swiss-PdbViewer: a historical perspective. *Electrophoresis* **30 Suppl 1**, S162-173
419. Kiefer, F., Arnold, K., Kunzli, M., Bordoli, L., and Schwede, T. (2009) The SWISS-MODEL Repository and associated resources. *Nucleic Acids Res* **37**, D387-392
420. Biasini, M., Bienert, S., Waterhouse, A., Arnold, K., Studer, G., Schmidt, T., Kiefer, F., Cassarino, T. G., Bertoni, M., Bordoli, L., and Schwede, T. (2014) SWISS-MODEL: modelling protein tertiary and quaternary structure using evolutionary information. *Nucleic Acids Res* **42**, W252-258
421. Bowie, J. U., Luthy, R., and Eisenberg, D. (1991) A method to identify protein sequences that fold into a known three-dimensional structure. *Science* **253**, 164-170
422. Luthy, R., Bowie, J. U., and Eisenberg, D. (1992) Assessment of protein models with three-dimensional profiles. *Nature* **356**, 83-85
423. Laskowski, R. A., MacArthur, M. W., Moss, D. S., and Thornton, J. M. (1993) PROCHECK: a program to check the stereochemical quality of protein structures. *Journal of Applied Crystallography* **26**, 283-291
424. Laskowski, R. A., Rullmannn, J. A., MacArthur, M. W., Kaptein, R., and Thornton, J. M. (1996) AQUA and PROCHECK-NMR: programs for checking the quality of protein structures solved by NMR. *J Biomol NMR* **8**, 477-486
425. Glaser, F., Pupko, T., Paz, I., Bell, R. E., Bechor-Shental, D., Martz, E., and Ben-Tal, N. (2003) ConSurf: Identification of Functional Regions in Proteins by Surface-Mapping of Phylogenetic Information. *Bioinformatics* **19**, 163-164
426. Landau, M., Mayrose, I., Rosenberg, Y., Glaser, F., Martz, E., Pupko, T., and Ben-Tal, N. (2005) ConSurf 2005: the projection of evolutionary conservation scores of residues on protein structures. *Nucleic Acids Research* **33**, W299-W302
427. Ashkenazy, H., Erez, E., Martz, E., Pupko, T., and Ben-Tal, N. (2010) ConSurf 2010: calculating evolutionary conservation in sequence and structure of proteins and nucleic acids. *Nucleic Acids Research* **38**, W529-W533
428. Celniker, G., Nimrod, G., Ashkenazy, H., Glaser, F., Martz, E., Mayrose, I., Pupko, T., and Ben-Tal, N. (2013) ConSurf: Using Evolutionary Data to Raise Testable Hypotheses about Protein Function. *Israel Journal of Chemistry* **53**, 199-206
429. Davis, I. W., Leaver-Fay, A., Chen, V. B., Block, J. N., Kapral, G. J., Wang, X., Murray, L. W., Arendall, W. B., 3rd, Snoeyink, J., Richardson, J. S., and Richardson, D. C. (2007) MolProbity: all-atom contacts and structure validation for proteins and nucleic acids. *Nucleic Acids Res* **35**, W375-383
430. Chen, V. B., Arendall, W. B., 3rd, Headd, J. J., Keedy, D. A., Immormino, R. M., Kapral, G. J., Murray, L. W., Richardson, J. S., and Richardson, D. C. (2010) MolProbity: all-atom structure validation for macromolecular crystallography. *Acta Crystallogr D Biol Crystallogr* **66**, 12-21
431. Dolinsky, T. J., Nielsen, J. E., McCammon, J. A., and Baker, N. A. (2004) PDB2PQR: an automated pipeline for the setup of Poisson-Boltzmann electrostatics calculations. *Nucleic Acids Res* **32**, W665-667

432. Olsson, M. H., Sondergaard, C. R., Rostkowski, M., and Jensen, J. H. (2011) PROPKA3: Consistent Treatment of Internal and Surface Residues in Empirical pKa Predictions. *J Chem Theory Comput* **7**, 525-537
433. Sondergaard, C. R., Olsson, M. H., Rostkowski, M., and Jensen, J. H. (2011) Improved Treatment of Ligands and Coupling Effects in Empirical Calculation and Rationalization of pKa Values. *J Chem Theory Comput* **7**, 2284-2295
434. Levitt, M., Hirshberg, M., Sharon, R., and Daggett, V. (1995) Potential energy function and parameters for simulations of the molecular dynamics of proteins and nucleic acids in solution. *Computer Physics Communications* **91**, 215-231
435. Yildirim, M. A., Goh, K. I., Cusick, M. E., Barabasi, A. L., and Vidal, M. (2007) Drug-target network. *Nature biotechnology* **25**, 1119-1126
436. Sanders, C. R., and Myers, J. K. (2004) Disease-related misassembly of membrane proteins. *Annu Rev Biophys Biomol Struct* **33**, 25-51
437. Krachmer, J. H., Purcell, J. J., Jr., Young, C. W., and Bucher, K. D. (1978) Corneal endothelial dystrophy. A study of 64 families. *Arch Ophthalmol* **96**, 2036-2039
438. Vilas, G. L., Morgan, P. E., Loganathan, S. K., Quon, A., and Casey, J. R. (2011) A biochemical framework for SLC4A11, the plasma membrane protein defective in corneal dystrophies. *Biochemistry* **50**, 2157-2169
439. Vilas, G. L., Loganathan, S. K., Quon, A., Sundaresan, P., Vithana, E. N., and Casey, J. (2012) Oligomerization of SLC4A11 protein and the severity of FECD and CHED2 corneal dystrophies caused by SLC4A11 mutations. *Hum Mutat* **33**, 419-428
440. Reithmeier, R. A., and Moraes, T. F. (2015) Solute carriers keep on rockin'. *Nat Struct Mol Biol* **22**, 752-754
441. Bonar, P., and Casey, J. R. (2010) Purification of functional human Cl^-/HCO_3^- exchanger, AE1, over-expressed in *Saccharomyces cerevisiae*. *Protein Expr Purif* **74**, 106-115
442. Reva, B., Antipin, Y., and Sander, C. (2011) Predicting the functional impact of protein mutations: application to cancer genomics. *Nucleic Acids Res* **39**, e118
443. Sim, N. L., Kumar, P., Hu, J., Henikoff, S., Schneider, G., and Ng, P. C. (2012) SIFT web server: predicting effects of amino acid substitutions on proteins. *Nucleic Acids Res* **40**, W452-457
444. Pierige, F., Serafini, S., Rossi, L., and Magnani, M. (2008) Cell-based drug delivery. *Adv Drug Deliv Rev* **60**, 286-295
445. Bianconi, E., Piovesan, A., Facchin, F., Beraudi, A., Casadei, R., Frabetti, F., Vitale, L., Pelleri, M. C., Tassani, S., Piva, F., Perez-Amodio, S., Strippoli, P., and Canaider, S. (2013) An estimation of the number of cells in the human body. *Ann Hum Biol* **40**, 463-471
446. Mandal, D., Moitra, P. K., Saha, S., and Basu, J. (2002) Caspase 3 regulates phosphatidylserine externalization and phagocytosis of oxidatively stressed erythrocytes. *FEBS Lett* **513**, 184-188
447. Franco, R. S., Puchulu-Campanella, M. E., Barber, L. A., Palascak, M. B., Joiner, C. H., Low, P. S., and Cohen, R. M. (2013) Changes in the properties of normal human red blood cells during *in vivo* aging. *Am J Hematol* **88**, 44-51
448. Antonelou, M. H., Kriebardis, A. G., and Papassideri, I. S. (2010) Aging and death signalling in mature red cells: from basic science to transfusion practice. *Blood Transfus* **8 Suppl 3**, s39-47

449. Mandal, D., Mazumder, A., Das, P., Kundu, M., and Basu, J. (2005) Fas-, caspase 8-, and caspase 3-dependent signaling regulates the activity of the aminophospholipid translocase and phosphatidylserine externalization in human erythrocytes. *J Biol Chem* **280**, 39460-39467
450. Winterbourn, C. C., and Batt, R. D. (1970) Lipid composition of human red cells of different ages. *Biochimica et biophysica acta* **202**, 1-8
451. Lutz, H. U., and Fehr, J. (1979) Total sialic acid content of glycophorins during senescence of human red blood cells. *J Biol Chem* **254**, 11177-11180
452. Kadlubowski, M., and Agutter, P. S. (1977) Changes in the activities of some membrane-associated enzymes during *in vivo* ageing of the normal human erythrocyte. *Br J Haematol* **37**, 111-125
453. Jindal, H. K., Ai, Z., Gascard, P., Horton, C., and Cohen, C. M. (1996) Specific loss of protein kinase activities in senescent erythrocytes. *Blood* **88**, 1479-1487
454. Ramachandran, M., and Abraham, E. C. (1989) Age-dependent variation in the cytosol/membrane distribution of red cell protein kinase-C. *Am J Hematol* **31**, 69-70
455. Jansen, G., Hepkema, B. G., van der Vegt, S. G., and Staal, G. E. (1986) Glycolytic activity in human red cell populations separated by a combination of density and counterflow centrifugation. Evidence for an improved separation of red cells according to age. *Scand J Haematol* **37**, 189-195
456. Piomelli, S., and Seaman, C. (1993) Mechanism of red blood cell aging: relationship of cell density and cell age. *Am J Hematol* **42**, 46-52
457. Haram, S., Carriero, D., Seaman, C., and Piomelli, S. (1991) The mechanism of decline of age-dependent enzymes in the red blood cell. *Enzyme* **45**, 47-53
458. Inaba, M., and Maede, Y. (1988) Correlation between protein 4.1a/4.1b ratio and erythrocyte life span. *Biochimica et biophysica acta* **944**, 256-264
459. Linderkamp, O., and Meiselman, H. J. (1982) Geometric, osmotic, and membrane mechanical properties of density-separated human red cells. *Blood* **59**, 1121-1127
460. Dumaswala, U. J., and Greenwalt, T. J. (1984) Human erythrocytes shed exocytic vesicles *in vivo*. *Transfusion* **24**, 490-492
461. Waugh, R. E., Narla, M., Jackson, C. W., Mueller, T. J., Suzuki, T., and Dale, G. L. (1992) Rheologic properties of senescent erythrocytes: loss of surface area and volume with red blood cell age. *Blood* **79**, 1351-1358
462. Xiong, Z., Oriss, T. B., Cavaretta, J. P., Rosengart, M. R., and Lee, J. S. (2012) Red cell microparticle enumeration: validation of a flow cytometric approach. *Vox Sang* **103**, 42-48
463. Willekens, F. L., Roerdinkholder-Stoelwinder, B., Groenen-Dopp, Y. A., Bos, H. J., Bosman, G. J., van den Bos, A. G., Verkleij, A. J., and Werre, J. M. (2003) Hemoglobin loss from erythrocytes *in vivo* results from spleen-facilitated vesiculation. *Blood* **101**, 747-751
464. Willekens, F. L., Bosch, F. H., Roerdinkholder-Stoelwinder, B., Groenen-Dopp, Y. A., and Werre, J. M. (1997) Quantification of loss of haemoglobin components from the circulating red blood cell *in vivo*. *Eur J Haematol* **58**, 246-250
465. Willekens, F. L., Werre, J. M., Groenen-Dopp, Y. A., Roerdinkholder-Stoelwinder, B., de Pauw, B., and Bosman, G. J. (2008) Erythrocyte vesiculation: a self-protective mechanism? *Br J Haematol* **141**, 549-556

466. Lew, V. L., Daw, N., Etzion, Z., Tiffert, T., Muoma, A., Vanagas, L., and Bookchin, R. M. (2007) Effects of age-dependent membrane transport changes on the homeostasis of senescent human red blood cells. *Blood* **110**, 1334-1342
467. Bosman, G. J., Lasonder, E., Groenen-Dopp, Y. A., Willekens, F. L., and Werre, J. M. (2012) The proteome of erythrocyte-derived microparticles from plasma: new clues for erythrocyte aging and vesiculation. *J Proteomics* **76 Spec No.**, 203-210
468. Lutz, H. U., and Bogdanova, A. (2013) Mechanisms tagging senescent red blood cells for clearance in healthy humans. *Front Physiol* **4**, 387
469. Piomelli, S., Lurinsky, G., and Wasserman, L. R. (1967) The mechanism of red cell aging. I. Relationship between cell age and specific gravity evaluated by ultracentrifugation in a discontinuous density gradient. *J Lab Clin Med* **69**, 659-674
470. Lutz, H. U., Stammler, P., Fasler, S., Ingold, M., and Fehr, J. (1992) Density separation of human red blood cells on self forming Percoll gradients: correlation with cell age. *Biochimica et biophysica acta* **1116**, 1-10
471. Rettig, M. P., Low, P. S., Gimm, J. A., Mohandas, N., Wang, J., and Christian, J. A. (1999) Evaluation of biochemical changes during *in vivo* erythrocyte senescence in the dog. *Blood* **93**, 376-384
472. Vince, J. W., and Reithmeier, R. A. (1998) Carbonic anhydrase II binds to the carboxyl terminus of human band 3, the erythrocyte Cl^-/HCO_3^- exchanger. *J Biol Chem* **273**, 28430-28437
473. Appell, K. C., and Low, P. S. (1982) Evaluation of structural interdependence of membrane-spanning and cytoplasmic domains of band 3. *Biochemistry* **21**, 2151-2157
474. Korsgren, C., and Cohen, C. M. (1988) Associations of human erythrocyte band 4.2. Binding to ankyrin and to the cytoplasmic domain of band 3. *J Biol Chem* **263**, 10212-10218
475. Bustos, S. P., and Reithmeier, R. A. (2011) Protein 4.2 interaction with hereditary spherocytosis mutants of the cytoplasmic domain of human anion exchanger 1. *Biochem J* **433**, 313-322
476. Goel, V. K., Li, X., Chen, H., Liu, S. C., Chishti, A. H., and Oh, S. S. (2003) Band 3 is a host receptor binding merozoite surface protein 1 during the *Plasmodium falciparum* invasion of erythrocytes. *Proc Natl Acad Sci U S A* **100**, 5164-5169
477. Okoye, V. C., and Bennett, V. (1985) *Plasmodium falciparum* malaria: band 3 as a possible receptor during invasion of human erythrocytes. *Science* **227**, 169-171
478. Sherman, I. W., Eda, S., and Winograd, E. (2003) Cytoadherence and sequestration in *Plasmodium falciparum*: defining the ties that bind. *Microbes Infect* **5**, 897-909
479. Winograd, E., Eda, S., and Sherman, I. W. (2004) Chemical modifications of band 3 protein affect the adhesion of *Plasmodium falciparum*-infected erythrocytes to CD36. *Mol Biochem Parasitol* **136**, 243-248
480. Winograd, E., and Sherman, I. W. (2004) Malaria infection induces a conformational change in erythrocyte band 3 protein. *Mol Biochem Parasitol* **138**, 83-87
481. Kay, M. M., Goodman, S. R., Sorensen, K., Whitfield, C. F., Wong, P., Zaki, L., and Rudloff, V. (1983) Senescent cell antigen is immunologically related to band 3. *Proc Natl Acad Sci U S A* **80**, 1631-1635
482. Kay, M. M. (1981) Isolation of the phagocytosis-inducing IgG-binding antigen on senescent somatic cells. *Nature* **289**, 491-494

483. Turrini, F., Mannu, F., Arese, P., Yuan, J., and Low, P. S. (1993) Characterization of the autologous antibodies that opsonize erythrocytes with clustered integral membrane proteins. *Blood* **81**, 3146-3152
484. Turrini, F., Arese, P., Yuan, J., and Low, P. S. (1991) Clustering of integral membrane proteins of the human erythrocyte membrane stimulates autologous IgG binding, complement deposition, and phagocytosis. *J Biol Chem* **266**, 23611-23617
485. Kay, M. M., and Marchalonis, J. J. (1991) Molecular mapping of the active site of an aging antigen. *Adv Exp Med Biol* **307**, 303-316
486. Kay, M. M., and Lin, F. B. (1990) Molecular mapping of the active site of an aging antigen: senescent cell antigen requires lysine(s) for antigenicity and is located on an anion-binding segment of band 3 membrane transport protein. *Gerontology* **36**, 293-305
487. Kay, M. M. (1991) Band 3 in aging and neurological disease. *Ann N Y Acad Sci* **621**, 179-204
488. Zhu, Q., Lee, D. W., and Casey, J. R. (2003) Novel topology in C-terminal region of the human plasma membrane anion exchanger, AE1. *J Biol Chem* **278**, 3112-3120
489. Crandall, I., Collins, W. E., Gysin, J., and Sherman, I. W. (1993) Synthetic peptides based on motifs present in human band 3 protein inhibit cytoadherence/sequestration of the malaria parasite *Plasmodium falciparum*. *Proc Natl Acad Sci U S A* **90**, 4703-4707
490. Kay, M. M., Marchalonis, J. J., Hughes, J., Watanabe, K., and Schluter, S. F. (1990) Definition of a physiologic aging autoantigen by using synthetic peptides of membrane protein band 3: localization of the active antigenic sites. *Proc Natl Acad Sci U S A* **87**, 5734-5738
491. Wainwright, S. D., Mawby, W. J., and Tanner, M. J. (1990) The membrane domain of the human erythrocyte anion transport protein. Epitope mapping of a monoclonal antibody defines the location of a cytoplasmic loop near the C-terminus of the protein. *Biochem J* **272**, 265-268
492. Wainwright, S. D., Tanner, M. J., Martin, G. E., Yendle, J. E., and Holmes, C. (1989) Monoclonal antibodies to the membrane domain of the human erythrocyte anion transport protein. Localization of the C-terminus of the protein to the cytoplasmic side of the red cell membrane and distribution of the protein in some human tissues. *Biochem J* **258**, 211-220
493. Popov, M., Tam, L. Y., Li, J., and Reithmeier, R. A. (1997) Mapping the ends of transmembrane segments in a polytopic membrane protein. Scanning N-glycosylation mutagenesis of extracytosolic loops in the anion exchanger, band 3. *J Biol Chem* **272**, 18325-18332
494. Rivera-Santiago, R., Harper, S. L., Sriswasdi, S., Hembach, P., and Speicher, D. W. (2017) Full-Length Anion Exchanger 1 Structure and Interactions with Ankyrin-1 Determined by Zero Length Crosslinking of Erythrocyte Membranes. *Structure* **25**, 132-145
495. Erickson, H. K. (1997) Cytoplasmic disposition of aspartate 821 in anion exchanger from human erythrocytes. *Biochemistry* **36**, 9958-9967
496. Fujinaga, J., Tang, X. B., and Casey, J. R. (1999) Topology of the membrane domain of human erythrocyte anion exchange protein, AE1. *J Biol Chem* **274**, 6626-6633
497. Kuma, H., Abe, Y., Askin, D., Bruce, L. J., Hamasaki, T., Tanner, M. J., and Hamasaki, N. (2002) Molecular basis and functional consequences of the dominant effects of the

mutant band 3 on the structure of normal band 3 in Southeast Asian ovalocytosis. *Biochemistry* **41**, 3311-3320
498. Kay, M. M. (1992) Molecular mapping of human band 3 aging antigenic sites and active amino acids using synthetic peptides. *J Protein Chem* **11**, 595-602
499. Tanner, M. J. (1989) Proteolytic cleavage of the anion transporter and its orientation in the membrane. *Methods Enzymol* **173**, 423-432
500. Jarolim, P., Rubin, H. L., Zakova, D., Storry, J., and Reid, M. E. (1998) Characterization of seven low incidence blood group antigens carried by erythrocyte band 3 protein. *Blood* **92**, 4836-4843
501. Thevenin, B. J., Willardson, B. M., and Low, P. S. (1989) The redox state of cysteines 201 and 317 of the erythrocyte anion exchanger is critical for ankyrin binding. *J Biol Chem* **264**, 15886-15892
502. Zhu, Q., and Casey, J. R. (2007) Topology of transmembrane proteins by scanning cysteine accessibility mutagenesis methodology. *Methods* **41**, 439-450
503. Sekler, I., Lo, R. S., and Kopito, R. R. (1995) A conserved glutamate is responsible for ion selectivity and pH dependence of the mammalian anion exchangers AE1 and AE2. *J Biol Chem* **270**, 28751-28758
504. Dahr, W., Beyreuther, K., Kordowicz, M., and Kruger, J. (1982) N-terminal amino acid sequence of sialoglycoprotein D (glycophorin C) from human erythrocyte membranes. *Eur J Biochem* **125**, 57-62
505. Bengtsson, D. C., Sowa, K. M., and Arnot, D. E. (2008) Dual fluorescence labeling of surface-exposed and internal proteins in erythrocytes infected with the malaria parasite *Plasmodium falciparum*. *Nature protocols* **3**, 1990-1996
506. Schluter, K., and Drenckhahn, D. (1986) Co-clustering of denatured hemoglobin with band 3: its role in binding of autoantibodies against band 3 to abnormal and aged erythrocytes. *Proc Natl Acad Sci U S A* **83**, 6137-6141
507. Criddle, R. S. (1964) Dissociation and Separation of Gamma Globulin into Subunits. *Arch Biochem Biophys* **106**, 101-111
508. Jin, Y., Liang, Q., and Tieleman, D. P. (2020) Interactions between Band 3 Anion Exchanger and Lipid Nanodomains in Ternary Lipid Bilayers: Atomistic Simulations. *J Phys Chem B* **124**, 3054-3064
509. Wang, D. N., Kuhlbrandt, W., Sarabia, V. E., and Reithmeier, R. A. (1993) Two-dimensional structure of the membrane domain of human band 3, the anion transport protein of the erythrocyte membrane. *EMBO J* **12**, 2233-2239
510. Askin, D., Bloomberg, G. B., Chambers, E. J., and Tanner, M. J. (1998) NMR solution structure of a cytoplasmic surface loop of the human red cell anion transporter, band 3. *Biochemistry* **37**, 11670-11678
511. Goujon, M., McWilliam, H., Li, W., Valentin, F., Squizzato, S., Paern, J., and Lopez, R. (2010) A new bioinformatics analysis tools framework at EMBL-EBI. *Nucleic Acids Res* **38**, W695-699
512. Taylor, A. M., Zhu, Q., and Casey, J. R. (2001) Cysteine-directed cross-linking localizes regions of the human erythrocyte anion-exchange protein (AE1) relative to the dimeric interface. *Biochem J* **359**, 661-668
513. Van Regenmortel, M. H. (1989) Structural and functional approaches to the study of protein antigenicity. *Immunol Today* **10**, 266-272

514. Geysen, H. M., Rodda, S. J., and Mason, T. J. (1986) The delineation of peptides able to mimic assembled epitopes. *Ciba Found Symp* **119**, 130-149
515. Kay, M. M. (1984) Localization of senescent cell antigen on band 3. *Proc Natl Acad Sci U S A* **81**, 5753-5757
516. Casey, J. R., Pirraglia, C. A., and Reithmeier, R. A. (1992) Enzymatic deglycosylation of human Band 3, the anion transport protein of the erythrocyte membrane. Effect on protein structure and transport properties. *J Biol Chem* **267**, 11940-11948
517. Groves, J. D., and Tanner, M. J. (1994) Role of N-glycosylation in the expression of human band 3-mediated anion transport. *Mol Membr Biol* **11**, 31-38
518. Casey, J. R., and Reithmeier, R. A. F. (1991) Transport activity of deglycosylated band 3, the anion exchange protein of the erythrocyte membrane. *Glycoconj* **8**, 138
519. Hatae, H., Inaka, K., Okamura, R., Furubayashi, N., Kamo, M., Kobayashi, T., Abe, Y., Iwata, S., and Hamasaki, N. (2018) Crystallization of Human Erythrocyte Band 3, the anion exchanger, at the International Space Station "KIBO". *Anal Biochem* **559**, 91-93
520. Lassen, U. V., and Sten-Knudsen, O. (1968) Direct measurements of membrane potential and membrane resistance of human red cells. *J Physiol* **195**, 681-696
521. Jay, A. W., and Burton, A. C. (1969) Direct measurement of potential difference across the human red blood cell membrane. *Biophys J* **9**, 115-121
522. Hoffman, J. F., and Laris, P. C. (1974) Determination of membrane potentials in human and *Amphiuma* red blood cells by means of fluorescent probe. *J Physiol* **239**, 519-552
523. Cheng, K., Haspel, H. C., Vallano, M. L., Osotimehin, B., and Sonenberg, M. (1980) Measurement of membrane potentials (psi) of erythrocytes and white adipocytes by the accumulation of triphenylmethylphosphonium cation. *J Membr Biol* **56**, 191-201
524. De Vecchis, D., Reithmeier, R. A. F., and Kalli, A. C. (2019) Molecular Simulations of Intact Anion Exchanger 1 Reveal Specific Domain and Lipid Interactions. *Biophys J* **117**, 1364-1379
525. MacCallum, J. L., Bennett, W. F., and Tieleman, D. P. (2007) Partitioning of amino acid side chains into lipid bilayers: results from computer simulations and comparison to experiment. *J Gen Physiol* **129**, 371-377
526. Wimley, W. C., and White, S. H. (1996) Experimentally determined hydrophobicity scale for proteins at membrane interfaces. *Nat Struct Biol* **3**, 842-848
527. MacCallum, J. L., Bennett, W. F., and Tieleman, D. P. (2011) Transfer of arginine into lipid bilayers is nonadditive. *Biophys J* **101**, 110-117
528. Okubo, K., Hamasaki, N., Hara, K., and Kageura, M. (1991) Palmitoylation of cysteine 69 from the COOH-terminal of band 3 protein in the human erythrocyte membrane. Acylation occurs in the middle of the consensus sequence of F--I-IICLAVL found in band 3 protein and G2 protein of Rift Valley fever virus. *J Biol Chem* **266**, 16420-16424
529. Ensinck, A., Biondi, C. S., Marini, A., Garcia Borras, S., Racca, L. L., Cotorruelo, C. M., and Racca, A. L. (2006) Effect of membrane-bound IgG and desialysation in the interaction of monocytes with senescent erythrocytes. *Clin Exp Med* **6**, 138-142
530. Khansari, N., and Fudenberg, H. H. (1983) Phagocytosis of senescent erythrocytes by autologous monocytes: requirement of membrane-specific autologous IgG for immune elimination of aging red blood cells. *Cell Immunol* **78**, 114-121
531. Garratty, G. (1991) Effect of cell-bound proteins on the *in vivo* survival of circulating blood cells. *Gerontology* **37**, 68-94

532. Low, P. S., Waugh, S. M., Zinke, K., and Drenckhahn, D. (1985) The role of hemoglobin denaturation and band 3 clustering in red blood cell aging. *Science* **227**, 531-533
533. Beppu, M., Mizukami, A., Nagoya, M., and Kikugawa, K. (1990) Binding of anti-band 3 autoantibody to oxidatively damaged erythrocytes. Formation of senescent antigen on erythrocyte surface by an oxidative mechanism. *J Biol Chem* **265**, 3226-3233
534. Brandts, J. F., and Jacobson, B. S. (1983) A general mechanism for transmembrane signalling, based on clustering. in *Survey and Sythesis of Pathology Research* (S. Carter, A. G. ed.), Basel. pp 107-114
535. Arashiki, N., Kimata, N., Manno, S., Mohandas, N., and Takakuwa, Y. (2013) Membrane peroxidation and methemoglobin formation are both necessary for band 3 clustering: mechanistic insights into human erythrocyte senescence. *Biochemistry* **52**, 5760-5769
536. Alderman, E. M., Fudenberg, H. H., and Lovins, R. E. (1981) Isolation and characterization of an age-related antigen present on senescent human red blood cells. *Blood* **58**, 341-349
537. Durocher, J. R., Payne, R. C., and Conrad, M. E. (1975) Role of sialic acid in erythrocyte survival. *Blood* **45**, 11-20
538. Biondi, C., Cotorruelo, C., Ensinck, A., Garcia Borras, S., Racca, L., and Racca, A. (2002) Senescent erythrocytes: factors affecting the aging of red blood cells. *Immunol Invest* **31**, 41-50
539. Gallo, P., Goncalves, R., and Mosser, D. M. (2010) The influence of IgG density and macrophage Fc (gamma) receptor cross-linking on phagocytosis and IL-10 production. *Immunol Lett* **133**, 70-77
540. Huang, H., Kuenze, G., Smith, J. A., Taylor, K. C., Duran, A. M., Hadziselimovic, A., Meiler, J., Vanoye, C. G., George, A. L., Jr., and Sanders, C. R. (2018) Mechanisms of KCNQ1 channel dysfunction in long QT syndrome involving voltage sensor domain mutations. *Sci Adv* **4**, eaar2631
541. Anderson, C. L., Kuzmicki, C. E., Childs, R. R., Hintz, C. J., Delisle, B. P., and January, C. T. (2014) Large-scale mutational analysis of Kv11.1 reveals molecular insights into type 2 long QT syndrome. *Nat Commun* **5**, 5535
542. Kaushal, S., and Khorana, H. G. (1994) Structure and function in rhodopsin. 7. Point mutations associated with autosomal dominant retinitis pigmentosa. *Biochemistry* **33**, 6121-6128
543. Stenson, P. D., Mort, M., Ball, E. V., Evans, K., Hayden, M., Heywood, S., Hussain, M., Phillips, A. D., and Cooper, D. N. (2017) The Human Gene Mutation Database: towards a comprehensive repository of inherited mutation data for medical research, genetic diagnosis and next-generation sequencing studies. *Hum Genet* **136**, 665-677
544. Chang, M. H., DiPiero, J., Sonnichsen, F. D., and Romero, M. F. (2008) Entry to "HCO_3^- tunnel" revealed by SLC4A4 human mutation and structural model. *J Biol Chem* **283**, 18402-18410
545. Wang, H. W., and Wang, J. W. (2017) How cryo-electron microscopy and X-ray crystallography complement each other. *Protein science : a publication of the Protein Society* **26**, 32-39
546. Venien-Bryan, C., Li, Z., Vuillard, L., and Boutin, J. A. (2017) Cryo-electron microscopy and X-ray crystallography: complementary approaches to structural biology and drug discovery. *Acta Crystallogr F Struct Biol Commun* **73**, 174-183

547. Shoemaker, S. C., and Ando, N. (2018) X-rays in the Cryo-Electron Microscopy Era: Structural Biology's Dynamic Future. *Biochemistry* **57**, 277-285
548. Stock, D., Leslie, A. G., and Walker, J. E. (1999) Molecular architecture of the rotary motor in ATP synthase. *Science* **286**, 1700-1705
549. Palczewski, K., Kumasaka, T., Hori, T., Behnke, C. A., Motoshima, H., Fox, B. A., Le Trong, I., Teller, D. C., Okada, T., Stenkamp, R. E., Yamamoto, M., and Miyano, M. (2000) Crystal structure of rhodopsin: A G protein-coupled receptor. *Science* **289**, 739-745
550. Toyoshima, C., Nakasako, M., Nomura, H., and Ogawa, H. (2000) Crystal structure of the calcium pump of sarcoplasmic reticulum at 2.6 Å resolution. *Nature* **405**, 647-655
551. Unwin, N. (2005) Refined structure of the nicotinic acetylcholine receptor at 4 Å resolution. *J Mol Biol* **346**, 967-989
552. Midgett, C. R., and Madden, D. R. (2007) Breaking the bottleneck: eukaryotic membrane protein expression for high-resolution structural studies. *J Struct Biol* **160**, 265-274
553. Graham, F. L. (1987) Growth of 293 cells in suspension culture. *J Gen Virol* **68 (Pt 3)**, 937-940
554. Reeves, P. J., Kim, J. M., and Khorana, H. G. (2002) Structure and function in rhodopsin: a tetracycline-inducible system in stable mammalian cell lines for high-level expression of opsin mutants. *Proc Natl Acad Sci U S A* **99**, 13413-13418
555. Fan, S., Maguire, C. A., Ramirez, S. H., Bradel-Tretheway, B., Sapinoro, R., Sui, Z., Chakraborty-Sett, S., and Dewhurst, S. (2005) Valproic acid enhances gene expression from viral gene transfer vectors. *J Virol Methods* **125**, 23-33
556. Backliwal, G., Hildinger, M., Kuettel, I., Delegrange, F., Hacker, D. L., and Wurm, F. M. (2008) Valproic acid: a viable alternative to sodium butyrate for enhancing protein expression in mammalian cell cultures. *Biotechnol Bioeng* **101**, 182-189
557. Higgins, M. K., Demir, M., and Tate, C. G. (2003) Calnexin co-expression and the use of weaker promoters increase the expression of correctly assembled Shaker potassium channel in insect cells. *Biochimica et biophysica acta* **1610**, 124-132
558. Zhang, L., Wu, G., Tate, C. G., Lookene, A., and Olivecrona, G. (2003) Calreticulin promotes folding/dimerization of human lipoprotein lipase expressed in insect cells (Sf21). *J Biol Chem* **278**, 29344-29351
559. Fourneau, J. M., Cohen, H., and van Endert, P. M. (2004) A chaperone-assisted high yield system for the production of HLA-DR4 tetramers in insect cells. *J Immunol Methods* **285**, 253-264
560. Mariati, Ho, S. C., Yap, M. G., and Yang, Y. (2010) Evaluating post-transcriptional regulatory elements for enhancing transient gene expression levels in CHO K1 and HEK293 cells. *Protein Expr Purif* **69**, 9-15
561. Al-Fageeh, M. B., Marchant, R. J., Carden, M. J., and Smales, C. M. (2006) The cold-shock response in cultured mammalian cells: harnessing the response for the improvement of recombinant protein production. *Biotechnol Bioeng* **93**, 829-835
562. Goehring, A., Lee, C. H., Wang, K. H., Michel, J. C., Claxton, D. P., Baconguis, I., Althoff, T., Fischer, S., Garcia, K. C., and Gouaux, E. (2014) Screening and large-scale expression of membrane proteins in mammalian cells for structural studies. *Nature protocols* **9**, 2574-2585

563. Chng, Z., Peh, G. S., Herath, W. B., Cheng, T. Y., Ang, H. P., Toh, K. P., Robson, P., Mehta, J. S., and Colman, A. (2013) High throughput gene expression analysis identifies reliable expression markers of human corneal endothelial cells. *PLoS One* **8**, e67546
564. Alka, K., and Casey, J. R. (2018) Ophthalmic Nonsteroidal Anti-Inflammatory Drugs as a Therapy for Corneal Dystrophies Caused by SLC4A11 Mutation. *Invest Ophthalmol Vis Sci* **59**, 4258-4267
565. Hunte, C., and Michel, H. (2002) Crystallisation of membrane proteins mediated by antibody fragments. *Curr Opin Struct Biol* **12**, 503-508
566. Vitrac, H., MacLean, D. M., Jayaraman, V., Bogdanov, M., and Dowhan, W. (2015) Dynamic membrane protein topological switching upon changes in phospholipid environment. *Proc Natl Acad Sci U S A* **112**, 13874-13879
567. Vitrac, H., MacLean, D. M., Karlstaedt, A., Taegtmeyer, H., Jayaraman, V., Bogdanov, M., and Dowhan, W. (2017) Dynamic Lipid-dependent Modulation of Protein Topology by Post-translational Phosphorylation. *J Biol Chem* **292**, 1613-1624
568. Marquette, A., and Bechinger, B. (2018) Biophysical Investigations Elucidating the Mechanisms of Action of Antimicrobial Peptides and Their Synergism. *Biomolecules* **8**, 18
569. Andreev, O. A., Karabadzhak, A. G., Weerakkody, D., Andreev, G. O., Engelman, D. M., and Reshetnyak, Y. K. (2010) pH (low) insertion peptide (pHLIP) inserts across a lipid bilayer as a helix and exits by a different path. *Proc Natl Acad Sci U S A* **107**, 4081-4086
570. LeBarron, J., and London, E. (2016) Highly Hydrophilic Segments Attached to Hydrophobic Peptides Translocate Rapidly across Membranes. *Langmuir* **32**, 10752-10760
571. Seurig, M., Ek, M., von Heijne, G., and Fluman, N. (2019) Dynamic membrane topology in an unassembled membrane protein. *Nat Chem Biol* **15**, 945-948
572. Hoffmann, C., Gaietta, G., Bunemann, M., Adams, S. R., Oberdorff-Maass, S., Behr, B., Vilardaga, J. P., Tsien, R. Y., Ellisman, M. H., and Lohse, M. J. (2005) A FlAsH-based FRET approach to determine G protein-coupled receptor activation in living cells. *Nat Methods* **2**, 171-176
573. Griffin, B. A., Adams, S. R., and Tsien, R. Y. (1998) Specific covalent labeling of recombinant protein molecules inside live cells. *Science* **281**, 269-272
574. Brown, I. W., Jr., and Eadie, G. S. (1953) An analytical study of *in vivo* survival of limited populations of animal red blood cells tagged with radioiron. *J Gen Physiol* **36**, 327-343
575. Burwell, E. L., Brickley, B. A., and Finch, C. A. (1953) Erythrocyte life span in small animals; comparison of two methods employing radioiron. *Am J Physiol* **172**, 718-724
576. Bale, W. F., Yuile, C. L., and et al. (1949) Hemoglobin labeled by radioactive lysine; erythrocyte life cycle. *J Exp Med* **90**, 315-320
577. Weissman, S. M., Waldmann, T. A., and Berlin, N. I. (1960) Quantitative measurement of erythropoiesis in the dog. *Am J Physiol* **198**, 183-186
578. Christian, J. A., Rebar, A. H., Boon, G. D., and Low, P. S. (1996) Methodologic considerations for the use of canine *in vivo* aged biotinylated erythrocytes to study RBC senescence. *Exp Hematol* **24**, 82-88
579. Branch, D. R., Shulman, I. A., Sy Siok Hian, A. L., and Petz, L. D. (1984) Two distinct categories of warm autoantibody reactivity with age-fractionated red cells. *Blood* **63**, 177-180

580. Bloch, E. M., Sakac, D., Branch, H. A., Cserti-Gazdewich, C., Pendergrast, J., Pavenski, K., and Branch, D. R. (2015) Western immunoblotting as a new tool for investigating direct antiglobulin test-negative autoimmune hemolytic anemias. *Transfusion* **55**, 1529-1537
581. Iwamoto, S., Kamesaki, T., Oyamada, T., Okuda, H., Kumada, M., Omi, T., Takahashi, J., Tani, Y., Omine, M., and Kajii, E. (2001) Reactivity of autoantibodies of autoimmune hemolytic anemia with recombinant rhesus blood group antigens or anion transporter band3. *Am J Hematol* **68**, 106-114
582. Victoria, E. J., Pierce, S. W., Branks, M. J., and Masouredis, S. P. (1990) IgG red blood cell autoantibodies in autoimmune hemolytic anemia bind to epitopes on red blood cell membrane band 3 glycoprotein. *J Lab Clin Med* **115**, 74-88
583. Leddy, J. P., Falany, J. L., Kissel, G. E., Passador, S. T., and Rosenfeld, S. I. (1993) Erythrocyte membrane proteins reactive with human (warm-reacting) anti-red cell autoantibodies. *J Clin Invest* **91**, 1672-1680
584. Janvier, D., Sellami, F., Missud, F., Fenneteau, O., Vilmer, E., Cartron, J., and Rohrlich, P. (2002) Severe autoimmune hemolytic anemia caused by a warm IgA autoantibody directed against the third loop of band 3 (RBC anion-exchange protein 1). *Transfusion* **42**, 1547-1552
585. Barker, R. N., Casswell, K. M., Reid, M. E., Sokol, R. J., and Elson, C. J. (1992) Identification of autoantigens in autoimmune haemolytic anaemia by a non-radioisotope immunoprecipitation method. *Br J Haematol* **82**, 126-132
586. Kalfa, T. A. (2016) Warm antibody autoimmune hemolytic anemia. *Hematology Am Soc Hematol Educ Program* **2016**, 690-697
587. Salama, A. (2015) Treatment Options for Primary Autoimmune Hemolytic Anemia: A Short Comprehensive Review. *Transfus Med Hemother* **42**, 294-301
588. Howie, H. L., and Hudson, K. E. (2018) Murine models of autoimmune hemolytic anemia. *Curr Opin Hematol* **25**, 473-481
589. Bosman, G. J., Werre, J. M., Willekens, F. L., and Novotny, V. M. (2008) Erythrocyte ageing *in vivo* and *in vitro*: structural aspects and implications for transfusion. *Transfus Med* **18**, 335-347
590. Luten, M., Roerdinkholder-Stoelwinder, B., Schaap, N. P., de Grip, W. J., Bos, H. J., and Bosman, G. J. (2008) Survival of red blood cells after transfusion: a comparison between red cells concentrates of different storage periods. *Transfusion* **48**, 1478-1485
591. Dinkla, S., Novotny, V. M., Joosten, I., and Bosman, G. J. (2012) Storage-induced changes in erythrocyte membrane proteins promote recognition by autoantibodies. *PLoS One* **7**, e42250
592. Kay, M. (2005) Immunoregulation of cellular life span. *Ann N Y Acad Sci* **1057**, 85-111